INAUGURAL-DISSERTATION

zur
Erlangung der Doktorwürde
der
Gesamtfakultät für Mathematik,
Ingenieur- und Naturwissenschaften
der
Ruprecht-Karls-Universität
Heidelberg

Vorgelegt von

Lukas Heynck

Tag der mündlichen Prüfung:

Mittwoch, 16.11.2022

Title

Design and synthesis of anionic and photoactivatable fluorophores for super-resolution microscopy

Gutachter: Prof. Dr. Joachim P. Spatz

Prof. Dr. Dr. h. c. mult. Stefan W. Hell

Abstract

Small-molecule fluorophores have been recognized as efficient fluorescent reporters in the visualisation of living cells by super-resolution fluorescence microscopy. Much of the ongoing research focuses on positively charged fluorophores derived from rhodamine cores, which show good photostability, live cell permeability and brightness, but suffer from undesired off-targeting and accumulation in certain cell compartments, most typically in mitochondria. Furthermore, their derived photoactivatable labels often rely photocleavable caging groups as bulky nitrobenzene-type groups or α-diazoketones, which may generate toxic or non-fluorescent by-products.

Negatively charged fluorophores derived from fluorescein present a valuable alternative with no off-targeting and accumulation. Fluorescein, one of the oldest synthetic fluorophores, is a brightly emitting fluorophore, but suffer from low photostability and cell membrane-impermeability compared to rhodamines. Therefore, the rational design of negatively charged small-molecule fluorophores with improved photostability and cell membrane-permeability is desired. Furthermore, photoactivatable fluorescein analogs may rely on photocleavable groups less bulky than the nitrobenzene-types, which favor the generation of non-toxic by-products, and hence useful for super-resolution microscopy. Within this thesis, the chemical design and synthetic methods to access these fluorophores are discussed and the photophysical properties and application in live-cell super- resolution fluorescence microscopy examined.

As a result of this work, *N*-cyanorhodamines have been identified as bathochromically shifted fluorescein analogs with improved photostability and cell-permeability. Three different synthetic methods have been developed to access these fluorophores from known aryl triflates or iodides. Unlike tetramethylrhodamine, *N*-cyanorhodamines demonstrate no off-targeting affinity. Based on these fluorophores, fluorescent ligands for self-labeling protein tags HaloTag and SNAP-tag have been prepared and applied in combination with commercially available labels in multi-color confocal and stimulated emission depletion microscopy.

The second part of this thesis explores several different strategies to access photoactivatable fluorescein analogs bearing no or smallest possible photocleavable group. Protection of negatively charged fluorophores with photocleavable groups resulted in *N*-tetrazinylrhodamines and mercaptofluorans as unstable or non-photoactivatable compounds. On the other hand, a synthetic route towards 3,6-dihydroxyxanthones on previously described caging-group-free photoactivatable PaX dyes has been established. Efficient photoactivation of these compounds indicated their potential for future application in single-molecule localisation imaging and as enzymatic sensor activity probes.

In conclusion, it was demonstrated that negatively charged fluorescein analogs represents a valuable addition to the toolkit of live cell-compatible fluorescent dyes. Within this work, *N*-cyanorhodamines as highly photostable and cell membrane-permeable fluorescein derivatives and hydroxy analogs of PaX dyes as photoactivatable analogs of fluoresceins have been prepared. The application of such dyes as fluorophores in live cell imaging has been demonstrated.

Zusammenfassung

Fluoreszente Molekülen bieten effiziente Fluoreszenzmarker für die optische Nanoskopie und Visualisierung lebender Zellen. Die Entwicklung neuartiger Fluoreszenzfarbstoffe fokussiert sich primär auf positiv geladene Rhodamine. Diese zeichnen sich durch hohe Photostabilität, Zellpermeabilität und Helligkeit aus. Dem gegenüber weisen sie Fluoreszenzartefakte auf und akkumulieren in Zellregionen wie den Mitochondrien. Des Weiteren basieren photoaktivierbare Rhodamine zumeist auf sterisch anspruchsvollen Nitrobenzol oder α-Diazoketonverbindungen, welche toxische oder nicht fluoreszente Nebenprodukte bilden.

Negativ geladene Fluoresceinderivate stellen eine mögliche Alternative dar um Fluoreszenzartefakte und Akkumulieren in Zellregionen vorzubeugen. Fluorescein, eins der ältesten synthetischen Fluorophore, weißt hohe Helligkeit, aber auch geringe Photostabilität und Zellpermeabilität im Vergleich zu Rhodaminen auf. Hierbei kann das rationale Design von Fluoreszenzmolekülen negativ geladene Fluorophore mit erhöhter Photostabilität und Zellpermeabilität hervorbringen. Desweiteren vermögen negativ geladene, photoaktivierbare Fluorophore, die nicht auf sterisch anspruchsvolle Gruppen wie Nitrobenzolen basieren, potentiel nicht-toxische Photoprodukte zu erzeugen. Im Rahmen dieser Thesis werden Fluoresceinderivate in Hinblick auf ihre chemische Darstellung, ihre photophysiklaischen Eigenschaften und ihre Anwendbarkeit in der optischen Nanoskopie an lebenden Zellen evaluiert.

Der erste Teil dieser Thesis beschreibt die Entwicklung von *N*-Cyanorhodaminen. Die bathocrom verschobenen Fluoresceinderivate zeichnen sich durch erhöhte Photostabilität und Zellpermabilität aus und Abwesenheit von Fluoreszenzartefakten aus. Ausgehend von Aryltriflaten wurden verschiedene Syntheserouten entwickelt und Konjugate zu dem HaloTag-Ligand dargestellt. Diese wurden erfolgreich mit kommerziell erhältlichen Fluoreszenzmarkern eingesetzt, um Strukturen lebender Zellen mit Konfokal- und STED Mikroskopie zu beobachten.

Der zweite Teil dieser Thesis evaluiert verschiedene Strategien in der Darstellung photoaktivierbarer Fluoresceinderivate. *N*-Tetrazinylrhodamine und Mercaptofluorane wurden als negativ geladene, photoaktivierbare Fluorophore entwickelt. Allerdings erwiesen sich diese Verbindungen als inert zu Licht oder generell instabil. Des Weiteren wurden 3,6-Dihydroxyxanthone basierend auf zuvor beschriebenen PaX Verbindungen dargestellt. Diese Verbindungen sind photoaktivierbar und zeigen eine potentielle Anwendbarkeit in der optischen Nanoskopie Mikroskopie sowie als photoaktivierbare Sensorproben.

Zusammengefasst stellen negativ geladene Fluoresceinderivate eine interessante Alternative zu den etablierten und positiv geladene Rhodaminen dar. Im Rahmen dieser Thesis haben dabei *N*-Cyanorhodamine und neuartige PaX-Derivate ihrer Anwendbarkeit in der Fluoreszenzmikroskopie lebender Zellen demonstriert.

Acknowledgement

First I like to thank Prof. Dr. Stefan W. Hell for the unique opportunity to work and complete my PhD in his group, the Department of Optical Nanoscopy at the Max-Planck Institute for Medical Research (MPI MR). Thank you not only for your guidance and inspiration, but also the strong, supportive, and interdisciplinary working environment you create and hold in our group.

My sincere gratitude goes to Prof. Dr. Joachim Spatz for being my first supervisor and examiner. Thank you also for being part of my thesis advisory committee (TAC) and helpful discussions within the TAC meeting.

I thank Dr. Vladimir Belov for being part of my thesis advisory committee and his scientific advice and feedback during the TAC meetings.

My sincere thanks goes to Dr. Alexey Butkevich for being my scientific supervisor and for all his training, support, and guidance. I am grateful, that I could learn from your experience and enjoyed the research we did in our lab. Whenever there was a question, your door was open.

I thank Dr. Richard Lincoln for the great time we had in the lab together. You constantly supported me and I will miss our scientific and non-scientific debates inside and outside the lab.

I thank Dr. Jessica Matthias for her constant support and introducing me to the field of nanoscopy and biology. Your door was always open to launch you with all kinds of ideas or questions.

I thank Dr. Mariano Bossi for great discussions, concepts, and explanations on how to measure a fluorophore. I am thankful I could learn from your spectroscopic expertise.

I thank Dr. Jade Cottam Jones for all the discussions on science, career, and administration. Thank you for all your support and scientific guidance during my PhD.

I thank Dr. Elisa D'Este and Dr. Michael Dasbach for their support and comments on science, scientific writing, and science-related projects and for sharing their experience.

I also like to acknowledge all the people who made all the scientific research in our institute possible. I acknowledge Dr. Sebastian Fabritz and his team of the MS core facility from MPI MR for recording the mass spectra. I acknowledge Carmen Grosskurth, Dr. Richard Wombacher and their team for maintaining and granting access to the NMR equipment in the MPI MR. I acknowledge Alena Fischer from MPI MR for her assistance in cell culturing and cytotoxicity testing. I also like to acknowledge Prof. Kai Johnsson and his group (Department of Chemical Biology, MPI MR) for granting access to a Quantaurus-QY instrument. I acknowledge Dr. Miroslaw Tarnawski and his team (Protein Expression and Characterization facility, MPI MR) for the HaloTag7 protein samples. And I thank Dr. Elisa D'Este and her team (Optical Microscopy facility, MPI MR) for using their Abberior expert line STED microscope to test our labels.

I also like to acknowledge Prof. Stefan Jakobs (Max Planck Institute for Multidisciplinary Sciences, Georg-August-Universität Göttingen) for U-2 OS-Vim-Halo cells, the European Molecular Biology Laboratory (Heidelberg) for U-2 OS-CRISPR-NUP96-Halo clone #252 cells, and Prof. Karsten Rippe (German Cancer Research Center and BioQuant, Heidelberg) for pSNAP-PMLIII plasmids.

A special thanks goes to all the members and former members in Office R258 (now: E1.102, accessed 29.28.2022). We had a great time together, and I am thankful for all you for the, scientific, non-scientific, and funny discussions we shared during office work.

I also thank all my fellow colleagues of the Department of Optical Nanoscopy for the great time we had together in different labs, offices, and parties. While working alongside, there has always been a great exchange of thought, ideas, and inspirations.

Last but not least, I must express my gratitude to my parents, family, and friends. Your constant support helps me throughout my path with all the heights and depths, and I would not be where I am without you.

Especially, I must thank you, Ziregul Sait Kyzy, for your help, being my partner, and just be there, if I need you. I love you and I cannot wait to walk the road ahead with you on my side.

Publication

L. Heynck, J. Matthias, M. L. Bossi, A. N. Butkevich, S. W. Hell, *Chem. Sci.* **2022**, *13*, 8297–8306.

This work has been published and parts of it are reproduced in this thesis from Ref.[1] with permission from the Royal Society of Chemistry.

Table of Contents

List of Abbrevations

Numbers

2-ME 2-methoxyethanol.

A

AM acetoxymethyl.

AMCA 7-amino-4-methylcoumarin-3-acetic acid.

aq. aqueous.

B

BSA bovine serum albumin.

BTMG 2-tert-butyl-1,1,3,3-tetramethylguanidine.

C

CHAPS 3-[(3-cholamidopropyl)-dimethylammonio]-1-propansulfonate.

CLSM confocal laser scanning microscopy.

CTAB cetyltrimethylammonium bromide.

CW continuous wave.

D

DAPI 4',6-diamidino-2-phenylin-dole.

DEG diethylene glycol.

DIPEA *N*,*N*-diisopropylethylamine.

DMEM Dulbecco's modified Eagleś medium.

DMI 1,3-dimethyl-2-imidazolidinon.

dSTORM direct stochastic optical reconstruction microscopy.

E

ER endoplasmic reticulum.

ESI electronspray ionisation.

ETDS energy transfer to a dark state.

F

FBS fetal bovine serum.

FP fluorescence polarization.

G

gHSQC gradient-selective heteronuclear single quantum coherence.

H

HATU 1-[bis(dimethylamino)methylene]-1H-1,2,3-triazolo[4,5-b]pyridinium 3-oxide hexafluorophosphate.

HEPES 4-(2-hydroxyethyl)-1-piperazineethanesulfonic acid.

HPLC high-performance liquid chromatography.

HRMS high resolution mass spectroscopy.

HSQC heteronuclear single quantum coherence.

I

IEDDA inverse electron-demand Diels–Alder.

L

LCMS liquid chromatography-mass spectrometry.

M

MINFLUX minimal photon fluxes.

MOM methoxymethyl.

MS mass spectroscopy.

MTBD 7-methyl-1,5,7-triazabicyclo[4.4.0]dec-5-ene.

N

NA numerical aperture.

NIR near-infrared.

NMR nuclear magnetic resonance.

P

PAGE polyacrylamide gel electrophoresis.

PALM photo activated localization microscopy.

PaX photoactivatable xanthone.

PaX(–) negatively charged, photoactivatable xanthone.

PBS phosphate-buffered saline.

PLE porcine liver esterase.

ppm parts per million.

PSF point spread function.

S

sat. saturated.

SD standard deviation.

SDS sodium dodecyl sulfate.

SMLM single-molecule localization microscopy.

SRM super-resolution microscopy.

STED stimulated emission depletion.

STORM stochastic optical reconstruction microscopy.

T

TCP targeted coordinate pattern.

TICT twisted intramolecular charge transfer.

TLC thin layer chromatography.

TMR tetramethylrhodamine.

TX100 Triton X-100.

U

UV ultraviolet.

Chapter 1

Introduction

Super-resolution microscopy (SRM) holds the potential to visualize cellular structures with nanometer-scale resolution.[2,3] The different fluorescence microscopy techniques rely on small fluorescent reporters, which are labeling the structure of interest and are examined during optical imaging.[4] While the resolution in other fluorescence microscopy techniques such as confocal imaging is limited by the diffraction limit,[5] SRM achieves nanometer-scale resolution by control of the ON-OFF states of the fluorescent reporter.[3,6] The mechanism behind controlling the ON-OFF states varies from technique to technique and requires specially designed fluorescent reporters for each of the different SRM techniques.[2,6,7]

Unlike the methods relying on sample fixation by design, such as electron microscopy[8,9] or expansion microscopy,[10,11] SRM techniques (for example stimulated emission depletion (STED),[12] photo activated localization microscopy (PALM)[13], and minimal photon fluxes (MINFLUX)[14]) allow imaging and visualisation of living cells. Therefore, it is essential that the fluorescent reporter is biocomparable, cell membrane-permeable and non-toxic.[15,16] A key advantage of optical imaging is the molecular specificity in detecting a specific structure of interest such as, for example, a protein.[7,16] Accordingly, the design of fluorescent reporters allowing bioorthogonal labeling strategies such as non-canonical amino acid labeling[17] and using the self-labeling protein-tags[18] is highly desirable.

The design and synthesis of small-molecule fluorophores offers a pallet of fluorescent markers meeting the criteria of both SRM, live-cell imaging, and targeted-approached labeling.[7,15,19] By chemical transformations, specially designed small-molecule fluorophores are accessible with control of their ON-OFF state in SRM and biocomparability for live-cell imaging.[6,7] Furthermore, chemical transformations lead to the design of

probes applicable in targeted-approached, bioorthogonal labeling strategies.[19]

Triarylmethane dyes as rhodamines,[20,21] rhodols,[22] and fluoresceins[23] have been intensively studied as small-molecule fluorophores. Positively charged rhodamine probes are widely used in SRM and live-cell imaging, due to their good photostability[24] and cell membrane-permeability.[15] Fine-tuning of the absorption and emission expanded the scope of rhodamines and granted access to fluorophores emissive from the visible to near-infrared (NIR) range.[20] In particular NIR-emitting fluorophores feature improved tissue penetration, reduced photodamage and phototoxicity, and lower background during imaging.[15,19,25]

On the other hand, rhodamines are prone to accumulate in cell compartments such as mitochondria,[26] causing undesired off-targeting labeling artifacts. Accumulation in the mitochondria can also result in cytotoxic effect, as in case of Rhodamine 123[27] and Rhodamine 6G.[28] Furthermore, the photoactivatable fluorescent labels developed from rhodamine cores often rely on bulky photocleavable caging groups such as nitrobenzenyl carbamates[29,30] or α-diazoketones[31] and may generate potentially toxic or non-fluorescent by-products. While in the development of improved small-molecule fluorophores much of the ongoing research focuses on positively charged rhodamine dyes, negatively charged fluorescein-type dyes may present a viable alternative .

Fluorescein (firstly described by Baeyer in 1871[32]) is a brightly emitting fluorophore, but its emission is hypsochromically shifted by $\sim$ 60 nm compared to tetramethylrhodamine (TMR).[33] The disadvantages of fluoresceins as compared to rhodamine dyes are their generally low photostability[24] and cell membrane-impermeability.[34] Functionalized fluorescein derivatives have be developed as the fluorinated analog OregonGreen[35] with improved photostability and cell-permeant probes bearing enzymatically cleavable *O*-protecting groups.[36–38] The further development of fluorescein-type molecules may lead to negatively charged fluorescent reporters with no off-targeting and accumulation found for rhodamines, and with improved photostability and cell membrane-permeability without additional installation of fluorines or *O*-protecting groups. Photocleavable *O*-protecting groups may also render fluorecein-type molecules photoactivatable and extend to scope of photocleavable caging groups, which are less bulky and form non-toxic by-products than those based on nitrobenzene-type cages.[29,30].

This thesis comprises both the design and synthetic methodology to access photocontrollable and photostable fluorescent molecules inspired by negatively charged fluorescein and the applicability of these molecules in super-resolution live-cell imaging techniques as STED, PALM, and MINFLUX.

Chapter 1 and 2 describe the general scientific background behind the project within this thesis. Design principles of small-molecule fluorophores required for different SRM techniques (STED, PALM, MINFLUX) are discussed along with bioorthogonal labeling strategies and development of sensor probes. Furthermore, the general principles of design and synthesis of triarylmethane dyes will be overviewed.

Chapter 3 describes the materials and methods used within this thesis.

Chapter 4 introduces *N*-cyanorhodamines as photostable, cell-permeant, bathochromically shifted fluorescein analogs. First, the development of synthetic methods to access *N*-cyanorhodamine dyes and probes for live-cell imaging will be described. Next, the photophysical properties of *N*-cyanorhodamines will be presented together with the application of probes in live-cell imaging. This work has been published and parts of it are reproduced from Ref.[1] with permission from the Royal Society of Chemistry.

Chapter 5 presents the development of photocaged molecules generating negatively charged fluorophores and is comprised of in three sub-projects. First, the synthesis of *N*-(tetrazinyl)rhodamines and their attempted photoconversion to *N*-cyanorhodamines is described. Second, the synthesis and evaluation of thiocarbonyl analogs of fluoresceins and rhodols as photoactivatable probes is discussed. Lastly, a new group of previously reported photoactivatable xanthone (PaX) dyes[39] is described in which the 3,6-amino groups on the xanthone core were substituted by hydroxy groups. The photoactivated form of these compounds should hold the potential to increase the color-range of PaX dyes and enable further diversification by installation of enzymatically cleavable *O*-protecting groups.

Chapter 6 presents a summary of the projects and a conclusion discussing the future perspectives for negatively charged small-molecule fluorophores and the derived photoactivatable probes.

Chapter 2

Literature review

2.1 Overcoming the diffraction limit in super-resolution microscopy

Optical imaging allows *in vitro*, *in vivo*, and *ex vivo* imaging of biological samples.[40] Structures of different sizes can be studied from macroscopy to microscopy level,[41] as well as down to the single-molecule level.[2,42] Additionally, multi-dimensional imaging and visualisation of molecular dynamics by contrast and sensor molecules[40,42] highlights optical imaging as a powerful tool in biological studies.

Optical imaging is fundamentally based on the interaction of light and matter.[42] A molecule may absorb light and re-emit it in form of light (fluorescence, phosphorescence), sound (acoustic waves),[43] or a non-irradiative pathway.[42,44] In fluorescence microscopy, fluorescent markers emit photons upon irradiation, which are detected by the microscope. Since the fluorescent markers emit against a dark, non-emissive background, fluorescence microscopy features low background and low loading of fluorescent markers.[4]

2.1.1 Confocal imaging and the diffraction limit

Light and matter may interact in form of absorption, emission, or scattering. Scattering is a phenomenon which alters the direction and spectrum of the light[42] and fundamentally limits resolution and tissue penetration in optical imaging.[41] Minsky envisions to overcome this issue by not allowing the scattered light to enter or exit. According

to him "an ideal microscope would examine each point"[45] individually. He developed the confocal microscope (patented in 1966[46]), in which two pinholes limit the field of view and create an effective confocal point. Hereby, blurring by light scattering and background signal are reduced.[47]

Confocal imaging and confocal laser scanning microscopy (CLSM) mark a powerful technique in the visualisation of living cells[5] due to the reduced background and the possibility to raster the sample via lateral and axial direction.[47] However, the resolution is limited by the diffraction limit formulated by Abbe and Rayleigh in 19th century.[5,47,48]

In imaging, the intensity distribution detected from a single fluorophore is described as a point spread function (PSF).[5] When light passes through a pinhole, it broadens by diffraction and causes a pattern of the shape of an Airy disk (Figure 2.1). This diffraction pattern has an intensity maximum in the center with further local maxima (outer rings).[48,49] These blurred intensity profiles may overlap and, thereby, prevent discrimination between individual fluorophores close to each other.

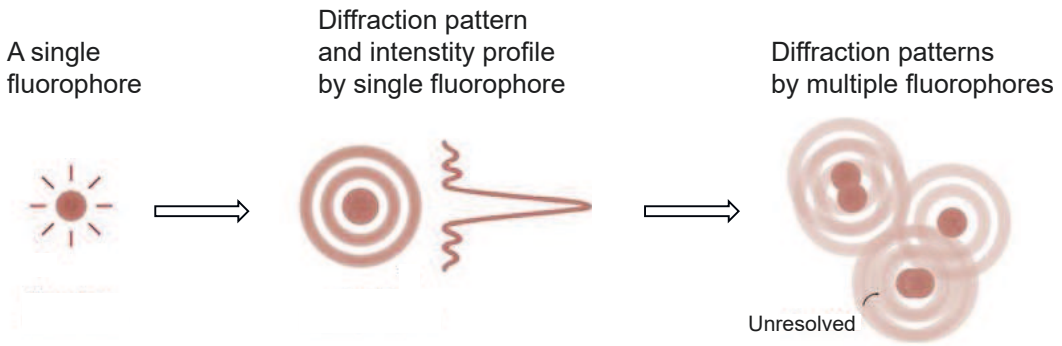

Figure 2.1 – Diffraction limit illustrated with Airy disks. A/C) Adapted by permission from Oxford University Press: Genetics[49], © (2021)

The maximal diffraction-limited resolution is quantified by the Abbe limit in equation 2.1:[5]

$$d = \frac{\lambda}{2n \cdot \sin(\alpha)} = \frac{\lambda}{2 \cdot NA} \tag{2.1}$$

with: d = lateral resolution; λ = wavelength of the light in the medium; n = refraction index of the medium; α = half opening angle of the objective; and NA = numerical aperture combining refraction index and half opening angle.

According to equation 2.1, the resolution is limited by the wavelength of the light. Using light in the visible range (400–700nm) limits the lateral resolution to the hundreds of nanometers. For example, light of λ = 400 nm results in a lateral resolution of 150 nm (NA = 1.4).[3]

2.1.2 The deterministic approach: STED microscopy

The diffraction limit allows resolution in fluorescence microscopy only to about half the wavelength of light. With SRM techniques, this limit can be surpassed.[2] The diffraction limit is based on overlapping PSFs of fluorophores close to each other (see Figure 2.1). SRM distinguished between these fluorophores by control of their fluorescent ON-OFF states, so that only one fluorophore emits at one time.[3,50] Hereby, SRM enables resolution below the diffraction limit to the nanometer scale. For the development and realisation of fluorescence super-resolution microscopy, Eric Betzig, Stefan W. Hell, and William E. Moerner were rewarded with the Nobel Prize in Chemistry 2014.[51]

STED microscopy[12,52] developed by Hell and coworkers was one of the first SRM techniques allowing subdiffractive resolution. Herein, control of the ON-OFF state of fluorophores was achieved by stimulated emission. Figure 2.2 illustrates the difference to diffraction limited CLSM. In CLSM, a laser (blue color) excites all fluorophores (marked as green stars) in the confocal point (Figure 2.2A) resulting in diffraction limited visualisation of HeLa cells (Figure 2.2B). In STED, a depletion laser (red color) is used in addition to an excitation laser (blue color) (Figure 2.2C). Hereby, already excited fluorophores are de-excited (marked as white stars) with a shaped depletion beam by the process of stimulated emission. Only fluorophores (marked as remaining green star) in the center of the donut-shaped depletion area can emit light. Since position and shape of the depletion laser is always known, well-defined PSFs of fluorophores are obtained by rastering the sample.[5,50]

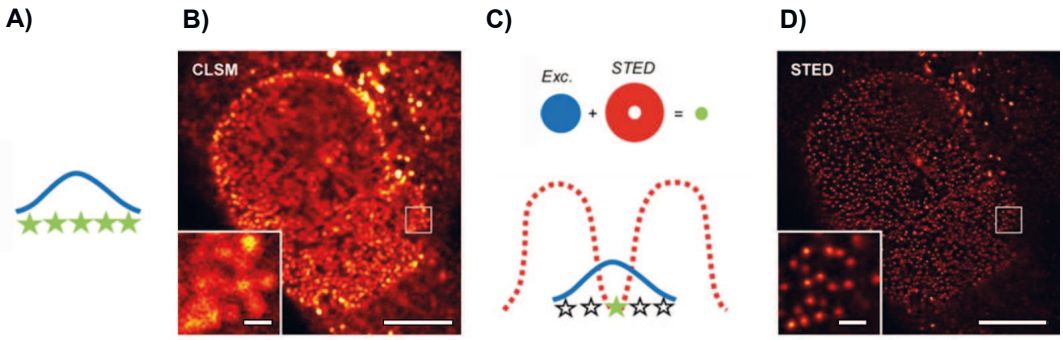

Figure 2.2 – Principle of STED microscopy. A) Confocal imaging is diffraction limited. Fluorophores close to each other cannot be distinguished. C) STED imaging overcomes diffraction limit by de-excitation of the outer fluorophores with a depletion laser. Only centrally positioned fluorophores are emitting. (B/D) Confocal and STED imaging of HeLa cell stained with primary antibodies against the nuclear pore complex protein Nup153 and secondary antibodies conjugated with label ATTO647N. Scale bars: 5 µm (insets: 0.5 µm). (A/C) Adapted by permission from Springer Nature Customer Service Centre GmbH: Springer Nature[3], © (2021) (B/D) Adapted by permission from Ref.[5].

Generally, red depletion layers are applied to de-exite at the bathochromic end of the fluorophore's emission spectrum to reduce photobleaching and re-excitation by low $S_0 \rightarrow S_1$ cross-section.[5,53]

The resolution of STED mircoscopy is described in equation 2.2:[3]

$$\Delta r = \frac{\Delta}{\sqrt{1 + I_{max}/I_s}} \tag{2.2}$$

with Δr = lateral resolution; Δ = FWHM of diffraction limited PSF; I_{max} = peak intensity of the STED depletion laser; and I_s = threshold intensity required for saturated depletion of fluorophores.

Based to equation 2.2, resolution in STED increased with the intensity of the depletion laser. Accordingly, this type of microscopy rely on photostable fluorophores, which undergo many excitation and de-excitation cycles without photobleaching.[3,54] In "The 2015 super-resolution microscopy roadmap", the fluorescent probes is even described as "the limiting factor".[2] In particular, rhodamines as Atto647N and KK114[55] perform well in STED due to their good photostability[24] and high brightness and have been intensively employed in the past.[20]

Further improvements in STED imaging are the development of 2-color STED and CW STED which imposes less strict requirement on the fluorescent dyes.[5]

2.1.3 The stochastic approach: single-molecule localisation microscopy

Another approach to overcome the diffraction limit is offered by single-molecule localization microscopy (SMLM) techniques as PALM[13] and stochastic optical reconstruction microscopy (STORM)[56] which are based on the precise localization of single fluorescent molecules. While STED is a deterministic approach, in which it is well defined where fluorophores are emissive or not, SMLM is a stochastic approach, in which a random fluorophore emit photons for a time period. Control over the ON and OFF state of the fluorescent molecules is essential so only a small fraction of molecules is fluorescent at a time to prevent overlapping PSFs.[6]

Scheme 2.1 gives an overview of different design principle for PALM and STORM.

In STORM, fluorophores undergo a repetitive cycle of activation, localisation, and deactivation.[57] This can be accomplished by addition of external blinking buffers, for example in direct stochastic optical reconstruction microscopy (dSTORM).[58] Hereby,

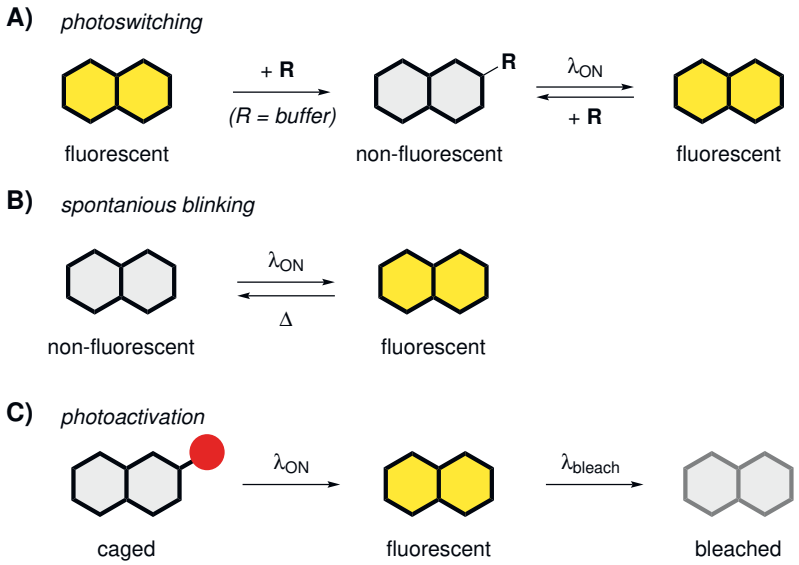

Scheme 2.1 – (A) Photoswitchable, (B) spontaneous blinking, and (C) photoactivatable fluorophores for SMLM. R corresponds to a reactive component in the imaging buffer (such as a thiol or reducing agent).[6]

the molecule is forced into an OFF state (Scheme 2.1A). Reversible activation by light, followed by re-addition of a reactive buffer component (R) results in blinking behavior.[57] However, this is undesirable in *in vivo* imaging, since the biological sample is perturbed with an artificial buffer. Therefore, spontaneously blinking dyes Scheme 2.1B) as HMSiR[59] have been developed, which are pH dependant and do no require addition of blinking buffers.[3]

In PALM, the fluorophore is initially non-fluorescent, which can be accomplished with photoactivatable or "caged" fluorophores containing photolabile "caging" groups. Caged fluorophores are initially weakly or non-fluorescent. Irradiation with a suitable wavelength λ_{ON} cleaves off the photolabile caging group in an irreversible photoreaction (Scheme 2.1C).[60,61] After localization, the fluorophores in the ON state are photobleached with a suitable wavelength λ_{bleach}, before photoactivation of the next fraction of molecules.[6] Design of new dyes is desired with different λ_{ON} and which are spectrally separated.[3]

This light-controlled, irreversible $OFF \rightarrow ON \rightarrow OFF$ approach is less complex to realize and superior to the spontaneous, reversible $OFF \leftrightarrow ON$ approach with photoswitchable fluorophores used in dSTORM, if the latter require additional blinking buffers.[6,57] Photoactivatable fluorophores containing photolabile "caging" groups will be discussed in Chapter 2.3.1 (22).

The precision of the localisation in SMLM can be estimated based on equation 2.3[6]

$$\sigma_{loc} \geq \frac{\sigma_0}{\sqrt{N}} \tag{2.3}$$

with σ_{loc} = precision of the localisation; σ_0 = SD of the PSF; N = number of photons detected during localisation.

According to equation 2.3, high localization precision in SMLM relies on high Photon numbers N, which requires long measurement times and bright fluorophores undergoing many ON-OFF cycles.

2.1.4 Combining the advantages of STED and SMLM in MINFLUX

While the classic SRM techniques push down the resolution to the tens of nanometers, recently published MINFLUX[14,62,63] achieves 1–5 nm resolution. MINFLUX combines the strengths of coordinate-targeted and stochastic SRM techniques,[63] illustrated in Figure 2.3.

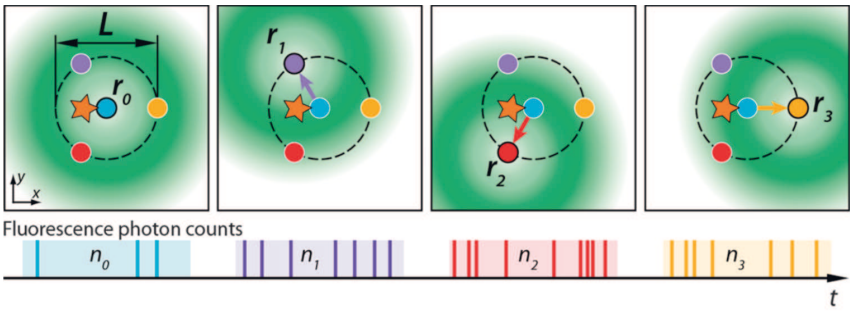

Figure 2.3 – Localisation of a fluorophore (orange star) using a donut-shaped excitation beam (green) in MINFLUX. Four coordinates (blue, violett, red, yellow) are assigned forming a targeted coordinate pattern (TCP) of a diameter L and photon counts are measured while excitation laser is applied on each individual coordinate. From Balzarotti *et al*[62] (2017). Reprinted with permission from AAAS.

In a similar manner to STED, MINFLUX uses a donut-shaped laser beam (green shadow) to excite the fluorophore (marked as orange star), which is at an unknown position. No emission occurs, if the fluorophore is positioned at the center of the donut-shaped laser beam, where the laser intensity is zero. To determine the position of the fluorophore, the excitation laser beam is applied at different coordinates forming a TCP of a diameter L with an optional midpoint.[63] For example, the excitation laser beam is applied at four coordinates (blue, violet, red, yellow) in Figure 2.3 and photon counts are collected at each coordinate. Since the position of the excitation laser beam is always known throughout the process, it can be used as reference to determine the position of the fluorophore based on the measured photon counts using localization algorhithms.[62]

The SD of the localisation is given by equation 2.4:[63]

$$\sigma \geq \frac{L}{4 \cdot \sqrt{N}} \tag{2.4}$$

with L = diameter of TCP; and N = number of photons detected during localisation.

According to equation 2.4, the localisation precision is dependant the number of detected photon N as in SMLM techniques, but also on the diameter L of the applied TCP. After the first localisation to estimate the position of the fluorophore, further measurements with smaller diameters L will increase the localisation precision. Thereby, the position of a fluorophore can be determined by iterative localisations with decreasing diameters L.[14]

As a coordinate-deterministic method, MINFLUX does not rely on measuring a large number of photons N for a precise localisation as other camera-based approaches.[14] With certain modifications, MINFLUX allows 3D imaging and multi-color imaging in fixed and living cells.[14] Furthermore, this allows micro-second range tracking due to short measurement times.[63] Recently, Remmel *et al*. demonstrated the localisation of spontaneously-blinking dyes with ON-times (1-3 ms) by MINFLUX.[64]

2.2 Small-molecule fluorophores in live-cell imaging

In fluorescence microscopy, biological samples are visualized by examination of fluorescent markers such as small-molecule fluorophores.[4] Therefore, the fluorophore must fulfill two criteria for an accurate visualisation:

1. The fluorescent marker is labeling the structure of interest exclusively and with high specificity.

2. The fluorescent marker is fluorescent under the cellular condition in the biological sample.

For the first criterion, a series of labeling techniques have been developed (Subsection 2.2.1). The second criterion is used in the development of sensor probes. These fluorescent markers change their photophysical properties in presence of an analyte enabling the visualisation of dynamic processes (Subsection 2.2.2).

2.2.1 Labeling the structure of interest

Small-molecule fluorophores conjugated to ligands have been designed to bind reversibly or irreversibly to biomolecules and cellular structures.[7,15] The different labeling strategies determine the perturbation,[16], the distance of the fluorophore to the structure of interest (linkage error),[6] and the incubation time and working concentrations of the label[17] for the biological sample. Figure 2.4 provides and overview a different labeling strategies relevant in the context of this thesis.

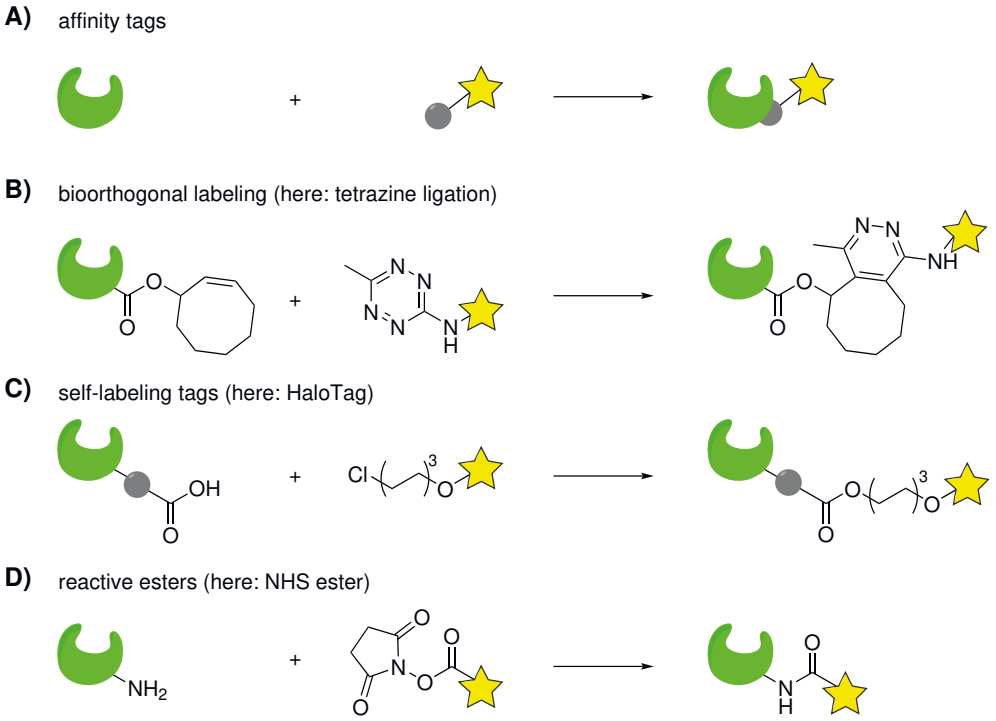

Figure 2.4 – Overview of different labeling strategies of fluorohores (yellow star) to proteins (green). Adapted by permission from Elsevier: Molecular Cell,[16], © (2015)

Labels such as Mitotracker, Hoechst, and other bind to the structure of interest based on their molecular interactions (Figure 2.4A). Mitotracker probes[65] are often based on positively charged fluorophores based on rhodamines, which are prone to accumulate into the mitochondria.[26] ER Tracker[66] is attached to the drug glibenclamide targeting the K^+ channels in the endoplasmic reticulum (ER).[19] The DNA stains DAPI[67] and Hoechst 33342[68] bind strongly to adenine–thymine-rich sequences of double-stranded DNA forming fluorescent complexes to stain the chromatin in the nucleus. To label F-actin, fluorophores attached to peptides as phalloidin[69] or Lifeact[70] have been developed to bind specifically to F-actin of the cell cytoskeleton.

Alternatively, bioorthogonal reactions allow site-selective protein modification in living systems. First, a protein is functionalized with a bioorthogonal reporter by chemical, biochemical or genetic methods. Then, bioorthogonal reporter reacts in a bioorthogo-

nal reaction with a reactive ligand to label the protein, for example with a fluorophore (Figure 2.4B). Herein, the inverse electron-demand Diels–Alder (IEDDA) reaction of strained alkynes (bioorthogonal reporter) and tetrazines (reactive ligand) presents one of the fastest bioorthogonal reactions so far $(k \sim 1 - 10^6 M^{-1} s^{-1})$.[17] For example, the Staudinger ligation $(k \sim 10^{-3} M^{-1} s^{-1})$ is $\sim$ 9 magnitudes of orders slower. Furthermore, the IEDDA reaction does not require external, toxic additives as copper in the CuAAC reaction.[17]

Tetrazines efficiently quench the fluorescence of conjugated fluorophores which is attributed to a energy transfer to a dark state (ETDS) mechanism.[71] Upon reaction with a strained alkyne, a pyridazine is formed and the fluorescence of conjugated fluorophore is recovered (Figure 2.4B). This effect led to the developement of no-wash labels.[72,73]

A common problem of the IEDDA reaction is the high chemical reactivity of the tetrazines, especially containing the electron-withdrawing substituents. To overcome this issue, less reactive dihydrotetrazine probes have been developed, which form the reactive tetrazine upon irradiation (e.g. by a photocleavable group or an external photo-catalysis). Such approaches give additional spatiotemporal control over the labeling process by light.[74,75]

Another protein modification strategy via bioorthogonal reactions is provided by self-labeling protein tags (Figure 2.4C). Here, the protein of interest is expressed as a fusion protein with a self-labeling tag. This protein tag has a bioorthogonal reactivity, forming a covalent bond with its ligand.[15,18] For example, the SNAP-tag protein is an engineered O^6-alkylguanine-DNA alkyltransferase. Its natural function is the repair of O^6-alkylguanine in damaged DNA by transferring the alkyl group to an active cystein. Using directed evolution strategy, the engineered SNAP-tag protein transfers the fluorophore and irreversibly binds it to the protein.[76] In a similar manner, HaloTag,[77] an modified haloalkane dehalogenase, reacts with chloroalkanes in a S_N2 reaction forming a covalent bond illustrated in Figure 2.4C.

The labeling kinetics of self-labeling protein tag with small molecule fluorescent ligands can be obtained by measuring fluorescence polarization (FP) changes during labeling. Biochemical reactions between the reactive ligand and the protein tags generally range between $\sim 10^3 - 10^9 M^{-1} s^{-1}$, with a lot of variation depending on the nature of ligand, protein tag and fluorophore.[78]

Reactive esters (Figure 2.4D) are a general approach to label exposed amino groups of the protein. However, this approach suffers from unselective labeling of biomolecules compared the methods described above.[79]

2.2.2 Measuring dynamics with sensor probes

Fluorescent sensor probes allow the visualisation of certain analytes and dynamic processes in live-cell imaging.[80,81] Sensors have been derived from small-molecule fluorophores to report metal ions,[82,83] the pH,[84,85] or enzymatic activity[36,86] in biological samples. Within this thesis, turn-on sensor probes interacting with enzymes as analytes will be discussed. Herein, a protecting group on an initially non- or weakly fluorescent molecule is cleaved by the enzyme (the analyte) generating a fluorescent product (Scheme 2.2A).[87] Importantly, the sensor must visualize the interaction with the designated analyte exclusively. Therefore, no signal must be generated in case of no interaction with the designated analyte, or in case of interaction with another analytes.[81]

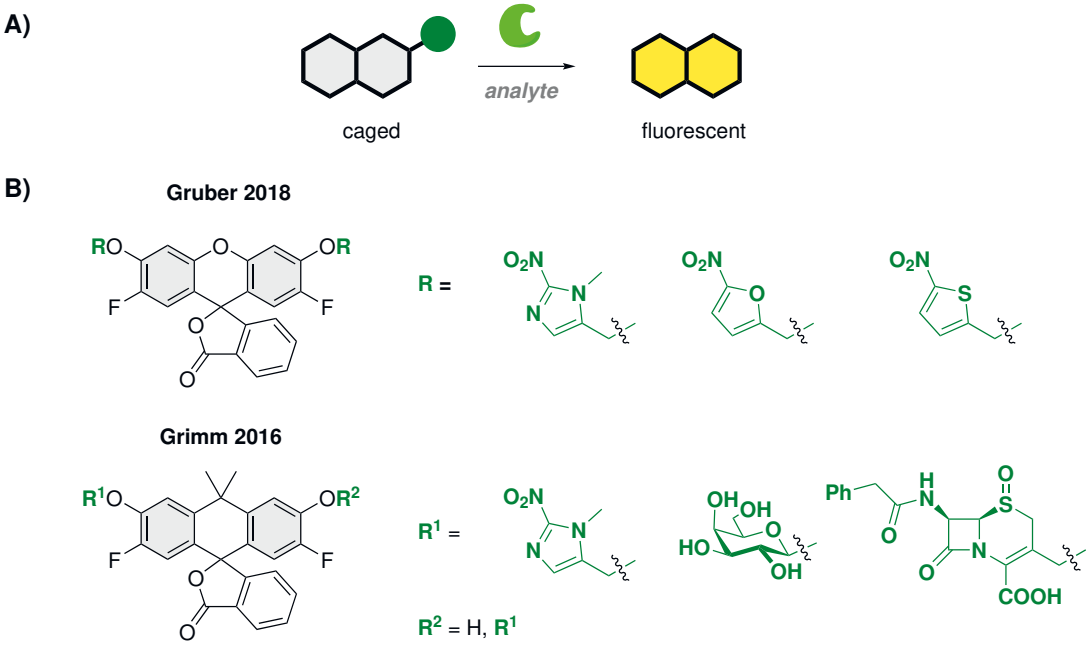

Scheme 2.2 – Sensor probes (A) Principle of a turn-on sensor probe. After cleavage of the protecting group by the analtye (here: an enzyme) a fluorescent product is generated. (B) Turn-on sensor probes bearing enzymatically cleavable *O*-protecting groups developed by Gruber *et al*.[36] and Grimm *et al*.[86].

Various enzymatically cleavable protecting groups have been explored in the design of turn-on sensor probes (Scheme 2.2B) Gruber *et al*. developed several OregonGreen derivatives bearing different *O*-protecting groups, which are cleavable by *E. coli* nitroreductase or its engineered variants. Hereby, the enzymatic activity to cleave the *O*-protecting group depends on both the sensor probe and the enzyme.[36] In a similar manner, Grimm *et al*. designed sensor probes based on VirginiaOrange against β-galactosidase, nitroreductase, and β-lactamase enzymes. These probes have either one *O*-protecting group to monitor the activity of a single enzyme or two independent *O*-protecting groups to visualise the activity of two enzymes within one sensing area.[86]

enzymatically cleavable protecting groups have been further used to alter the properties of photoactivatable fluorophore used in PALM imaging (Scheme 2.3A). Halabi *et al*. designed a rhodol derivative with an enzymatically cleavable *O*-acetyl group (highlighted in green) and a photolabile α-diazoketone (highlighted in red).[88] Before removal of the *O*-acetyl group (e.g. by an enzyme), the rhodol derivative is photoconverted to a non-fluorescent, dark product (Path A). Only if the probe is pre-reacted with carboxylesterases, its photoconversion yields the fluorescent product (Path B). This combination of enzymatically cleavable and photolabile protecting groups led to the design of photoactivatable sensor probes applicable in SRM.[88,89]

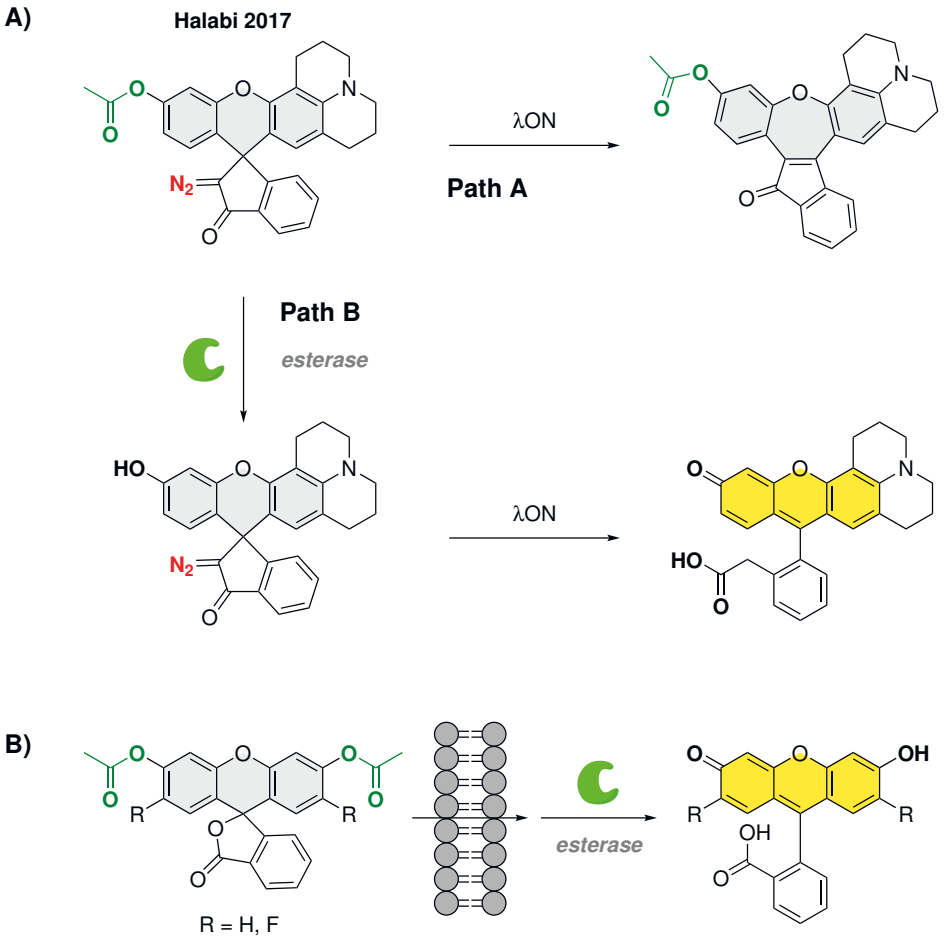

Scheme 2.3 – Sensor probes (A) Photoactivatable sensor[88] probe bearing both enzymatically cleavable and photolabile protecting groups. (B) *O*-Acetylated fluorescein analogs[37,38] as a modification to induce cell permeability.

As some fluorescein-based probes are not cell-permeant,[34] enzymatically cleavable groups have been installed on fluorescein derivatives as a modification to induce cell permeability. For example, *O*-acetylated, non-fluorescent fluorescein analogs can pass through the cell membrane. The *O*-acetyl groups are then cleaved *in situ* by cell esterases to the corresponding fluorescent fluoresceins.[37,38]

2.3 Design and synthesis of small-molecule fluorophores

Small-molecule fluorophores are accessible by chemical transformations. This enables diversification of their chemical structure which directs affect their photophysical behavior and other properties behaviors. Fine-tuning of small-molecule fluorophores, as triarylmethane dyes, makes them valuable source of fluorescent markers in live-cell imaging and different SRM techniques.[7,19]

Rhodamines, fluoresceins, and rhodols are triarylmethane dyes,[90] which all share a fluoran core[91] with an amino and/or hydroxyl group in position 3' and 6' (Figure 2.5). A common modification strategy for along rhodamines and fluoresceins is the replacement of the bridging oxygen with dimethylmethylene and dimethylsilylene. These analogs are commonly named carbofluoresceins/-rhodamines[33] and Si-fluoresceins/rhodamines.[92] Within this thesis, these terms will be used for respective triarylmethane dyes and their derivatives.

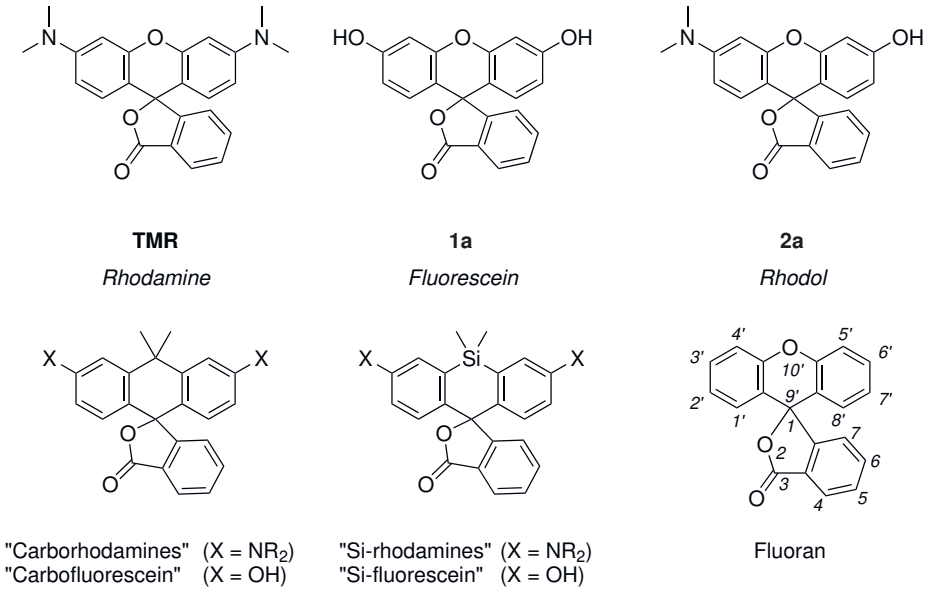

Figure 2.5 – Chemical structures and naming conventions of rhodamines, rhodols, fluroesceins, their bridge-substituted analogs,[33,92] and numbering of fluoran.[91]

2.3.1 Fine-tuning of triarylmethane dyes

Rhodamines

Due to their good photostability[24] and cell membrane-permeability, positively charged rhodamine probes are widely used in SRM and live-cell imaging. Systematic studies of fine-tuning their absorption and emission expanded the scope of available rhodamines and granted access to fluorophores emitting from the blue-green to NIR range.[20] In particular red-emissive and NIR fluorophores generally provide improved tissue penetration, reduced photodamage and phototoxicity, and lower background by reducing auto-fluorescence, which are important considerations when choosing fluorescent probes for live-cell imaging.[15,19,25]

Color-tuning of rhodamines can be realized by alkylation or installation of saturated fused rings. However, these approaches bring along increased bulkiness and lipophilicity.[20] An alternative approach is the substitution of the bridging oxygen by other units as dimethylmethylene and dimethylsilylene (see Figure 2.5, p. 16). Due to conjugation between the σ^* orbital of the installed C-atom and the π^* orbital of the fluorophore, the LUMO orbital in carbo-rhodamine is stabilized resulting in bathochromically shifted derivative.[93] Carborhodamines, Si-rhodamines and heteroatom-substituted rhodamines shared this feature and are bathochromically shifted rhodamine analogs with good water-solubility and without installation of bulky groups.[94]

The relatively good cell-permeability of rhodamines is attributed to their open-close equilibrium between the fluorescent form and the non-fluorescent spirolactone form[15] and has been subject of further fine-tuning (Figure 2.6A-C). Grimm *et al*. studied the effect of azetidine substituents azetidines on the brightness and cell membrane permeability of rhodamines.[95] Butkevich *et al*. prepared a series of membrane-permeant rhodamine derivatives by introducing bridge-substitution, fluorination and a different pendant aromatic ring to the rhodamine core.[96] In both cases tuning of the open-close equilibrium was found alongside undesired changes in the photophysical properties absorption and emission. Wang *et al*. addressed this issue by replacing the spirolactone ring in rhodamines with spirolactames substituted at the amido nitrogen with different electron-withdrawing groups such as sulfonamido and nitrile (Figure 2.6D).[97] With this approach the open-close equilibrium was successfully altered independently from the fluorophore' absorption and emission maxima.

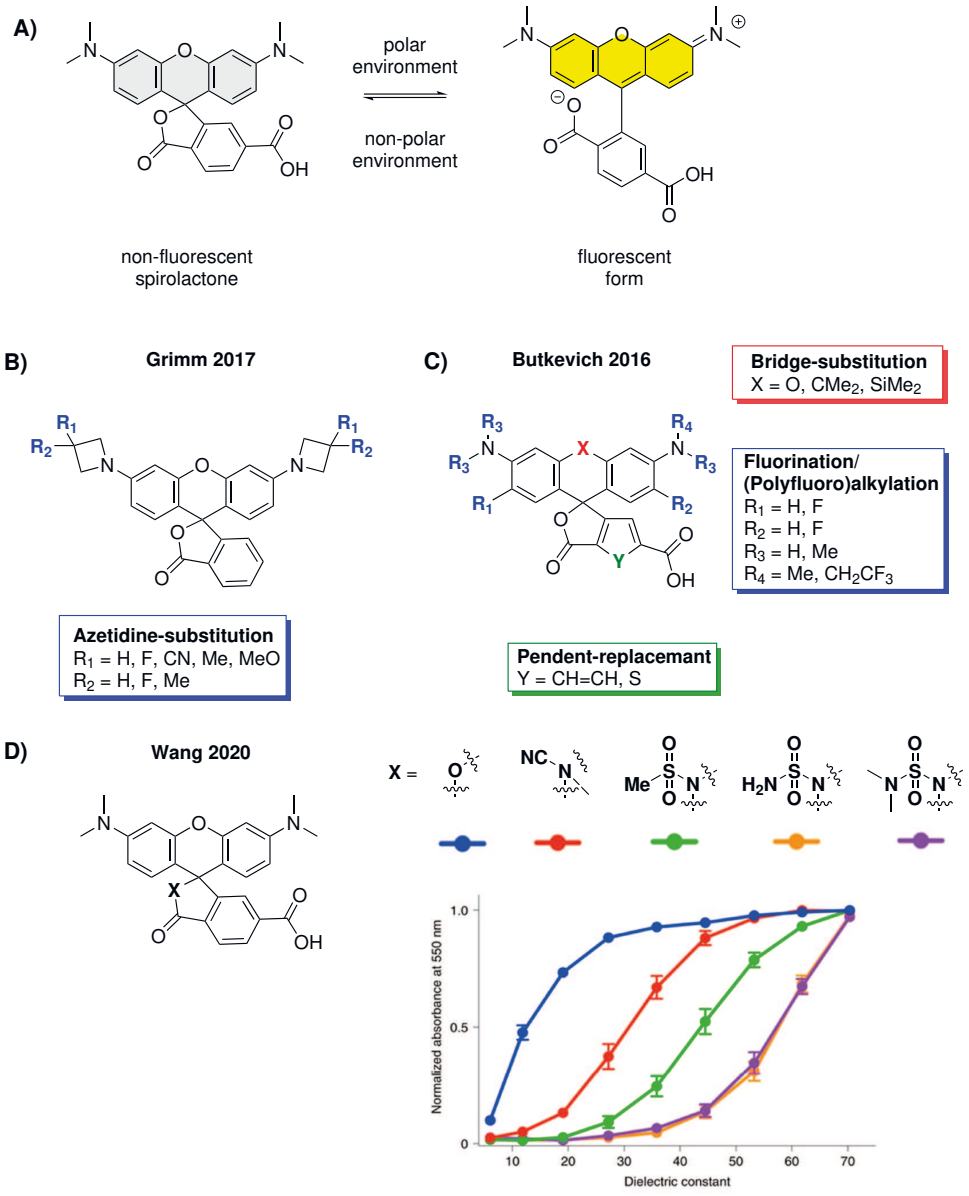

Figure 2.6 – (A) Open-close equilibrium and (B-D) fine-tuning of rhodamines by Grimm *et al.*,[95] Butkevich *et al.*,[96] and Wang *et al.*.[97] (D) Adapted by permission from Springer Nature Customer Service Centre GmbH: Nature Chemistry[97] © (2020)

Fluoresceins

Fluorescein **1a** is a strongly emissive fluorophore ($\epsilon = 90.000\,M^{-1}cm^{-1}$, $\Phi_{FL} = 0.86$, in 10 mM HEPES pH 7.3),[33] but hypsochromically shifted by $\sim$ 60 nm compared to TMR ($\epsilon = 78.000\,M^{-1}cm^{-1}$, $\Phi_{FL} = 0.45$, in 10 mM HEPES pH 7.3).[33] Fluoresceins are generally less photostable than rhodamine dyes.[24] Under the physiological pH conditions, fluorescein-based probes are anionic and do not cross the cell membrane analogs unlike many other neutral or cationic small-molecule fluorophores.[34]

Different design strategies have been explored to address these issues. Replacement of the bridging oxygen with dimethylmethylene and dimethylsilylene yields carbofluorescein **1b**[33] and Si-fluorecein **1c**[92] (Figure 2.7). These derivatives exhibit bathochromic shifts of $\sim$60 nm and $\sim$90 nm, respectively. Additionally, they demonstrate cell-permeability, unlike the cell-impermeant O-fluorescein **1a**.[86,92] Another design principle to induce a bathochromic shift is annulation of aromatic rings onto the core of fluorescein. However, the naphthofluoresceins as **3** suffer from poor solubility in aqueous medium.(Figure 2.7).[98] Halogenated fluorescein derivatives **4** and **6** are presented in Figure 2.7. The fluorinated analog, OregonGreen,[35] shows improved photostability over its parent molecule **1a**. On the other hand, chlorinated fluorescein showed increased fluorescent quantum yield, while the fluorescence of bromides and iodides is quenched due to the heavy atom effect.[99]

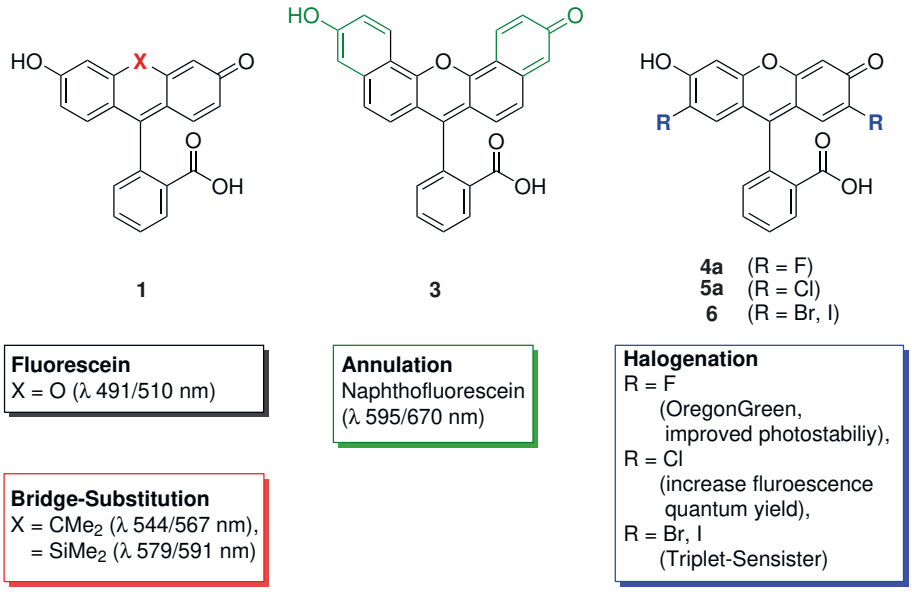

Figure 2.7 – Design strategies to optimize fluorescein (**1a**) by brigde-substituions,[33,92] annulation,[98] or halogenation.[35,99]

Unlike TMR, absorption and emission of fluorescein (**1a**) are pH-dependent in aqueous solution.[44] The molecular forms of fluorescein (**1a**) present in acid-base equilibrium are shown in Figure 2.8. Under acidic conditions, the non-fluorescent forms **I** and **II** are

dominant. The form **II** is also in equilibrium with non-fluorescent spirolactone **III**, which is dominant in non-polar solvents similarly to the polarity dependence of rhodamines (Figure 2.6A). The fluorescent forms of fluorescein (**1a**) are the weakly fluorescent form **IV** and the relatively bright form **V** present in neutral and basic environment.

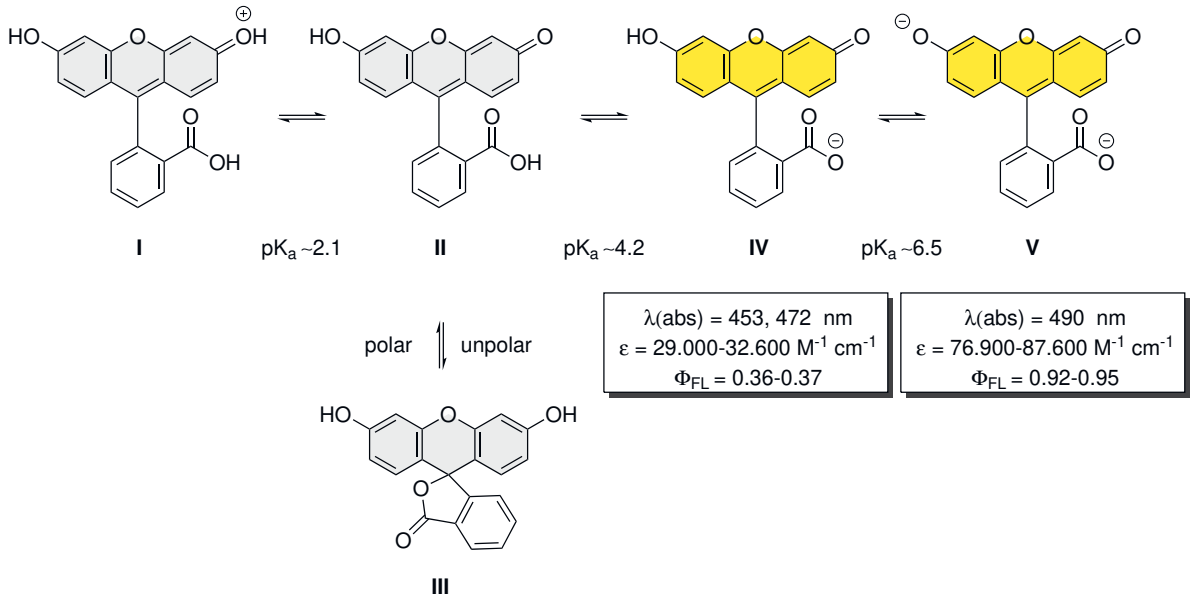

Figure 2.8 – Equilibria of fluorescein (**1a**). Here: $pK_a = -log_{10}K_a$ in which K_a is the constant of an equibrium HA $\rightleftharpoons$ H^+ + A^-. Adapted by permission from Springer Nature Customer Service Centre GmbH: Springer Nature, "Principles of Fluorescence Spectroscopy" by J. R. Lakowicz[44] © (2006). Photophysical properties of form **IV** and **V** are reported in[100].

Because of this complex acid-base equilibrium, the photophysical properties of fluorescein are pH-dependent. As shown in Figure 2.8, fluoresceins may express multiple equilibria. Since the term "pK_a value" may refer to each of these equilibria and may lead to confusion, pK_a values in this work is defined as follows:

1. pK_a value of an acid:

   $pK_a = -log_{10}K_a$ in which K_a is the constant of an equilibrium HA $\rightleftharpoons$ H^+ + A^-.

2. $pK_{a,FL}$ value of a fluorophore:

   The pH of the aqueous medium in which the normalized absorption of a fluorophore is half the maximal absorption across the pH-range.

Since fluorescence microscopy can only interrogate the fluorescent species, it is important to have an understanding of whether a molecule is fluorescent under the imaging conditions. Table 2.1 provides an overview of various $pK_{a,FL}$ values of fluoresceins dyes and analogs. Fluorescein **1a** expresses a $pK_{a,FL}$ value of 6.3. The carbo- and

Si-fluorescein analogs **1b** and **1c** show increased $pK_{a,FL}$ values. The fluorinated compounds **4** display reduced $pK_{a,FL}$ values compared to their non-fluorinated analogs. Rhodol **2b** behaves similarly to fluorescein with a lower $pK_{a,FL}$ value.

While fluoresceins and rhodols are generally fluorescent under basic conditions (Table 2.1, type a), other dyes express the opposing behaviour. Replacement of the carboxyl group by alcohols or amines results in fluorophores fluorescent under acidic conditions (Table 2.1, type b). Such dyes may act as spontaneously blinking dyes in SMLM imaging.[101] Additionally, these probes tend to label cell compartments as lysosomes.[102] Lysosomes maintain acidic environment (pH $\sim$ 4.7)[103] under which fluoresceins as **1a** or non-fluorescent.

Table 2.1 – Overview of $pK_{a,FL}$ values of fluoresceins dyes and analogs.

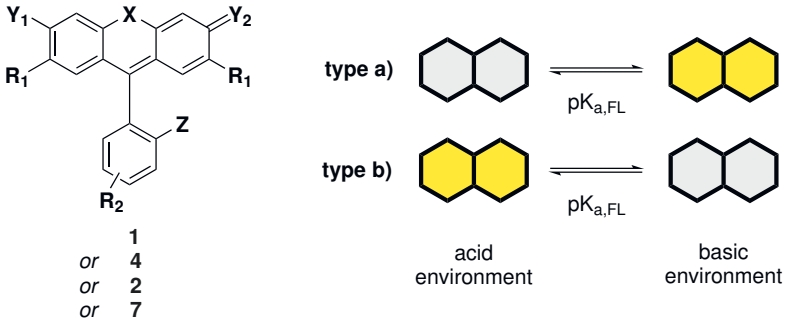

dye	X	Y^1	Y^2	R^1	R^2	Z	$pK_{a,FL}$	Ref.
type a								
1a	O	OH	O	H	H	COOH	6.3	[104]
1b	CMe_2	OH	O	H	H	COOH	7.5	[86]
1c	$SiMe_2$	OH	O	H	H	COOH	8.3	[92]
1d	$SiMe_2$	OH	O	H	F_4	COOH	7.1	[92]
1e	O	OH	O	Et	H	COOH	6.6	[100]
4a	O	OH	O	F	H	COOH	4.6	[104]
4b	CMe_2	OH	O	F	H	COOH	6.8	[86]
4c	$SiMe_2$	OH	O	F	H	COOH	7.4	[92]
2b	O	NH_2	O	H	5‘/6‘-COOH	COOH	5.6	[105]
type b								
7a	O	NH_2	NH_2^+	H	H	CH_2NH_2	6.2	[101]
7b	O	NH_2	NH_2^+	H	H	CH_2OH	8.1	[101]
7c	O	OMe	NH_2^+	H	H	CH_2OH	5.7	[102]

Photoactivatable triarylmethane fluorophores

In SMLM techniques as PALM[13] control over the ON and OFF state of the fluorescent molecules is essential so only a small fraction of molecules is fluorescent at a time to prevent overlapping PSFs.[6] This can be realized with caged fluorophores bearing photolabile groups. Hereby, irradiation with a wavelength λ_{ON} suitable to trigger an irreversible photoreaction is used to remove the photolabile groups(Figure 2.9A). The resulting fluorescent molecules are then localized and must be photobleached with a suitable wavelength λ_{bleach}, before photoactivation of the next fraction of caged fluorophores.[6]

Triarylmethane dyes bearing photolabile nitrobenzyl carbamate or ethers have been successfully applied as photoactivatable probes in super-resolution microscopy[29,30] and live-cell imaging.[106,107] Irradiation with ultraviolet (UV) light cleaves the carbamate or ether, converting the caged dye irreversibly to the fluorescent molecule and an aldehyde as by-product. (Figure 2.9B).[108–110] The installation of the nitrobenzyl cage, however, increases the bulkiness and lipophilicity of the probe and may lead to poor solubility, aggregation and precipitation in aqueous medium during labeling.[111] To improve solubility, Butkevich *et al*. designed caged rhodamines bearing sulfonyl groups at the nitrobenzene cage.[112] These probes were soluble in water, but also cell membrane-impermeant before photoactivation limiting their application in live-cell nanoscopy. For cellular imaging, another downside is the formation of cytotoxic by-products as aldehydes[113–115] during the photoactivation of nitrobenzene-caged fluorophores.

Other approaches rely on introduction of few atoms avoiding bulky and lipophilic photocages. One notable example are the non-fluorescent, α-diazoketone-caged rhodamines (Figure 5.1C), undergoing a Wolff rearrangement to yield fluorescent rhodamine analogs upon irradiation.[31] Ideally, inert N_2 is the only expected by-product, however, depending on the nature of the dye and solvent, up to 40% non-fluorescent by-products may form.[116]

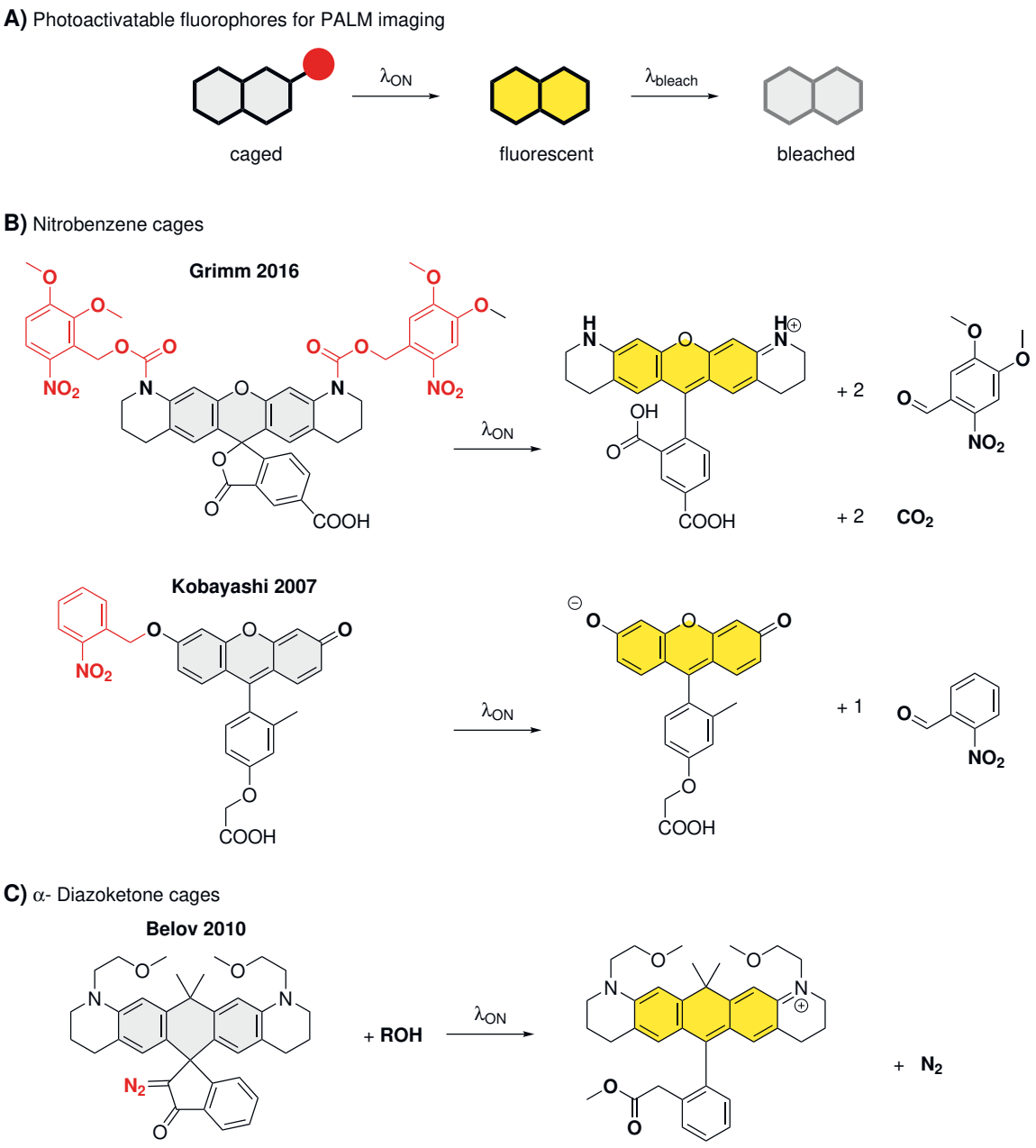

Figure 2.9 – Photoactivatable dyes. (A) Principle of a photoactivatable dye. A caging group (red) behaves as a photolabile protecting group. The fluorescent product is bleached after localisation. (B) Nitrobenzly-based caged triarylmethane dyes from Kobayashi *et al*[106] and Grimm *et al*.[30] (C) α-Diazoketone-caged rhodamine from Belov *et al*.[31]

2.3.2 Synthetic methodologies to access triarylmethane dyes suitable for super-resolution live-cell imaging

A historically oldest and the most straightforward approach to prepare rhodamines and fluoresceins and rhodamines is the condensation of (amino)phenols with phthalic anhydrides.[21,23] However, this approach require strongly acidic conditions limiting the functional group tolerance. Furthermore, use of trimellitic anhydride to install a carboxylic acid for labeling yields a mixture of two regioisomers (Scheme 2.4).

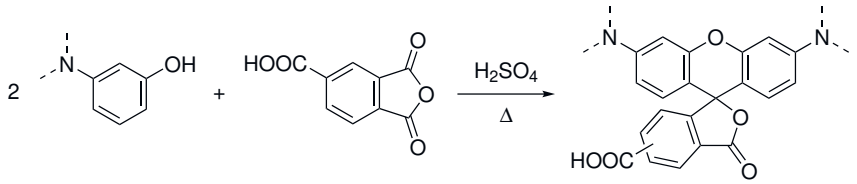

Scheme 2.4 – Preparation of rhodamines by condensation of amino phenols with trimellitic anhydride.[21]

The regioselective preparation of triarylmethanes with a carboxylic acid at the pendant ring usually relies on metalation of an aryl halide followed by an electrophilic attack of a carbonyl. Herein two different approaches have been realized (Scheme 2.5). In one approach, xanthones function as electrophile under strong basic Grignard or lithiation conditions.[96,117] The second approach rely on the preparation of a bimetallic intermediate which reacts with phthalic anhydride derivatives or esters to form triarylmethane dyes.[92,118]

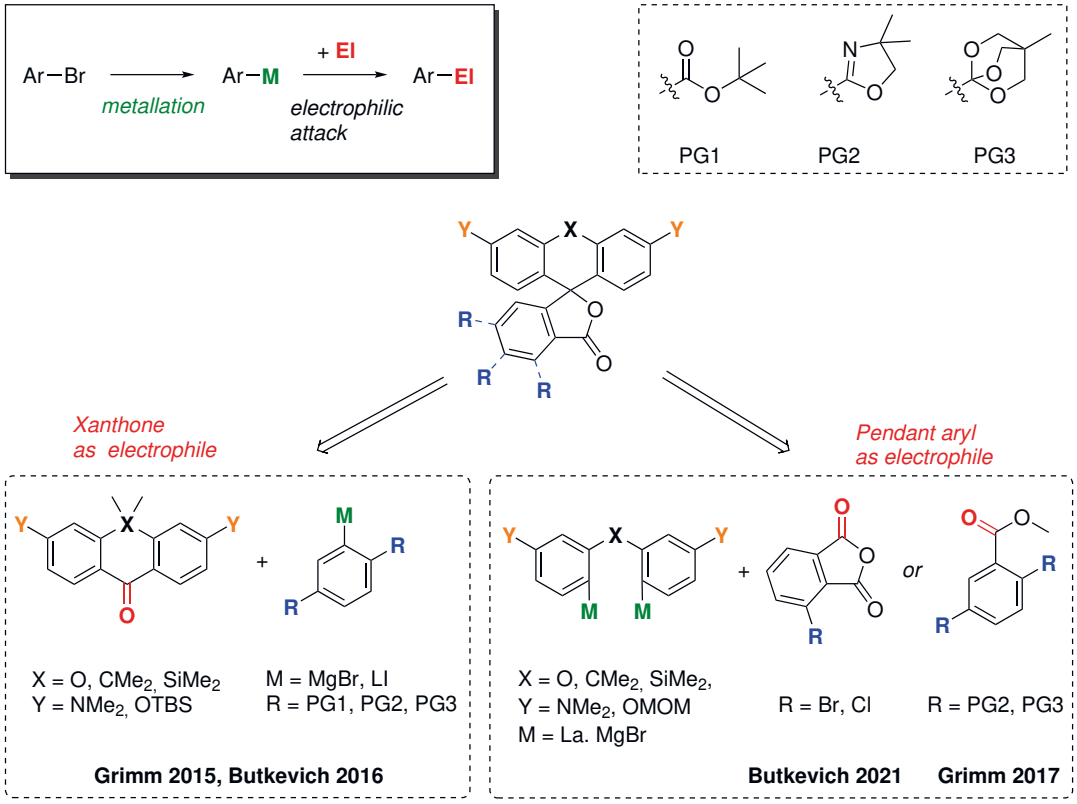

Scheme 2.5 – General strategies in the regioselective preparation of fluoresceins and rhodamines by reaction of metal aryl species with electronic carbonyls (xanthones[96,117] or pendant aryls[92,118]).

The regioselective approaches in Scheme 2.5 yield either rhodamines or protected fluoresceins bearing a substituted pendant ring ready for installation of reactive ligands for bioorthogonal labeling. Protected fluoresceins can be deprotected under suitable conditions and either used as labels or further converted to the corresponding triflates. Fluorescein triflates **8** present valuable building blocks in the preparation of a variety of rhodamine labels. Grimm *et al*. demonstrated the accessibility of various rhodamines by Buchwald-Hartwig amination of triflates **8** (Scheme 2.6).[119] This method grands access to both rhodamine dyes, as **9a**, as well as their photoactivatable, nitrobenzyl-caged analogs like **9b**.

Using a previously reported ruthenium-catalysed substitution,[120] Fluorescein triflates **8** can be converted to the corresponding dihalofluorans **10** (Scheme 2.7). These aryl halides present another valuable building block, which has different reactivity and is less base-sensitive than aryl triflates. Dihalofluorans **10** have been successfully applied in the Ullmann coupling to extent the scope of rhodamines **9**.[121]

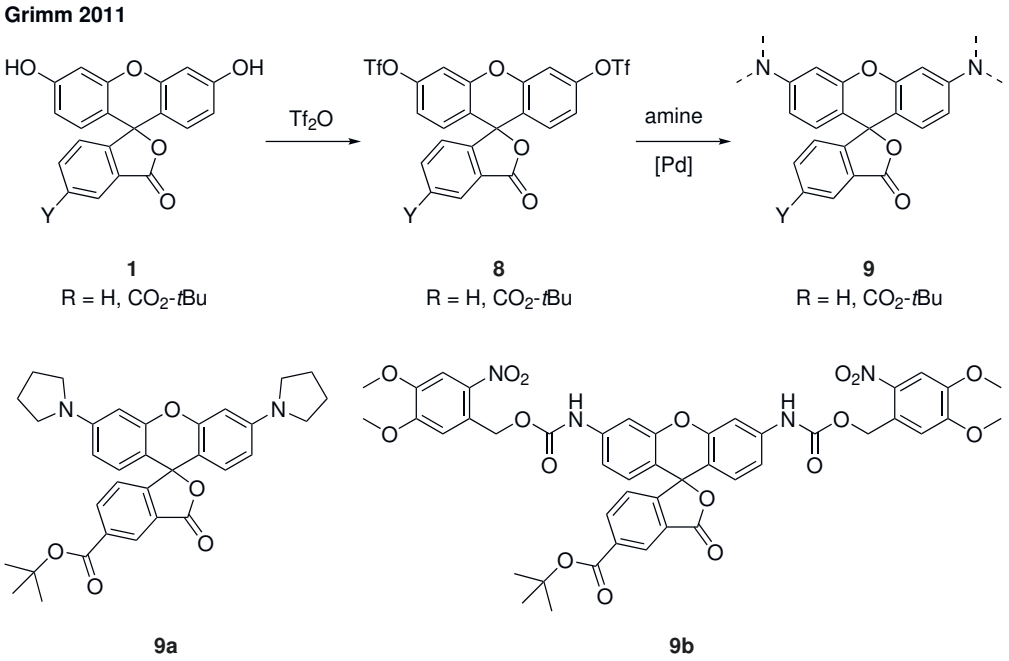

Scheme 2.6 – Synthesis of rhodamines **9** by Buchwald-Hartwig amination of fluroesceins **8**.[119]

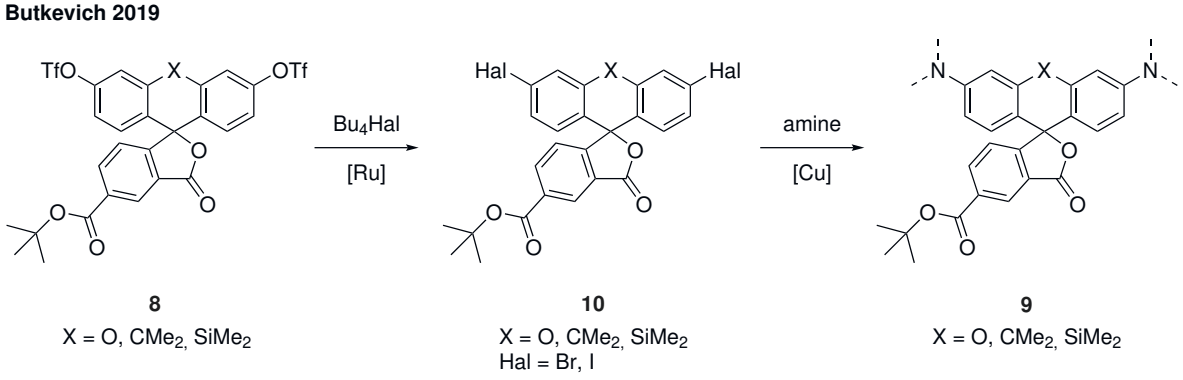

Scheme 2.7 – Synthesis of rhodamines **9** by Ullmann coupling of dihalofluoranes **10**.[121]

Chapter 3

Materials and Methods

3.1 Preparation and purification of compounds

Reaction mixtures were heated up immersed in a silicon oil bath (for reaction flasks) or in an aluminum reaction block with silicon oil (for reaction tubes) by means of Heidolph MR Hei-Tec magnetic stirrer equipped with a Pt1000 thermometer. Reaction mixtures were cooled using cooling baths (0 °C: ice/water bath; –78 °C: dry ice/acetone bath; –100 °C: liquid N_2/Et_2O bath) which were monitored with low-temperature thermometers. Air- and moisture-sensitive reactions were conducted under an argon atmosphere using standard Schlenk techniques. Microwave reactions were performed in a Monowave 450 Microwave Reactor (Anton Paar, Austria) in indicated reaction vials.

Dry solvents were purchased in AcroSeal bottles over molecular sieves (Thermo Fischer Scientific) stored under inert atmosphere and used without further purification. For purification and analysis, solvents of technical, HPLC or LCMS grades have been used.

Chemicals were purchased from Sigma-Aldrich (Merck), Alfa Aesar (Thermo Fisher Scientific), Acros (Thermo Fisher Scientific), TCI Europe, Strem Chemicals, abcr GmbH and Activate Scientific GmbH and were used without further purification, unless stated otherwise. Compounds were purchased or prepared according to indicated literature reference.

The following non-commercial compounds have been prepared within the working group (Department of Optical Nanoscopy, MPI for Medical Research).

Purification of prepared compounds was done by preparative flash column chro-

Table 3.1 – Compounds prepared within the working group.

Compound	Reference	Prepared from
10d	[1]	Dr. Alexey Butkevich
L6	[121]	Dr. Alexey Butkevich
$Py_2P_2S_5$	[122]	Dr. Richard Lincoln
L8	[123]	Dr. Alexey Butkevich
65	[39]	Dr. Alexey Butkevich

matography or preparative HPLC. Preparative flash column chromatography was performed with an Isolera Spektra One system (Biotage AG, Sweden) with pre-packed cartridges and solvent systems as indicated. Preparative high-performance liquid chromatography (HPLC) was performed on a Reveleris® Prep system (Büchi Labortechnik, Switzerland) and a Puriflash® 5.250 P system (Interchim®, France) using suitable preparative columns and solvent systems as indicated.

3.2 Analysis and characterisation of compounds

Thin layer chromatography (TLC) to analyze reaction mixtures and chromatography fractions was conducted on Merck Millipore ready-to-use aluminum sheets (coated with silica gel 60 (F254), Cat. No. 1.05554.0001). Compounds were detected by eyeball approach using day-light, UV-light (254 nm, 366 nm) and/or heating with stains listed in Table 3.2.

Table 3.2 – Table of stains.

Stain	Prepared from
1 M NaOH	Merck Titripur®, CN: 1091371000
0.1 M NaoH	dist. water/1 M NaOH (1:9)
1 M HCl	Merck Titripur®, CN: 1090571000
$KMnO_4$ stain	600 mg of $KMnO_4$ and 4 g of K_2CO_3 mixed in 1.4 mL of 1 M NaOH and 80 mL water
PMA stain	10 g of phosphomolybdic acid hydrate dissolved in 100 mL ethanol
Vanillin stain	6 g vanillin and 1.5 mL conc. H_2SO_4 mixed in 100 mL ethanol

Liquid chromatography-mass spectrometry (LCMS) was performed on an LC-MS system (Shimadzu, Japan): 2x LC-20AD HPLC pumps with DGU-20A3R solvent degassing unit, SIL-20ACHT autosampler, CTO-20AC column oven, SPD-M30A diode array detector and CBM-20A communication bus module, FCV-20AH2 diverter valve

and LCMS-2020 spectrometer with electronspray ionisation (ESI). Gradient method: 1–10 µL sample volume, analytical ThermoScientific Hypersil Gold 50×2.1 mm 1.9 µm column thermostated at 30 °C, ESI = 100–1000 m/z. Standard solvent system: isocratic 95/5 A:B for 2 min, then gradient 95/5 to 0/100 A:B for 5 min, then isocratic 0/100 A:B for 2 min; flow rate 0.5 mL/min, A = H_2O + 0.1 % formic acid, B = MeCN + 0.1 % formic acid.

High-performance liquid chromatography (HPLC) was performed as method scouting for preparative HLPC. The test runs were conducted with matching analytical columns and solvent systems as indicated. Analytical HPLC was conducted on a HPLC system (Shimadzu, Japan): 2x LC-20AD HPLC pumps with DGU-20A3R solvent degassing unit, CTO-20AC column oven equipped with a manual injector with a 20 µL sample loop, SPD-M20A diode array detector, RF-20A fluorescence detector and CBM-20A communication bus module, 1.2 mL/min solvent flow rate. Additionally, analytical HPLC was conducted on a Dionex Ultimate 3000 UPLC system: LPG-3400SD pump, WPS-3000SL autosampler, TCC-3000SD column compartment with 2x 7-port 6-position valves and DAD-3000RS diode array detector, 0.5 mL/min solvent flow rate.

Nuclear magnetic resonance (NMR) spectroscopy was performed on a Bruker Ascend 400 spectrometer (Bruker, Germany) with samples diluted in commercially available, deuterated solvents (Deutero GmbH, Germany) at 25 °C. Chemical shifts were reported in parts per million (ppm) and referenced to the signals of tetramethylsilane as internal standard or signals of residual non-deuterated solvent[124]: tetramethylsilane (1H/13C: δ = 0.00 ppm), $CDCl_3$ (1H: 7.26 ppm, 13C: 77.16 ppm), CD_3OD (1H: 3.31 ppm, 13C: 49.00 ppm), CD_3CN (1H: 1.94 ppm, 13C: 1.32 ppm, to CH_3), DMSO-d_6 (1H: 2.50 ppm, 13C: 39.52 ppm), pyridine-d_5[125] (1H: 8.74 ppm, 13C: 150.35 ppm, to C−2,6). Coupling constants were reported in Hz and multiples abbreviated as followed: s = singlet, d = doublet, t = triplet, q = quartet, p = quintet, m = multiplet, br s = broad singlet. Only proton-coupled carbon nuclei were resolved, if ^{13}C chemical shifts were obtained by indirect detection via 2-dimensional gradient-selective heteronuclear single quantum coherence (gHSQC) NMR experiments. The multiplicity (CH_3/CH_2/CH/quaternary) was verified by phase-sensitive heteronuclear single quantum coherence (HSQC) NMR experiments.

High resolution mass spectroscopy (HRMS) was performed on a maXis II ETD (Bruker) with ESI. Spectra were measured by the Mass Spectrometry Core facility of the Max-Planck Institute for Medical Research (Heidelberg, Germany).

3.3 Optical spectroscopy

Absorption spectra of dye solutions were recorded in air-saturated solvents in quartz cuvettes (1 cm optical path length) at ambient temperature with a Varian Cary 5000 UV-Vi-NIRs double-beam spectrophotometer (Agilent Technologies, USA).

Emission spectra of dye solutions were recorded in air-saturated solvents in quartz cuvettes (1 cm optical path length) at ambient temperature with a Varian Cary Eclipse fluorescence spectrophotometer (Agilent Technologies, USA).

Fluorescence quantum yields were measured of dye solutions in indicated, air-saturated solvent in quartz cuvettes (1 cm optical path length) at ambient temperature with a Quantaurus-QY absolute PL quantum yield spectrometer (model C11347-11, Hamamatsu, Japan) at the Department of Chemical Biology (MPI for Medical Research, Prof. K. Johnsson) according to the manufacturer's instructions using integrating sphere detection[126] (absolute method).

Fluorescence lifetime measurements were conducted by Dr. Mariano Bossi and Dr. Alexey Butkevich. Dye solutions in indicated, air-saturated solvent at 25 °C were measured on a FluoTime 300 fluorescence lifetime spectrometer FluoTime 300 (PicoQuant, Germany) using a picosecond pulsed diode laser LDH-P-C-470, LDH-D-TA-560 or LDH-P-C-640B (PicoQuant, Germany) and the manufacturer's EasyTau 2 fitting/analysis software.

Photobleaching reaction kinetic measurements were conducted by Dr. Mariano Bossi. Dye solutions stirred in air-saturated, borate buffer (0.1 M, pH 9.9) at 20 °C were measured using a previously described, custom setup[127]: a peltier-based temperature-controlled cuvette holder (Luma 40, Quantum Northwest, Inc., USA), a 530 nm LED (ML530L3, Thorlabs Inc.) as irradiation source, a fiber-based spectrometer (Flame-S-UV-Vis-ES, Ocean Insight, USA) for monitoring absorption and emission spectra, and a deuterium and tungsten halogen source (DH-2000-BAL, Ocean Insight) for absorption measurements. Emission was recorded in a 90° configuration with a short pulse (<10 ms) of the same LED (530 nm) for fluorescence excitation. Data collection and analysis was performed with in-house protocols written in Matlab R2020a (MathWorks).

Photobleaching quantum yield (Φ_{Bleach}) were calculated based on equitation (3.1):[128]

$$-\frac{\Delta[dye]}{\Delta t} \approx \frac{d[dye]}{dt} = \Phi_{Bleach} \cdot I_0 \cdot \epsilon_{530} \cdot F \cdot [dye]$$

$$-\frac{\Delta Abs_{max}/\epsilon_{530}}{\Delta t} \approx \Phi_{Bleach} \cdot I_0 \cdot \epsilon_{530} \cdot F \cdot \left(\frac{Abs_{max}}{\epsilon_{530}}\right)_0$$

$$-\frac{\Delta Abs_{max}/(Abs_{max})_0}{\Delta t} = -slope \approx \Phi_{Bleach} \cdot I_0 \cdot \epsilon_{530} \cdot F \tag{3.1}$$

with: F = photokinetic factor at 530 nm, I_0 = volumetric photon flux of irradiation light (previously measured with a chemical actinometer) in $mol_{photons} \cdot L^{-1} \cdot s^{-1}$.

Photoactivation measurements of caged fluorophores were conducted by Dr. Mariano Bossi. Dye solutions stirred in air-saturated, borate or phosphate buffer (0.1 M, pH 7) at 20 °C were measured using a previously described, custom setup[127]: a peltier-based temperature-controlled cuvette holder (Luma 40, Quantum Northwest, Inc., USA), a series of LEDs (ML365L2, ML405L3, NL470L3, ML505L3, and ML530L3, Thorlabs Inc.) as irradiation sources, a fiber-based spectrometer (Flame-S-UV-Vis-ES, Ocean Insight, USA) for monitoring absorption and emission spectra, and a deuterium and tungsten halogen source (DH-2000-BAL, Ocean Insight) for absorption measurements. Emission was recorded in a 90° configuration with a short pulse (<10 ms) of a LED (405 nm, 445 nm, or 505 nm) for fluorescence excitation. Data collection and analysis was performed with in-house protocols written in Matlab R2020a (MathWorks).

Photolysis of caged fluorophores was conducted on a Photoreactor m1 (Penn PhD, USA). On semipreparative scale, a solution of caged dye in indicated solvent was stirred in a capped, 4 mL reaction vial (clear glass, flatt bottum) equipped with a stir bar. Unless stated otherwise, the capped vial was placed in a in-house 3D-printed holder on top of a 365 nm LED unit ($/sim$ 0.8 cm distance between bottom of vial and LED unit) and irradiated at indicated LED power at ambient temperature while stirring. The solution of caged dye was analysed by LCMS before and after irradiation.

$\mathbf{pK_{a,FL}}$ **values** of dyes were determined using a previously described protocol.[129] 10 µM dye solutions in air-saturated, 0.1 M phosphate buffers of different pH values were transferred (3x 200 µL/well) to a 96-well microplate (non-binding polystyrene F-bottom, µClear, Greiner Bio-One GmbH, Ref. 655906). Absorption and emission spectra were measured in triplicates at ambient temperature with a CLARIOstar Plus microplate reader (BMG LABTECH GmbH, Germany).

The pH of buffer vs the background corrected, normalized absorbance abs_{norm} at fixed wavelength λ_{max} (absorption maximum in the visible range with highest absorption of the series) was plotted and the data were fitted to equation (3.2)[129] to calculated $pk_{a,FL}$ values:

$$abs_{norm} = \frac{1}{1 + 10^{-n \cdot (pH - pK_{a,FL})}} \tag{3.2}$$

with: n = steepness of the curve; pH = pH of buffer.

Solvent polarity response values $(\mathbf{D_{0.5}})$ were determined for dyes using a previously described protocol.[96] 10 µM dye solutions in air-saturated, aqueous dioxane solution of different water contents were transferred (3x 200 µL) to a 96-well microplate polypropylene F-bottom (Greiner Bio-One GmbH, Ref. 655201). Absorption and emission spectra were measured in triplicates at ambient temperature with a CLARIOstar Plus microplate reader.

The water content (given in %(v/v) water) of the solution vs the background corrected, normalized absorbance abs_{norm} at fixed wavelength λ_{max} (absorption maximum in the visible range with highest absorption of the series) was plotted and the data were fitted to equation (3.3)[96] to calculate $D_{0.5}$ values:

$$abs_{norm} = \frac{1}{1 + 10^{-n \cdot (D - D_{0.5})}} \tag{3.3}$$

with: n = steepness of the curve, D = dielectric constant of aqueous dioxane solution.[130]

3.4 Fluorescence intensity changes of dyes upon addition of detergents

Fluorescence intensity changes upon addition of detergents were measured using a previously described protocol.[96] In 1.5 mL Eppendorf tubes, mixtures of 10 µL of 25 µM dye solutions in DMSO was added to 490 µL 0.1 mg BSA in PBS (pH 7.4) with:

1. 0.5 % sodium dodecyl sulfate (SDS), *or*
2. 0.5 % cetyltrimethylammonium bromide (CTAB), *or*

3. no additive.

After incubation at 37 °C for 2 h, the mixtures were loaded (3x 100 µL/well) on a 96-well microplate (non-binding polystyrene black F-bottom, Greiner Bio-One GmbH, Ref. 655900). Full emission spectra were measured in triplicates at ambient temperature with a CLARIOstar Plus microplate reader (BMG LABTECH GmbH, Germany) using suitable excitation wavelengths for each dye as indicated.

For data processing, the fluorescence intensities at λ_{max} (emission maximum in the visible range) under same conditions were averaged and fluorescence intensity ratios (SDS or CTAB / no detergent) in BSA/PBS calculated.

3.5 Fluorescence intensity changes of dyes upon binding to HaloTag7 protein

Fluorescence intensity changes upon binding to HaloTag protein were measured using a previously described protocol.[96] In 1.5 mL Eppendorf tubes, 10 µL of 25 µM dye solutions in DMSO was added to 490 µL 10 % FBS (HI, lot: 08F0597K) in DMEM (Gibco, 4.5 g/L D-Glucose, L-Glutamine, 25 µM HEPES, no sodium pyruvate) containing:

1. 1 µM HaloTag 7, *or*

2. no additive.

After incubation at 37 °C for 2 h, the mixtures were loaded (3x 100 µL/well) on a 96-well microplate (non-binding polystyrene black F-bottom, Greiner Bio-One GmbH, Ref. 655900). Fluorescence intensities were measured in triplicates at ambient temperature with a CLARIOstar Plus microplate reader (BMG LABTECH GmbH, Germany) for 1 h in 10 min intervals using suitable excitation and emission wavelengths for each dye as indicated.

For data processing, the first 3 readings per sample (9 values per dye) were averaged and fluorescent intensity ratios (HaloTag7 / no protein) in FBS/DMEM calculated.

3.6 HaloTag7 labeling kinetics

HaloTag7 labeling kinetic measurements were performed by recording FP changes with a CLARIOstar Plus microplate reader (BMG LABTECH GmbH, Germany) using a previously described protocol.[96] A series HaloTag 7 concentrations (0–320nM) in 0.1 % CHAPS in PBS (pH 7.4) was loaded (3x 100 µL/well) on a 96-well microplate (non-binding polystyrene black F-bottom, Greiner Bio-One GmbH, Ref. 655900). The injector of the plate reader was loaded with 10 nM solution of dye in 0.1 % CHAPS in PBS (pH 7.4). 100 µL dye solution (300 µL/s) was injected to the protein solution at 25 °C, followed by 3 s orbital shaking, and, next, FP changes were measured (in 3 s intervals over 10 min) using optical setups suitable for each dye as indicated.

For data processing, the data were fitted to previously described equation (3.4)[78] using DynaFit software (http://www.biokin.com/dynafit/) (processing by Dr. Alexey Butkevich).

$$\mathrm{P} + \mathrm{S} \xrightarrow{\mathrm{k_{app}}} \mathrm{PS} \tag{3.4}$$

with: P = HaloTag7 protein, S = the fluorescent substrate, PS = protein-substrate conjugate.

3.7 Cell culture

Cells were cultured by Dr. Jessica Matthias as described in Table 3.3 and frequently tested by mycoplasma testing and cell line authentication.

Table 3.3 – Cell cultures and cultivation media.

Cell line [A]	Cultivation medium [B]
U-2 OS Line (human bone osteosarcoma epithelial, ATCC HTB-96)	DMEM (Gibco, high Glucose, GlutaMAX™, pyruvate (31966, ThermoFisher))
U-2 OS-Vim-Halo (variant of cell line above)	DMEM (Gibco, high Glucose, GlutaMAX™, pyruvate (31966, ThermoFisher))
U-2 OS-CRISPR-NUP96-Halo clone #252 (genetically engineered human bone osteosarcoma epithelial)[131]	McCoy's 5a (modified) Medium (L-Glutamate, pyruvate)

[A] Cells were cultivated in 5 % CO_2 in humidified air at 37 °C. [B] All media contain 10 % FBS (10500064, ThermoFisher) and 1 % penicillin/streptomycin (15140122, Gibco) as additives.

After cultivating, cells were harvested with TrypLE Express (12604013, Gibco) with <20 passages between thawing and experimental use.

U-2 OS cells at 70–90 % confluency were transiently transfected with the N-terminal fusion construct pSNAP-PMLIII (in facile manner to previous plasmid construct[132]) and jetPRIME Transfection Reagent (101000027, Polyplus) using the manufacturer's protocol to overexpress PMLIII. Live cell staining of overexpressing cells was performed 24 h after transfection.

3.8 SDS PAGE

Analysis of sample by SDS polyacrylamide gel electrophoresis (PAGE) was conducted by Dr. Jessica Matthias according to the protocol below (unless specified otherwise).

Protein samples were diluted to $\sim$ 1 mg/mL or $\sim$ 3 mg/mL solutions in tris-glycine-SDS buffer (25 mM tris and 190 mM glycine + 0.1 % SDS). Samples were further diluted 1:4 in Laemmli Sample Buffer (1610747, BIO RAD) containing 10 % 2-mercaptoethanol. After short incubating at 95 °C for 5 min, samples (20 µL/well) and references (3 µL/well, Precision Plus Protein Dual Color Standards (1610374, BIO RAD)) were loaded on 10 % Mini-PROTEAN TGX Stain-Free Precast Gels (4568035, BIO RAD) in a Mini-PROTEAN Tetra Vertical Electrophoresis Cell (BIO Rad). The gels was run at 50 V for 5 min and further at 150 V for 45 min Fluorescence was measured with a UVP Chem-Studio PLUS imager (Analytik Jena, Germany).

3.9 Cytotoxicity studies

Potential cytotoxicity of dye was studied by Dr. Jessica Matthias using Holographic time-lapse imaging and Cell viability assays.

Holographic time-lapse imaging was performed by monitoring U-2 OS cell proliferation in presence of 5 µM dye solutions. U-2 OS cells were seeded in lumox 96-multiwell plates (94.6120.096, Sarstedt; 100 µL/well1, 10^4 cells/mL) and stored in 5 % CO_2 in humidified air at 37 °C for 24 h. Next, cells were imaged in 5 % CO_2 in humidified air at 37 °C for 48 h in 30 min intervals with a HoloMonitor® M4 cytometer (PHI AB). Data analysis was conducted with AppSuite 3.5 (PHI AB) software to track cells ,cell counts, dividing cells and comprised cell segmentation.

Cell viability assay was performed by evaluating the metabolic activity of U-2 OS cells in presence of 5 µM dye solutions. U-2 OS cells were seeded in lumox 96-multiwell

plates (94.6120.096, Sarstedt; 100 µL/well1, 104 cells/mL) and stored in 5 % CO_2 in humidified air at 37 °C for 1 day. Next, the cells were incubated with 5 µM dye solutions for 24 h, washed with DMEM (3x), and CellTiter-Blue Reagent (G8080, Promega) was added (20 µL/well). Cells were incubated in 5 % CO_2 in humidified air at 37 °C for 4 h, before 50 µL of 3 % SDS was added to stop resofurin formation. Fluorescence intensities were measured at 590 nm (excitation at 560 nm) with a CLARIOstar Plus microplate reader (BMG Labtech). Obtained fluorescence intensities were background-corrected to an assay conducted without cells.

Quantitative data are reported as mean ± SD and the number of replicates $n \leq 3$. Data were visualized as bar plots (presenting mean (bar), and standard deviation (SD) (whisker)) and/or box plots (presenting interquartile range (box), median (center line), mean (triangle), and outer-most data points falling within 1.5x interquartile range (whiskers)). Means were compared using the Student´s t-test, if suitable, considering P-values < 0.05 as statistically significant.

3.10 Live cell STED and confocal imaging

Imaging and data analysis with STED and confocal microscopy was performed by Dr. Jessica Matthias.

DMSO solutions of prepared dyes were diluted in DMEM to the indicated concentrations. Commercially available dyes were used as solution in DMEM, respectively, unless stated otherwise. SiR-Hoechst was used as DMEM solution with 10 µM verapamil.

1×10^5 cells/well were seeded in 4-well chambered coverslips (Nunc Lab-Tek II chambered coverglasses, 154526, ThermoFisher) and stored in 5 % CO_2 in humidified air at 37 °C for 24 h. Then, cells were stained with dye solution in 5 % CO_2 in humidified air at 37 °C for 6 h or overnight. Cells were further stained with Hoechst 33342 (H1399, Invitrogen) for the last 10 min of incubation, followed by washing with DMEM for 1 h.

Living cells were imaged in FluoroBrite DMEM (Gibco, A1896701, ThermoFisher) containing 10 % FBS (10500064, ThermoFisher) and 4 mM GlutaMAX (Gibco, 35050061, ThermoFisher) on an Abberior expert line microscope (Abberior Instruments): excitation CW laser (405 nm), 40 MHz excitation pulsed lasers (458 nm, 561 nm and 640 nm), 40 MHz pulsed STED laser (775 nm), and spectral detection.

STED and confocal images were acquired with indicated imaging parameters suitable per experiment with following settings: 100x/1.4 NA magnification oil immersion lens,

100 µm pinhole, z-focus drift compensation.

The imaging data are presented as raw data. Line profiles were averaged over 5 pixels and fitted to a Gaussian function (for confocal line profiles) and a Lorentzian function (for STED line profiles), if suitable. For further data analysis, the following ImageJ plugins were applied: ImageJ plugin JACoP[133] for off-targeting experiments and calculations of the Pearson correlation coefficient, ImageJ plugin Colocalization Finder[134] colocalization experiments and fluorogram plotting.

Chapter 4

N-Cyanorhodamines as photostable and cell-permeant fluorescein analogs for STED imaging

4.1 Introduction

Positively charged rhodamine dyes are widely used in SRM because of their good photostability, brightness and cell-permeability.[15] However, they are prone to accumulate into certain cell compartments (typically in mitochondria), which can have cytotoxic effects for the biological sample.[27,28] Additionally, rhodamines remain fluorescent under acidic conditions naturally found in lysosomes (pH $\sim$ 4.7)[103] and endosomes (pH $\sim$ 5.5–6.5)[103] causing undesired off-targeting labeling artifacts. Fluoresceins, bearing a negative charge and being non-fluorescent under acid conditions,[44] are not expected to demonstrate these side effects. Fluorescein dyes, however, are known to display low photostability,[24] and are hypsochromically shifted compared to the corresponding rhodamines.[33] Therefore, a negatively charged rhodamine dye may in principle combine the strengths of fluoresceins and rhodamines.

Recently, Sharma *et al*. reported sulfonamido-substituted rhodol **11a** and rhodamine **11b**, which can be considered analogs of fluorescein (Figure 4.1A).[135] These analogs exhibit a similar acid-base behavior as fluoresceins, being fluorescent under basic conditions exclusively. Additionally, the emission maxima of these dyes were bathochromically shifted by $\sim$ 20 nm per sulfonamido group replacing a hydroxy group.

Wang *et al*. recently studied the effects of several electron-withdrawing groups on

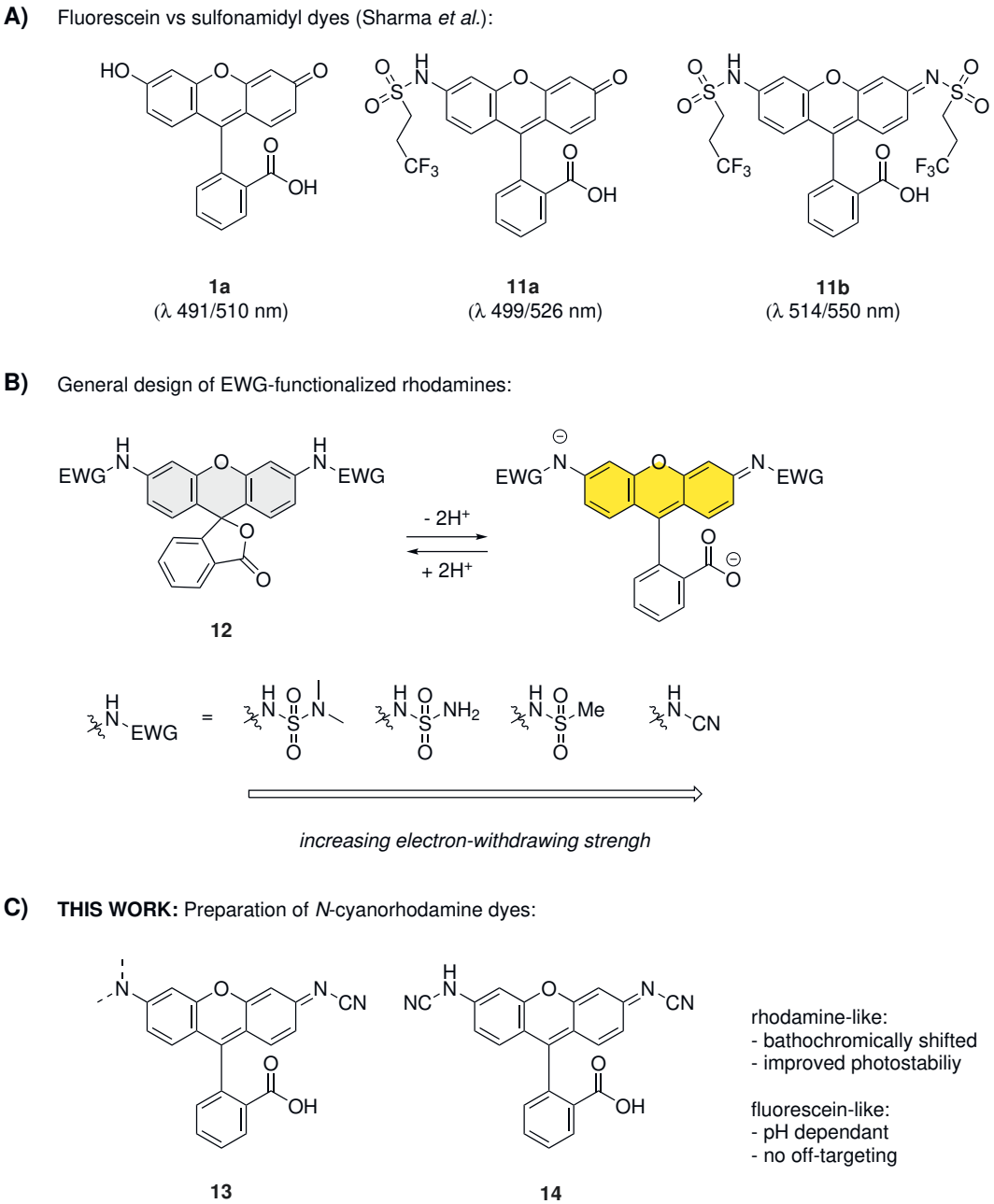

Figure 4.1 – Fine-tuning of fluorescein dyes by introducing electron-withdrawing groups. (A) Fluorescein (**1a**) and sulfonamidofluran dyes **11** by Sharma *et al.*[135]. (B) Proposed design principle to fine-tune dyes with electron-withdrawing groups of varying strength. (C) **This work:** Preparation of *N*-Cyanorhodamine dyes.

the properties of spirolactam rhodamine analogs to fine-tune their open-close behavior. The cyanoamido group displayed the strongest electron-withdrawing effect among the series stabilizing the negatively charged form of the spirolactam rhodamine.[97] In a facile manner, different electron-withdrawing groups in compounds **12** may enable tuning of the NH-acidity and spirolactonization of the dyes (Figure 4.1B) Herein, the cyanoamido group might have the strongest electron-withdrawing effect and, thereby, would favor the negatively charged, fluorescent form under physiological conditions (pH $\sim$ 7.3–7.4).[103] These negatively charged *N*-cyanorhodamine dyes **13** and **14a** are thought to prevent potential off-targeting in cell-compartments as mitochondria,[26] where positively charged rhodamines are prone to accumulated. Furthermore, the proposed dyes might exhibit bathochromical shifts in absorption and emission similar to the electron-deficient sulfonamido-substituted dyes **11**.

4.2 Synthesis of *N*-cyanorhodamines

N,N-Dimethylrhodol (**2a**) and fluorescein (**1a**) were converted to the corresponding triflates **15** and **8** using the triflation reagents recommended in literature (Scheme 4.1).[119,136] The triflates were further converted to iodides **16** and **10** in a ruthenium-catalyzed aromatic substitution[120] with excess of tetrabutylammonium iodide. These building blocks were chosen for testing the reaction conditions towards the preparation of *N*-cyanorhodamines, as rhodamine dyes are often prepared via metal-catalyzed transformations as the Buchwald-Hartwig amination.[119]

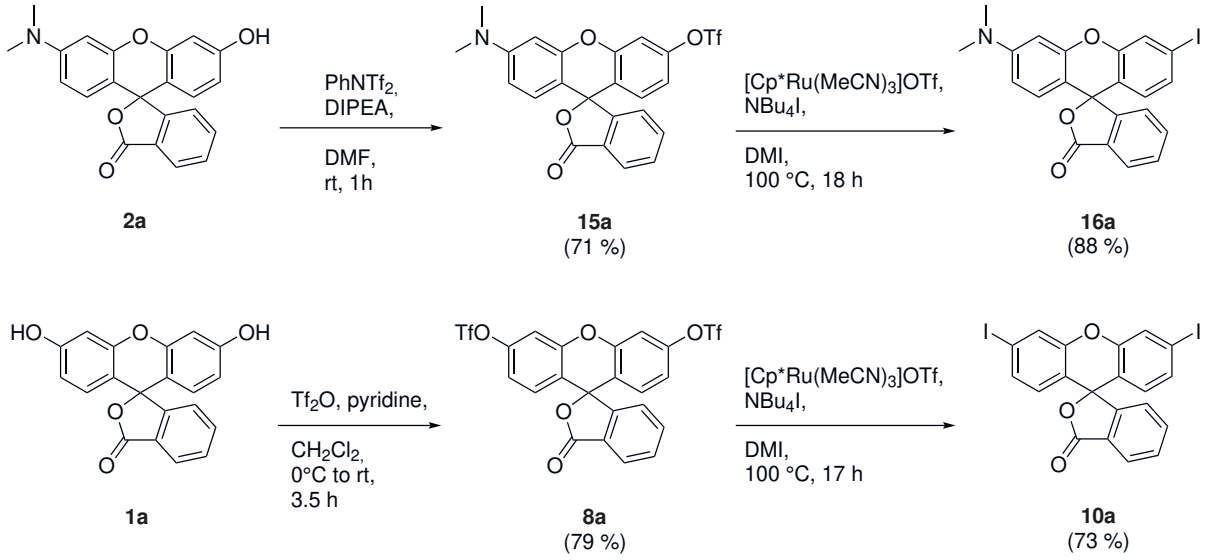

2a | **15a** (71 %) | **16a** (88 %)

1a | **8a** (79 %) | **10a** (73 %)

Scheme 4.1 – Preparation of starting materials.

4.2.1 Buchwald-Hartwig amination of aryl triflates and iodides

The mono-functionalization of rhodol triflate **2a** was chosen as model system for method scouting, before investigating the more complex bis-functionalization of fluorescein triflate **14a**. Firstly, rhodol triflate **15a** was reacted with commercially available cyanamide using the Pd2(dba)3/t-BuXPhos catalytic system (Table 4.1, Entry 1) based on a previously reported method.[137] After 1 h reaction time, consumption of starting material but no product formation was observed by LCMS analysis. Other Buchwald ligands XPhos (Entry 2) and Xantphos (Entry 3) were found to form *N*-cyanorhodamine **13a** in 24 % and 30 % HPLC yield, but with incomplete conversion. After 3 h reaction time, **13a** was isolated in 50 % yield with Xantphos as ligand. Another cyanamide source, BocNHCN, was evaluated, too, but resulted in hydrolysis of the starting material (Entry 4).

With these conditions in hand, a series of three *N*-cyanorhodamines **13** has been ac-

Table 4.1 – Optimization table for the preparation of *N*-cyanorhodamine **13a**

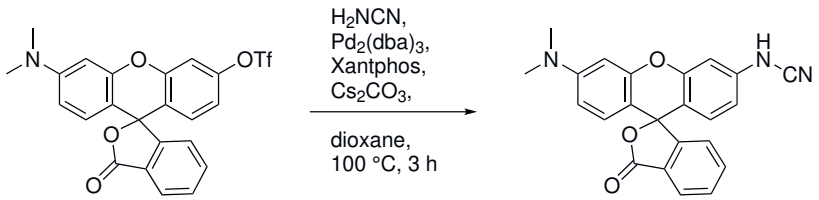

15a **13a** (50 %)

Entry	Changes from above	HPLC yield (after 1 h)
1	*t*-BuXPhos instead of Xantphos	0 % [A]
2	XPhos instead of Xantphos	24 % [B]
3	*none*	30 % [B]
4	BocNHCN (2 equiv) instead of NH_2CN, 80 °C, 18 h	- [C,D]

0.1 mmol **15a**, 3 equiv. NH_2CN, 10 mol% $Pd_2(dba)_3$, 20 mol% Xantphos, and 3 equiv. Cs_2CO_3 and 0.5 equiv. 4,4'-di(tert-butyl)biphenyl as internal standard were stirred in 1.0 mL dioxane at 100 °C in a reaction vial with modification indicated above. [A] Starting material consumed. [B] Incomplete conversion. [C] No internal standard added. [D] LCMS analysis after 18 h revealed no product formation of Boc-protected **13a** and partial hydrolysis of starting material.

cessed from their corresponding rhodol triflates (Scheme 4.2A). Besides *N*, *N*-dimethylamino derivative **13a**, julolidine **13b** and azetidine analog **13c** were prepared to later study the variations in the quantum yields due to suppressed fluorescence quenching pathways.[117,138]

The Buchwald-Hartwig protocol further enables the cross-coupling of fluorescein triflate **14a** with methanesulfonamide to yield *N*,*N*-bis(methylsulfonyl)rhodamine (**17**) (Scheme 4.2B), which is similar to the dyes described by Sharma *et al*. (Figure 4.1). and will be used for comparison to *N*-cyanorhodamines.

Despite the successful bis-functionalization with a sulfonamide, the bis-functionalization of fluorescein triflates **14** with cyanamide was unsuccessful (Scheme 4.2C). Consumption of the starting material was observed and traces of the mono-aminated product, as well as values m/z(+) $>$ 1000 were spotted by LCMS analysis. These findings suggests that the scope is not limited by the formation of product but the products' reactivity to undergo dimerization and oligomerization under the coupling conditions. Aryl cyanamides are generally prone to undergo oligomerization, especially when exposed to heat or Lewis acids.[139] For example, cyclotrimetrization was reported for small aryl cyanamides.[139]

Different Buchwald-Hartwig coupling conditions were tested to overcome this limitation.

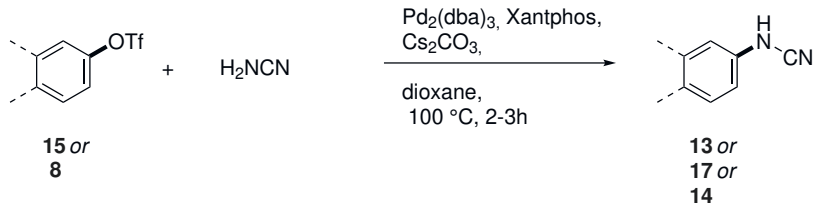

15 *or* **8** → **13** *or* **17** *or* **14**

A) *N*-Cyanorhodamines:

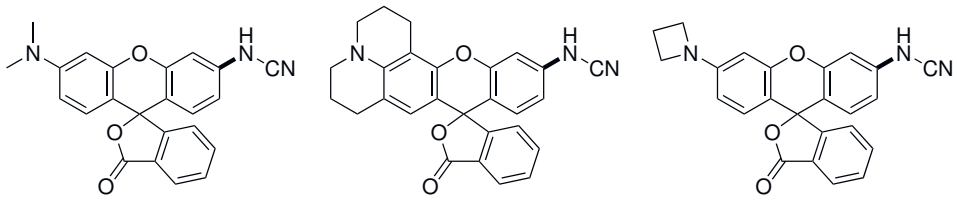

13a (50 %) | **13b** (45 %) | **13b** (35 %)

B) *N*,*N*′-bis(methylsulfonyl)rhodamine:

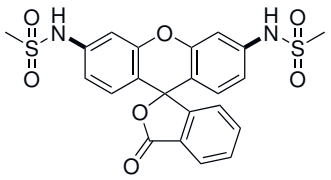

17 (64 %) [A]

C) Unsucessful examples: *N*,*N*′-cyanorhodamines:

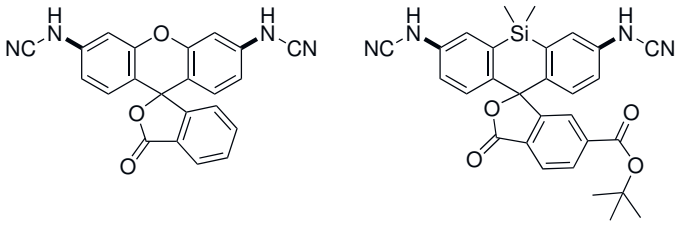

14a (decomposition) [B] | **14b** (decomposition) [B]

Scheme 4.2 – Substrate scope of the Pd-catalyzed Buchwald-Hartwig amination of aryl trilfates **13**. Reproduced from Ref.[1] with permission from the Royal Society of Chemistry. [A] H_2NSO_2Me and XPhos instead H_2NCN and Xantphos. [B] 80 ℃ to 120 ℃ for 2–28 h.

The guanidine bases BTMG and MTBD under homogeneous conditions[140] were found to hydrolyze **8a** to fluorescein **1a** (Scheme 4.3A). Next, 3',6'-diiodofluoran **10a** was tested as an alternative substrate (Scheme 4.3B). Aryl iodides are more hydrolytically stable and have different reactivity compared to aryl triflates in palladium-catalyzed cross-couplings. However, iodide **10a** showed to be non-reactive under these coupling conditions and any consumption of starting material was attributed to the competing dehalogenation reaction.

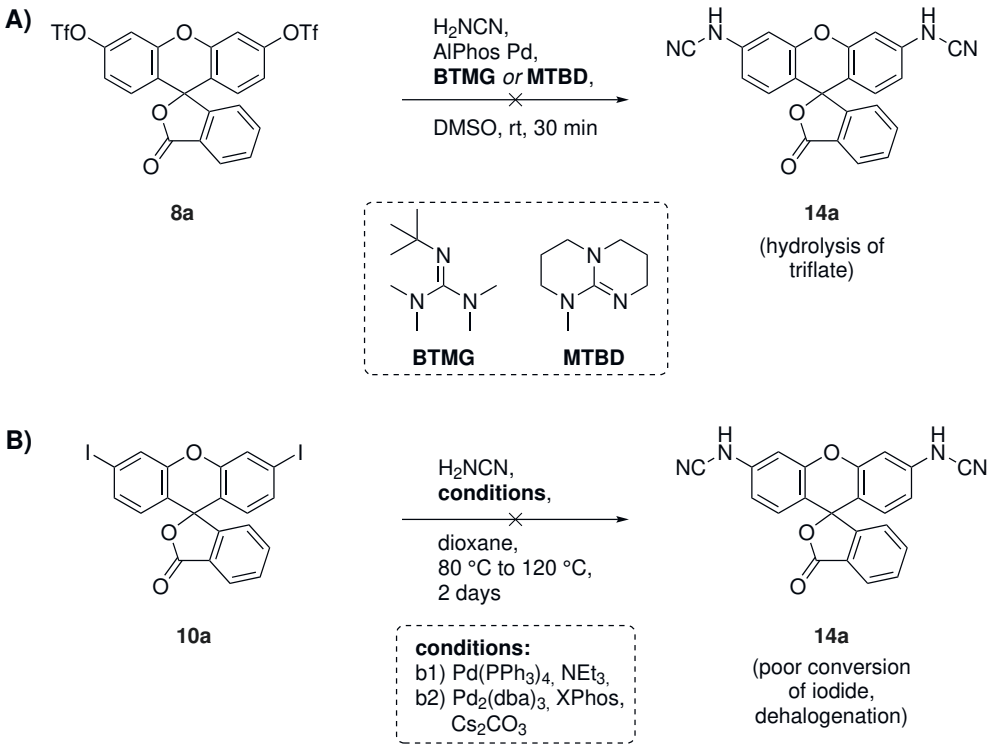

Scheme 4.3 – Method scouting of Buchwald-Hartwig conditions to yield **14a**.

4.2.2 Ullmann coupling of aryl iodides

Fluorescein iodides have been further used in the copper-catalyzed Ullmann reaction to access rhodamine dyes.[121] Furthermore, Boddapati *et al*. recently described the Ullmann coupling of aryl iodides with *in situ* generated cyanamide.[141] Testing these coupling conditions with iodide **10a** and commercially available cyanamide yielded *N*,*N'*-dicyanorhodamine **14a** in 9 % HPLC yield (Table 4.2, Entry 1). The base Cs_2CO_3 was found to increase the HPLC yield significantly to 28 % (Entry 2). Increasing the amount of cyanamide to 10 equiv. resulted in no improvement (Entry 3). Next, a ligand screening was conducted to optimized the reaction conditions further. Diketone **L2** was found to increase the yield significantly to 49 % (Entry 4). L-Proline (**L3**) as ligand increased the yield further to 64 % (Entry 5), but *N*-arylated prolin was identified

as an inseparable side-product. Applying a copper/ligand ratio of 1:1 did not prevent the *N*-arylated side-product (Entry 6). *N*-Methyl glycine (**L4**) as an alternative amino acid ligand was found to decrease the yield (Entry 7). Diamine **L5** as ligand (Entry 8) and DEG as ligand and co-solvent (Entry 9) let to no or decreased yield of **14a**. Ding *et al*. recently reported a CuI/hydrazide catalytic system as efficient for the amination of aryl halides.[142] Testing the hydrazide ligand **L6** yielded the *N*,*N'*-dicyanorhodamine in 70 % HPLC yield (Entry 10). Further optimization was conducted and the best result was obtained with **L6** and K_3PO_4 in 2-ME affording **14a** in 81 % HPLC yield (Entry 11). On the contrary, DEG was found to afford **14a** in 53 % HPLC yield (Entry 12).

After optimization, a short series of *N*,*N'*-dicyanorhodamine was prepared (Scheme 4.4A). The protocol also allowed to access *N*-cyanorhodamines **13** from their corresponding rhodol iodides (Scheme 4.4B), providing an alternative route to the Pd-catalyzed Buchwald-Hartwig amination (Scheme 4.2). Adapting the coupling conditions, fluorescein iodide **10a** can be mono-aminated to **18** in 35 % yield (Scheme 4.5C), which can be potentially tested as a building block to access various asymmetric *N*-cyanorhodamines.

For multi-color, live-cell imaging with self-labeling protein tags, fluorescent dyes with well-separated absorption maxima and emission in distinct ranges and conjugated to a reactive ligand are required. In a smiliar manner to carbo- and Si-rhodamines (see chapter 2.3.1, 17), the preparation of the carbo- and Si-analogs of the *N*,*N'*-dicyanorhodamines for color-tuning was attempted. The carborhodamine analog **14d** was prepared from its corresponding iodide under the Ullmann coupling conditions described above. The method further tolerates the presence of a free carboxyl group. Compound **NCR1** was prepared in 72 % yield. Next, the HaloTag and SNAP-tag ligands were introduced via peptide coupling chemistry through the carboxylic acid yielding the two conjugates **NCR1-Halo** and **NCR1-SNAP** for live-cell imaging (Scheme 4.4A).

Table 4.2 – Optimization table for preparation of *N*,*N'*-cyanorhdamine **14a**.

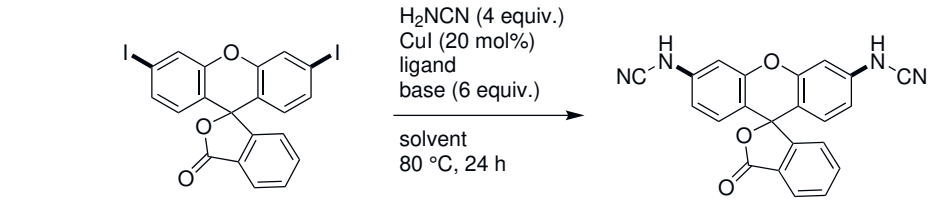

10a **14a**

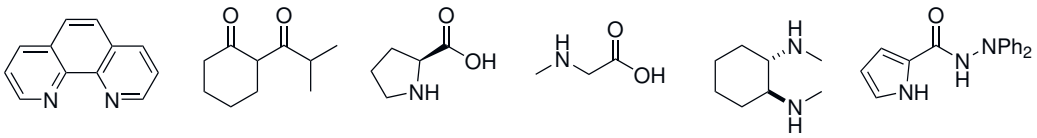

L1 **L2** **L3** **L4** **L5** **L6**

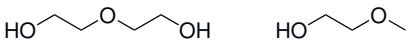

DEG **2-ME**

Entry	Ligand	Base	Solvent	HPLC yield (after 24 h)
1	**L1** (50 mol%)	K_3PO_4	DMSO	9 % [A]
2	**L1** (50 mol%)	Cs_2CO_3	DMSO	28 %
3	**L1** (40 mol%)	Cs_2CO_3	DMSO	20 % [A,B]
4	**L2** (50 mol%)	Cs_2CO_3	DMSO	49 %
5	**L3** (50 mol%)	Cs_2CO_3	DMSO	64 % [C]
6	**L3** (50 mol%)	Cs_2CO_3	DMSO	49 % [C,D]
7	**L4** (50 mol%)	Cs_2CO_3	DMSO	14 %
8	**L5** (40 mol%)	Cs_2CO_3	DMSO	0 %
9	-	Cs_2CO_3	DMSO/DEG (10:1)	22 %
10	**L6** (20 mol%)	Cs_2CO_3	DMSO	70 %
11	**L6** (20 mol%)	K_3PO_4	2-ME	81 %
12	**L6** (30 mol%)	K_3PO_4	DEG	53 %

0.1 mmol **10a**, 4 equiv. NH_2CN, 20 mol% CuI, 20–50 % ligand, 6 equiv. base and 0.5 equiv. 4,4'-di(tert-butyl)biphenyl as internal standard were stirred in 1.0 mL dioxane at 80 °C in a reaction vial with modification indicated above. Reproduced from Ref.[1] with permission from the Royal Society of Chemistry. [A] Formation of multiple side-products. [B] 10 equiv. NH_2CN. [C] Partial *N*-arylation of the ligand. [D] 50 mol% CuI.

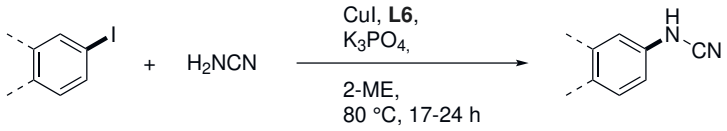

16 *or* **10** → **13** *or* **14** *or* **NCR1**

A) *N,N'*-Dicyanorhodamines:

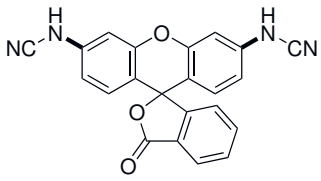

14a (49 %)

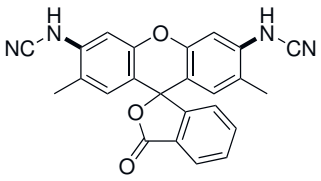

14c (49 %)

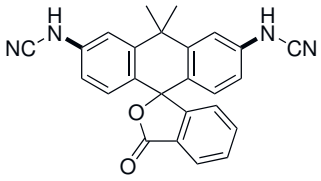

14d (81 %)

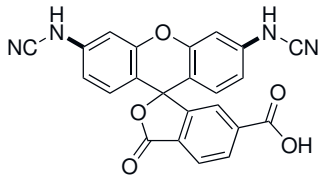

NCR1 (72 %)

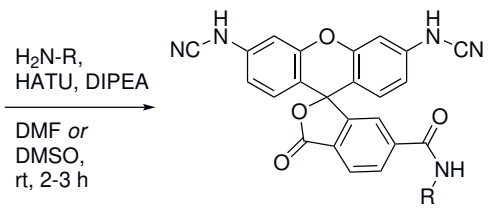

NCR1-Halo (R = Halo, 37 %)
NCR1-SNAP (R = SNAP, 22 %)

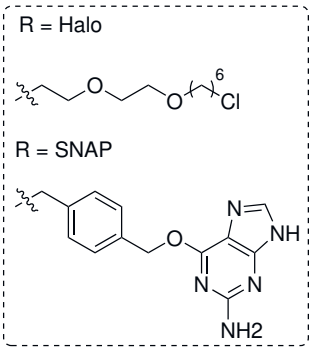

B) *N*-cyanorhodamines:

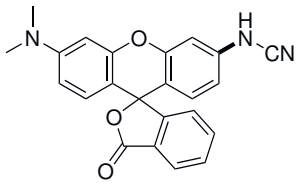

13a (57 %)

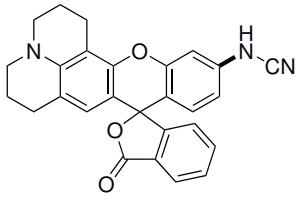

13b (51 %)

C) Mono-functionalized product:

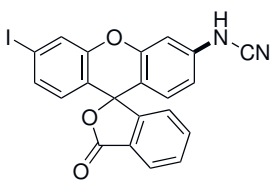

18 (34 %) [A]

Scheme 4.4 – Substrate scope of the copper-catalyzed Ullmann coupling. Reproduced from Ref.[1] with permission from the Royal Society of Chemistry. [A] Method B: CuI, **L1**, Cs_2CO_3, DMSO, 80 °C, 24 h

Next, the synthesis of more complex *N*-cyanorhodamines was investigated. On one hand, the preparation of halogenated and annulated analogs was attempted to study the photophysical properties of this new class of fluorophore. On the other hand, color-tuning of **NCR1** will enable multi-color, live-cell imaging. For this, the carbo- and Si-analogs of the conjugates **NCR1-Halo** and **NCR1-Halo** are required.

At first, the Ullmann coupling of aryl iodides was revisited to extend the library of *N*-cyanorhodamines to the compounds of interest described above. Contrary to the previously described substrates (Scheme 4.4), *N*-cyanorhodamines could not be accessed (Scheme 4.5). Reaction of halogenated and annulated iodides under the cross-coupling conditions to prepare the corresponding *N*-cyanorhodamines **14e**, **14f** and **14g** resulted in formation of multiple inseparable side-products (Scheme 4.5A). It was found that the conversion of bridge-substituted iodides to compounds **14b**, **NCR3** and **NCR2** occurred (Scheme 5B). Unfortunately, formation of side-products (among them the solvent adducts) were observed. The formation of solvent adducts can be explained by a nucleophilic addition of the solvent 2-ME to the electron-deficient fluorescent core **I** at the amphiphilic cyanamide forming adduct **II**. Lastly, the *t*-butyl protected iodide was also tested under the Ullmann coupling conditions to obtained compound **14h** (Scheme 4.5C). Here, partial deprotection of the *t*-butyl ester **14h** to carboxyl acid **NCR1** was observed. To overcome this issue, the crude reaction mixture was stirred in MeCN/TFA to completely deprotect the *t*-butyl ester. This approach yielded not the *N,N'*-dicyanorhodamine **NCR1** but the hydrolyzed, non-fluorescent urea compound **19** in 11 %, demonstrating the acid-sensitivity of the aryl cyanamide once installed on the fluorescent molecule.

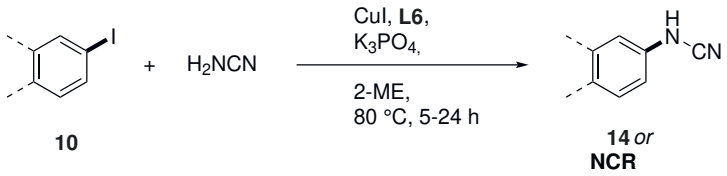

A) halogenated/anullated derivatives:

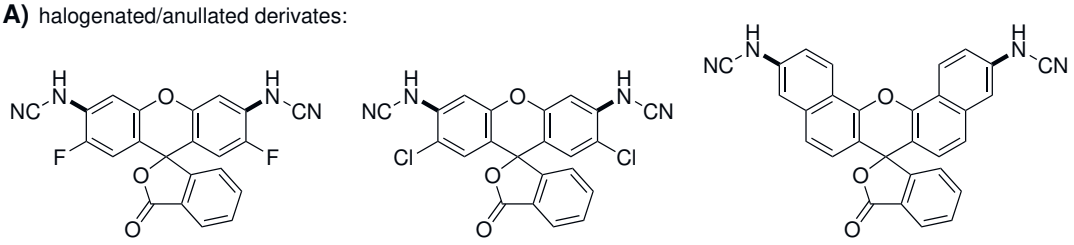

B) bridge-substituted derivatives:

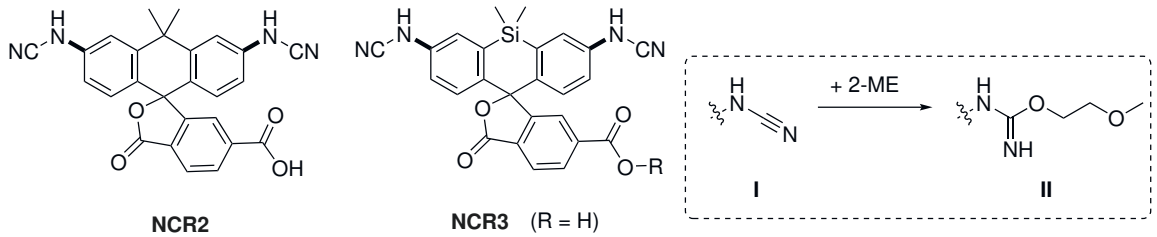

C) *t*-butyl ester derivative:

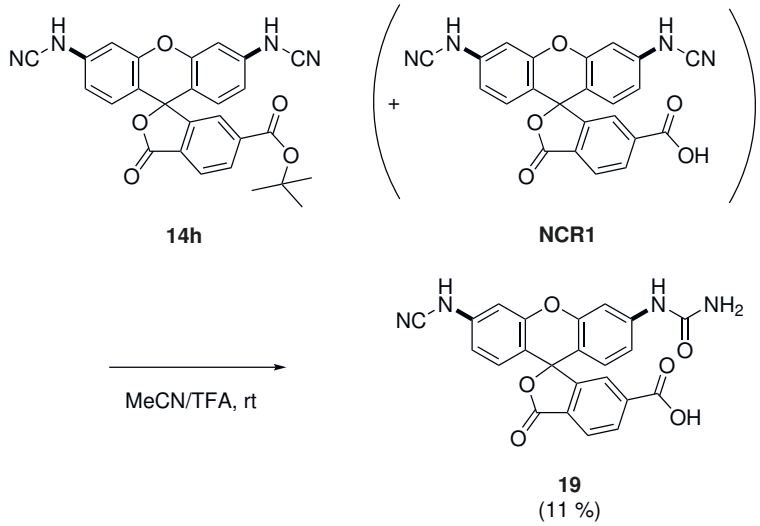

Scheme 4.5 – Unsuccessful examples within the Ullmann coupling.

4.2.3 Base induced degradation of 1-aryl tetrazoles

Since it was shown that aryl cyanamides underwent undesired side transformations under the reaction conditions, a different synthetic strategy was explored and tested on model compound **20**. Anilines may react with sodium azide and orthoesters to give tetrazoles in a condensation reaction.[143] These 1-aryltetrazoles decompose upon deprotonation under basic conditions to aryl cyanamide by releasing dinitrogen.[143] The synthetic strategy was validated on aniline **20** yielding tetrazole **21** in 84 % yield and cyanamide **22** in 87 % yield (Scheme 4.6).

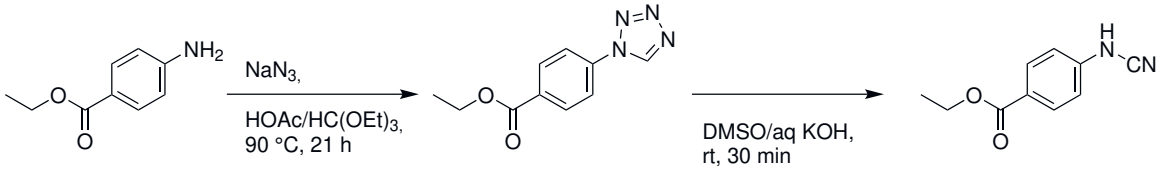

20 **21** (84 %) **22** (87 %)

Scheme 4.6 – Formation and deprotonation of tetrazole **21**.

Next, it was attempted to find milder reaction conditions for the tetrazole ring-formation. Based on the literature precedent,[144,145] $TMS-N_3$ as an alternative azide source and ionic liquid **IL-1** as (co)solvent were briefly evaluated (Table 4.3). No product formation was found applying these conditions and, therefore, the previous protocol described in Scheme 4.6 was used in the preparation of dyes.

Table 4.3 – Attempted optimization of tetrazole ring-formation.

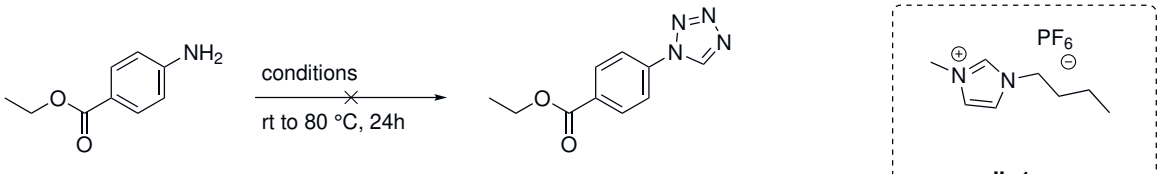

20 **21** (no product formation observed) **IL-1**

Entry	Azide	IL-1	solvent
1	$TMS-N_3$	0.50 mL	-
2	$TMS-N_3$	-	HOAc (1.0 mL)
3	NaN_3	0.10 mL	DMSO (1.0 mL)

0.1 mmol **20**, 1.5 equiv $HC(OEt)_3$, 1.2 equiv azide, and **IL-1** were stirred in 1.0 mL solvent at 80 °C in a reaction vial with modification indicated above.

Rhodamine dyes **25** were prepared from their corresponding triflates **23** in a two-step approach (Scheme 4.7). The triflates were cross-coupled with $BocNH_2$ under Buchwald-Hartwig amination conditions. The products **24** were deprotected to rho-

damine 110 analogs **25** under acidic decomposition removing both the Boc and the *t*-butyl protecting group.

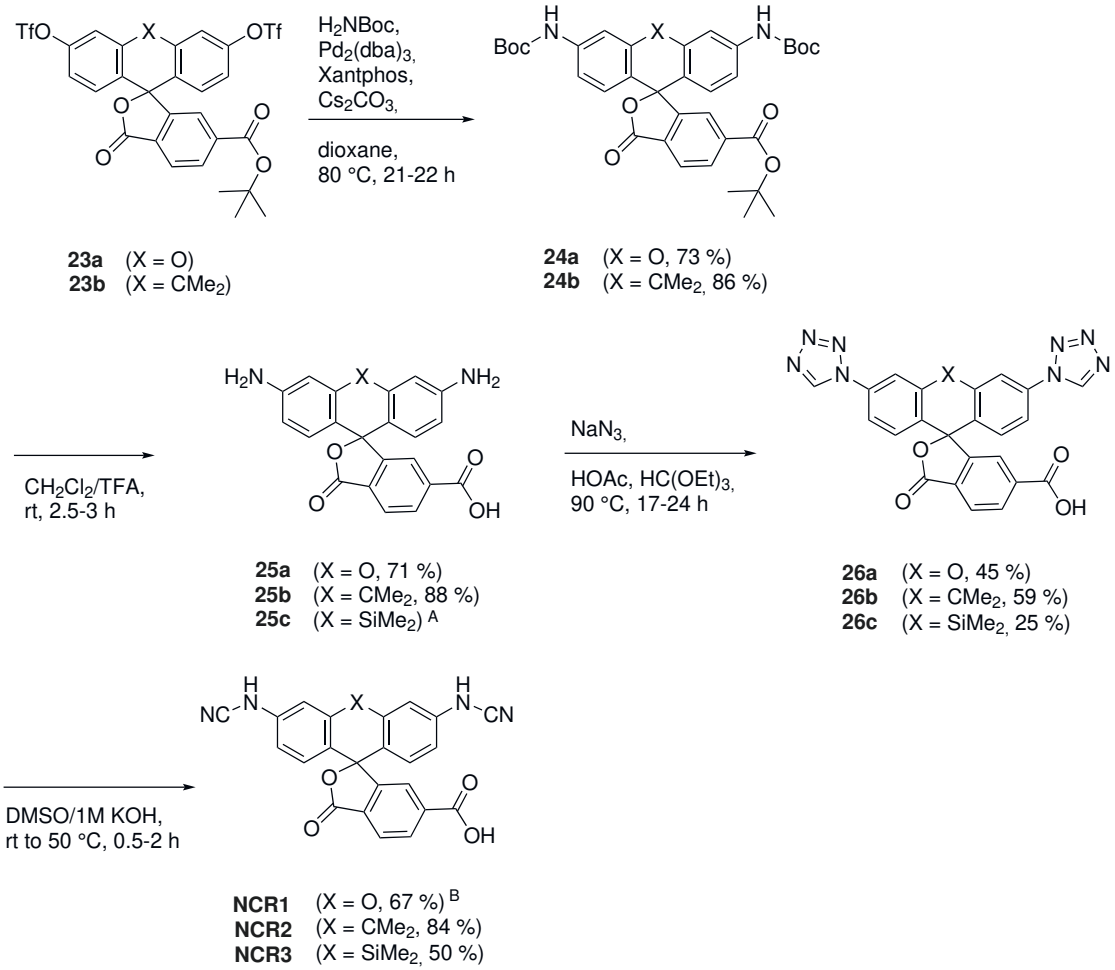

Scheme 4.7 – *N*-Cyanorhodamines prepared via alkaline decomposition of tetrazoles **26**. Reproduced from Ref.[1] with permission from the Royal Society of Chemistry. A **25c** prepared by Dr. Alexey Butkevich. B Yield over 2 steps.

Next, the above evaluated synthetic strategy to access *N,N'*-dicyanorhodamines was applied on Rhodamine 110 analogs **25**. The ring-forming condensation yielded the three tetrazole compounds **26** in varying yields. Under basic conditions the tetrazoles decomposed to the three differently colored *N,N'*-dicyanorhodamine dyes **NCR1**, **NCR2** and **NCR3**. Notably, *N,N'*-dicyanorhodamine dye **NCR1** was prepared in a 2-step approach from crude tetrazole **26a**, increasing the overall yield. Tetrazole **26a** has poor solubility in organic solvents (hexane/EtOAc), which resulted in loss of material during the purification work-up.

After obtaining bridge-substituted *N,N'*-cyanorhodamine dyes **NCR1**, **NCR2** and **NCR3**, the next task was the synthesis of these fluorescent dyes attached reactive Halo-ligands for live-cell imaging. Peptide-coupling conditions to amidate the free carboxylic acid failed for compounds **NCR2** and **NCR3** due to a reaction of the nucleophilic aryl

cyanamide with the coupling reagent. Therefore, the previously prepared tetrazole compounds **26b** and **26c** were amidated with the $H_2N-Halo$ ligand, instead (Scheme 4.8). The tetrazole compounds **27** were finally converted to the *N*,*N'*-cyanorhodamine ligands **NCR2** and **NCR3** by base-mediated decomposition.

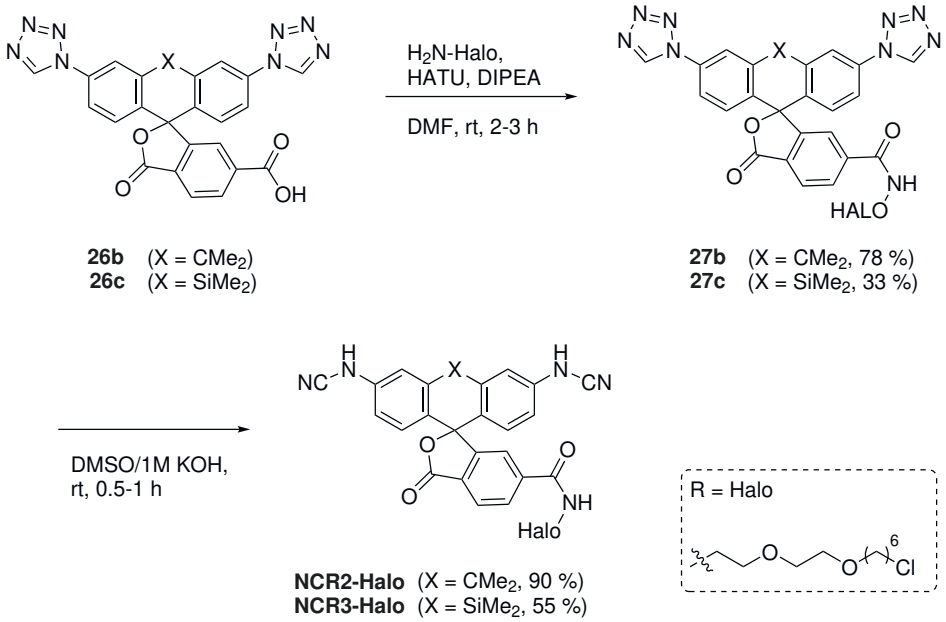

Scheme 4.8 – Preparation of *N*,*N'*-cyanorhodamine ligands. Reproduced from Ref.[1] with permission from the Royal Society of Chemistry.

In summary, three different methods have been designed to synthesize *N*-cyanorhodamine dyes. Asymmetric *N*-cyanorhodamines were prepared via a Buchwald-Hartwig amination of aryl triflates (Scheme 4.2, p. 44). Symmetric derivatives could not be prepared using this methodology, and were accessed via the copper-catalyzed Ullmann coupling with hydrazide **L6** ligand from aryl iodides (Scheme 4.5, p. 48). Furthermore, asymmetric *N*-cyanorhodamines are accessible by this method as well. Finally, carbo- and Si-analogs of *N*,*N'*-cyanorhodamine (**14a**) and their reactive ligand conjugates for self-labeling Halo and SNAP protein tags were designed via a third synthetic route involving alkaline decomposition of tetrazoles (Scheme 4.7, p. 52; Scheme 4.8, p. 53).

4.3 Photophysical characterisation of anionic *N*-cyanorhodamines

4.3.1 *N*-cyanorhodamine dyes

Photophysical properties of fluorescein dyes depend on their protonation state and therefore differ in acidic and basic environments. For example, fluorescein **1a** displays weak absorption and emission in acidic aqueous solutions (λ_{abs} = 453, 472 nm, $\epsilon \sim$ 30.000 $M^{-1}cm^{-1}$, $\Phi_{FL} \sim 0.4$)[100] and is strongly absorbant and emissive (λ_{abs} = 490 nm, $\epsilon \sim$ 80.000 $M^{-1}cm^{-1}$, $\Phi_{FL} \sim 0.9$)[100] in basic aqueous solutions. Similarly, fluorescein is less absorbant and non-fluorescent in non-polar solvents and strongly absorbant and fluorescent in aqueous media. Similar behavior was assumed for *N,N'*-dicyanorhodamine **14** being negatively charged fluorophore like fluorescein.

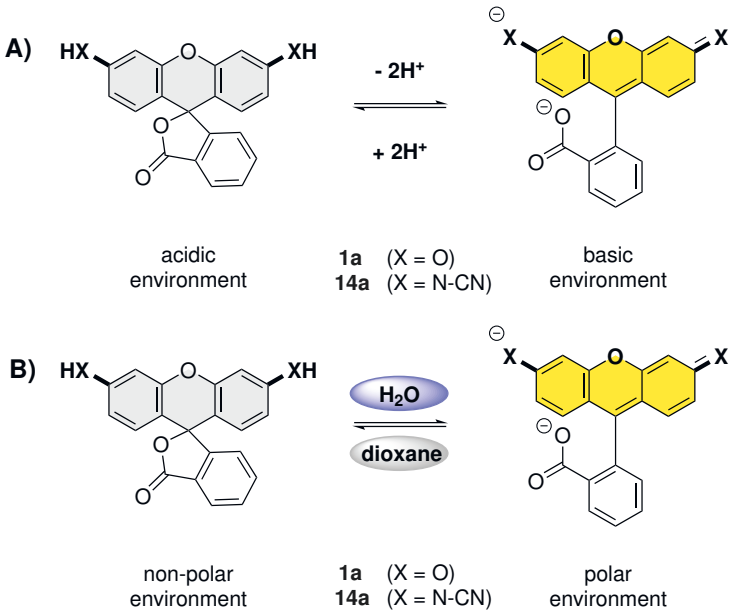

Scheme 4.9 – Simplified equilibria of negatively charged fluorescein-like compounds. (A) Acid-base equilibrium. (B) Polarity-dependant equilibrium.

To investigate the acid-base behavior of *N*-cyanorhodamines, dye solutions (10 µM) in phosphate buffers (0.1 M) were measured at different pH values (Appendix Figure 9.1, p. 164). Figure Scheme 4.9A compares the acid-base behavior of the absorption displayed by **TMR**, fluorescein **1a** and *N,N'*-dicyanorhodamine **14a**. The absorption of **TMR** is not significantly affected by the changes in pH. Fluorescein **1a** demonstrated the acid-base behavior reported in literature. The absorption increased with increasing pH value following a titration curve.[146] The absorption of *N,N'*-dicyanorhodamine **14a** displayed a similar trend as the fluorescein (Figure 4.2).

To quantify the acid-base behavior of **1a** and **14a**, the data in Figure 4.2A were fitted to a sigmoid function 3.2 (p. 32). The multiple protonation and proton-transfer steps of **1a** and **14a** is represented by a simplified equilibrium between a non-fluorescent spirolactone and a twice-deprotonated, fluorescent form (Scheme 4.9). Since the Henderson-Hasselbalch equation describes a single protonation step, the data in Figure 4.2 were fitted to a general sigmoid function 3.2 (p. 32). From this equation, the values $pK_{a,FL}$ (sigmoid's midpoint) and n (steepness of the curve) are derived. Hereby, a $pK_{a,FL}$ of 6.1 (lit. $pK_{a,FL}$ 6.3)[86] for fluorescein **1a** and a $pK_{a,FL}$ of 5.1 for *N,N'*-dicyanorhodamine **14a** were obtained. The reduced $pK_{a,FL}$ value in **14a** can be attributed to the electron-withdrawing cyanamido groups. Same measurement of *N,N'*-bis(methylsulfonyl)rhodamine **17**, bearing a different electron-withdrawing group, displayed a value of $pK_{a,FL}$ 6.5 close to fluorescein **1a**.

The coefficients n describes the steepness of the sigmoid curve and the transition width between the non-fluorescent spirolactone and the fluorescent form. In literature reports, fine-tuning of the structures of triarylmethane fluorophores led to the design of Hill-type pH probes, which display a broad transition width (low n), against Henderson-Hasselbalch-type probes with a narrow transition width (high n).[85,147] Different values of coefficients n were obtained for fluorescein (**1a**) ($n = 0.67$), *N,N'*-bis(methylsulfonyl)rhodamine (**17**) ($n = 1.6$), and *N,N'*-dicyanorhodamine (**14a**) ($n = 1.9$). Substitution of the hydroxyl group by methylsulfonyl or cyanamido results in a decrease of coefficients n and a short transition width and can be considered a possible strategy in the design of Henderson-Hasselbalch-type pH probes. Based on the three studied compounds, a trend is assumed that the values $pK_{a,FL}$ and n of negatively charged fluorophores can be altered via installation of groups with electron-withdrawing strength.

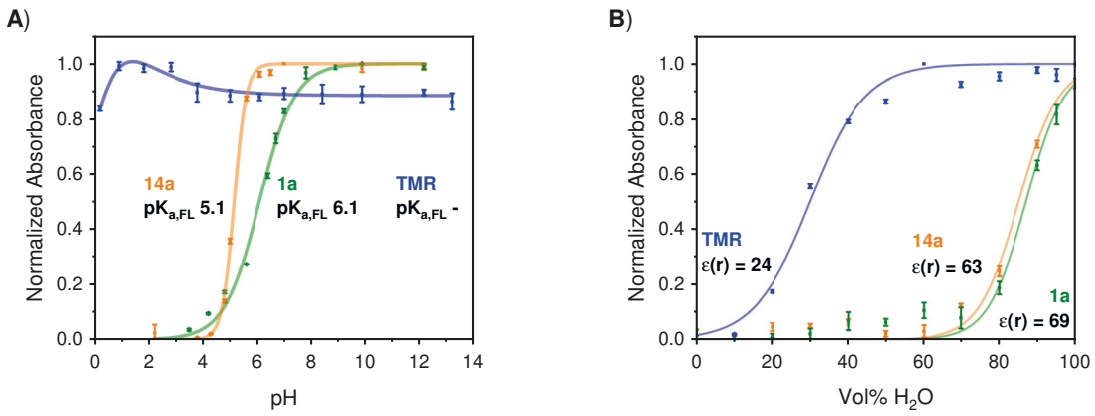

Figure 4.2 – abs_{norm} at fixed wavelength λ_{max} (absorption maximum in the visible range with highest absorption of the series) plotted vs (A) pH or (B) Vol% H_2O for different dyes. $pK_{a,FL}$ or $D_{0.5}$ values were calculated according to equations 3.2 (p. 32) and 3.3 (p. 32). Reproduced from Ref.[1] with permission from the Royal Society of Chemistry.

Next, *N,N'*-dicyanorhodamine (**14a**), fluorescein (**1a**), and TMR were measured in aqueous dioxane solution with different contents of water (Appendix Figure 9.2) to study the polarity dependence of absorption and emission (Figure Scheme 4.9). $D_{0.5}$ was defined as the solvent polarity response value of the medium, at with the normalized absorbance of the dye is one-halve of its maximum along the gradient,[96] and corresponds to the midpoint of the step of the sigmoid curve.

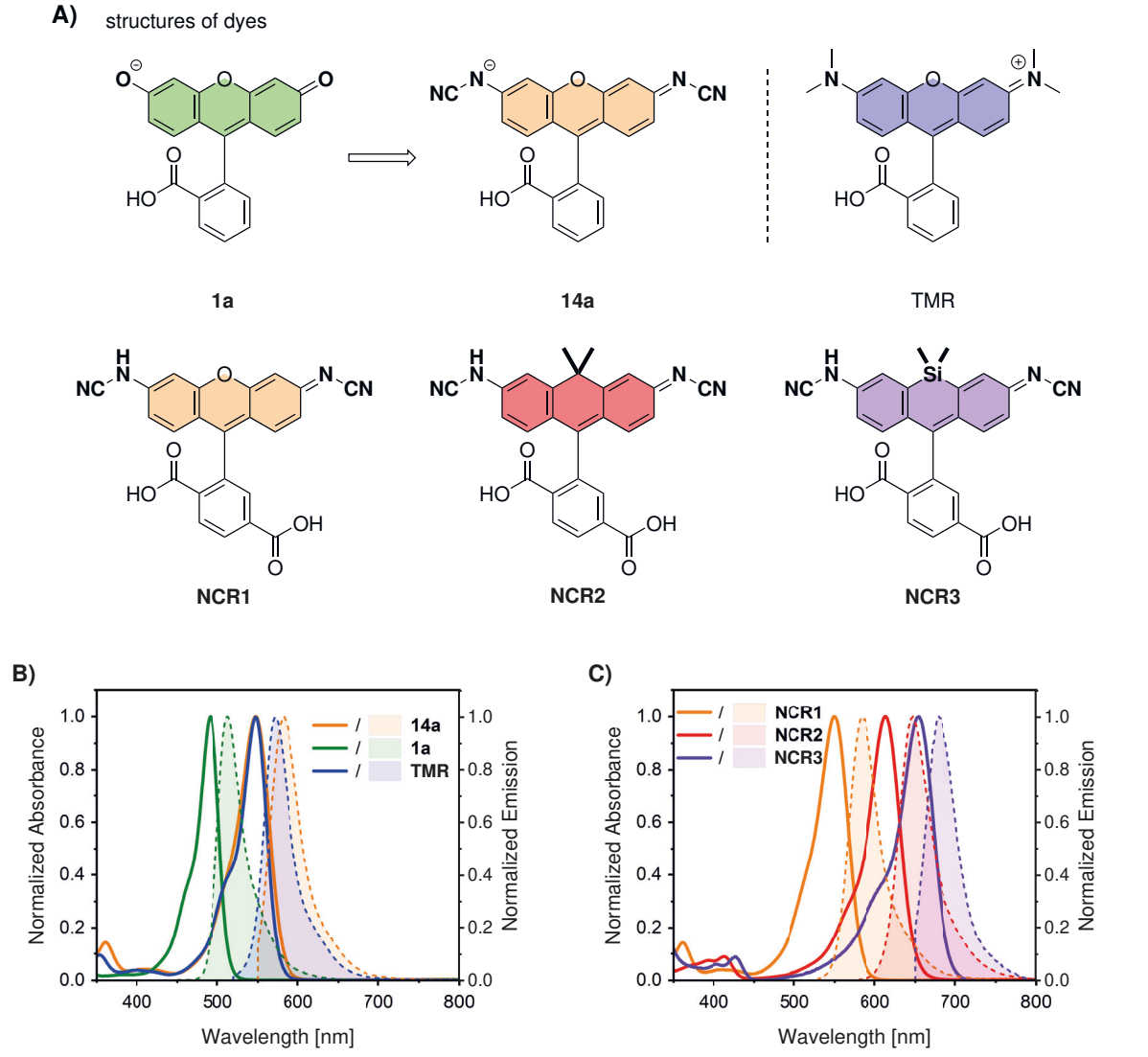

Figure 4.3 – Absorption and emission of *N,N'*-dicyanorhodamine dyes. (A) Chemical structures. (B)/(C) Absorption and emission spectra of **1a** (pH 9), **14a** (pH 9), **TMR**, **NCR1**, **NCR2**, and **NCR3** in 0.1 M phosphate buffer (pH 10). Reproduced from Ref.[1] with permission from the Royal Society of Chemistry.

The negatively charged fluorecein **1a** and *N,N'*-dicyanorhodamine **14a** displayed high solvent polarity response values $D_{0.5}$ indicating the dyes would be non-fluorescent in non-polar environment such as lipophilic membrane structures. TMR, on the other hand, has a relatively low solvent polarity response value $D_{0.5}$ indicating the dye to be fluorescent under mild lipophilic conditions.

Next, the photophysical properties of *N,N'*-dicyanorhodamine (**14a**) were compared to fluorescein **1a** and **TMR** (Figure 4.3C). The replacement of the two hydroxyl groups in **1a** with cyanamido groups in **14a** resulted in a bathochromic shift of emission ($\sim$ 70 nm). The same effect was observed by Sharma *et al*., where substituting one or two hydroxyl groups with sulfonamide induced a weaker bathochromic shift of $\sim$ 10 nm or $\sim$ 40 nm, respectively. Similarly, the prepared *N,N'*-bis(methylsulfonyl)rhodamine **17** displays a shift of $\sim$ 40 nm relatively to fluorescein [**1a**]. Replacement with cyanamido groups seems to result in a stronger bathochromic shift yielding *N,N'*-dicyanorhodamine **14a** with comparable absorption and emission as **TMR** while being negatively charged.

For color-tuning, the substitution of the bridging oxygen by dimethylmethylene and dimethylsilylene is known to yield the bathochromically shifted carbo- and Si-rhodamine derivatives.[93] Accordingly, carbo- and Si-*N,N'*-dicyanorhodamines **NCR2** and **NCR3** have been prepared. **NCR2** and **NCR3** display bathochromic shifts in absorption and emission compared to the O-derviate **NCR1** Figure 4.3D.

Next, the stability of *N,N'*-dicyanorhodamine **14a** against hydrolysis and oligomerisation[139] of the cyanamido group was studied. Absorption spectra of phosphate buffer solutions (pH 5, pH 7, pH 10; 20 % DMSO as co-solvent) indicated no changes over 20 h. Further analysis by LCMS confirmed no irreversible chemical change of the fluorophore within this time period (Appendix Figure 9.5, 168).

The installation of electron-withdrawing fluorine atoms on fluorescein **1a** yielded OregonGreen, which displayed improved photostability.[35] The photostability of *N*-cyanorhodamines **13a** and **14a** was studied as the electron-withdrawing cyanamido group was suspected to increase the photostability as well. *N*-cyanorhodamine **13a** and *N,N'*-dicyanorhodamine **14a** were compared to **TMR**, rhodol **2a**, carbofluorecein **1b** Figure 4.4, which all display similar absorption maxima. As expected, carbofluorecein **1b** was the least photostable dye of the series followed by rhodol **2a**. The two *N*-cyanorhodamines **13a** and **14a** were found to be as photostable as **TMR**.

Full photophysical characterisation of *N*-cyanorhodamines **14** and **13** is summarized in Table 4.4. Overall, dyes **14** show similar extinction coefficient but reduced fluorescence quantum yields and life times compared to fluorescein (**1a**) and **TMR**. Furthermore, $pK_{a,FL}$ and $D_{0.5}$ values are reduced compared to fluorescein (**1a**) as discussed above. Notably, the carbo- and Si-*N,N'*-dicyanorhodamines display increased $pK_{a,FL}$ and $D_{0.5}$ values, which is in agreement with literature data.[86] $D_{0.5}$ values could not be determined for **NCR2** and **NCR3** because of their low absorption even in 100 % H_2O.

Mono-*N*-cyanorhodamine **13a** is the cyanamido analog of rhodol **2a**. The replacement of hydroxy with the cyanamido group induced of bathochromic shift of $\sim$ 30 nm corre-

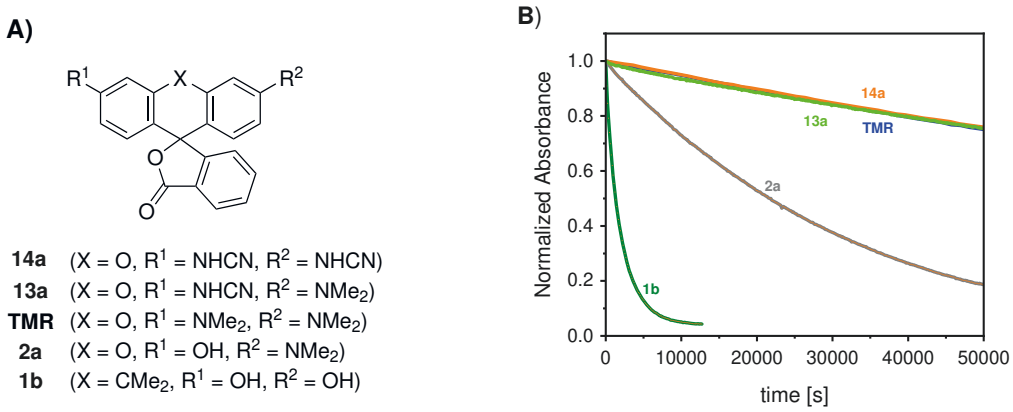

Figure 4.4 – (A) Chemical structures. (B) Photobleaching of dyes in borate buffer (0.1 M, pH 9.9) irradiated with a 530 nm LED (conducted by Dr. Mariano Bossi). Full photobleaching data are provided in the Appendix (Figure 9.6, p. 169). Reproduced from Ref.[1] with permission from the Royal Society of Chemistry.

sponding to one-half of the effect produced by replacing two hydroxyl groups in **14a**. Furthermore, the replacement caused a reduced $pK_{a,FL}$, while the solvent polarity response value $D_{0.5}$ changes insignificantly (Appendix Figure 9.3, p. 166, Figure 9.4, p. 167). The julolidine derivative **13b** displayed a bathochromic shift of $\sim$ 20 nm due to the effect of annulated alkyl rings, which function as a stronger donor compared to methyl groups.[22] Furthermore, an increase in fluorescent quantum yield Φ_{fl} and lifetime τ_{fl} to **13a** was found. The same increases were observed in azetidine derivative **13c** and can be explained by the suppression of the non-radiative twisted intramolecular charge transfer (TICT) pathway.[105,117] Interestingly, these modifications also cause an decreasing photostability and an increasing photobleaching rate Φ_{bl}.

In summary the replacement of hydroxyl groups in fluoresceins and rhodols by electron-withdrawing cyanamido groups results in bathochromically shifted, photostable *N*-cyanorhodamines acid-base behavior and fluroesceins but reduced $pK_{a,FL}$ values.

Table 4.4 – Photophysical data of *N*-cyanorhodamines compared to reference compounds.

Dye	λ_{abs} [nm]	$\epsilon(\lambda_{abs})$ [$\cdot 10^3$ $M^{-1}cm^{-1}$]	λ_{em} [nm]	Φ_{fl}	τ_{fl} [ns]	$pK_{a,FL}$	$D_{0.5}$	Φ_{bl} [$\cdot 10^{-6}$]
Reference Compounds								
1a	491[A] (502)	88[A] (102)	512[A] (521)	0.90[126]	4.1[105]	6.1	69	-
TMR	547 (548)[B]	123 (113)[B]	571 (574)[B]	0.55[B]	2.7[B]	n.d.	24	0.30
2a	518[A] (511)	81[A] (78)	547[A] (536)	0.22	1.0	5.8	43	2.2
17	519[C] (539)	80[C] (46)	553[C] (569)	0.22	1.1	6.5	-	-
***N,N'*-dicyanorhodamines**								
14a	547[A] (568)	101[A] (111)	582[A] (597)	0.24	1.2	5.1	63	0.16
14c	552[A] (574)	65[A] (79)	584[A] (600)	0.30	2.2	5.1	50	0.68
14d	611 (633)	77 (30)	644 (658)	0.36	2.0	7.0	67	-
NCR1	549 (569)	105 (119)	584 (597)	0.23	1.2	4.6	72	-
NCR2	614 (623)	94 (35)	647 (658)	0.34	1.9	7.0	n.d.	-
NCR3	654 (675)	n.d.	679 (694)	0.22	1.3	7.3	n.d.	-
***N*-cyanorhodamines**								
13a	547[A] (553)	90[A] (86)	577[A] (584)	0.38	1.7	4.6	39	0.63
13b	560 (565)	55 (84)	597 (589)	0.55	3.5	4.9	12	2.2
13c	547 (554)	62 (72)	576 (583)	0.61	2.9	4.7	43	1.2

Absorption maxima λ_{abs}, extinction coefficient $\epsilon(\lambda_{abs})$, emission maxima λ_{em} fluorescence quantum yields Φ_{fl} fluorescence lifetimes τ_{fl} and photobleaching quantum yields Φ_{bl}were determined in phosphate buffer (0.1 M) at pH 10 and EtOH + 1 % NEt_3 (in brackets), unless stated otherwise. $pK_{a,FL}$ values or solvent response value $D_{0.5}$ were determined from absorption spectra of a series of phosphate buffers (0.1 M) or aqueous dioxane solutions. Reproduced from Ref. [1] with permission from the Royal Society of Chemistry. n.d. = not determined. - = not measured. [A] Measured at pH 9. [B] Values from Ref.[121], measure in EtOH + 0.1 % TFA. [C] Measured at pH 8.

4.3.2 HaloTag-ligand conjugates derived from *N,N'*-dicyanorhodamines

Self-labeling protein tags allow bioorthogonal labeling of a protein of interest. The protein of interest is expressed as a fusion protein with a protein tag, which then forms a covalent bond with a specifically designed ligands conjugated to a fluorophore.[15,18] For example, the HaloTag[77] irreversibly binds to linear chloroalkanes.

To confirm the binding of the HaloTag-ligand conjugates **NCR1-Halo**, **NCR2-Halo** and **NCR3-Halo**, HaloTag7 protein with and without addition of the HaloTag-ligand conjugates was analysed by SDS PAGE (Figure 9.7, p. 170). In case of samples with protein pretreated with fluorescent ligand, red fluorescent bands of the fluorophores were observed at $\sim$ 30 kDa molecular weight, which corresponds to the mass of the protein. Further conformation by ESI MS analysis shows an increase in mass of the protein ($\Delta m = 593$ Da) corresponding to single labeling with conjugate **NCR1-Halo** (Figure 9.8, p. 170). This results confirm the covalent binding of the HaloTag-ligand conjugates **NCR1-Halo**, **NCR2-Halo** and **NCR3-Halo** to HaloTag7 protein *in vitro*.

It has been shown that the fluorescence intensity of rhodamines may alter upon binding to protein. On one hand, fluorescence intensity of rhodamines bound reversibly to BSA increases upon addition of negatively charged detergent SDS, while addition of positively charged detergent CTAB results in intensity decrease.[96] On the other hand, Si-rhodamines bound irreversibly to HaloTag7 protein display a fluorescence increase.[19] These fluorogenic responses are important considerations in live-cell imaging. For example, rhodamine probes have found to be non-fluorescent while imaging structures like G-protein receptors within the plasma membrane because of their fluorogenic responses.[148]

Initially, fluorogenic responses of *N,N'*-dicyanorhodamines bound reversibly to BSA in presence of detergents has been studied (Figure 4.5B). Presence of the negatively charged detergent SDS or the positively charged CTAB showed minor effects on the fluorescence of **TMR-Halo** and **1a-Halo** bound to BSA. In case of **6-SiR-Halo**, a increase in fluorescence with negatively charged SDS was found and a decrease of fluorescence with positively charged CTAB, whith is in agreement with the literature.[96] On the contrary, negatively charged *N,N'*-dicyanorhodamines **NCR2-Halo** and **NCR3-Halo** bound to BSA display the opposite behaviour. Fluorescence intensity decreased in presence of SDS and increased in the presence of cationic detergent CTAB. This results display *in vitro* fluorescence responses of the *N,N'*-dicyanorhodamines **NCR2-Halo** and **NCR3-Halo** bound to reversibly to BSA and a fluorescence decrease in negatively charged environments, which can result in no to low signal.

Next, fluorogenic responses of *N,N'*-dicyanorhodamines bound irreversibly to HaloTag7 has been studied (Figure 4.5C). Herein, *N,N'*-dicyanorhodamine **NCR3-Halo** bound to HaloTag7 protein displays a strong fluorescence increase in a similar manner to its Si-rhodamine analog **6-SiR-Halo**. Other compounds bound to HaloTag7 showed weak to no fluorogenic response.

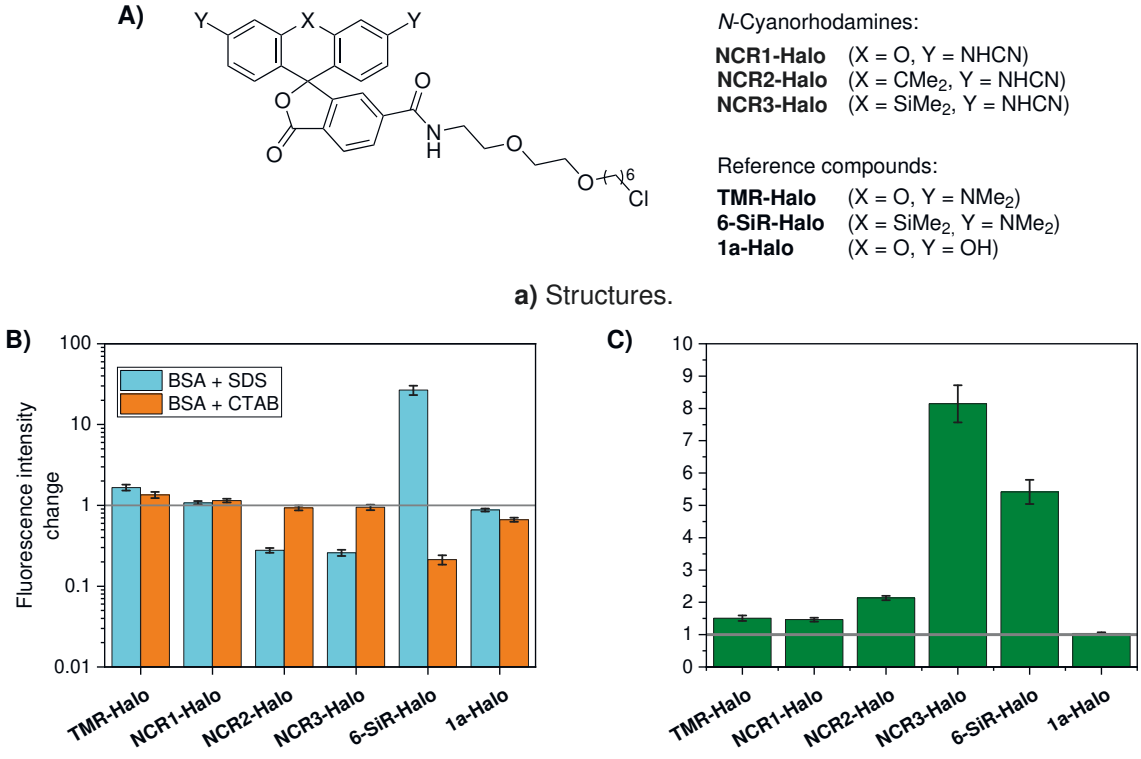

Figure 4.5 – Fluoresence intensity changes in HaloTag ligand conjugates. (A) Chemical structures. (B) Fluorescence intensity change of conjugates in 0.1 mg/mL BSA in phosphate-buffered saline (PBS) (pH 7.4) upon addition of 0.5 % SDS (blue bar) or CTAB (orange bar). (C) Fluorescence intensity change of conjugates in Dulbecco's modified Eagleś medium (DMEM) plus 10 % FBS upon addition of HaloTag7 protein. Experimental settings are provided in the Appendix (Table 9.1, Table 9.2, p. 153). Reproduced from Ref.[1] with permission from the Royal Society of Chemistry.

The labeling strategy determines the incubation time for the biological sample to efficiently label the structure of interest. Compared to slow chemical labeling strategies such as the Staudinger ligation $(k \sim 10^{-3} M^{-1} s^{-1})$ or the fast IEDDA cycloaddition $(k \sim 1 - 10^{6} M^{-1} s^{-1})$,[17] the biochemical reaction between the reactive ligand and the protein tag (Figure 4.6) is relatively fast $(k \sim 10^{3} - 10^{9} M^{-1} s^{-1})$, but depends on both the nature of the fluorophore, the reactive ligand, and the protein tag.[78] The labeling kinetics of *N,N'*-dicyanorhodamines conjugated to reactive HaloTag ligand were evaluated by measuring FP changes during the biochemical reaction. The data were then fitted to a pseudo-second order reaction (equation 3.4, p. 34), as previously described by Wilhelm *et al*. HaloTag ligand conjugates **NCR1-Halo** to **NCR3-Halo** displayed labeling reaction rates $(k \sim 10^{6} M^{-1} s^{-1})$ comparable with positively charged labels such as JF_{669} and JF_{549} $(k \sim 10^{7} M^{-1} s^{-1})$ and two orders of magnitude faster than the neg-

atively charged label Alexa488 $(k \sim 10^4 M^{-1} s^{-1})$.[78]

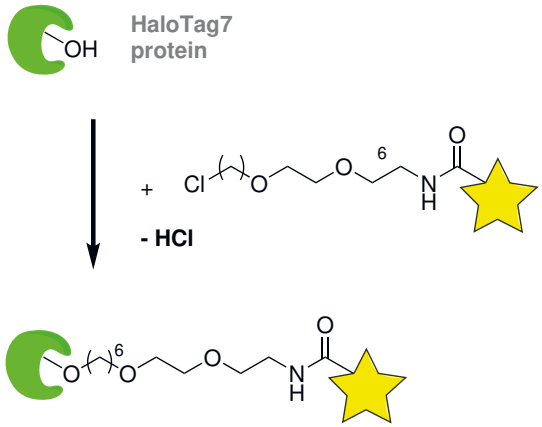

conjugate	$\mathbf{k_{app}}$ $[\mathbf{M^{-1}s^{-1}}]$ (value ± SD)
NCR1-Halo	$(4.07 \pm 0.02) \cdot 10^6$
NCR2-Halo	$(3.92 \pm 0.03) \cdot 10^6$
NCR3-Halo	$(2.85 \pm 0.05) \cdot 10^6$
FL-Halo	$(1.01 \pm 0.01) \cdot 10^6$
TMR-Halo	$(2.86 \pm 0.01) \cdot 10^7$

Figure 4.6 – Labeling reaction rates of HaloTag ligand conjugates to HaloTag7 protein determined by measuring FP changes over time (Appendix Figure 9.9, p. 171). Optical settings are provided in the Appendix (Table 9.3, p. 154). Reproduced from Ref.[1] with permission from the Royal Society of Chemistry.

4.4 Biocompability of *N*-cyanorhodamines and their application in live-cell STED imaging.

Imaging experiments have been conducted by Dr. Jessica Matthias.

4.4.1 Off-targeting of rhodamine fluorophores

Positively charged rhodamine dyes are known to accumulate in cell compartments, most typically mitochondria,[26] and remain fluorescent in the acidic environments of lysosomes and endosomes (see 4.1, p. 39). Indeed, use of **TMR** or **TMR-Halo** resulted in diffuse fluorescence of membrane structures in U-2 OS cells (Figure 4.7). The colocalisation experiment with **TMR-Halo** and ER-Tracker confirmed that **TMR-Halo** has an off-targeting affinity to the ER of the cells (average Pearson's correlation coefficient $0.62 \pm 0.05, N = 9$).

These undesired off-targeting labeling artifacts could be overcome with the negatively charged *N*-cyanorhodamine labels. With both **14a** and **NCR1-Halo**, no intercellular labeling was observed in the treated U-2 OS cells (Figure 4.7)

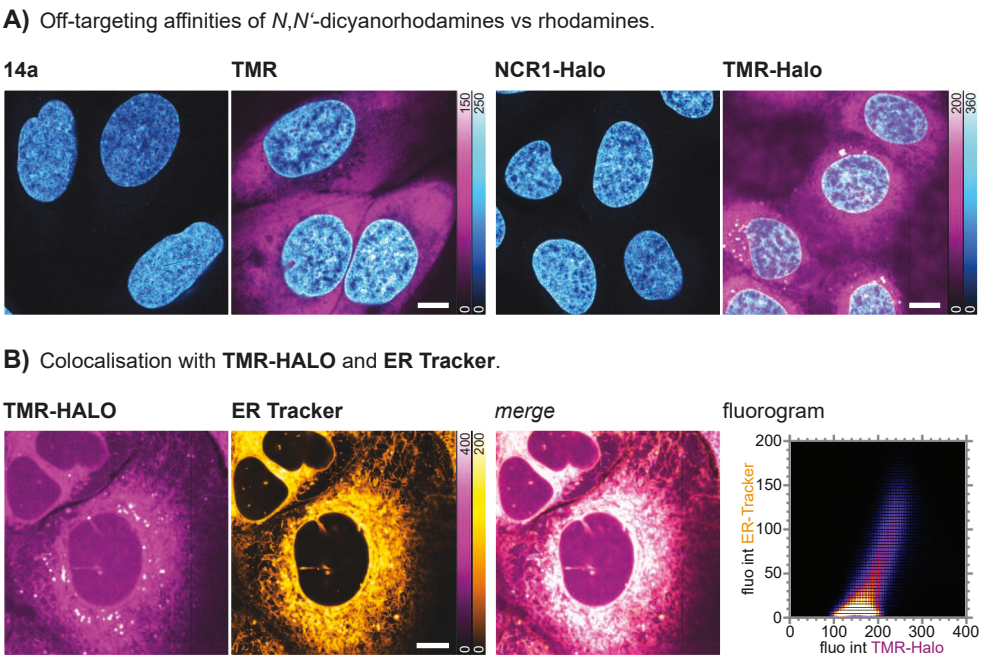

Figure 4.7 – Off-target affinities of *N*,*N'*-dicyanorhodamine and rhodamine dyes. (A) Living U-2 OS cells were stained with indicated dye (5 mM, over 18 h) and counter-stained with Hoechst 33342 (8 mM, for 10 min). (B) Colocalization in living U-2 OS cells. Left to right: cells stained with **TMR-Halo** (5 mM) and ER-Tracker Blue-White DPX (1 mM); overlay image; fluorogram of colocalization. Scale bars: 10 µm. The experiment was conducted by Dr. Jessica Matthias. Reproduced from Ref.[1] with permission from the Royal Society of Chemistry.

4.4.2 Toxicity studies

To be used for live cell imaging, a prerequisite is that the probes are not cytotoxic for the biological sample. For example, the accumulation of positively charged rhodamine dyes to mitochondria can result in cytotoxic effect, as in case of Rhodamine 123[27] and Rhodamine 6G.[28] Hereby, the adenosine triphosphate production of the cells is disturbed by the accumulation.

The cytotoxicity of *N*-cyanorhodamine dyes **13a** and **14a** was compared to **TMR** and the loading solvent DMSO (Figure 4.8A). The CellTiter-Blue cell viability assay relies on the metabolic activity of cells. Viable cells reduce the non-fluorescent sensor-probe resazurin to the fluorescent resorfurin. Therefore, the number of viable cells in a sample is proportional to the fluorescent signal (Figure 4.8D).[149]

The CellTiter-Blue cell viability assay did not show any toxicity in case of **13a**, **14a**, and **TMR**, compared to DMSO in the concentration range of 1–33 µM over 24 h, which are exceeding the loading concentrations and labeling times used for live cell labeling of HaloTag substrates. Cytotoxic effects were only observed by applying loadings of 100 µM dye or DMSO. A second CellTiter-Blue cell viability assay was conducted with

several *N*-cyanorhodamine dyes (5 µM over 24 h), compared to a series of reference dyes and the non-ionic surfactant Triton X-100 (TX100) as a positive control for cytotoxicity (Figure 9.10, p. 172). Herein, the cells displayed similar viability if exposed to a dye or not (no additive, negative control). Only with the HaloTag-ligand conjugate JF_{549}-Halo diminished cell viability was observed.

The CellTiter-Blue cell viability assay gives insights in the metabolic stress of cells, but not in the ability of the cells to proliferate. Cell proliferation of living U-2 OS cells was checked via holographic imaging cytometry for 48 h after treatment with various dyes (5 µM). Since cells have an higher refractive index compared to the cell medium, the phase of the sample beam of the microscope is delayed and a hologram is generated from the interference of the altered and the reference beam (Figure 4.8D). The length of cell division cycles and cell proliferations were comparable in control sample and treated cells. It was found that *N*-cyanorhodamines do not affect the cell proliferations within this time period. On the contrary, rhodamine JF_{549}-Halo displaying cytotoxic effects as in the CellTiter-Blue cell viability assay (Figure 4.8C, Figure 9.11C, p. 173).

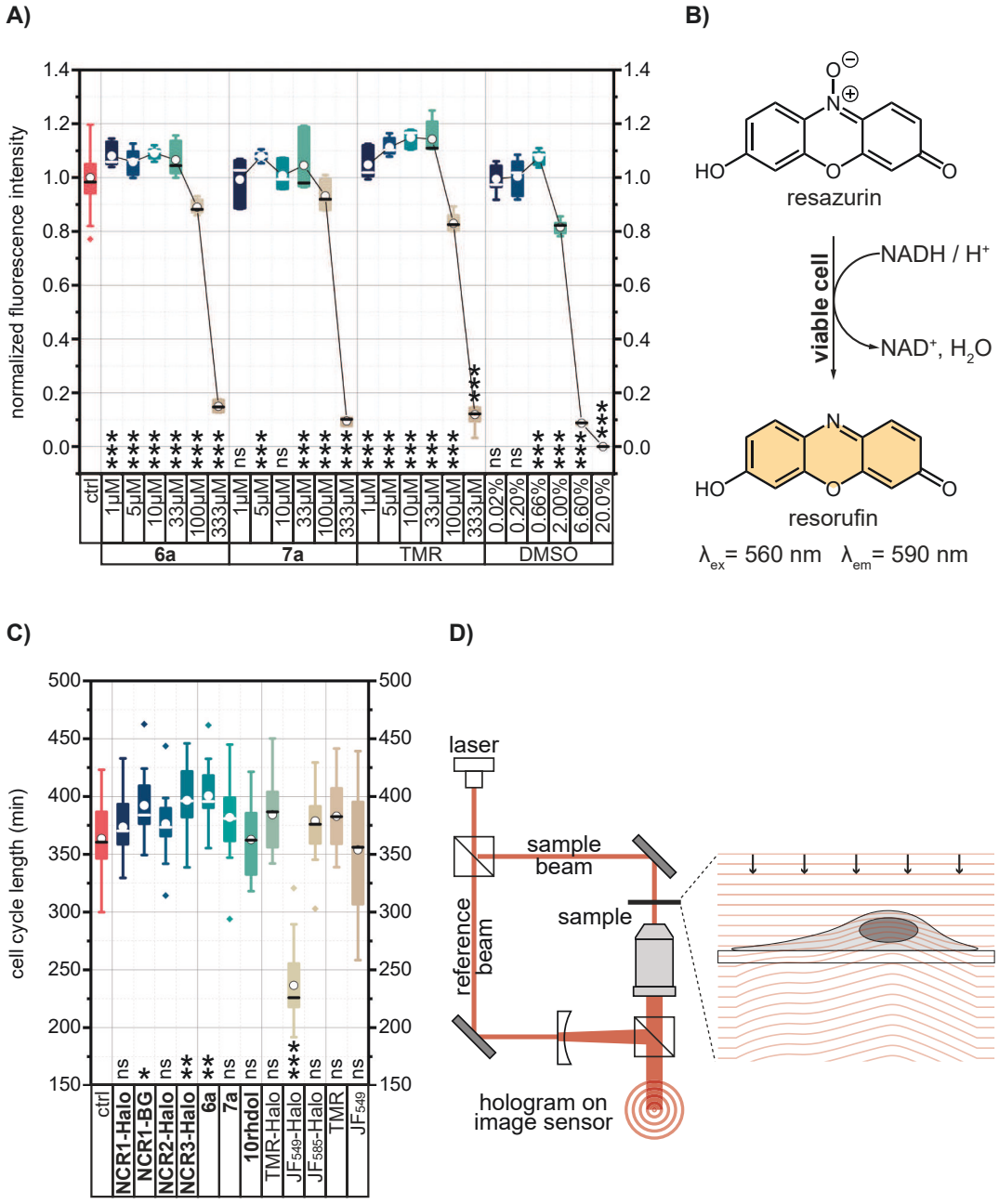

Figure 4.8 – Toxicity studies of dyes via CellTiter-Blue cell viability assay and cell proliferation as followed by holographic imaging cytometry. (A) CellTiter-Blue cell viability assay of U-2 OS cells exposed to various dyes at different concentrations over 24 h. (B) Principle of the CellTiter-Blue cell viability assay. (C) Cell cycle length obtained via time-lapse imaging cytometry of U-2 OS cells exposed to dyes (5 µM) over 48 h. (D) Principle and schematic depiction of the time-lapse imaging cytometry and digital holographic microscope. Statistical significance: ns: no significant difference to control, $*p < 0.05, **p < 0.005, ***p < 0.0005$ The experiment was conducted by Dr. Jessica Matthias. Statistic information are provided in the appendix (Table 9.4, p. 155; Table 9.5, p. 157) Reproduced from Ref.[1] with permission from the Royal Society of Chemistry.

4.4.3 Live-cell STED imaging

N-cyanorhodamines have demonstrated lower fluorogenicity compared to **TMR** in combination with fast labeling kinetics to HaloTag7 protein. Furthermore, off-targeting affinity to mitochondria or the lipophilic ER was not observed with **14a** and **NCR1-Halo** in initial cellular imaging. Also, insignificant cytotoxicity was found with various *N*-cyanorhodamine dyes. Next, the application in multi-color live-cell STED of **NCR1-Halo**, **NCR2-Halo** and **NCR3-Halo** was investigated.

To this aim, U-2 OS in which the nuclear pore complex protein Nup96 is endogenously expressed in fusion with HaloTag was labelled with **NCR1-Halo**, showing efficient labeling of the protein tag in living cell. Additionally, the sample was labelled with abberior LIVE 510 tubulin to label microtubules, with SiR-Hoechst to label the nuclear DNA, and with ER-Tracker Blue-White DPX to label the ER (Figure 4.9A). This combination of labels enables four-colour (2x confocal, 2x STED) imaging of the living U-2 OS-NUP96-Halo cells. 775 nm STED nanoscopy significantly improved resolution of the Nup96 structure labelled with **NCR1-Halo** with low background and, simultaneously, resolved the nuclear chromatin labeled with SiR-Hoechst with subdiffractive precision (Figure 4.9B).

The labels **NCR2-Halo** and **NCR1-SNAP** were applied in multi-colour STED imaging, too. **NCR2-Halo** was successfully applied in visualizing fused HaloTag-vimentin protein in U-2 OS cells expressing a genome-edited Vimentin-HaloTag fusion protein in combination with well-established labels abberior LIVE 550 tubulin and Hoechst 33342 (Appendix Figure 9.12, p. 174).

U-2 OS cells with overexpressed SNAPTag fusion with the promyelocytic leukemia protein (PML) were labelled with **NCR1-SNAP** alongside with Mito-Tracker Green FM, GeR-tubulin, and Hoechst 33342 to co-stain tubulin, mitochondria and nulcear DNA, respectively (Appendix Figure 9.13, p. 175). In both cases, subdiffraction resolution of the structure labeling with the *N,N'*-dicyanorhodamine was accomplished, while a second, commercial label visualized a different structure with subdiffraction resolution.

STED imaging of the vimentin network in U- 2 OS Vim-Halo cells labelled with NCR3-Halo (5 µM)

NCR3-Halo has been shown to be fluorogenic among the series of *N,N'*-dicyanorhodamine probes conjugated to HaloTag ligands (4.3), and its carboxyl analog **NCR3** was found to have a $pK_{a,FL}$ around 8, which is higher than the physiological pH of cells. **NCR3-Halo** probe was successfully applied in confocal imaging of fused HaloTag-

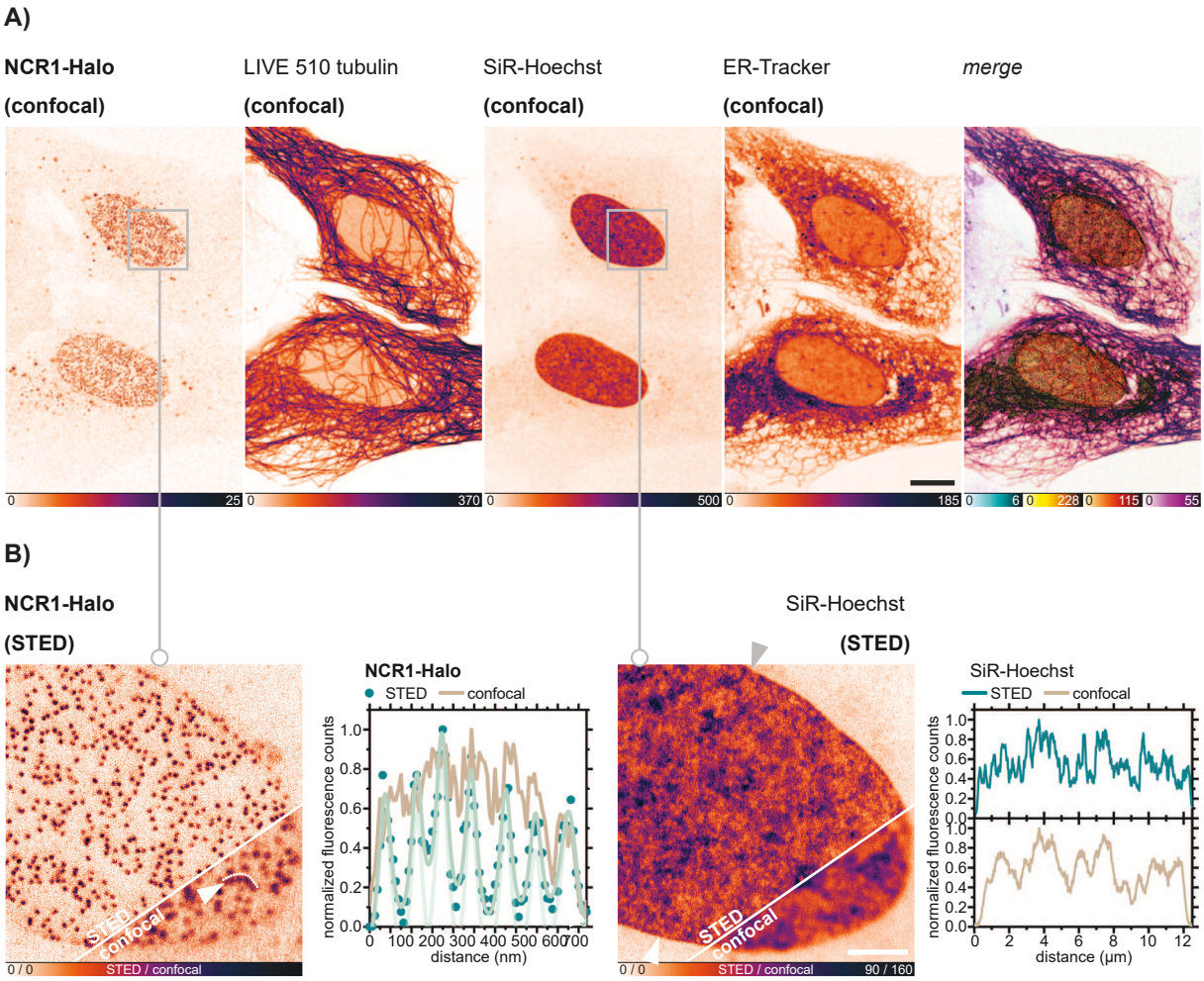

Figure 4.9 – Four-color live-cell super-resolution imaging with *N,N'*-dicyanorhodamine probe **NCR1-Halo**. (A) Confocal imaging of living U-2 OS-NUP96-Halo cells[131] labelled over 6 h with **NCR1-Halo** (5 µM, for Nup96), abberior LIVE 510 tubulin (0.25 µM, for β-tubulin), 6-SiR-Hoechst44[150] (0.2 µM, for DNA), and ER-Tracker Blue-White DPX (0.25 µM, for ER). Scale bar: 10 µm. (B) STED imaging (750 nm depletion laser) with **NCR1-Halo** and 6-SiR-Hoechst44 and intensity profiles along the marked regions (arrows). Scale bar: 1 µm. Imaging parameters are provided in the appendix (Table 9.7, p. 163). The experiment was conducted by Dr. Jessica Matthias. Reproduced from Ref.[1] with permission from the Royal Society of Chemistry.

vimentin protein in U-2 OS cells.(Appendix Figure 9.14, p. 175). However, no continuous signal was obtained under STED conditions, which can be attributed to the pH-dependant open-close equilibrium between the fluorescent form of **NCR3-Halo** and its non-fluorescent spirolactone form. This "blinking" behavior makes the label unsuitable for super-resolution STED conditions due to fluctuating fluorescent signal. However, this probe might be useful in other, stochastic super-resolution microscopy techniques. Uno *et al*. have developed a series of pH-dependant, blinking dyes, which were successfully applied in SMLM.[101]

In summary, *N*,*N'*-dicyanorhodamines conjugated to the HaloTag or SNAPTag ligand were successfully applied in live-cell STED imaging. Subdiffraction resolution of the labeled structures was demonstrated with 750 nm STED nanoscopy. The combination with other, commercially available labels enables multi-color imaging of living cells. Despite relatively high concentrations (1–5 µM) and long incubation times (overnight) have been used, *N*,*N'*-dicyanorhodamine conjugates display no visible off-targeting artifacts and very little fluorescence background. Furthermore, no off-targeting affinity was seen with *N*,*N'*-dicyanorhodamines as compared to **TMR** and **TMR-Halo**. These properties together with the reduced cytotoxicity and high photostability make these dyes ideal for multi-color live-cell super-resolution imaging.

4.5 Extending the scope to coumarins

Coumarin dyes are known for their absorption in the UV range as well as their low photostability.[24,104] In fluoresceins and rhodols, the replacement of the hydroxy group with cyanamide resulted in a bathochromic shift and improved photostability (4.3). It was hypothesized that this strategy might also improve the properties of coumarin dyes, which was investigated in this section.

In an initial attempt, the cyanamide analog of 7-amino-4-methylcoumarin-3-acetic acid (AMCA) was accessed by the base-mediated decomposition of tetrazoles (Scheme 4.10). AMCA (**30**) was reacted with sodium azide and triethyl orthoformate to tetrazole **31** n 29 % yield. Then, tetrazole **31** was converted to cyanamide **29** in 70 % yield.

Photophysical properties of cyanamide **29** was compared to coumarins **28** and **30** (Figure 4.10). The replacement of the hydroxy group with cyanamide resulted in bathochromic shifts in both absorption and emission $\sim$ 30 nm. The photostability was evaluated in a similar manner to *N*-cyanorhodamines (4.3), but fast photobleaching was found with compounds in the initial experiment. Cyanamide **29** demonstrated a

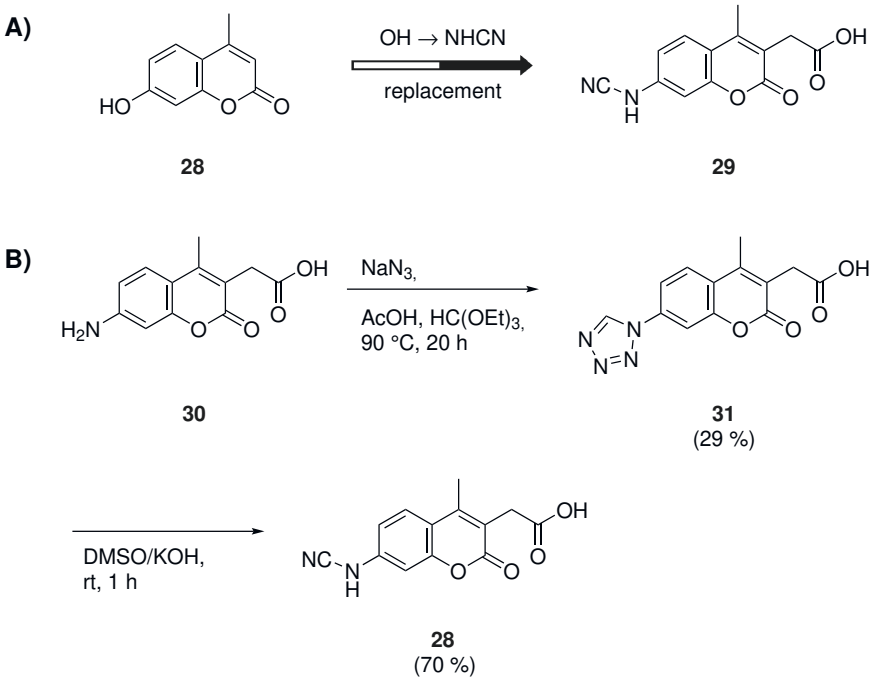

Scheme 4.10 – (A) Design strategy and (B) synthesis of *N*-cyanocoumarin **29**.

relatively higher photostability compared to hydroxy coumarin **28**, but was still less photostable than AMCA **30** (full photophysical characterisation is provided in the Appendix, Table 9.6, p. 159)

Since the *N*-cyanamido derivative provided no advantages over the hydroxy- or amino-substituted coumarin dyes, its potential use for fluorescent labeling was not further investigated.

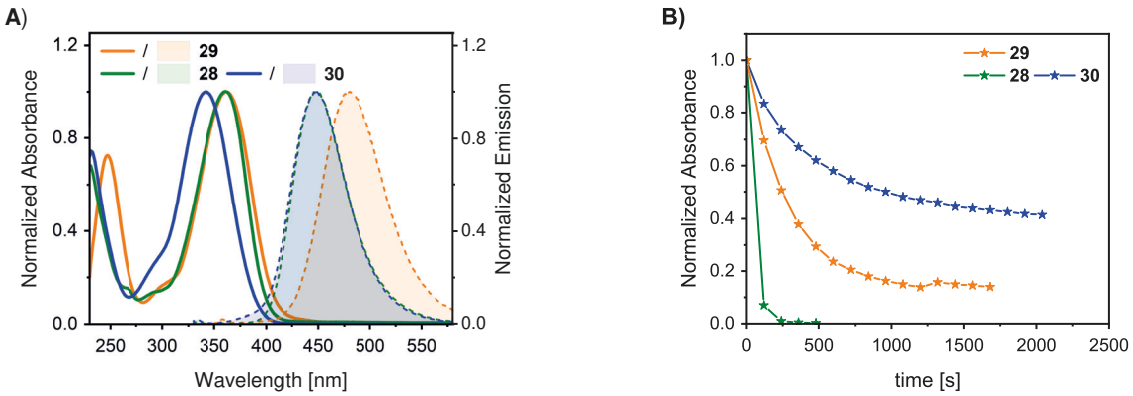

Figure 4.10 – Photophysical properties of coumarin dyes. (A) Absorption and emission spectra of of dyes in phosphate buffer (0.1 M, pH 10). (B) Initial photostability experiment with coumarin dyes. Equimolar dye solutions in borate buffer (0.1 M, pH 11) were irradiated with a 365 nm LED. (Experiment was conducted by Dr. Mariano Bossi)

Chapter 5

Photoactivatable fluorophores for PALM and MINFLUX imaging

5.1 Introduction

SMLM achieves subdiffractive resolution by temporarily discrimination of single fluorophores, which do not emit simultaneously. Control over the ON- and OFF-state of the fluorescent molecules is essential, so that only a small fraction of molecules is fluorescent at one time.[6]

Photoactivatable or "caged" fluorophores containing photocleavable protecting (so-called "caging") groups enable this ON-OFF switch. However, photoactivatable fluorophores often rely on bulky and lipophilic nitrobenzene-type cages.[30,106] To improve their solubility for immunostainig, anionic sulfonate groups have been installed onto the photolabile caging groups affording water-soluble but cell membrane-impermeant probes.[112] Another downside of nitrobenzene caged probes is the stoichiometric formation of potentially toxic aldehydes as by-products.[113–115]

Accordingly, less bulky, water-soluble, and cell membrane-permeable probes are desired for live-cell imaging, which are photoactivatable without formation of toxic by-products. Figure 5.1 summarises different design principles sorted by the size of the photocage.

Tetrazines are known as efficient fluorescence quenchers which is attributed to a ETDS mechanism.[71] On the other hand, s-tetrazine is a well-established photocleavable group in peptide chemistry due to its photofragmentation to nitriles and inert N_2.[151,152] Photoactivatable, tetrazine-caged coumarin, BODIPY and Si-rhodamine analogs re-

ported by Loredo *et al*. combine the quenching and photoactivation effect (Figure 5.1A).[153] These probes were successfully employed for confocal and PALM imaging. Upon irradiation with short UV light (254 nm), the quenching tetrazine group undergoes photofragmentation to a non-quenching nitrile group with MeCN and inert N_2 as by-products. Based on cytotoxicity studies with zebrafish embryos and larvae tolerating 0.5–1Vol% MeCN, the stoichiometric release of MeCN upon irradiation of micromolar concentrated probes can be considered not-lethal for living cell.[154] Similarly, we supposed that an amino tetrazine might undergoes photofragmentation to cyanamide and other non-toxic by-products. For the previously described, negatively charged *N*-cyanorhodamine dyes, the corresponding *N*-(tetrazinyl)rhodamines analogs may function as photoactivatable probes expanding the potential application of *N*-cyanorhodamine probes to SMLM methods.

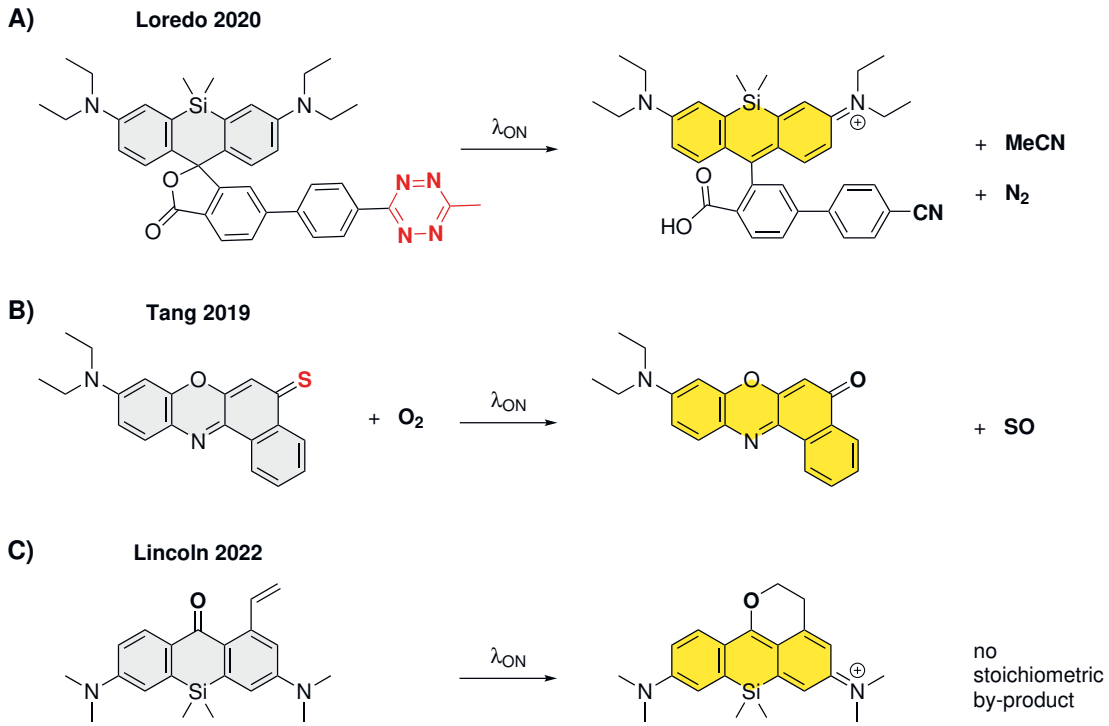

Figure 5.1 – Photoreactions and by-products of caged fluorophores sorted by size of the photolabile group (red). (A) Tetrazine-caged Si-rhodamines.[153] (B) Thiocarbonyl-caged NileRed.[155] (C) "Caging-group free" PaX dyes.[39]

Another example based on a single-atom substitution are the series of thiocarbonyl-caged fluorophores reported by Tang *et al*. (Figure 5.1B).[155] Photoactivation of these compounds yields the corresponding fluorescent oxo derivatives, which is attributed to the photooxidation of thioketones by oxygen to ketones and sulfur monoxide.[156] Tang *et al*. applied this strategy to a variety of fluorescent molecules such as coumarins, BODIPYs, and oxazines, but not on triarylmethane dyes like fluoresceins and rhodols. Furthermore, the combination of the color-tuning strategy of fluoreceins with this photocage strategy might enable multi-color SMLM with thiocarbonyl-caged probes.

Recently, Lincoln *et al*. reported PaX dyes as "caging-group free", photoactivatable fluorophores (Figure 5.1C).[39] Herein, the fluorophore does not bear a quencher, which is released to the environment, but the non-fluorescent molecule tracelessly forms a fluorescent photoproduct upon light-induced cyclisation. The PaX dyes are designed around 3,6-diaminoxanthone core structures and can be considers as photoactivatable rhodamine analogs without an aromatic pendant ring. It was similarly hypothesized that the xanthones bearing 3,6-hydroxy substituents would behave as the fluorescein analogs of PaX dyes. Even through fluorescein as compared to TMR is hypsochromically shifted[33] and is less-photostable,[24] it allows installation of various enzymatically cleavable *O*-protecting groups for the development of sensor probes.[36,86] Substitution of the dimethyl amino group in PaX dyes may transfer these properties and increase the color-palette of available PaX fluorophores by inducing a hypsochromic shift and may facilitate photobleaching in SMLM techniques after localisation. Furthermore, enzymatically cleavable PaX sensor probes may allow dynamic fluorescence measurement based on enzymatic activity.

5.2 *N*-(Tetrazinyl)rhodamines as photoactivatable *N*-cyanorhodamine analogs

Light-induced decomposition of 3-amino-tetrazines to cyanamide and non-toxic by-products MeCN and N_2 presents an attractive strategy to cage negatively charged *N*-cyanorhodamines for live-cell SMLM. To test this hypothesis, *N*-(tetrazinyl)rhodamines bearing one (**32a**) or two (**32b**) *N*-tetrazino substitutents have been prepared, which are expected to form previously described *N*-cyanorhodamines **13a** and **14a** upon irradiation (Scheme 5.1).

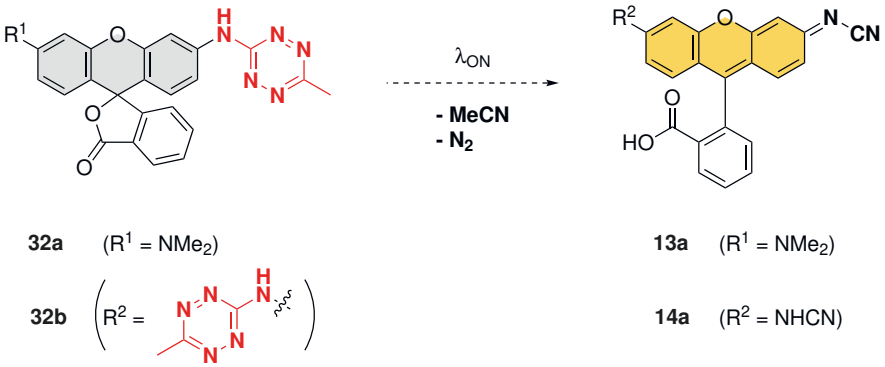

Scheme 5.1 – Proposed photoactivation of *N*-(tetrazinyl)rhodamines **32** to *N*-cyanorhodamines **13a** and **14a**.

Based on a literature report,[157] aryl iodides **10a** and **16a** were reacted with 6-methyl-s-

tetrazine-3-amine (**33**) by a Buchwald-Hartwig amination using $Pd_2(dba)_3$/Xantphos as catalytic system (Scheme 5.2). The target *N*-(tetrazinyl)rhodamine **32a** was obtained in 66 % yield. *N,N'*-(tetrazinyl)rhodamine **32b** was obtained in lower yield (10 %), which was attributed to the low solubility in aqueous medium and loss of material during preparative HPLC.

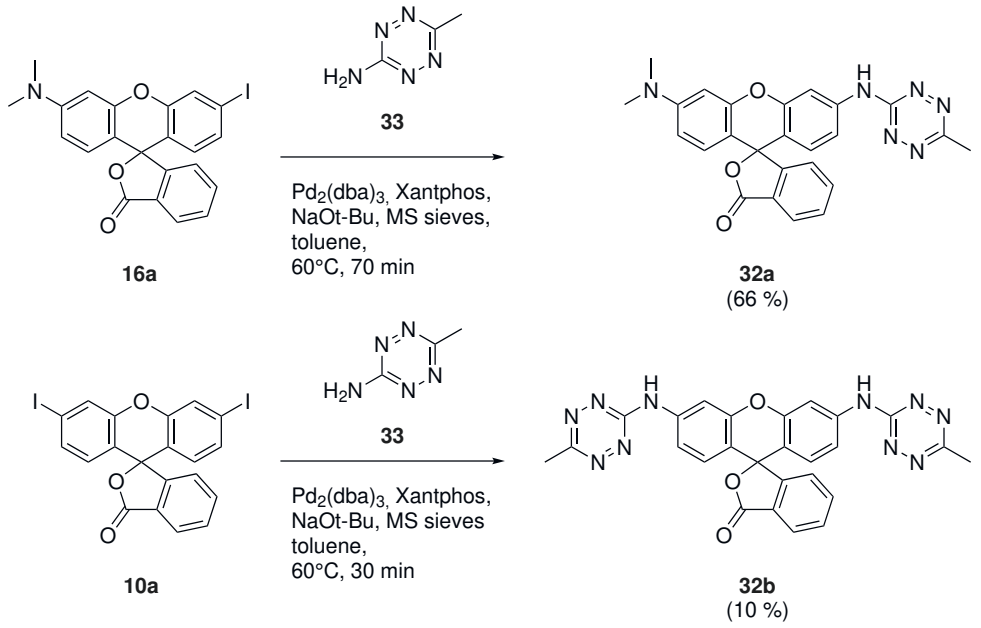

Scheme 5.2 – Preparation of *N*-(tetrazinyl)rhodamines **32**.

Next, the hypothetical photoactivation of *N*-(tetrazinyl)rhodamines to *N*-cyanorhodamines (Scheme 5.1) was evaluated. A solution of **32a** (5 µM) in phosphate buffer (0.1 M, pH 7) was irradiated at 505 nm. Hereby, no photoconversion of the amino tetrazine to cyanamide was found (Appendix Figure 9.16, p. 176). Furthermore, **32a** showed partial decomposition upon irradiation over $\sim$ 5 h, as decomposition products were displayed by LCMS analysis after irradiation.

Photoactivation kinetics have been previously found to be dependant on the environment. For example, PaX dyes show higher photoactivation rates in basic media.[39] Under basic conditions, *N*-(tetrazinyl)rhodamines might exist in their deprotonated form. As fluoresceins, these deprotonated forms might have altered photophysical properties due to changes of the delocalized π-system and grant access the excited states from which the molecule undergo a photoconversion. To test the chemical stability of , a solution (5 µM **32a**) in borate buffer (0.1 M, pH 11) was measured over time, without irradiation. Hereby an increase in fluorescence was found (Appendix Figure 9.15c, p. 176), and confirmed by LCMS analysis. This thermal conversion was attributed to the formation of rhodamine **34a** (Scheme 5.3) by LCMS analysis (Appendix Figure 9.15e, p. 176). These initial results with compound **32a** mark *N*-(tetrazinyl)rhodamines as unsuitable photoactivatable probes for *N*-cyanorhodamines. At pH 7, representing

physiological conditions, no photoactivation was found, while under basic conditions *N*-(tetrazinyl)rhodamine **32a** is chemically unstable.

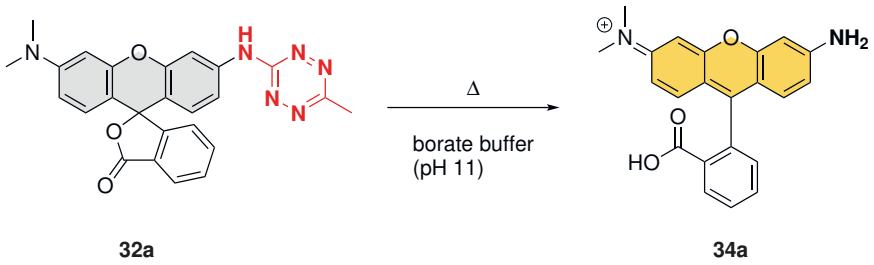

32a **34a**

Scheme 5.3 – Thermal decomposition of *N*-(tetrazinyl)rhodamine **32a** in basic aqueous medium (0.1 M borate buffer, pH 11).

5.3 Single-atom substitution in triarylmethanes to mercaptofluorans

Compound **35** (Figure 5.2)is a fluorescein analog prepared by Gattermann, who named the compound "Thiofluorescein" (german).[158] Later, Wroński preferred the term "dithiofluorescein".[159] The term "thiofluorescein" was further used to describe compound **36**, in which the not the phenolic groups but the bridging oxygen atom is replaced with sulfur.[160,161] Since the the term "thiofluorescein" has been used interchangeably and may lead to confusion, the compounds studied in this work are named based on the substitution of the parent fluoran core. Accordingly, compound **35** is 3',6'-dimercaptofluoran and compound **37** are 3'-(dimethylamino)-6'-mercaptofluoran (Scheme 5.4).

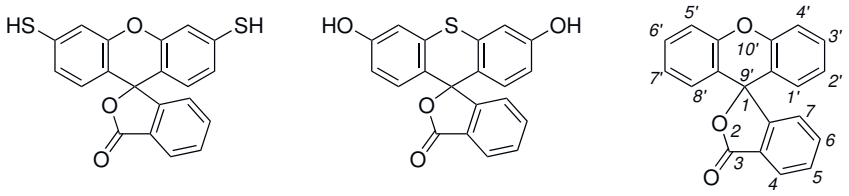

35 **36**

"thiofluorescein" Ref.[158]
"dithiofluorescein" Ref.[159]
"mercactofluorane" **This work**

"thiofluorescein" Ref.[160],[161]

Fluoran Ref.[91]

Figure 5.2 – Naming of **35** in literature and in this work.

Upon irradiation with UV or visible light, mercaptofluorans may photoactivate to the corresponding fluoresceins and rhodols (Scheme 5.4), based on the earlier literature precedent.[155] To evaluate the photoactivation and potential applications in live-cell SMLM techniques, synthetic methodologies to access mercaptofluorans **35** and **37**

were investigated. Ideally, the same synthetic methodologies should yield the corresponding (acetylthio)fluorans **39** and **40** as *S*-protected mercaptofluorans to test the intact cell membrane permeability or measurement of enzymatic activities in living cells.

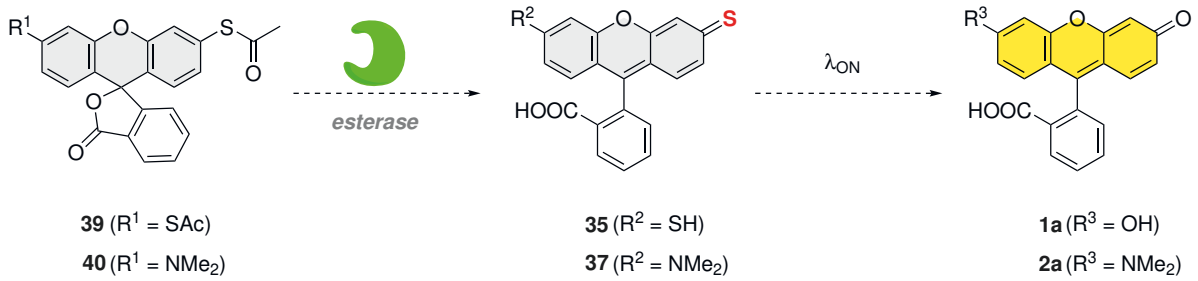

39 (R^1 = SAc)
40 (R^1 = NMe_2)

35 (R^2 = SH)
37 (R^2 = NMe_2)

1a (R^3 = OH)
2a (R^3 = NMe_2)

Scheme 5.4 – Enzymatic cleavage of (acetylthio)fluorans **39** and **40** and photoactivation of mercaptofluorans **35** and **37** to fluroescein **1a** and rhodol **2a**.

5.3.1 3',6'-Dimercaptofluoran 35

Based on a literature report,[162] fluorescein triflate **8a** was reacted with KSAc in a palladium-catalyzed cross-coupling reaction with $Pd_2(dba)_3$/Xantphos as catalytic system (Scheme 5.5). The (acetylthio)fluoran **39** was isolated in 58 % yield and further converted to mercaptofluoran **35** by the basic cleavage of the acetyl protecting groups. 3',6'-Dimercaptofluoran **35** was then isolated by extraction in 67 % yield and used without further purification.

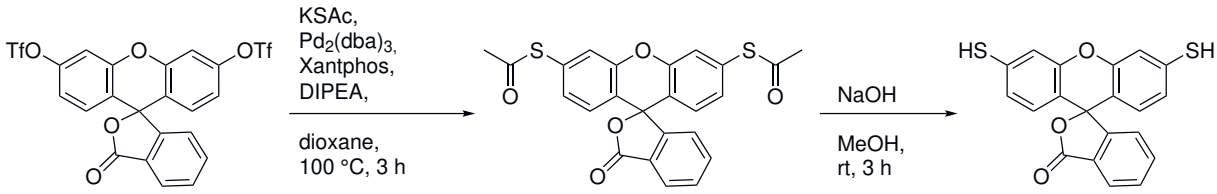

8a

39
(58 %)

35
(67 %)

Scheme 5.5 – Preparation of mercaptofluoran **35**.

The photoactivation of thiocarbonyl-caged dyes is attributed to the photooxidation of thioketones to ketones.[156] Accordingly, stepwise photoactivation of dimercaptofluoran **35** bearing two sulfur atoms was expected as shown in Scheme 5.6. Photooxidation of the first thiocarbonyl group to the ketone would form weakly or non-fluorescent intermediate **41**, in which the second thiocarbonyl group would undergo photooxidation yielding fluorescent fluorescein (**1a**).

On a semipreparative scale, a solution of **35** ($\sim$ 1 mg) in aqueous MeCN (1.2 mL) was irradiated in a Penn Photoreactor m1 at 365 nm and monitored by LCMS to check if

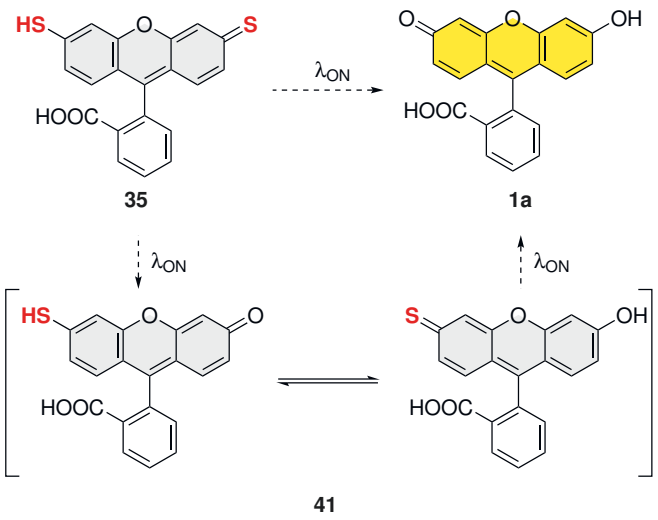

Scheme 5.6 – Pausible mechanism of photoactivation of mercaptofluoran **35**.

the photoactivation occures to the proposed mechanism. Hereby, the degradation of **35** was found using an internal standard, without the buildup of the intermediate **41** or fluorescein **1a** as photoproducts (Appendix Figure 9.17, 178). This raises the question, whether **35** undergoes rapid photobleaching or intermediate **41** or fluorescein **1a** undergo photobleaching at the rates faster than their formation. Fluorescein is known for its low photostability compared to other fluorescent dyes as **TMR**.[24] To evaluate the photobleaching of fluorescein under these conditions, a solution of fluorescein was irradiated. Hereby, under identical conditions and within the timeframe of the experiment, the photobleaching of fluorescein was incomplete (Appendix Figure 9.18, 179). Accordingly, the direct photobleaching of mercaptofluoran **35** as the major reaction pathway might be a more feasible explanation than the rapid photobleaching of its photoproduct(s).

5.3.2 3'-(Dimethylamino)-6'-mercaptofluoran 37

To prepare compound **37** and its thioacetate **40**, rhodol triflate **15a** was reacted with KSAc or HSAc. However, this initial attempt resulted only in hydrolysis of the triflate (Scheme 5.7).

Based on a literature report,[163] triisopropylsilanethiol (HS-TIPS) was used as an alternative surrogate (Scheme 5.8A). LCMS analysis of the reaction mixture did not show the formation of TIPS-protected mercaptofluoran **42**, but the free compound **37**. This finding is in agreement with the acid-sensitivity of the labile S-Si bond reported by Kreis *et al*.[163] in TIPS-protected compounds. The isolation of either **42** or **37** by column chromatography was unsuccessful. Therefore, the mercaptofluoran was trapped

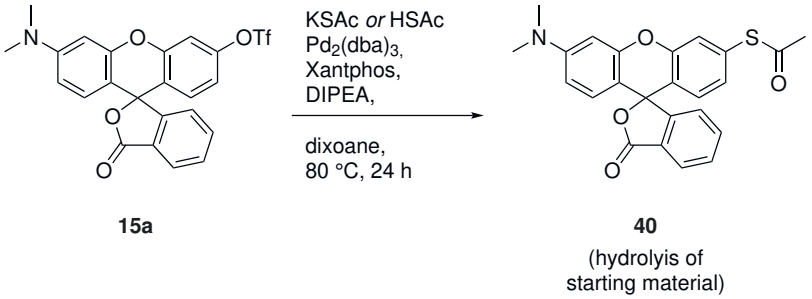

Scheme 5.7 – Unsuccessful preparation of thioacetate **40** in facile manner to thioacetate **39**.

as its more stable thioacetate by addition of acetic anhydride to the reaction mixture (Scheme 5.8B). The thioacetate **40** was successfully isolated by column chromatography in 66 % yield.

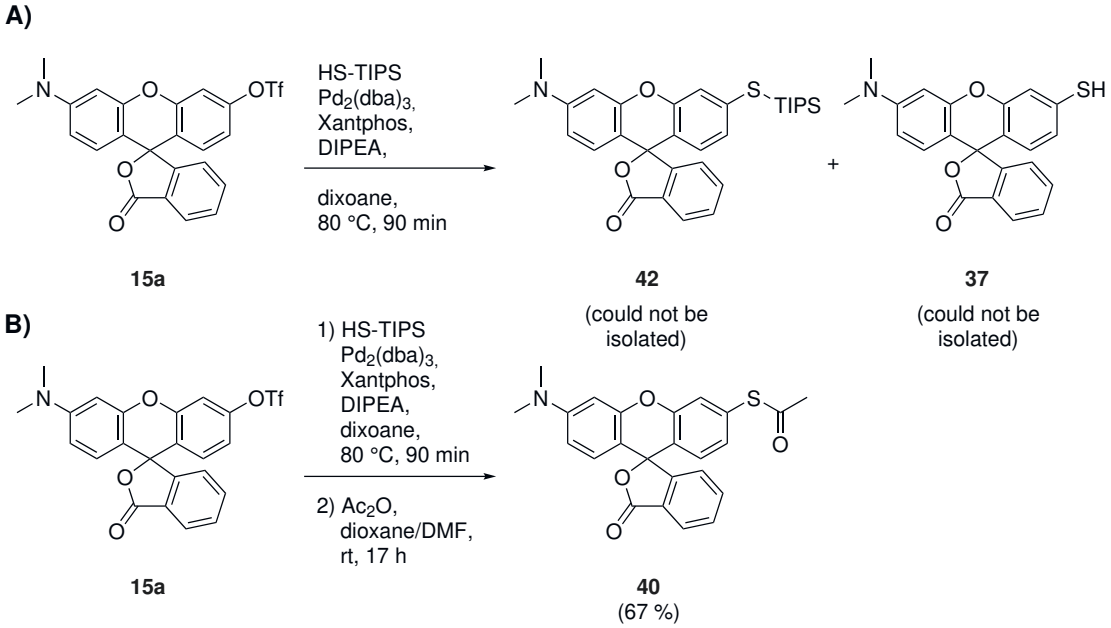

Scheme 5.8 – HS-TIPS as surrogate in the preparation of thioacetate **40**.

Contrarily to mercaptofluoran **35**, the photoactivation of **37** to the corresponding rhodol **2a** should involve a single photooxidation step. This simplified mechanism was expected to prevent potential side-reactions of intermediates. The photolysis experiments were conducted with thioacetate **40**. After *in situ* cleavage of the acetate with NaOH, the formed mercaptofluoran **37** was expected to convert to fluorescent rhodol **2a** upon irradiation with light (Scheme 5.9).

Initially, a solution of thioacetate **40** in MeCN was irradiated with a 365 nm LED for 10 minutes. The compound was showed to be stable during this time period (Appendix Figure 9.19a-b, p. 180). Next, thioacetate was deprotected with aq. NaOH (1 M, 10 min) to form mercaptofluoran **37**. However, LCMS analysis of the hydrolysis mixture showed the formation of a crude mixture (Appendix Figure 9.19b, p. 180). The main

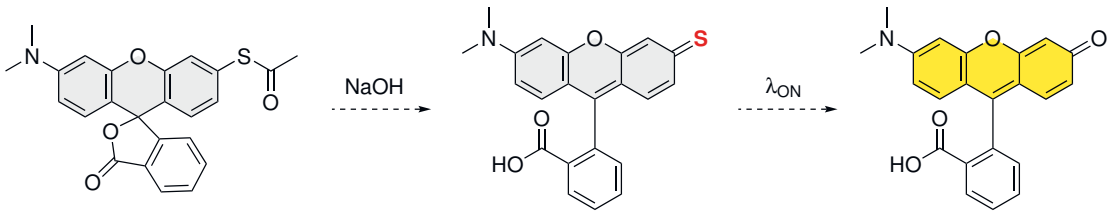

Scheme 5.9 – Basic cleavage of thioacetate **40** and photoactivation of mercaptofluran **37**. LCMS analysis data are provided in the Appendix, Figure 9.19, 180

product demonstrated a molecular ion of *m/z* $[408]^+$, which corresponds to the expected compound **37** plus dioxygen ([M+O_2+H]$^+$). To test the potential photoactivation of **37**, thioacetate **40** thioacetate was treated with aq. NaOH (1 M) followed by irradiation (365 nm, 15 min) (Appendix Figure 9.19c-e, p. 180). LCMS analysis displayed not the formation of **37** or rhodol **2a** as photoproducts. Observed molecular ions with *m/z* $[408]^+$, *m/z* $[424]^+$, and *m/z* $[375]^+$ correspond to the oxidized and dimerised products of **37** ([M+O_2+H]$^+$], [M+O_4+H]$^+$, [2M+2 H]$^{2+}$). These findings indicate that after basic cleavage of the thioacetate the free mercaptofluoran **37** is prone to undergo oxidation and dimerisation.

5.3.3 3-Thioxo-9-arylxanthene 38

The photoactivation of thiocarbonyl-caged dyes reported by Tang *et al*. is based on the photooxidation of the thioketone. Mercaptofluorans **35** and **37** may exist in the equilibrium between their open form bearing a potentially photoactivatable thioketone and in their closed, spirolactone form incorporating oxidation-sensitive thiols (Scheme 5.10). Thus, it was suspected that the spirolactonization may prevent the photoactivation of **35** and **37** and; in case of **37**, the presence of a free thiol group may have led to the oxidation and dimerisation detected by LCMS analysis.

Replacement of the ortho-carboxyl group in fluoresceins and rhodamines with methyl results in 9-arylxanthene derivatives which can only exist in their open forms. Accordingly, 3-thioxo-9-arylxanthene **38** presents a thiocarbonyl-caged dye which is "locked" in its potentially photoactivatable thioketone form.

Following a literature presence,[164] Tokyo Green analog **44** was treated with $PhNTf_2$ to give the corresponding triflate **45** in 75 % yield (Scheme 5.11). Next, the triflate was aminated under Buchwald-Hartwig conditions using RuPhos Pd G4/RuPhos as catalytic system. 6-Dimethylamino-9-(o-tolyl)xanthene **43**, a rhodol analog locked in its open form, was obtained in 88 % yield.

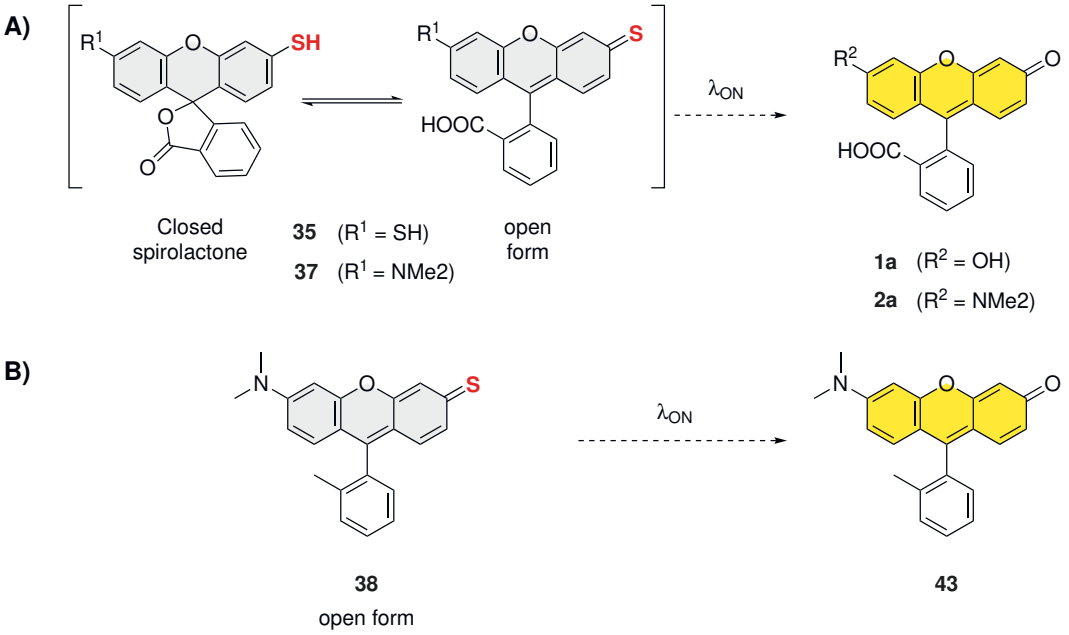

Scheme 5.10 – Proposed photoactivatation of (A) mercaptofluorans and (B) 3-thioxo-9-arylxanthene **38**. Photoactivation of mercaptofluorans **35** and **37** relys on the formation of their open forms.

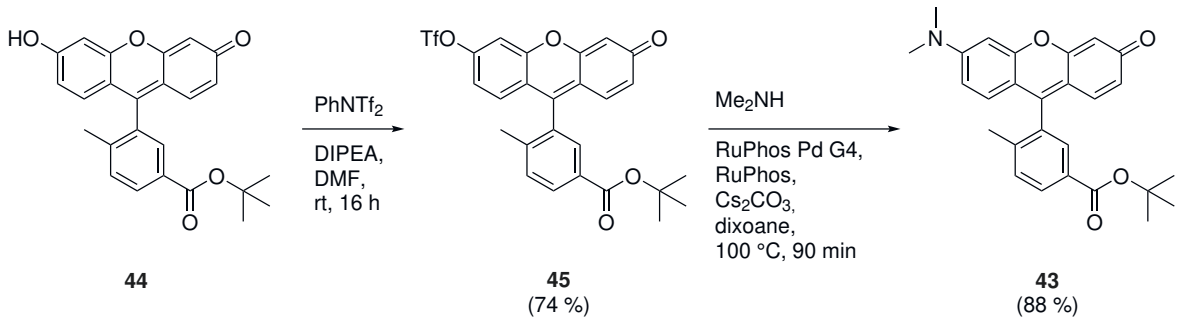

Scheme 5.11 – Preparation of rhodol analog **43**.

With the rhodol analog in hand, the conversion to the thiocarbonyl-caged 9-arylxanthene was attempted (Scheme 5.12). Based on the procedure of Tang *et al*.,[155] **43** was treated with the Lawesson reagent or alternatively $Py_2P_2S_5$.[122] Heating up to 80 °C in MeCN was required to convert the rhodol analog. TLC analysis (silica, 10 % EtOH/CH_2Cl_2) displayed formation of a blue-color spot with a molecular ion of *m/z* $[446]^+$ (by TLCMS) which corresponds to product **38**. Furthermore, the Lawesson reagent preformed better than $Py_2P_2S_5$ based on TLC analysis. However, isolation of the product **38** by column chromatography (silica, 0 % to 80 % EtoH/CH_2Cl_2) failed due to its instability and air-sensitivity in solution.

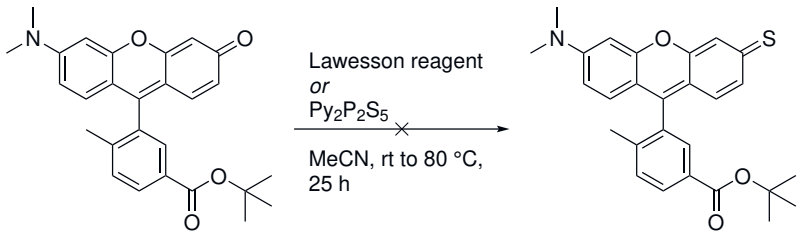

43 **38** (unstable)

Scheme 5.12 – Unsuccessful thionation of rhodol analog **43**.

5.3.4 Outlook

Different synthetic methods have been screened to obtain thiocarbonyl-caged triarylmethane dyes. The palladium-catalyzed cross-coupling of aryl triflates with either potassium thioacetate or triisopropylsilanethiol followed by addition of acetic anhydride yielded two (thioacetyl)fluorans, with basic cleavage yielding the corresponding mercaptofluorans. However, 3'-(dimethylamino)-6'-mercaptofluoran **37** was found to be unstable and underwent oxidation and dimerisation; 3-thioxo-9-arylxanthene **38**, prepared by another method, was also found to be unstable to air. Moreover, the photoactivation of 3',6'-dimercaptofluoran **35** did not yield the expected fluorescein photoproduct (**1a**), but resulted in partial photobleaching.

In summary, it was concluded that thiocarbonyl-caged triarylmethane dyes do not seem to be feasible photoactivatable fluorophores. Photoactivation of the stable derivative **35** to fluorescein (**1a**) was not observed, while other derivatives suffer from chemical instability.

5.4 PaX(–) dyes as negatively charged, hypsochromically shifted PaX analogs and sensor probes

Recently proposed "caging-group free" PaX dyes[39] can be considered as positively charged, photoactivatable rhodamines. Replacement of the 3,6-amino groups of the xanthone core by hydroxy groups results in the core with a proposed name negatively charged, photoactivatable xanthone (PaX(–)), which can be considered as photoactivatable fluorescein analog. Accordingly, PaX(–) dyes were thought to have hypsochromically shifted absorption and emission maxima similar to the hypsochromic shifts observed in fluoresceins to rhodamines,[33] which could extend the available color-range of PaX dyes. Furthermore, installation of enzymatically cleavable *O*-protecting groups may lead to the design of photoactivatable sensor probes like **PaX(–)2-OAc** to monitor enzymatic activities[88,89] (Scheme 5.13). To evaluate this hypothesis, two PaX(–) dyes and *O*-protected analogs have been prepared. Photoactivation experiments were conducted by Dr. Mariano Bossi.

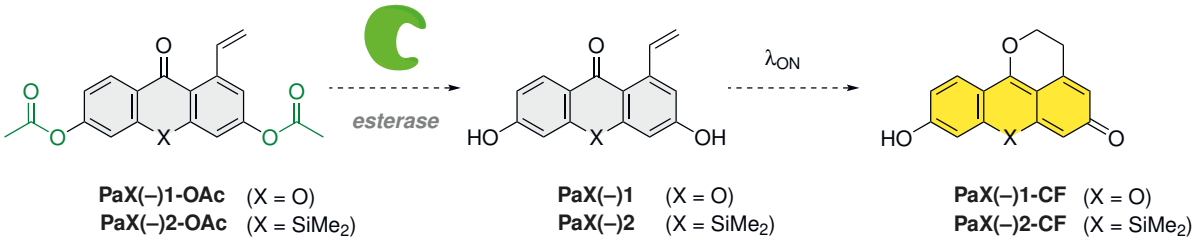

Scheme 5.13 – Proposed PaX(–) dyes to increase the color-range and to access enzymatic cleavable probes.

5.4.1 PaX(–)1

The synthetic pathway to access PaX dyes relies on a Ir-catalyzed selective monoborylation ortho to the keto group of the xanthone core followed by a Cu(II)-mediated halo-deborylation. An alkene as intramolecular radical trap is then installed under Suzuki-Miyaura coupling conditions.[39] In order to find an suitable protecting group for phenol groups in this sequence, several xanthones bearing different protecting groups have been prepared. The protected xanthones **46** were reacted with B_2pin_2 using an Ir-catalyst and the reactions were monitored by LCMS analysis (Table 5.1). With xanthones **46a** and **46b**, the major product demonstrated a molecular ion of *m/z* $[583]^+$ (Entry 1,2) or $[443]^+$ which corresponds to the mono-borylated xanthones **47a** and **47b**. However, the products could not be isolated in pure form by flash column chromatography (silica, 0 % to 100 % EtOAc/hexane) due to partial hydrolysis of the borates **47** to

the xanthones **46** on silica. Tosyl-protected xanthone **46c** (Entry 5,6) was found to be an unsuitable substrate under these conditions, since the formation of a side-product (molecular io with *m/z* $[583]^+$) was noticed, which is attributed to **48**.

Table 5.1 – Optimization table for the preparation of **47** by Ir-catalyzed mono-borylation.

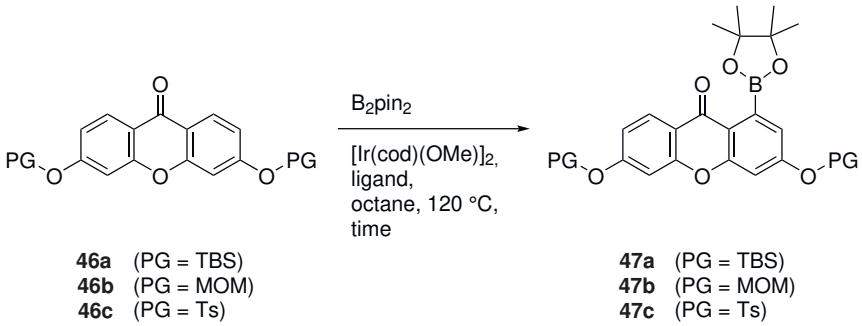

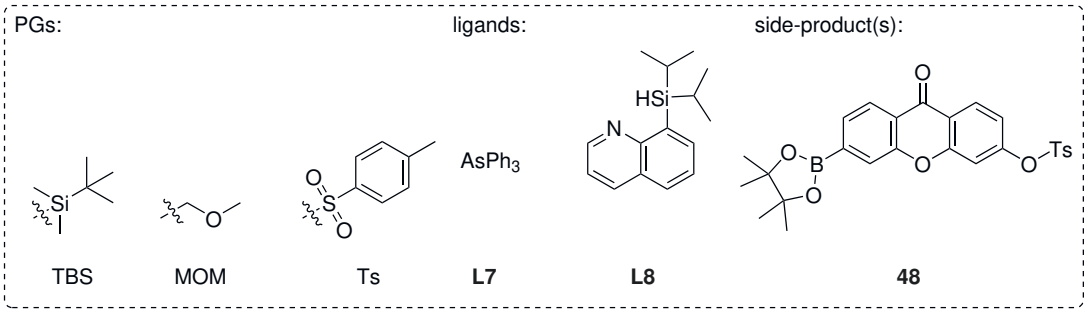

Entry	xanthone	[Ir]	ligand	time	result by LCMS analysis
1	**46a**	$[Ir(cod)(OMe)]_2$ (10 mol%)	**L7** (20 mol%)	22 h	incomplete conversion to **47a**
2	**46a**	$[Ir(cod)(OMe)]_2$ (10 mol%)	**L8** (20 mol%)	22 h	full conversion to **47a**
3	**46b**	$[Ir(cod)(OMe)]_2$ (20 mol%)	**L7** (40 mol%)	17 h	no product formation
4	**46b**	$[Ir(cod)(OMe)]_2$ (20 mol%)	**L8** (40 mol%)	17 h	full conversion to **47b**
5	**46c**	$[Ir(cod)(OMe)]_2$ (20 mol%)	**L7** (40 mol%)	20 h	conversion to **48**
6	**46c**	$[Ir(cod)(OMe)]_2$ (20 mol%)	**L8** (40 mol%)	20 h	conversion to **47c** and **48**

0.1 mmol **46**, 1 equiv. B_2pin_2, $[Ir(cod)(OMe)]_2$, and ligand were stirred in 1.0 mL octane at 120 °C in a reaction tube overnight, and analyzed by LCMS.

Generally, the silylquinoline ligand **L8** performed better than triphenylarsine (**L8**), resulting in full conversion of the xanthones **46a** and **46b** overnight. Mono-borylated xanthones **47a** and **47b** could be prepared using silylquinoline ligand **L8**, but could not isolated by chromatography due to partially hydrolysis on silica. Therefore, the crude mono-borylated xanthones were directly used in the next synthetic step. The sequence

was first conducted with the MOM-protected xanthone, since it is inert to fluoride salt used in the next step unlike silyl ether-based protecting groups (Scheme 5.14). After borylation of **46b**, the crude product **47b** was directly converted to the corresponding bromide **49** with $CuBr_2$ in presence of KF and used without further purification (NMR analysis showed the non- and bis-brominated products as minor impurities). The crude bromide was reacted with vinyltrifluoroborate in a Suzuki-Miyaura coupling with Pd(dppf)Cl_2 catalyst. Vinyl **49** was obtained in 24 % yield over 2 steps containing the bis-vinylated product as a minor impurity. Finally, MOM-protecting groups were removed by acidic hydrolysis yielding **PaX(–)1** in 87 % yield.

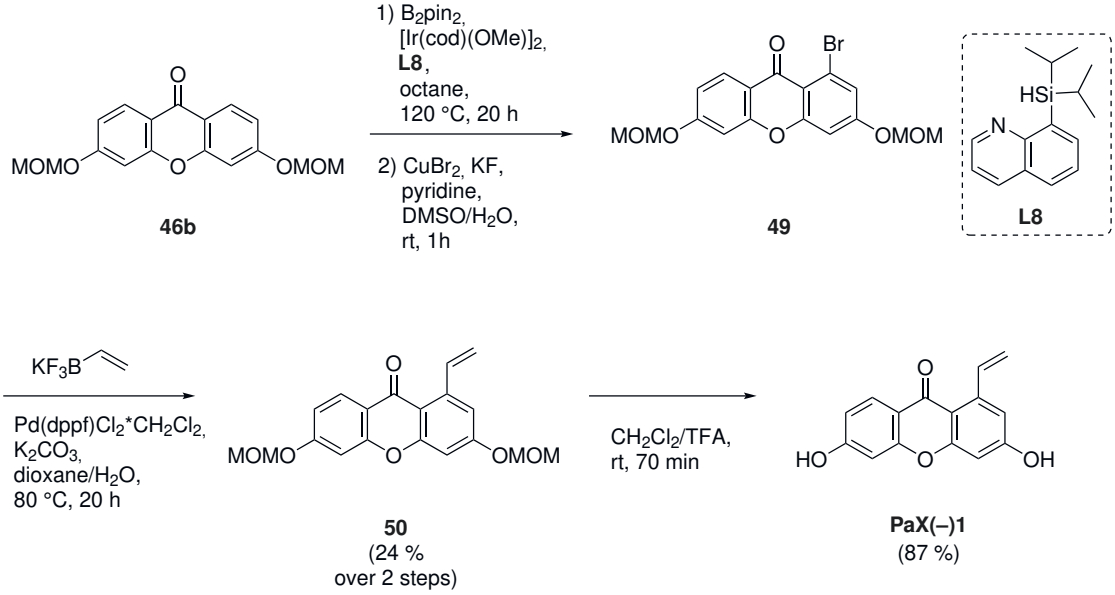

Scheme 5.14 – Preparation of **PaX(–)1**.

Compound **PaX$_{480}$** (λ_{abs} = 399 nm) (Scheme 5.15) undergoes conversion to its cyclized, fluorescent form (with: λ_{abs} = 480 nm, λ_{em} = 514 nm) upon irradiation (λ_{ON} = 405 nm).[39] In the same manner, it was suspected that the hydroxy analog **PaX(–)1** forms **PaX(–)1-CF** upon irradiation and that both **PaX(–)1** and **PaX(–)1-CF** display hypsochromic shifts in absorption and emission similar to the hypsochromic shifts observed in fluoresceins to rhodamines.[33] Indeed, a solution of **PaX(–)1** (6.5 µM) in phosphate buffer (0.1 M, pH 7) displayed an absorption maximum of λ_{abs} = 334 nm (Appendix Figure 9.20b, p.181), which demands irradiation with shorter wavelengths than λ_{ON} = 405 nm. Accordingly, the sample was irradiated with λ_{ON} = 365 nm for $\sim$ 1 min (Scheme 5.15), which triggered rapid photoconversion of **PaX(–)1** to **PaX(–)1-CF** (λ_{abs} = 434 nm, λ_{em} = 478 nm) confirmed by LCMS (Appendix Figure 9.20b-e, p.181). This initial experiment shows **PaX(–)1-CF** to be photoactivatable similar to the corresponding PaX dyes. Both the photoactivatable and fluorescent form **PaX(–)1** and **PaX(–)1-CF** displayed an expected hypsochromic shift in absorption and emission compared to **PaX$_{480}$**. However, a shorter activation wavelength λ_{ON} is required due to

this hypsochromic shift.

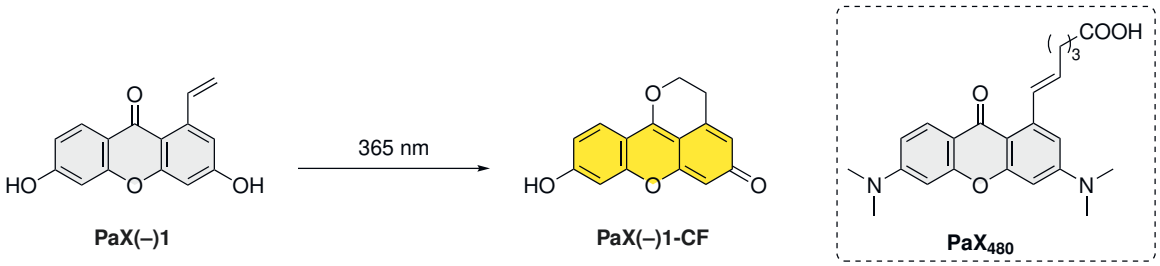

Scheme 5.15 – Photoactivation of **PaX(–)1** to **PaX(–)1-CF**. A solution of **PaX(–)1** (6.5 µM) in phosphate buffer (0.1 M, pH 7) was irradiated at 365 nm. The experiment was conducted by Dr. Mariano Bossi.

5.4.2 PaX(–)2

Similarly to Si-fluorescein,[92] the silicon analog **PaX(–)2** might represent a probe, which is bathochromically shifted to **PaX(–)1**. Following the synthetic route described in Scheme 5.14, Si-xanthone **51** was protected with MOM-Cl yielding **52** (Scheme 5.16). Next, the protected xanthone was mono-borylated with B_2pin_2 using $[Ir(cod)(OMe)]_2$ with $AsPh_3$ as catalytic system. Hereby, milder reaction temperatures (80 °C instead 120 °C) have turned out to be sufficient. The crude product **53** was then converted to the corresponding halide to prevent hydrolysis of the borate. Herein, chloride instead bromide was installed, because the xanthone chlorides were found in our laboratory to be generally more stable compared to bromides and iodides. Compound **54** was obtained in 90 % yield and Suzuki coupling with vinyltrifluoroborate yielded the corresponding vinyl xanthone **55** in 93 % percent yield.

The compound was then attempted to convert to **PaX(–)2** by removal of the MOM-protecting groups under acidic conditions (Scheme 5.17). This attempt, however, generated the cyclized, fluorescent form **PaX(–)2-CF** ($t_r = 4.5min$, *m/z*: $[297]^+$), more polar based on its shorter retention time in LCMS analysis. For photophysical characterisation of the fluorescent compound **PaX(–)2-CF**, a solution of **55** in CH_2Cl_2 was treated with TFA to yield **PaX(–)2-CF**, and the conversion to **PaX(–)2-CF** was confirmed by LCMS analysis (Appendix Figure 9.21b, p. 182). Interestingly, the fluorescent compound **PaX(–)2-CF** was not obtained after work-up, but a yellow powder, those analytic data (NMR, HRMS) indicate the formation of compound **56** (Appendix Figure 9.21c-d, p. 182). Since **56** is a non-fluorescent by-product and not of interest in this study, the mechanism of this reaction was not further studied at this point.

The acidic cleavage of MOM-protecting groups in **55** led to the formation of **PaX(–)2-CF**, which further react to a dark product (Scheme 5.17). In order to prevent the acid-induced cyclisation, an alternative method reported by Han *et al*. was applied which

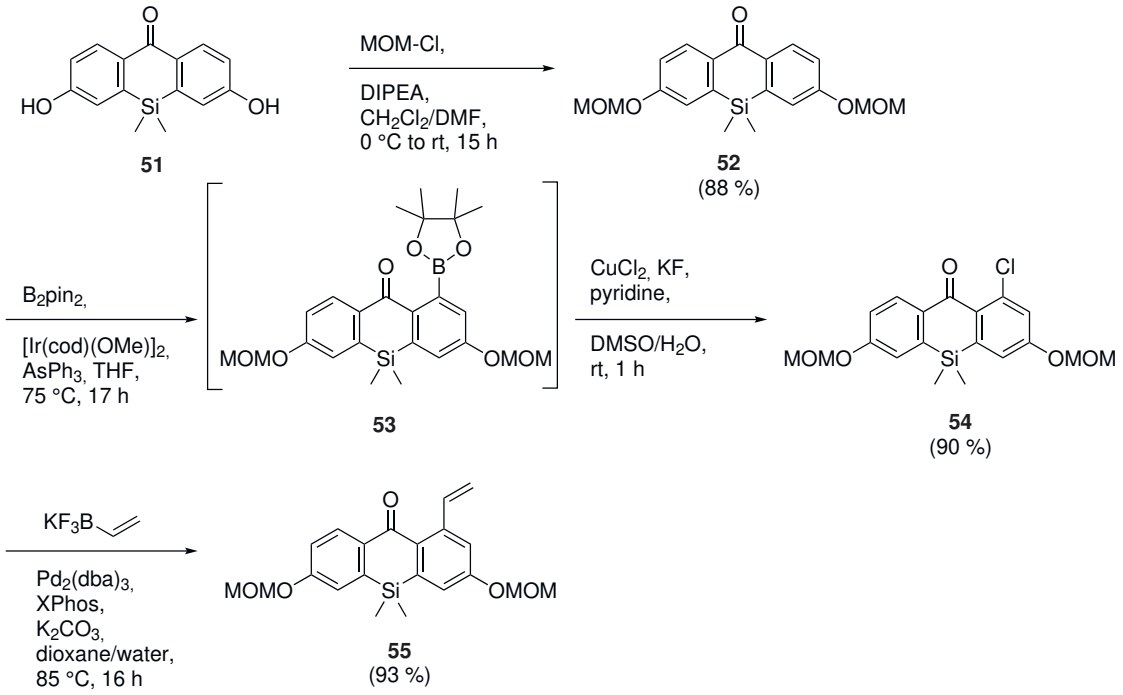

Scheme 5.16 – Preparation of MOM-protected PaX(–) dye **55**.

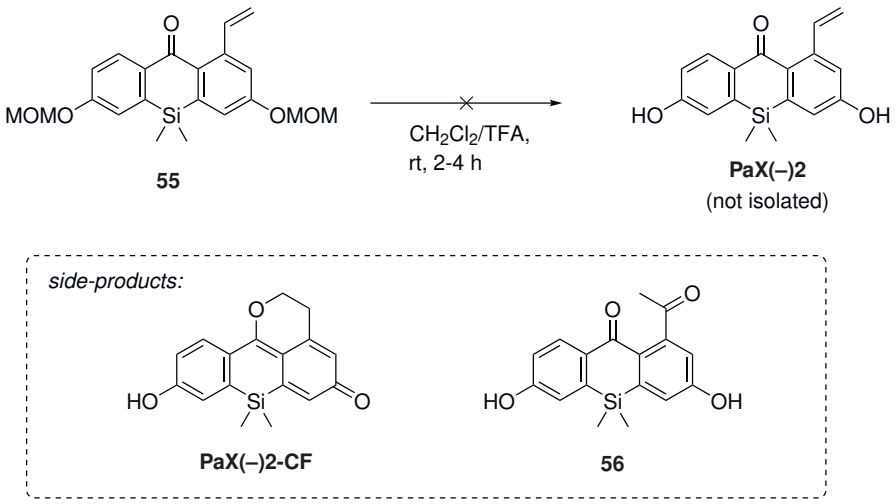

Scheme 5.17 – Unsuccessful acidic deprotection of **55** to **PaX(–)2**.

relies on the Zn(II)-mediated deprotection of MOM-groups using thiols as nucleophiles (Scheme 5.18).[165] This approach successfully converted **55** to **PaX(–)2** in 61 % yields. The moderate yield was attributed to partial cyclisation of **PaX(–)2** to **PaX(–)2-CF** on acidic silica during column chromatography (silica, 20 % to 100 % EtOAc/hexane).

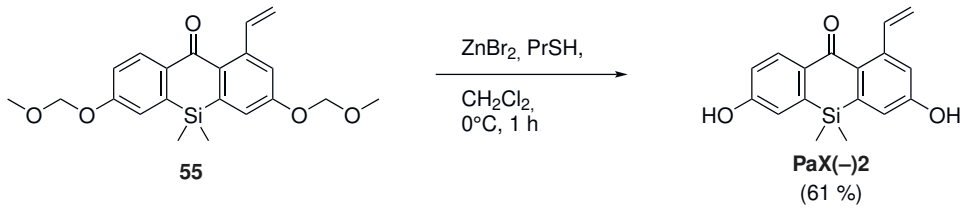

Scheme 5.18 – Preparation of **PaX(–)2** by a Zn-mediated MOM-deprotection.[165]

To test, whether Si-analog **PaX(–)2** and its fluorescent form display bathochromic shifts in absorption and emission to the O-analog **PaX(–)1** and its fluorescent form, a solution of **PaX(–)2** (5.6 µM) in phosphate buffer (0.1 M, pH 7) was irradiated for $\sim$ 1 min (Scheme 5.19) and **PaX(–)2** (λ_{abs} = 325 nm) underwent photoconversion to a fluorescent product (λ_{abs} = 477, 503 nm, λ_{em} = 538 nm) (Appendix Figure 9.22b-c, p.183). However, LCMS analysis detected a major product ionizing with *m/z* $[315]^+$ alongside traces of the expected product **PaX(–)2-CF** (Appendix Figure 9.22e, p.183). After irradiation, a decay of fluorescence was observed within minutes (Appendix Figure 9.23b-c, p.184). After full decay of fluorescence, a compound with a molecular ion of *m/z* $[315]^+$ was found as main product by LCMS analysis (Appendix Figure 9.23e, p.184). The observed *m/z* value corresponds to compound **57**, which may form upon hydrolysis of the fluorescent form **PaX(–)2-CF**.

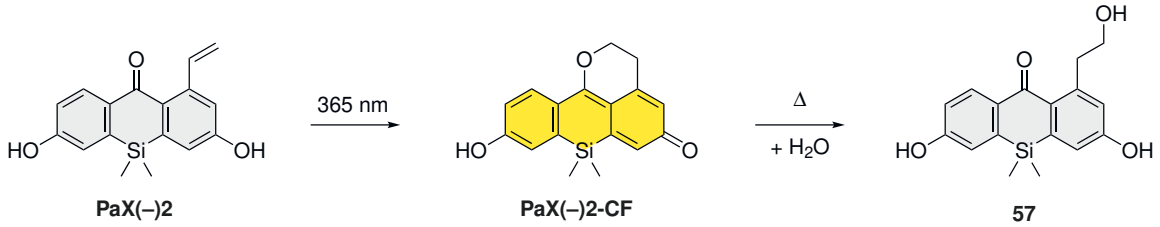

Scheme 5.19 – Photoactivation of **PaX(–)2** to **PaX(–)2-CF**. A solution of **PaX(–)2** (5.6 µM) in phosphate buffer (0.1 M, pH 7) was irradiated at 365 nm. The experiment was conducted by Dr. Mariano Bossi.

To get further insight on the rates, in which the fluorescent product **PaX(–)2-CF** is formed upon irradiation and then thermally hydrolysed to a non-fluorescent dark product, the absorption near the local absorption maximum of **PaX(–)2-CF** (λ_{abs} = 480 nm) was plotted vs the time during and after irradiation (Appendix Figure 9.24d-e, p.185). Rate constants τ of photoactivation and hydrolysis were obtained by mono-exponential fitting to equation 5.1.[39] Hereby, rate constants of $\tau_1 = 14.9 \pm 0.2$ s^{-1} for the photoactivation and $\tau_2 = 385 \pm 2$ Hereby, rate constants of $\tau_1 = 14.9 \pm 0.2$ s^{-1} for the thermal hydrolysis were obtained indicating a fast photoactivation of **PaX(–)2** on the scale of

seconds. This is followed by a slower thermal reaction to a dark product on the scale of minutes.

$$Abs_t = Abs_{t=0} \cdot e^{\tau \cdot t} + Abs_{BG} \tag{5.1}$$

with: $Abs_{t=0}$ = the absorbance at $t = 0$; τ = the rate constant; and $Abs_{t=0}$ = the absorbance of the background.

In summary, the bathochromically shifted Si-analog **PaX(–)2** is photoactivatable similar to the the *O*-derivative **PaX(–)1**, but undergoes a slow thermal reaction to a non-fluorescent product on the time scale of minutes. This opens a time-frame to localize the fluorescent molecule, potentially suitable for SMLM techniques as PALM or other SRM techniques as MINFLUX.

5.4.3 Sensor probes derived from PaX(–) dyes

With the second photoactivatable PaX(–) in hand, the goal was to design photoactivatable sensor probes for live-cell imaging. Non-fluorescent diacetyl fluoresceins as a modification to induce cell-permeability are enzymatically cleaved *in vivo* by esterases to fluorescent fluoresceins.[37,38] Furthermore, the installation of the *O*-acetyl group on a photoactivatable rhodol analog has shown to alter the photoproduct upon irradiation (see 2.2.2, p. 14). While the *O*-acetyl group is installed, the rhodol analog would photoreact to a non-fluorescent product. After enzymatic cleavage of the *O*-acetyl group, the light-induced Wolff rearrangement generates a high emissive fluorophore instead.[88]

This raises the question, how the installation of the *O*-acetyl group effects the photoactivation of PaX(–) dyes. It is possible that *O*-acetylated PaX(–) analogs form non-fluorescent photoproducts in a similar manner to the photoactivatable rhodol analog reported by Halabi *et al*.[88] Alternatively, *O*-acetylated PaX(–) analogs might be stable and do not photoconvert upon irradiation. In both cases, *O*-acetylated PaX(–) analogs would be suitable photoactivatable sensor probes, since they would generate fluorescent photoproducts only after enzymatic cleavage of the *O*-acetyl groups. Lastly, it is possible that *O*-acetylated PaX(–) analogs form undesired, fluorescent photoproducts upon irradiation.

To evaluate the effect of the *O*-acetyl group on the photoactivation of PaX(–) dyes, the acetate **PaX(–)2-OAc** was prepared by reaction of **PaX(–)2** with acetic anhydride in acetonitrile (Scheme 5.20).

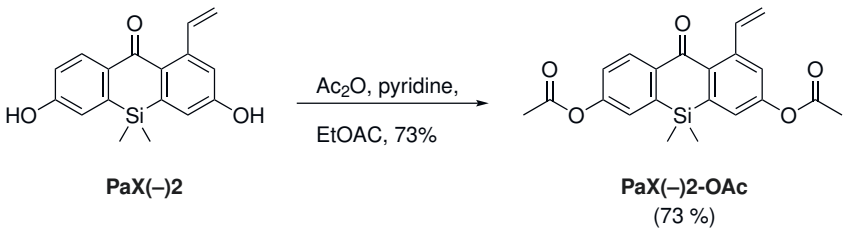

Scheme 5.20 – Preparation of acetate **PaX(–)2-OAc**.

Next, a solution of non-fluorescent **PaX(–)2-OAc** (5.6 µM) in phosphate buffer (0.1 M, pH 7) was irradiated (Scheme 5.21, Path A). A decay of absorbance at 300 nm was found, but no fluorescence enhancement (Appendix Figure 9.25b-c, p. 186). LCMS analysis of the irradiated sample displayed a compound with a molecular ion of *m/z* $[399]^+$ which corresponds to the non-fluorescent xanthones **59** and **60** (Appendix Figure 9.25e, p. 186). This finding can be explained by light-induced cyclisation of **PaX(–)2-OAc** to intermediate **58** followed by nucleophilic attack of water to form **59** or **60** by a ring-opening. These results show that **PaX(–)2-OAc** is photoconverted upon irradiation to desired non-fluorescent product(s).

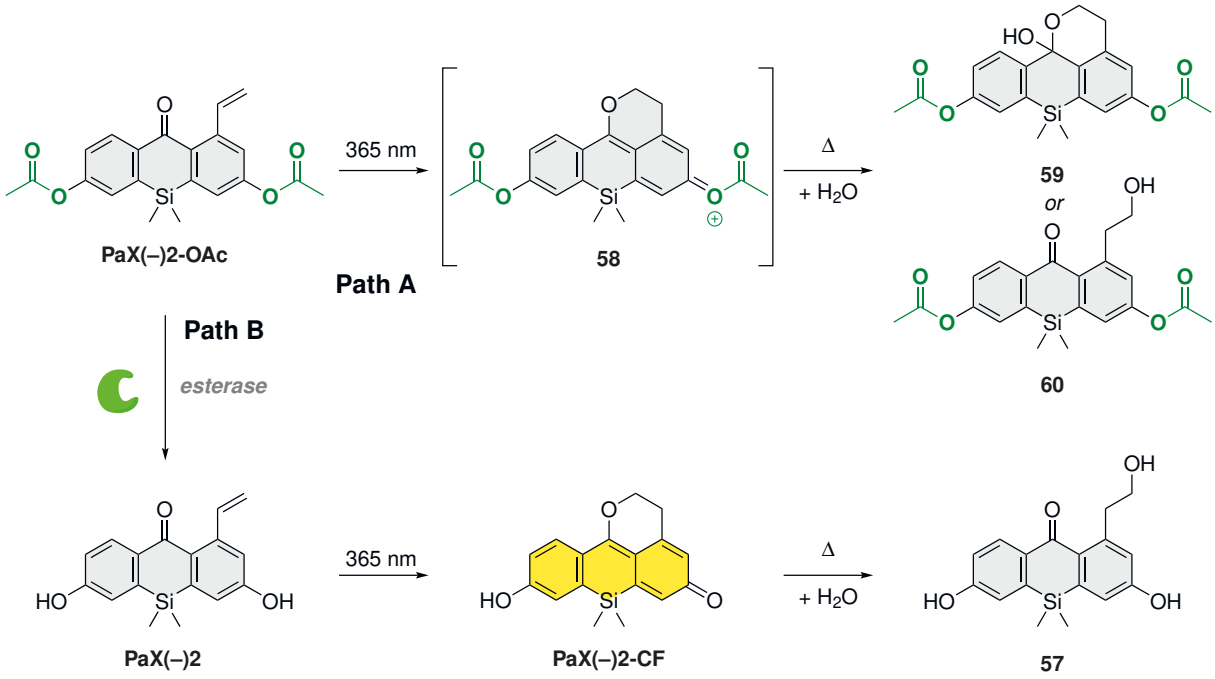

Scheme 5.21 – Photoconversion of **PaX(–)2-OAc** with no (Path A) or after (Path B) pre-treatment with PLE. **PaX(–)2-OAc** (5.6 µM) in phosphate buffer (0.1 M, pH 7) was irradiated at 365 nm. Path A: No addition of enzyme. Path B: Pre-treatment with porcine liver esterase (PLE) (2 µg/mL. The experiment was conducted by Dr. Mariano Bossi.

Next, the enzymatic cleavage of **PaX(–)2-OAc** by esterases followed by photoactivation was evaluated (Scheme 5.21, Path B). Treatment of **PaX(–)2-OAc** (5.6 µM) in phosphate buffer (0.1 M, pH 7) with porcine liver esterase (PLE) (2 µg/mL) resulted in a increase of absorbance at 320 nm due to the enzymatic cleavage of acetate

PaX(–)2-OAc to **PaX(–)2** (Appendix Figure 9.26b-c, p. 187). The formation of **PaX(–)2** was further confirmed by LCMS analysis. Then, the sample was irradiated at 365 nm and absorbance at 505 nm increased over time due to photoconversion of **PaX(–)2** to **PaX(–)2-CF** (Appendix Figure 9.27d, p. 188). After $\sim$ 1 min, a decay in absorbance was observed because of the thermal conversion of **PaX(–)2-CF** to a non-fluorescent product confirmed by LCMS analysis (Appendix Figure 9.27e, p. 188). These results show that the *O*-acylated **PaX(–)2-OAc** is enzymatically cleavable to **PaX(–)2**, which is photoactivatable under *in vitro* conditions.

O-acylated compound **PaX(–)2** have shown to undergo photoconversion to desired non-fluorescent product(s) before enzymatic cleavage of the *O*-protecting group. This raises the question whether PaX(–) dyes bearing different enzymatically cleavable *O*-protecting groups behave similarly. The acetoxymethyl (AM) group is sensitive to esterases in facile manner to the *O*-acylatyl group, and is structurally similar to the MOM-protecting group, which has been applied in the synthetic pathway to access PaX(–) dyes. Therefore, a solution of the MOM-protected building block **50** (5.0 µM) phosphate buffer (0.1 M, pH 7) was irradiated at 365 nm. Hereby, no photoconversion of **50** to a photoproduct was found (Appendix Figure 9.28d, p. 189), but minor photobleaching. Accordingly, enzymatically cleavable *O*-protecting groups, which are structurally similar to the MOM-protecting group, might not undergo photoconversion to potentially fluorescent products, too, and thereby be suitable for the design of photoactivatable sensor probes.

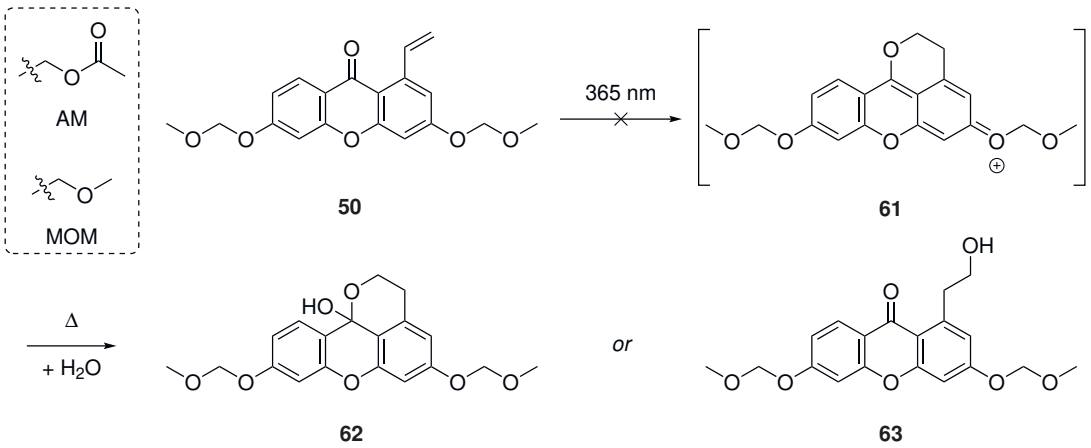

Scheme 5.22 – AM- and MOM-protecting groups and proposed photoconversion of **50** in facile manner to acetate **PaX(–)2** (Scheme 5.21). **64** (5.0 µM) in phosphate buffer (0.1 M, pH 7) was irradiated at 365 nm. No photoconversion was found. The experiment was conducted by Dr. Mariano Bossi.

In summary, the installation of the *O*-acetyl and MOM-protecting group yields non-fluorescent PaX(–) analogs which either form non-fluorescent photoproducts or do not react upon irradiation. Furthermore, the acetate **PaX(–)2-OAc** has shown to be enzymatically cleavable and then photoactivatable to its fluorescent product **PaX(–)2-CF**.

5.4.4 HaloTag ligand conjugate of PaX(–)2

The next goal was to design a probe for live-cell fluorescence microscopy based on **PaX(–)2** dye targeting the HaloTag ligand conjugate **PaX(–)2-Halo**.

For the preparation of probe **PaX(–)2-Halo**, chloride **54** was cross-coupled with the boronate ester building block **65** under Suzuki-Miyaura coupling conditions (Scheme 5.23), and **66** was obtained in 81 % yield. Both the *tert*-butyl ester and the MOM-protecting groups were removed under acidic conditions. **67** was yielded in 48 % yield, which can be attributed to partial cyclisation on the product to its fluorescent form, that was observed in case of **PaX(–)2**. Finally, the free carboxylic acid in **67** was aminated with the HaloTag(O2) ligand with HATU as peptide coupling reagent. The conjugate **PaX(–)2-Halo** was afforded in 34 % yield. LCMS analysis of the reaction mixture indicated partial addition of the coupling reagent to the nucleophilic phenol, which lowered the yield of the reaction. Notably, the adduct was successfully converted back to the phenol by addition of base.

The label **PaX(–)2-Halo** was then tested in confocal imaging. **PaX(–)2-Halo** was successfully applied in visualizing fused HaloTag-vimentin protein in U-2 OS cells expressing a genome-edited Vimentin-HaloTag fusion protein in combination with the well-established counter-stain Hoechst 33342 (Figure 5.3). **PaX(–)2-Halo** was pre-activated with a 405 nm laser, and these initial results demonstrates the successful photoactivation of this dyes under live-cell conditions.

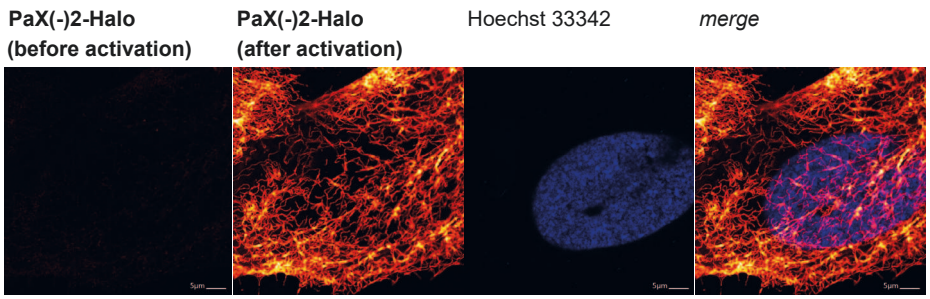

Figure 5.3 – Living U-2 OS cells were stained overnight with **PaX(–)2-Halo** (250 nM, for 12 h) and counter-stained with Hoechst 33342 (8 µM, for 10 min). **PaX(–)2-Halo** was pre-activated with a 405 nm laser. The experiment was conducted by Dr. Mariano Bossi.

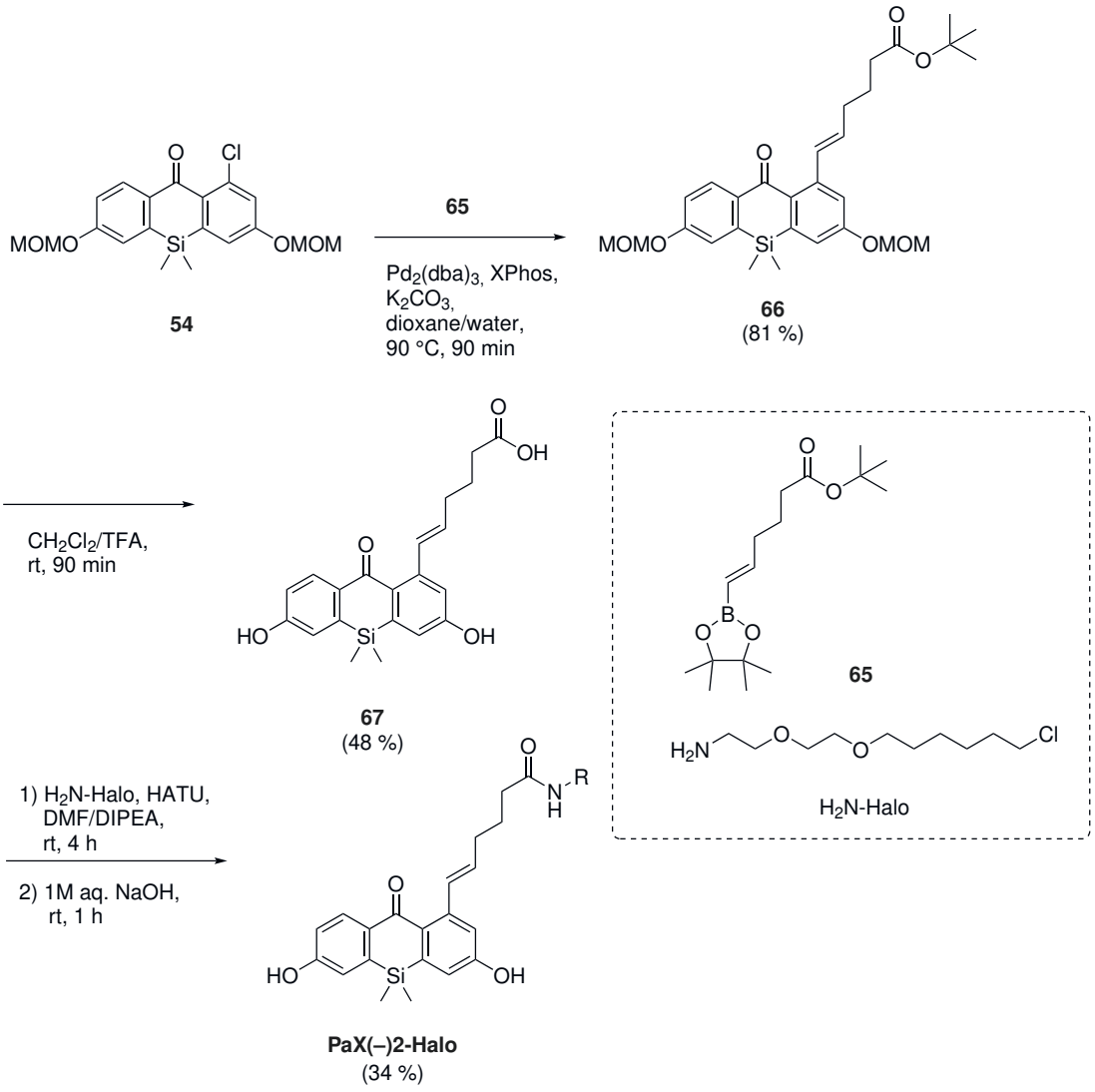

Scheme 5.23 – Preparation of HaloTag ligand conjugate **PaX(–)2-Halo**.

5.4.5 Outlook

Within this work, two 3,6-dihydroxyxanthones as analogs of previously described PaX dyes have been established. The compounds **PaX(–)1** and **PaX(–)2** show efficient photoactivation suitable for SMLM techniques. Notable, **PaX(–)2** undergoes a thermal reaction to a non-fluorescent product after photoactivation within minutes. The efficient photoactivation of **PaX(–)1** and **PaX(–)2** was further used for developing an *O*-actylated derivative **PaX(–)2-OAc** as enzymatic sensor activity probes, which undergoes photoactivation exclusively after enzymatic cleavage of the acetyl group. Finally, a HaloTag ligand conjugate of **PaX(–)2-OAc** was prepared and successfully applied in confocal imaging of living cells. These initial results indicate the potential of PaX(–) for future applications in live-cell single-molecule localisation imaging and as photoactivatable enzymatic sensor probes.

Chapter 6

Conclusion

The scope of the thesis is the chemical design and development of synthetic methodologies to access negatively charged and photoactivatable fluorescent reporters based on fluoresceins for live-cell super- resolution fluorescence microscopy. The development of negatively charged probes based on fluoresceins were suspected to suppress off-targeting and accumulation found in positively charged probes based on rhodamines. Furthermore, photocleavable *O*-protecting groups were envisaged as a way to design of photocleavable caging groups of small size, which often rely on bulky nitrobenzene-type cages forming toxic by-products during photoactivation.

The replacement of hydroxyl groups in fluorescein with cyanamido groups yielded *N*-cyanorhodamine dyes with improved photostability and cell-permeability and no visible off-targeting. These dyes were prepared by Buchwald-Hartwig amination of the corresponding triflates, Ullmann coupling of corresponding aryl iodides or the alkaline decomposition of rhodamine-derived aryl tetrazoles. Hereby, easily accessible fluorescein or rhodol triflates serve as starting materials in the one-step or multi-step synthetic methodologies. HaloTag and SNAP-tag ligand conjugates representing three different emission colors have been successfully prepared. These labels showed fast labeling kinetics and have been applied in combination with commercially available labels in multi-color confocal and STED imaging of living cells. The labels were found suitable for resolving diverse structures with subdiffractive resolution under STED microscopy conditions, with sole exception of the *N,N'*-dicyano-Si-rhodamine derivative. This can be attributed to its relatively high $pK_{a,FL}$ value, but for the same reason this dye and derivative should not be overlooked as a potential blinking fluorophore in future studies.

Several design strategies have been evaluated towards the development of photoactivatable fluorescein analogs bearing small caging moieties. *N*-(tetrazinyl)rhodamines were successfully prepared from their corresponding aryl iodides, but showed poor solubility in aqueous solutions and no photoconversion to *N*-cyanorhodamines in neutral aqueous solutions. Several thiocarbonyl-caged triarylmethane were explored, but were found particularly unstable towards oxidation and none of then display the desired photoactivation properties.

Fluorescein analogs PaX(–) derived from previously described PaX dyes were designed as a feasible alternative. Involving the MOM-group as protecting group strategy throughout the synthetic routes, two PaX(–) dyes have been prepared alongside with an *O*-acetyl protected photoactivatable dye and a HaloTag ligand conjugate for live-cell imaging. These compounds display fast photoactivation, the HaloTag ligand conjugate was successfully applied in initial tests using confocal imaging by pre-activation of the conjugate. Furthermore, the acetate derivative is photoactivatable exclusively after the enzymatic cleavage. These initial findings marks PaX(–) dyes as a valuable extension of PaX dyes. In future works, the PaX(–) dyes could be potentially applied to SMLM and MINFLUX imaging as well as the fluorogenic visualization of specific enzymatic activity in living cells.

In conclusion, this thesis provides concepts and synthetic methodologies for negatively charged small-molecule fluorophores in live-cell SRM imaging. The installation of cyanamido groups improved the photophysical properties of fluorescein dyes significantly and might be a concept for other fluorophores. The installation of hydroxyl groups on PaX dyes extended their scope and may enable the design sensor probes in future works.

Chapter 7

Experimental section

Preparation and characterisation of compounds **NCR1**, **NCR2**, **NCR3**, **NCR1-Halo**, **NCR2-Halo**, **NCR3-Halo**, **NCR1-SNAP**, **10**, **13**, **14**, **15**, **16**, **18**, **24**, **25**, **26** and **27** have been previously reported and are reproduced from Ref.[1] with permission from the Royal Society of Chemistry.

7.1 Chapter 4

7.1.1 Preparation of aryl triflates and iodides

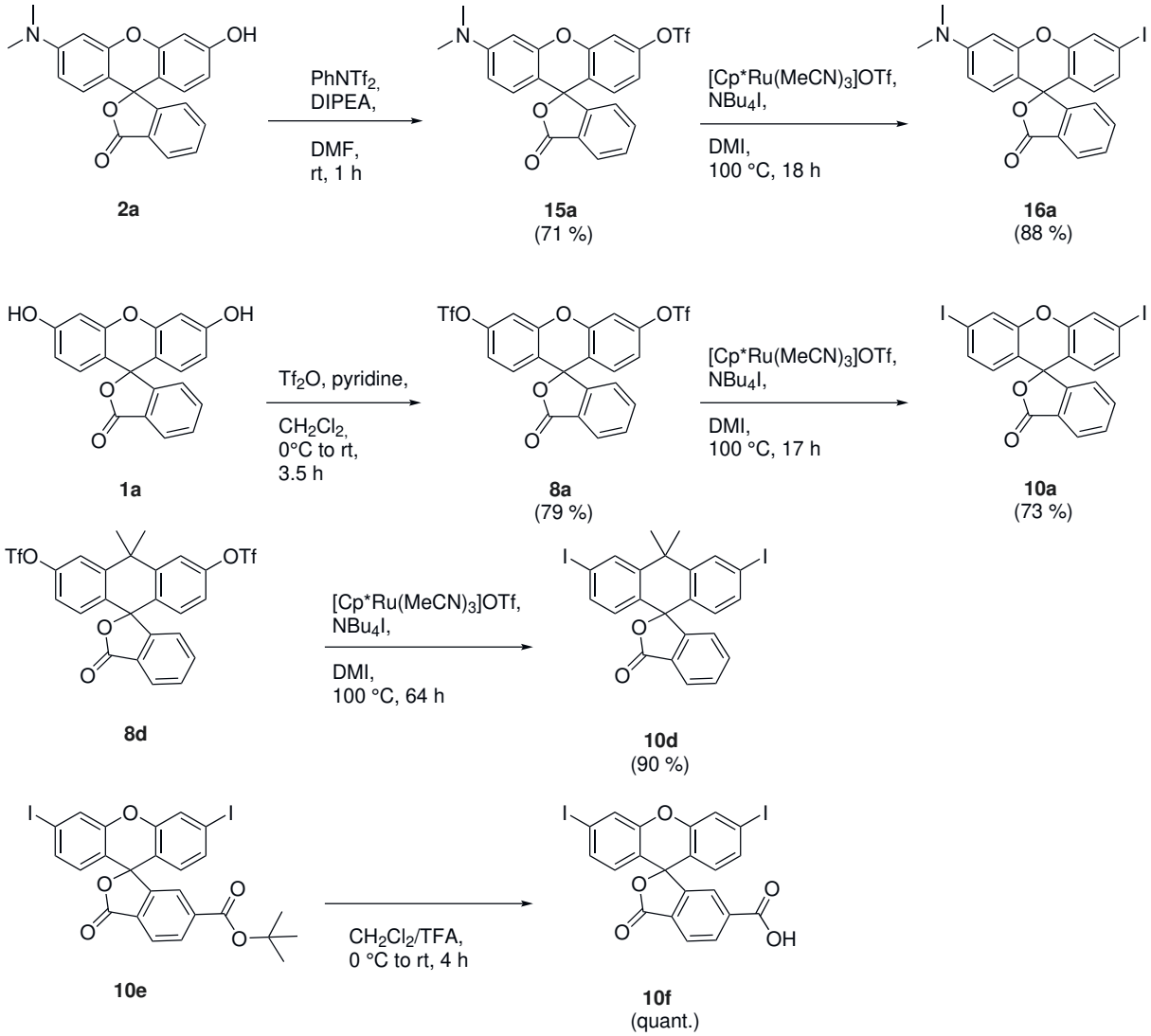

Triflate 15a

Following an adapted procedure,[136] DIPEA (4.4 equiv., 16.1 mmol, 2.80 mL) was added to a mixture of rhodol **2a**[166] (1.0 equiv., 3.65 mmol, 1.31 g) and $PhNTf_2$ (1.5 equiv., 5.41 mmol, 1.93 g) in DMF (15 mL) at ambient temperature under argon. The mixture was stirred at ambient temperature for 1 h, before it was diluted with water (50 mL) and extracted with EtOAc (3x 25 mL). The combined organic phases were washed with water (3x 10 mL) and brine (25 mL), dried with anhydrous Na_2SO_4, filtered, and evaporated. The crude product was purified by flash column chromatography (80 g Redisep

Rf, 0 % to 90 % EtOAc/hexane).

Triflate **15a** was obtained as 1.28 g pink powder (containing 8 mol% hexane as remainder) in 71 % yield.

^{1}H NMR (400 MHz, $CDCl_3$) δ 8.07 – 8.00 (m, 1H), 7.73 – 7.60 (m, 2H), 7.22 (d, *J* =2.3 Hz, 1H), 7.18 (d, *J* =7.5 Hz, 1H), 6.92 (dd, *J* =8.8, 2.4 Hz, 1H), 6.87 (d, *J* =8.7 Hz, 1H), 6.62 (d, *J* =8.8 Hz, 1H), 6.52 (d, *J* =2.5 Hz, 1H), 6.46 (dd, *J* =8.9, 2.6 Hz, 1H), 3.00 (s, 6H).

^{19}F NMR (376 MHz, $CDCl_3$) δ -72.67.

^{13}C NMR (101 MHz, $CDCl_3$) δ 169.3, 152.8, 152.6, 152.3, 152.2, 150.0, 135.3, 130.2, 130.1, 128.8, 126.9, 125.3, 124.1, 120.3, 118.8 (q, $^1J_{C\text{-}F}$ = 320.9 Hz), 116.4, 110.5, 109.7, 105.7, 98.7, 82.7, 40.4.

HRMS (ESI) m/z: 492.0723 (calcd. for $C_{23}H_{17}F_3NO_6S$, $[M+H]^+$), 492.0719 (found).

Iodide 16a

Following an adapted procedure,[121] triflate **15a** (1 equiv., 0.40 mmol, 194 mg), *n*-Bu_4NI (6 equiv., 2.40 mmol, 882 mg), and [Cp*Ru(MeCN)$_3$]OTf (5 mol%, 0.02 mmol, 10 mg) were placed in a dried flask. It was evacuated and backfilled with argon (3 cycles) and DMI (3.0 mL) was added. After stirring at 100 °C for 18 h, the mixture was diluted with water and extracted with hexane/EtOAc (3x 25 mL, 1:4). The combined organic phases were washed with water/brine (2x 30 mL, 1:1) and brine (30 mL), dried with anhydrous Na_2SO_4, filtered, and evaporated. The crude product was purified by flash column chromatography (25g Puriflash 30 µm, 20 % to 50 % EtOAc/hexane).

Iodide **16a** was obtained as 177 mg pinkish powder (containing 27 mol% dioxane as remainder) in 88 % yield.

^{1}H NMR (400 MHz, $CDCl_3$) δ 8.01 (ddd, *J* = 7.3, 1.4, 0.8 Hz, 1H), 7.70 – 7.56 (m, 3H), 7.31 (dd, *J* = 8.3, 1.7 Hz, 1H), 7.18 – 7.12 (m, 1H), 6.60 (d, *J* = 8.8 Hz, 1H), 6.53 – 6.45 (m, 2H), 6.42 (dd, *J* = 8.9, 2.6 Hz, 1H), 2.99 (s, 6H).

^{13}C NMR (101 MHz, $CDCl_3$) δ 169.6, 153.1, 152.3, 152.1, 152.1, 135.2, 132.5, 129.9, 129.6, 128.8, 126.9, 126.3, 125.2, 124.0, 119.4, 109.3, 105.7, 98.5, 95.2, 83.3, 40.4.

HRMS (ESI) m/z: 470.0248 (calcd. for $C_{22}H_{17}INO_3$, $[M+H]^+$), 470.0240 (found).

Triflate 8a

Following an adapted procedure,[119] pyridine (8.1 equiv., 39.8 mmol, 3.20 mL) was added to a slurry of **1a** (1.00 equiv., 4.94 mmol, 1.64 g) in CH_2Cl_2 (20 mL) and the mixture cooled at 0 °C. Tf_2O (4.07 equiv., 20.1 mmol, 3.40 mL) in CH_2Cl_2 (24 mL) was added dropwise over a period of 10 min. Next, the resulting mixture was allowed to warm up and stirred at ambient temperature overnight (19 h). The mixture was quenched by addition of sat. aq. $NaHCO_3$ (25 mL), diluted with water (25 mL), the two phases separated, and the aqueous phase was extracted with CH_2Cl_2 (3x 25 mL). The combined organic phases were washed with brine (50 mL), dried with anhydrous Na_2SO_4, filtered, and evaporated. The crude product was purified by flash column chromatography (80 g Redisep Rf, 0 % to 30 % EtOAc/hexane).

Triflate **8a** was obtained as 2.33 g off-white powder in 79 % yield.

^{1}H NMR (400 MHz, $CDCl_3$) δ 8.14 – 8.02 (m, 1H), 7.81 – 7.66 (m, 2H), 7.30 (d, J = 2.4 Hz, 2H), 7.21 – 7.16 (m, 1H), 7.03 (dd, J = 8.8, 2.4 Hz, 2H), 6.96 (d, J = 8.8 Hz, 2H).

^{19}F NMR (376 MHz, $CDCl_3$) δ -72.60.

The analytical data correspond to the literature.

Iodide 10a

Following an adapted procedure,[121] triflate **8a** (1.0 equiv., 2.01 mmol, 1.20 g), *n*-Bu_4NI (5.9 equiv., 12.0 mmol, 4.41 g), and [Cp*Ru(MeCN)$_3$]OTf (5 mol%, 1.01 mmol, 51.2 mg) were placed in an dried flask. It was evacuated and backfilled with argon (3 cycles) and DMI (8.0 mL) was added. After stirring at 100 °C for 17 h, the mixture was diluted with water (100 mL) and extracted with hexane/EtOAc (4x 50 mL, 1:1). The combined organic phases were washed with water/brine (2x 100 mL, 1:1) and brine (100 mL), dried with anhydrous Na_2SO_4, filtered, and evaporated. The crude product was purified by flash column chromatography (80 g Redisep Rf, 20 % to 80 % CH_2Cl_2/hexane).

Iodide **10a** was obtained as 811 mg green powder in 73 % yield.

^{1}H NMR (400 MHz, $CDCl_3$) δ 8.10 – 7.99 (m, 1H), 7.72 – 7.61 (m, 4H), 7.38 (dd, J = 8.4, 1.7 Hz, 2H), 7.16 – 7.09 (m, 1H), 6.54 (d, J = 8.3 Hz, 2H).

The analytical data correspond to the literature.

Iodide 10d

Following an adapted procedure,[121] triflate **8a** (1.0 equiv., 0.48 mmol, 300 mg), *n*-Bu_4NI (6 equiv., 2.89 mmol, 1.07 g), and [Cp*Ru(MeCN)$_3$]OTf (10 mol%, 0.048 mmol, 25 mg) were placed in an dried flask. It was evacuated and backfilled with argon (3 cycles) and DMI (2.0 mL) was added. After stirring at 100 °C for 44 h, LCMS analysis display incomplete conversion of the starting material. Another portion of [Cp*Ru(MeCN)$_3$]OTf (5 mol%, 0.024 mmol, 12 mg) was added, and the mixture was stirred at 100 °C for further 20 h. Next, the mixture was diluted with water (200 mL) and extracted with hexane/$CHCl_3$ (3x 40 mL, 1:3). The combined organic phases were washed with water/brine (2x 200 mL, 1:1) and brine (100 mL), dried with anhydrous Na_2SO_4, filtered, and evaporated. The crude product was purified by flash column chromatography (12 g Puriflash 30 µm, 0 % to 30 % EtOAc/hexane).

Iodide **10d** was obtained as 250 mg white powder (containing 29 mol% dioxane as remainder) in 90 % yield.

^{1}H NMR (400 MHz, $CDCl_3$): δ 8.05 – 8.00 (m, 1H), 7.97 (d, *J* = 1.7 Hz, 2H), 7.64 – 7.56 (m, 2H), 7.46 (dd, *J* = 8.4, 1.7 Hz, 2H), 6.99 – 6.94 (m, 1H), 6.50 (d, *J* = 8.4 Hz, 2H), 1.85 (s, 3H), 1.76 (s, 3H).

^{13}C NMR (101 MHz, DMSO-d_6): δ 70.2, 154.8, 146.6, 136.3, 136.0, 135.3, 130.9, 129.8, 129.6, 125.8, 125.7, 123.5, 96.0, 85.0, 38.0, 34.9, 33.4.

HRMS (ESI) m/z: 578.9312 (calcd. for $C_{23}H_{17}I_2O_2$, $[M+H]^+$), 578.9298 (found).

Iodide 10f

Ester **10e** (1.0 equiv., 0.051 mmol, 33 mg) was dissolved in CH_2Cl_2 (0.75 mL) and cooled at 0 °C. TFA (0.25 mL) was added and the resulting mixture was stirred at 0 °C for 10 min, before it was allowed to warm up and stirred at ambient temperature for 4 h. Next, the mixture was diluted and evaporated to dryness from toluene (3 cycles) and CH_2Cl_2 (1 cycle) and lyophilized from aqueous dioxane.

Carboxylic acid **10f** was obtained as 32 mg off-white powder (containing 22 mol% dioxane as remainder) in quant. yield.

^{1}H NMR (400 MHz, DMSO-d_6): δ 13.6 (br s, 1H, CO2H), 8.25 (dd, *J* = 8.0, 1.4 Hz, 1H), 8.16 (dd, *J* = 7.9, 0.8 Hz, 1H), 7.83 – 7.81 (m, 3H), 7.48 (dd, *J* = 8.3, 1.7 Hz, 2H), 6.67 (d, *J* = 8.3 Hz, 2H).

^{13}C NMR (101 MHz, DMSO-d_6): δ 167.6, 165.9, 152.2, 150.4, 137.8, 133.3, 131.4, 129.8, 128.6, 125.7, 125.6, 124.7, 117.8, 97.2, 81.0.

HRMS (ESI) m/z: 596.8690 (calcd. for $C_{21}H_{11}I_2O_5$, $[M+H]^+$), 596.8685 (found).

7.1.2 Preparation of *N*-cyanorhodamines 13 by Buchwald-Hartwig amination

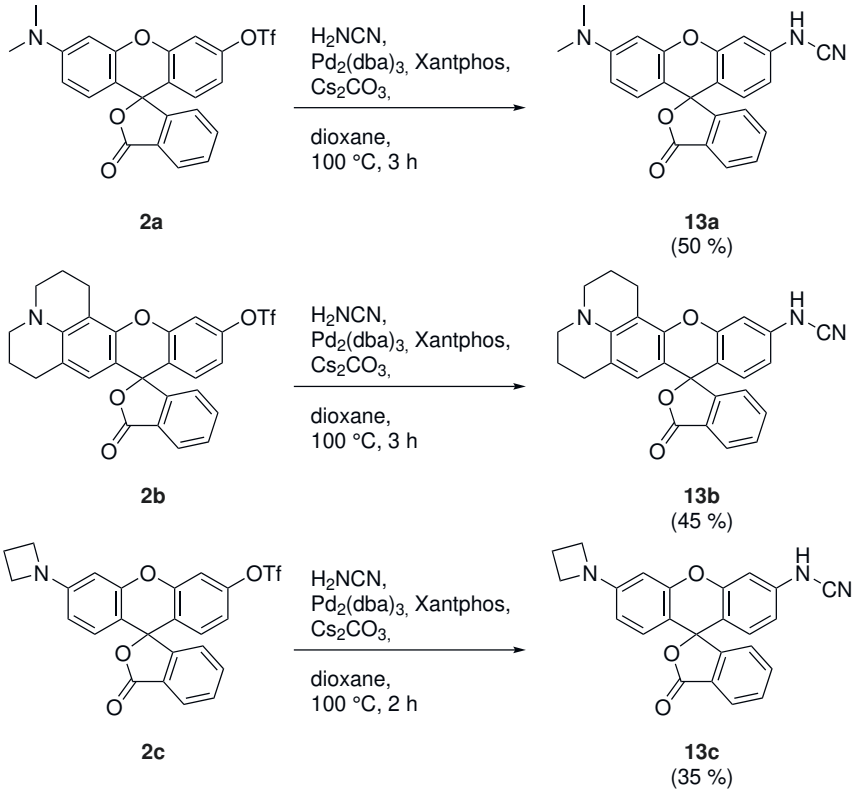

N-Cyanorhodamine 13a

In a 10 mL reaction tube, Cs_2CO_3 (3.0 equiv., 0.30 mmol, 97 mg) was dried under vacuum. Cyanamide (2.9 equiv., 0.29 mmol, 12 mg), $Pd_2(dba)_3$ (10 mol%, 0.01 mmol, 9.2 mg), and Xantphos (20 mol%, 0.020 mmol, 11.5 mg) were added, and the tube was evacuated and backfilled with argon (3 cycles). Next, triflate **15a** (1.0 equiv., 0.1 mmol, 49 mg) in dioxane (1.0 mL) was added and the resulting mixture was stirred at 100 °C for 3 h. The crude product was purified by flash column chromatography (12 g Puriflash 30 µm, 0 % to 100 % A/B, A = CH_2Cl_2 + 20 % EtOH + 0.1 % NEt_3, B = CH_2Cl_2 + 0.1 % NEt_3).

N-Cyanorhodamine **13a** was obtained as 22.6 mg violett powder (containing 43 mol% NEt_3 as remainder) in 50 % yield.

^{1}H NMR (400 MHz, pyridine-d_5) δ 8.31 (d, *J* = 7.6 Hz, 1H), 7.74 (td, *J* = 7.5, 1.3 Hz, 1H), 7.67 (td, *J* = 7.5, 1.1 Hz, 1H), 7.39 (dt, *J* = 7.6, 1.0 Hz, 1H), 6.98 – 6.84 (m, 3H), 6.63 (d, *J* = 2.6 Hz, 1H), 6.50 (dd, *J* = 9.0, 2.6 Hz, 1H), 2.86 (s, 6H).

^{13}C NMR (101 MHz, pyridine-d_5) δ 169.9, 135.2, 130.8, 130.6, 129.8, 115.3, 110.8, 103.8, 99.0, 40.4.

HRMS (ESI) m/z: 384.1343 (calcd. for $C_{23}H_{18}N_3O_3$, $[M+H]^+$), 384.1341 (found).

N-Cyanorhodamine 13b

In a 10 mL reaction tube, Cs_2CO_3 (2.8 equiv., 0.15 mmol, 47 mg) was dried under vacuum. Triflate **15b**[136] (1.0 equiv., 0.05 mmol, 28 mg), cyanamide (2.5 equiv., 0.13 mmol, 5.4 mg), $Pd_2(dba)_3$ (20 mol%, 0.01 mmol, 9.2 mg), and Xantphos (40 mol%, 0.02 mmol, 11.2 mg) were added, and the tube was evacuated and backfilled with argon (3 cycles). Dioxane (0.5 mL) was added and the resulting mixture was stirred at 100 °C for 3 h. The crude product was purified by flash column chromatography (12 g Puriflash 30 µm, 0 % to 100 % A/B, A = CH_2Cl_2 + 20 % EtOH + 0.5 % HOAc, B = CH_2Cl_2 + 0.5 % HOAc) and further purified by preparative HPLC (Interchim PhenC4 250x21.2 mm 5 µm, gradient 35/65 to 65/35 A:B, A = MeCN + 0.1 % formic acid, B = H_2O + 0.1 % formic acid).

N-Cyanorhodamine **13b** was obtained as 10.2 mg violet powder in 45 % yield.

^{1}H NMR (400 MHz, pyridine-d_5) δ 8.53 (d, *J* = 8.0 Hz, 1H), 7.80 – 7.65 (m, 2H), 7.50 (dd, *J* = 7.3, 1.4 Hz, 1H), 7.39 (s, 1H), 7.11 – 7.01 (m, 2H), 6.77 (s, 1H), 3.19 – 2.92 (m, 4H), 2.81 – 2.56 (m, 2H), 2.41 – 2.25 (m, 2H), 1.85 – 1.69 (m, 2H), 1.67 – 1.43 (m, 2H).

^{13}C NMR (101 MHz, pyridine-d_5) δ 169.1, 133.5, 130.8, 130.3, 126.4, 115.4, 106.2, 103.5, 50.7, 50.24, 27.9, 21.5, 20.7, 20.6 (not all quarternary carbon nuclei were detected).

HRMS (ESI) m/z: 436.1656 (calcd. for $C_{27}H_{22}N_3O_3$, $[M+H]^+$), 436.1656 (found).

N-Cyanorhodamine 13c

In a 10 mL reaction tube, Cs_2CO_3 (6 equiv., 0.14 mmol, 47 mg) was dried under vacuum. Triflate **15c**[117] (1 equiv., 0.023 mmol, 11 mg), cyanamide (2.6 equiv., 0.058 mmol, 2.5 mg), $Pd_2(dba)_3$ (30 mol%, 0.007 mmol, 6.4 mg), and Xantphos (60 mol%, 0.014 mmol, 8.2 mg) were added, and the tube was evacuated and backfilled with argon (3 cycles). Dioxane (0.50 mL) was added and the resulting mixture was stirred at 100 °C for 2 h. The crude product was purified by flash column chromatography (12 g Puriflash 30 µm, 0 % to 100 % A/B, A = CH_2Cl_2 + 20 % EtOH + 0.5 % HOAc, B = CH_2Cl_2 + 0.5 % HOAc) and further purified by preparative HPLC (Interchim PhenC4 250x21.2 mm 5 µm, gradient 35/65 to 65/35 A:B, A = MeCN + 0.1 % formic acid, B = H_2O + 0.1 % formic acid).

N-Cyanorhodamine **13b** was obtained as 3.2 mg violet powder in 35 % yield.

^{1}H NMR (400 MHz, pyridine-d_5): δ 8.32 (d, *J* = 7.6 Hz, 1H), 7.71 (td, *J* = 7.5, 1.3 Hz, 1H), 7.65 (td, *J* = 7.5, 1.2 Hz, 1H), 7.36 (d, *J* = 7.7 Hz, 1H), 6.95 – 6.86 (m, 3H), 6.31 (d, *J* = 2.3 Hz, 1H), 6.18 (dd, *J* = 8.7, 2.3 Hz, 1H), 3.77 (t, *J* = 7.3 Hz, 4H), 2.10 (p, *J* = 7.3 Hz, 2H).

^{13}C NMR (101 MHz, pyridine-d_5): δ 135.8, 134.4, 130.0, 129.9, 129.5, 126.6, 123.8, 109.0, 103.3, 97.1, 51.8, 16.4 (obtained by indirect detection from gHSQC NMR experiment, only proton-coupled carbon nuclei are resolved).

HRMS (ESI) m/z: 396.1343 (calcd. for $C_{24}H_{18}N_3O_3$, $[M+H]^+$), 396.1340 (found).

7.1.3 Preparation of *N,N'*-bis(methylsulfonyl)rhodamine 17 by Buchwald-Hartwig amination

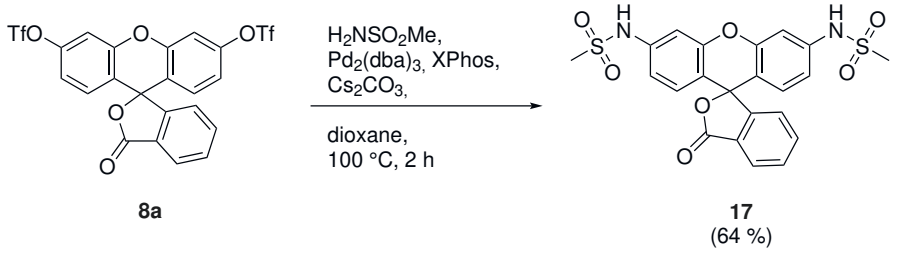

8a → **17** (64 %)

***N,N'*-bis(methylsulfonyl)rhodamine 17**

In a 10 mL reaction tube, Cs_2CO_3 (4.0 equiv., 0.396 mmol, 129 mg) was dried under vacuum. Triflate **8a** (1.0 equiv., 0.100 mmol, 59.6 mg), methanesulfonamide (4.2 equiv., 0.421 mmol, 37.0 mg), $Pd_2(dba)_3$ (10 mol%, 0.011 mmol, 9.9 mg), and XPhos (20 mol%, 0.022 mmol, 10.4 mg) were added, and the tube was evacuated and backfilled with argon (3 cycles). Dioxane (1.0 mL) was added and the resulting mixture was stirred at 100 °C for 2 h. The crude product was purified by flash column chromatography (12 g Puriflash 30 µm, 50 % to 100 % EtOAc/hexane), and further purified by preparative HPLC (HypersilGoldC18 250x21.2 mm 5 µm, gradient 35/65 to 65/35 A:B, A = MeCN + 0.1 % formic acid, B = H_2O + 0.1 % formic acid).

N,N'-Bis(methylsulfonyl)rhodamine **17** was obtained as 33.3 mg pinkish powder (containing 23 mol% dioxane as remainder) in 64 % yield.

^{1}H NMR (400 MHz, DMSO-d_6) δ 10.25 (br s, 2H), 8.03 (dt, *J* = 7.5, 1.1 Hz, 1H), 7.80 (td, *J* = 7.5, 1.2 Hz, 1H), 7.74 (td, *J* = 7.4, 1.1 Hz, 1H), 7.31 (dt, *J* = 7.7, 1.0 Hz, 1H), 7.19 (d, *J* = 2.2 Hz, 2H), 6.94 (dd, *J* = 8.6, 2.2 Hz, 2H), 6.77 (d, *J* = 8.6 Hz, 2H), 3.11 (s, 6H).

^{13}C NMR (101 MHz, DMSO-d_6) δ 168.6, 152.4, 151.1, 141.0, 135.9, 130.4, 129.3, 125.7, 124.9, 124.1, 114.9, 113.3, 105.6, 81.6, 39.8.

HRMS (ESI) m/z: 487.0628 (calcd. for $C_{22}H_{19}N_2O_7S_2$, $[M+H]^+$), 487.0625 (found).

7.1.4 Preparation of *N*-cyanorhodamines 13, 14 and 18 by Ullmann coupling

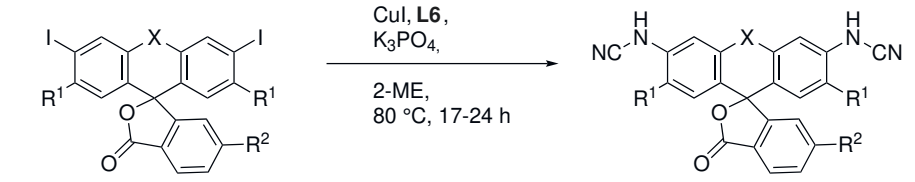

10a (X = O, R^1 = H, R^2 = H)
10c (X = O, R^1 = Me, R^2 = H)
10d (X = CMe_2, R^1 = H, R^2 = H)
10f (X = O, R^1 = H, R^2 = COOH)

14a (X = O, R^1 = H, R^2 = H, 49 %)
14c (X = O, R^1 = Me, R^2 = H, 49 %)
14d (X = CMe_2, R^1 = H, R^2 = H, 81 %)
NCR1 (X = O, R^1 = H, R^2 = COOH, 72 %)

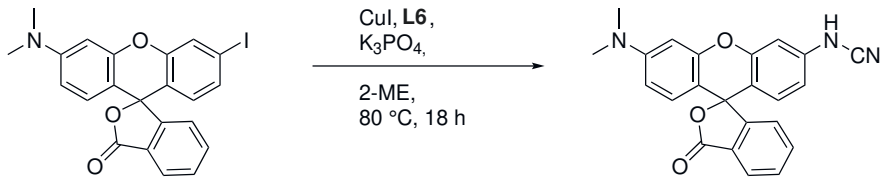

16a → **13a** (57 %)

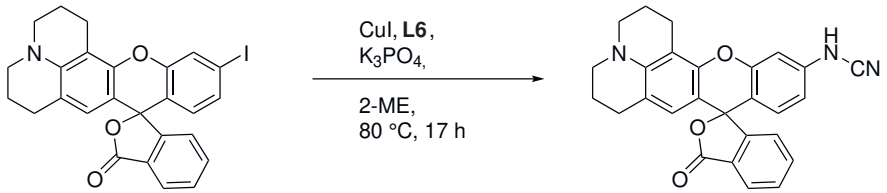

16b → **13b** (51 %)

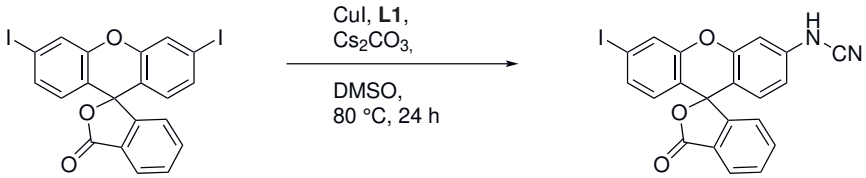

10a → **18** (34 %)

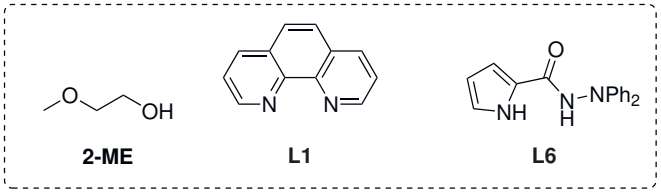

N,N'-Dicyanorhodamine 14a

In a 10 mL reaction tube, K_3PO_4 (6 equiv., 0.62 mmol, 131 mg) was dried under vacuum. Iodide **10a** (1 equiv., 0.10 mmol, 55 mg), cyanamide (4 equiv., 0.40 mmol, 17 mg), CuI (30 mol%, 0.03 mmol, 5.2 mg), and **L6** (30 mol%,

0.03 mmol, 7.2 mg) were added, and the tube was evacuated and backfilled with argon (3 cycles). 2-ME (1.0 mL) was added and the resulting mixture was stirred at 80 °C for 17 h. After cooling down, it was diluted with water (20 mL), acidifed with HOAc to pH 4, and extracted with EtOAc (5x 10 mL). The combined organic phases were washed with brine (20 mL), dried with anhydrous Na_2SO_4, filtered, and evaporated. The crude product was purified by flash column chromatography (12 g Puriflash 30 µm, 20 % to 80 % A/B, A = hexane + 0.5 % HOAc, B = EtOAc + 0.5 % HOAc) and further purified by preparative HPLC (Interchim PhenC4 250x21.2 mm 5 µm, gradient 30/70 to 60/40 A:B, A = MeCN + 0.1 % formic acid, B = H_2O + 0.1 % formic acid).

N,N'-Dicyanorhodamine **14a** was obtained as 19.0 mg pink powder in 49 % yield.

^{1}H NMR (400 MHz, DMSO-d_6): δ 10.66 (br s, 2H), 8.03 (dt, *J* = 7.5, 1.0 Hz, 1H), 7.81 (td, *J* = 7.5, 1.2 Hz, 1H), 7.74 (td, *J* = 7.5, 1.1 Hz, 1H), 7.30 (dt, *J* = 7.7, 1.0 Hz, 1H), 6.89 (d, *J* = 2.2 Hz, 2H), 6.80 (d, *J* = 8.6 Hz, 2H), 6.76 (dd, *J* = 8.6, 2.2 Hz, 2H).

^{13}C NMR (101 MHz, DMSO-d_6): δ 168.6, 152.3, 151.3, 141.4, 135.9, 130.4, 130.0, 125.6, 124.9, 124.0, 112.9, 111.9, 111.2, 102.4, 81.5.

HRMS (ESI) m/z: 381.0982 (calcd. for $C_{22}H_{13}N_4O_3$, $[M+H]^+$), 381.0980 (found).

N,N'-Dicyanorhodamine 14c

In a 10 mL reaction tube, K_3PO_4 (6 equiv., 0.62 mmol, 132 mg) was dried under vacuum. Iodide **10c**[121] (1 equiv., 0.10 mmol, 59 mg), cyanamide (4 equiv., 0.40 mmol, 18 mg), CuI (30 mol%, 0.03 mmol, 5 mg), and **L6** (30 mol%, 0.03 mmol, 7 mg) were added, and the tube was evacuated and backfilled with argon (3 cycles). 2-ME (1.0 mL) was added and the resulting mixture was stirred at 80 °C for 22 h. After cooling down, it was diluted with water, acidifed with HOAc to pH 4, and extracted with EtOAc (3x 10 mL). The combined organic phases were washed with brine (10 mL), dried with anhydrous Na_2SO_4, filtered, and evaporated. The crude product was purified by flash column chromatography (12 g Puriflash 30 µm, 20 % to 100 % A/B, A = hexane + 0.5 % HOAc, B = EtOAc + 0.5 % HOAc) and further purified by preparative HPLC (Interchim PhenC4 250x21.2 mm 5 µm, gradient 40/60 to 80/20 A:B, A = MeCN + 0.1 % formic acid, B = H_2O + 0.1 % formic acid).

N,N'-Dicyanorhodamine **14c** was obtained as 21.9 mg pink powder (containing 26 mol% dioxane as remainder) in 49 % yield.

^{1}H NMR (400 MHz, DMSO-d_6): δ 9.75 (s, 2H), 8.02 (dt, *J* = 7.4, 1.1 Hz, 1H), 7.82 –

7.67 (m, 2H), 7.29 – 7.20 (m, 1H), 6.94 (s, 2H), 6.60 (s, 2H), 2.03 (s, 6H).

^{13}C NMR (101 MHz, DMSO-d_6): δ 168.7, 152.6, 149.5, 139.5, 135.8, 130.3, 129.9, 125.5, 125.0, 123.9, 121.5, 112.7, 111.8, 102.4, 81.4, 16.5.

HRMS (ESI) m/z: 409.1295 (calcd. for $C_{24}H_{17}N_4O_3$, $[M+H]^+$), 409.1293 (found).

N,N'-Dicyanorhodamine 14d

In a 10 mL reaction tube, K_3PO_4 (6 equiv., 0.30 mmol, 65 mg) was dried under vacuum. Iodide **10d** (1 equiv., 0.054 mmol, 31 mg), cyanamide (4.4 equiv., 0.24 mmol, 10 mg), CuI (50 mol%, 0.028 mmol, 5.4 mg), and **L6** (60 mol%, 0.034 mmol, 7.6 mg) were added, and the tube was evacuated and backfilled with argon (3 cycles). 2-ME (1.0 mL) was added and the resulting mixture was stirred at 80 °C for 22 h. After cooling down, it was diluted with EtOAc, acidified with HOAc to pH 4, and evaporated on Celite. The product was isolated by flash column chromatography (12 g Puriflash 30 µm, 20 % to 80 % A/B, A = hexane + 0.5 % HOAc, B = EtOAc + 0.5 % HOAc) and further purified by preparative HPLC (Interchim PhenC4 250x21.2 mm 5 µm, gradient 35/65 to 65/35 A:B, A = MeCN + 0.1 % formic acid, B = H_2O + 0.1 % formic acid).

N,N'-Dicyanorhodamine **14d** was obtained as 18.9 mg pinkish powder (containing 25 mol% dioxane as remainder) in 81 % yield.

^{1}H NMR (400 MHz, DMSO-d_6): δ 10.38 (br s, 2H), 8.06 – 7.99 (m, 1H), 7.71 (dtd, J = 20.6, 7.3, 1.2 Hz, 2H), 7.24 (d, J = 2.4 Hz, 2H), 7.11 – 7.06 (m, 1H), 6.85 (dd, J = 8.6, 2.4 Hz, 2H), 6.71 (d, J = 8.6 Hz, 2H), 1.79 (s, 3H), 1.68 (s, 3H).

^{13}C NMR (101 MHz, DMSO-d_6): δ 169.6, 154.6, 146.0, 139.7, 135.7, 129.9, 129.4, 125.2, 125.1, 125.0, 123.6, 114.6, 112.3, 111.7, 84.9, 37.8, 34.3, 33.0.

HRMS (ESI) m/z: 407.1503 (calcd. for $C_{25}H_{19}N_4O_2$, $[M+H]^+$), 407.1503 (found).

N,N'-Dicyanorhodamine NCR1

In a 10 mL reaction tube, K_3PO_4 (16 equiv., 0.32 mmol, 67 mg) was dried under vacuum. Iodide **10f** (1 equiv., 0.02 mmol, 10.3 mg), cyanamide (11 equiv., 0.22 mmol, 9.1 mg), CuI (100 %, 0.02 mmol, 3.6 mg), and **L6** (100 %, 0.02 mmol, 4.5 mg) were added, and the tube was evacuated and backfilled with argon (3 cycles). 2-ME (1.0 mL) was added and the resulting mixture was stirred at 80 °C for 22 h. After cooling down,

it was diluted with EtOAc, acidified with HOAc to pH 4, and evaporated on Celite. The product was isolated by flash column chromatography (12 g Puriflash 30 µm, 0 % to 100 % A/B, A = CH_2Cl_2 + 20 % EtOH + 0.5 % formic acid, B = CH_2Cl_2 + 0.5 % formic acid) and further purified by preparative HPLC (Interchim PhenC4 250x21.2 mm 5 µm, gradient 30/70 to 60/40 A:B, A = MeCN + 0.1 % formic acid, B = H_2O + 0.1 % formic acid).

N,N'-Dicyanorhodamine **NCR1** was obtained as 5.5 mg pinkish powder (containing 22 mol% dioxane as remainder) in 72 % yield.

^{1}H NMR (400 MHz, DMSO-d_6): δ 8.24 (dd, *J* = 8.0, 1.4 Hz, 1H), 8.15 (d, *J* = 8.0 Hz, 1H), 7.73 (s, 1H), 6.89 (d, *J* = 2.2 Hz, 2H), 6.85 (d, *J* = 8.6 Hz, 2H), 6.75 (dd, *J* = 8.6, 2.4 Hz, 2H).

^{13}C NMR (101 MHz, DMSO-d_6): δ 167.3, 166.0, 153.1, 151.4, 141.5, 137.3, 131.2, 130.1, 128.8, 125.5, 124.6, 112.3, 111.9, 111.2, 102.5, 81.9.

HRMS (ESI) m/z: 425.0880 (calcd. for $C_{23}H_{13}N_4O_5$, $[M+H]^+$), 425.0875 (found).

N-Cyanorhodamine 13a

In a 10 mL reaction tube, K_3PO_4 (3 equiv., 0.30 mmol, 63 mg) was dried under vacuum. Iodide **16a** (1 equiv., 0.10 mmol, 48 mg), cyanamide (2 equiv., 0.21 mmol, 9 mg), CuI (50 mol%, 0.05 mmol, 9.4 mg), and **L6** (50 mol%, 0.05 mmol, 13 mg) were added, and the tube was evacuated and backfilled with argon (3 cycles). 2-ME (1.0 mL) was added and the resulting mixture was stirred at 80 °C for 18 h. After cooling down, it was diluted with water (10 mL), acidified with HOAc to pH 4, and extracted with EtOAc (2x 20 mL). The combined organic phases were washed with brine (20 mL), dried with anhydrous Na_2SO_4, filtered, and evaporated. The product was purified by flash column chromatography (12 g Puriflash 30 µm, 20 % to 80 % A/B, A = hexane + 0.5 % HOAc, B = EtOAc + 0.5 % HOAc) and further purified by preparative HPLC (Interchim PhenC4 250x21.2 mm 5 µm, gradient 30/70 to 60/40 A:B, A = MeCN + 0.1 % formic acid, B = H_2O + 0.1 % formic acid).

N-Cyanorhodamine **13a** was obtained as 22.3 mg dark-red powder in 57 % yield.

The analytical data correspond to the data obtained from **13a** prepared by Buchwald-Hartwig amination (p. 102)

N-Cyanorhodamine 13b

In a 10 mL reaction tube, K_3PO_4 (36 equiv., 0.64 mmol, 137 mg) was dried under vacuum. Iodide **16b**[121] (1 equiv., 0.018 mmol, 9.3 mg), cyanamide (32 equiv., 0.57 mmol, 24 mg), CuI (100 mol%, 0.017 mmol, 3.2 mg), and **L6** (100 mol%, 0.017 mmol, 3.8 mg) were added, and the tube was evacuated and backfilled with argon (3 cycles). 2-ME (1.0 mL) was added and the resulting mixture was stirred at 80 °C for 17 h. After cooling down, it was diluted with CH_2Cl_2 , acidified with HOAc to pH 4, and evaporated on Celite. The product was isolated by flash column chromatography (12 g Puriflash 30 µm, 0 % to 100 % A/B, A = CH_2Cl_2 + 20 % EtOH + 0.5 % formic acid, B = CH_2Cl_2 + 0.5 % formic acid).

N-Cyanorhodamine **13b** was obtained as 4.0 mg violet powder in 51 % yield.

The analytical data correspond to the data obtained from **13b** prepared by Buchwald-Hartwig amination (p. 103)

Cyanamide 18

In a 10 mL reaction tube, K_3PO_4 (6 equiv., 0.60 mmol, 196 mg) was dried under vacuum. Iodide **10a** (1 equiv., 0.10 mmol, 55 mg), cyanamide (4 equiv., 0.42 mmol, 18 mg), CuI (25 mol%, 0.025 mmol, 4.6 mg), and **L1** (50 mol%, 0.055 mmol, 9.8 mg) were added, and the tube was evacuated and backfilled with argon (3 cycles). DMSO (1.0 mL) was added and the resulting mixture was stirred at 80 °C for 24 h. After cooling down, it was diluted with EtOH, acidified with HOAc to pH 4, and evaporated. The product was isolated by flash column chromatography (25 g Puriflash 30 µm, 0 % to 100 % A/B, A = hexane + 0.5 % HOAc, B = EtOAc + 0.5 % HOAc).

Cyanamide **18** was obtained as 16.3 mg pink powder (containing 18 mol% dioxane as remainder) in 34 % yield.

^{1}H NMR (400 MHz, DMSO-d_6): δ 8.04 (dt, *J* = 7.5, 1.1 Hz, 1H), 7.84 (d, *J* = 1.7 Hz, 1H), 7.81 (td, *J* = 7.5, 1.3 Hz, 1H), 7.74 (td, *J* = 7.4, 1.1 Hz, 1H), 7.48 (dd, *J* = 8.3, 1.7 Hz, 1H), 7.33 (dt, *J* = 7.7, 1.0 Hz, 1H), 6.86 (d, *J* = 2.3 Hz, 1H), 6.82 (d, *J* = 8.6 Hz, 1H), 6.77 (dd, *J* = 8.6, 2.2 Hz, 1H), 6.59 (d, *J* = 8.3 Hz, 1H).

^{13}C NMR (101 MHz, DMSO): δ 168.5, 152.2, 151.0, 150.7, 141.7, 136.0, 133.2, 130.5, 130.0, 129.6, 125.6, 125.4, 125.0, 124.0, 118.6, 112.4, 112.1, 111.3, 102.4, 96.8, 81.1.

HRMS (ESI) m/z: 466.9887 (calcd. for $C_{21}H_{12}IN_2O_3$, $[M+H]^+$), 466.9883 (found).

7.1.5 Preparation of tetrazole 21 and cyanamide 22

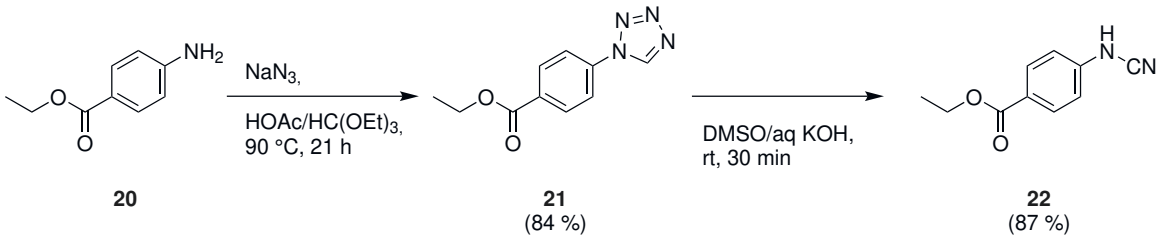

20 **21** (84 %) **22** (87 %)

Tetrazole 21

Following an adapted procedure,[143] $H(OEt)_3$ (2.0 mL) was added to a mixture of amine **20** (1.0 equiv., 1.00 mmol, 160 mg) and NaN_3 (1.2 equiv., 1.20 mmol, 78.2 mg) in HOAc (8.0 mL). The resulting mixture was stirred at 90 °C for 21 h and the product was isolated by flash column chromatography (25 g Puriflash 30 µm, 20 % to 80 % EtOAc/hexane).

Tetrazole **21** was obtained as 184 mg off-white powder in 84 % yield.

^{1}H NMR (400 MHz, $CDCl_3$) δ 9.09 (s, 1H), 8.31 – 8.23 (m, 2H), 7.87 – 7.80 (m, 2H), 4.43 (q, J = 7.1 Hz, 2H), 1.43 (t, J = 7.1 Hz, 3H).

The analytical data correspond to the literature.[167]

Cyanamide 22

To a mixture of tetrazole **21** (1.0 equiv., 0.192 mmol, 42.0 mg) in DMSO (1.0 mL), 1 M aq. KOH (0.20 mL) was added. The resulting mixture was stirred at ambient temperature for 30 min. Next, the mixture was diluted in water (5 mL), adjusted with 1 M aq. HCl to pH 2, and extracted with EtOAc (3x 5 mL). The combined organic layer were washed with water/brine (10 mL, 1:1), and brine (10 mL), dried with anhydrous Na_2SO_4, filtered, and evaporated. The crude product was purified by flash column chromatography (12 g Puriflash 30 µm, 20 % to 80 % A/B, A = hexane + 0.5 % HOAc, B = EtOAc + 0.5 % HOAc).

Cyanamide **22** was obtained as 31.7 mg off-white powder in 87 % yield.

^{1}H NMR (400 MHz, DMSO-d_6) δ 10.72 (s, 1H), 7.97 – 7.92 (m, 2H), 7.09 – 7.04 (m, 2H), 4.28 (q, J = 7.1 Hz, 2H), 1.30 (t, J = 7.1 Hz, 3H).

The analytical data correspond to the literature.[168]

7.1.6 Preparation of tetrazoles 26 and *N*-cyanorhodamines NCR1, NCR2 and NCR3

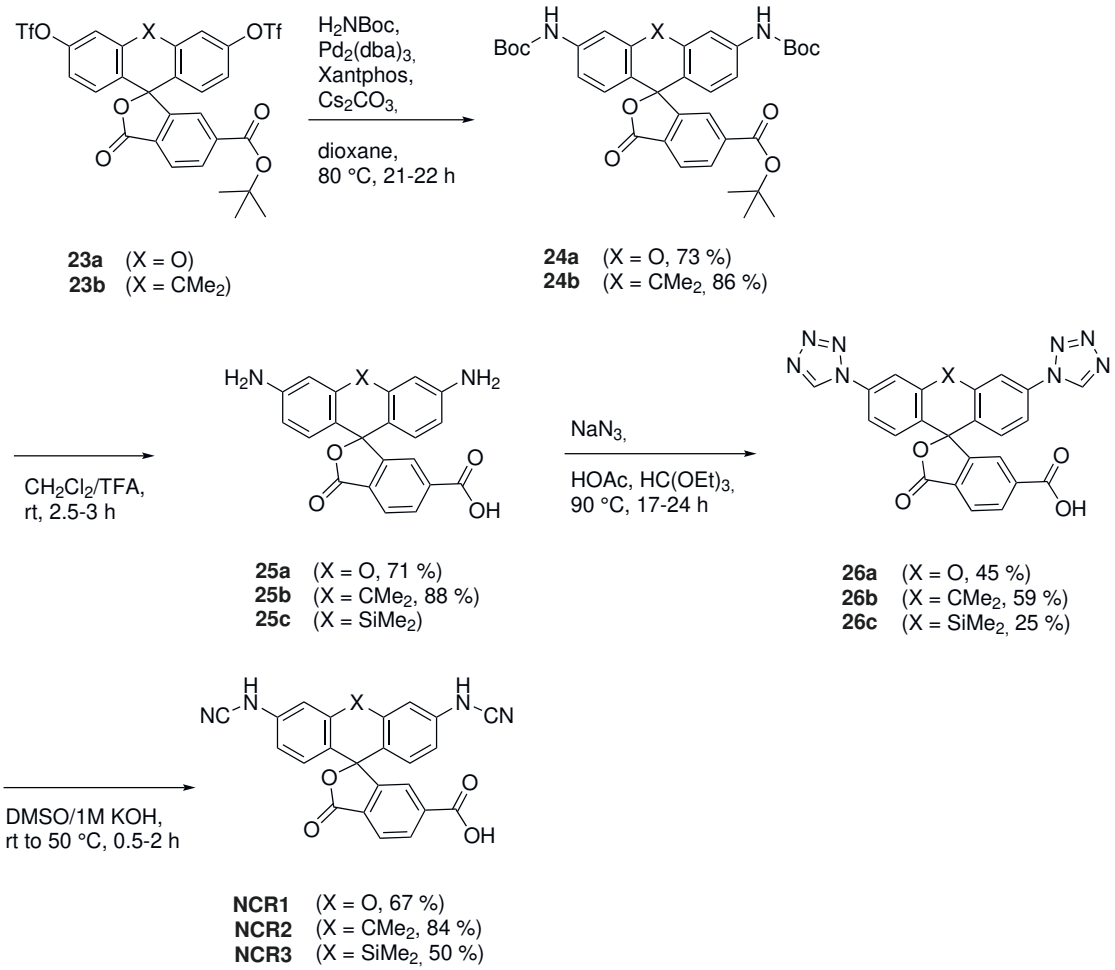

Boc-amide 24a and rhodamine 25a

In a 25 mL round-bottom flask, Cs_2CO_3 (3.9 equiv., 1.06 mmol, 344 mg) was dried under vacuum. Triflate **23a**[117] (1.0 equiv., 0.27 mmol, 214 mg), $BocNH_2$ (2.6 equiv., 0.71 mmol, 83 mg), $Pd_2(dba)_3$ (10 mol%, 0.03 mmol, 27.5 mg), and Xantphos (15 mol%, 0.045 mmol, 26 mg) were added, and the tube was evacuated and backfilled with argon (3 cycles). Dioxane (5.0 mL) was added and the resulting mixture was stirred at 80 °C

for 21 h. After cooling down, it was diluted with water (20 mL), and extracted with EtOAc (3x 10 mL). The combined organic phases were washed with brine (20 mL), dried with anhydrous Na_2SO_4, filtered, and evaporated. The crude product was purified by flash column chromatography (25 g Puriflash 30 µm, 0 % to 40 % EtOAc/hexane).

Crude Boc-amide **24a** was obtained as 139 mg beige-colored powder (containing 28 mol% $BocNH_2$ as remainder) in 73 % yield and used without further purification.

^{1}H NMR (400 MHz, $CDCl_3$): δ 8.22 (dd, *J* = 8.0, 1.3 Hz, 1H), 8.04 (dd, *J* = 8.0, 0.8 Hz, 1H), 7.66 (dd, *J* = 1.4, 0.8 Hz, 1H), 7.47 (d, *J* = 2.2 Hz, 2H), 6.92 (dd, *J* = 8.6, 2.2 Hz, 2H), 6.66 (d, *J* = 8.6 Hz, 2H), 6.60 (s, 2H), 1.54 (s, 9H), 1.52 (s, 18H).

Crude Boc-amide **24a** (111 mg) was dissolved in CH_2Cl_2 (5.0 mL). TFA (1.0 mL) was added and the resulting mixture was stirred at ambient temperature for 3.5 h. Next, the mixture was diluted and evaporated to dryness from toluene (3 cycles) and CH_2Cl_2 (3 cycles) and lyophilized from aqueous dioxane.

Rhodamine **25a** was obtained as 97.5 mg red powder (TFA salt) (containing 46 mol% dioxane as remainder) in 71 % yield.

^{1}H NMR (400 MHz, DMSO-d_6 + 1 % TFA-d): δ 8.32 (dd, *J* = 8.2, 0.7 Hz, 1H), 8.28 (dd, *J* = 8.2, 1.6 Hz, 1H), 7.90 (dd, *J* = 1.6, 0.7 Hz, 1H), 7.02 (d, *J* = 9.1 Hz, 2H), 6.83 (dd, *J* = 9.1, 2.1 Hz, 2H), 6.79 (d, *J* = 2.1 Hz, 2H).

^{13}C NMR (101 MHz, DMSO-d_6 + 1 % TFA-d): δ 166.0, 165.7, 159.3, 158.4, 157.5, 134.5, 134.2, 133.6, 131.8, 131.4, 130.8, 130.8, 116.9, 113.1, 97.0.

HRMS (ESI) m/z: 375.0975 (calcd. for $C_{21}H_{15}N_2O_5$, $[M+H]^+$), 375.0974 (found).

Boc-amide 24b and rhodamine 25b

In a 25 mL round-bottom flask, Cs_2CO_3 (4.0 equiv., 0.78 mmol, 259 mg) was dried under vacuum. Triflate **23b**[96] (1.0 equiv., 0.20 mmol, 143 mg), $BocNH_2$ (3.0 equiv., 0.60 mmol, 70 mg), $Pd_2(dba)_3$ (10 mol%, 0.02 mmol, 18 mg), and Xantphos (30 mol%, 0.061 mmol, 35 mg) were added, and the flask was evacuated and backfilled with argon (3 cycles). Dioxane (2.0 mL) was added and the resulting mixture was stirred at 80 °C for 21 h. After cooling down, it was diluted with water (10 mL) and sat. aq. NH_4Cl (10 mL), and extracted with EtOAc (3x 20 mL). The combined organic phases were washed with brine (30 mL), dried with anhydrous Na_2SO_4, filtered, and evaporated. The crude product was purified by flash column chromatography (25 g Puriflash 30 µm,

0 % to 60 % EtOAc/hexane).

Crude Boc-amide **24b** was obtained as 127 mg beige-colored powder (containing 36 mol% $BocNH_2$ and 10 mol% dioxane as remainder) in 86 % yield and used without further purification.

^{1}H NMR (400 MHz, $CDCl_3$): δ 8.16 (dd, *J* = 8.0, 1.3 Hz, 1H), 8.03 (dd, *J* = 8.0, 0.8 Hz, 1H), 7.83 – 7.70 (m, 2H), 7.54 – 7.49 (m, 1H), 7.03 (dd, *J* = 8.6, 2.3 Hz, 2H), 6.67 (d, *J* = 8.6 Hz, 2H), 6.63 (s, 2H), 1.87 (s, 3H), 1.76 (s, 3H), 1.52 (s, 27H).

^{13}C NMR (101 MHz, $CDCl_3$): δ 170.0, 164.2, 155.6, 152.7, 146.3, 139.4, 138.2, 130.5, 129.2, 128.6, 125.3, 125.2, 124.7, 117.6, 116.2, 86.4, 82.6, 81.0, 38.5, 34.8, 33.7, 28.5, 28.1.

HRMS (ESI) m/z: 657.3170 (calcd. for $C_{38}H_{45}N_2O_8$, $[M+H]^+$), 657.3169 (found).

Crude Boc-amide **24b** (116 mg) was dissolved in CH_2Cl_2 (2.0 mL). TFA (0.4 mL) was added and the resulting mixture was stirred at ambient temperature for 3 h. Next, the mixture was diluted and evaporated to dryness from toluene (3 cycles) and CH_2Cl_2 (3 cycles) and lyophilized from aqueous dioxane.

Rhodamine **25b** was obtained as 124 mg red powder (TFA salt) in 88 % yield.

For photophysical characterization, 22.3 mg of rhodamine **25b** were further purified by preparative HPLC (Interchim PhenC4 250x21.2 mm 5 µm, gradient 10/90 to 50/50 A:B, A = MeCN + 0.1 % formic acid, B = H_2O + 0.1 % formic acid) to obtain rhodamine **25b** as 13.7 mg violet powder (containing 64 mol% dioxane as remainder).

^{1}H NMR (400 MHz, CD_3OD): δ 8.35 (dd, *J* = 8.2, 0.7 Hz, 1H), 8.32 (dd, *J* = 8.2, 1.5 Hz, 1H), 7.87 (dd, *J* = 1.6, 0.7 Hz, 1H), 7.17 (d, *J* = 2.2 Hz, 2H), 6.92 (d, *J* = 9.0 Hz, 2H), 6.61 (dd, *J* = 9.0, 2.2 Hz, 2H), 1.80 (s, 3H), 1.69 (s, 3H).

^{13}C NMR (101 MHz, CD_3OD): δ 167.9, 167.6, 159.8, 159.0, 139.4, 138.8, 136.0, 135.5, 132.4, 132.1, 131.6, 122.1, 119.0, 116.1, 114.0, 42.4, 35.1, 31.8.

HRMS (ESI) m/z: 401.1496 (calcd. for $C_{24}H_{21}N_2O_4$, $[M+H]^+$), 401.1494 (found).

Tetrazole 26a

$H(OEt)_3$ (0.2 mL) was added to a mixture of rhodamine **25a** (1.0 equiv., 0.082 mmol, 40 mg, TFA salt) and NaN_3 (3.2 equiv., 0.26 mmol, 17 mg) in HOAc (0.8 mL). The re-

sulting mixture was stirred at 90 °C for 24 h and the product was purified by preparative HPLC (Interchim PhenC4 250x21.2 mm 5 µm, gradient 35/65 to 65/35 A:B, A = MeCN + 0.1 % formic acid, B = H_2O + 0.1 % formic acid).

Tetrazole **26a** was obtained as 15.6 mg pink powder in 45 % yield.

^{1}H NMR (400 MHz, DMSO-d_6 + 1 % TFA-d): δ 10.2 (s, 2H), 8.30 (dd, *J* = 8.0, 1.3 Hz, 1H), 8.23 (dd, *J* = 8.0, 0.8 Hz, 1H), 8.13 (d, *J* = 2.2 Hz, 2H), 7.93 (dd, *J* = 1.3, 0.8 Hz, 1H), 7.75 (dd, *J* = 8.6, 2.2 Hz, 2H), 7.30 (d, *J* = 8.6 Hz, 2H).

^{13}C NMR (101 MHz, DMSO-d_6 + 1 % TFA-d): δ 167.6, 165.9, 152.4, 150.8, 142.7, 137.8, 135.6, 131.6, 130.5, 128.6, 126.0, 124.8, 119.0, 117.2, 109.7, 80.4.

HRMS (ESI) m/z: 481.1003 (calcd. for $C_{23}H_{13}N_8O_5$, $[M+H]^+$), 481.1003 (found).

Tetrazole 26b

$H(OEt)_3$ (0.15 mL) was added to a mixture of rhodamine **25b** (1.0 equiv., 0.066 mmol, 26 mg, TFA salt) and NaN_3 (5.7 equiv., 0.37 mmol, 24 mg) in HOAc (1 mL). The resulting mixture was stirred at 90 °C for 20 h and the product was purified by preparative HPLC (Interchim PhenC4 250x21.2 mm 5 µm, gradient 35/65 to 65/35 A:B, A = MeCN + 0.1 % formic acid, B = H_2O + 0.1 % formic acid).

Tetrazole **26b** was obtained as 19.9 mg off-white powder in 59 % yield.

^{1}H NMR (400 MHz, DMSO-d_6): δ 13.7 (br s, 1H, CO2H), 10.22 (s, 2H), 8.44 (d, *J* = 2.3 Hz, 2H), 8.24 (s, 1H), 7.80 (dd, *J* = 8.7, 2.2 Hz, 2H), 7.54 – 7.52 (m, 1H), 7.16 (d, *J* = 8.7 Hz, 2H), 2.04 (s, 3H), 1.93 (s, 3H).

^{13}C NMR (101 MHz, DMSO-d_6): δ 168.6, 165.8, 154.5, 146.1, 142.6, 137.8, 134.8, 131.1, 131.0, 129.6, 127.8, 126.3, 123.6, 120.4, 120.0, 83.8, 38.6, 33.7.

HRMS (ESI) m/z: 507.1524 (calcd. for $C_{26}H_{19}N_8O_4$, $[M+H]^+$), 507.1522 (found).

Tetrazole 26c

$H(OEt)_3$ (0.2 mL) was added to a mixture of rhodamine **25c** (1.0 equiv., 0.066 mmol, 34 mg) and NaN_3 (2.5 equiv., 0.20 mmol, 13 mg) in HOAc (0.8 mL). The resulting mixture was stirred at 90 °C for 21 h and the product was purified by preparative HPLC (Interchim PhenC4 250x21.2 mm 5 µm, gradient 40/60 to 70/30 A:B, A = MeCN +

0.1 % formic acid, B = H_2O + 0.1 % formic acid).

Tetrazole **26c** was obtained as 10.6 mg pink powder in 25 % yield.

^{1}H NMR (400 MHz, DMSO-d_6): δ 13.7 (br s, 1H, CO_2H), 10.16 (s, 2H), 8.46 (d, *J* = 2.5 Hz, 2H), 8.18 (s, 1H), 8.17 (s, 1H), 7.96 (dd, *J* = 8.7, 2.5 Hz, 2H), 7.82 (t, *J* = 1.0 Hz, 1H), 7.46 (d, *J* = 8.8 Hz, 2H), 0.88 (s, 3H), 0.75 (s, 3H).

^{13}C NMR (101 MHz, DMSO-d_6): δ 168.8, 165.7, 154.0, 144.2, 142.5, 137.6, 136.2, 133.6, 130.9, 127.9, 127.0, 126.8, 126.3, 123.7, 123.5, 88.0, -0.6, -0.7.

HRMS (ESI) m/z: 523.1293 (calcd. for $C_{25}H_{19}N_8O_4Si$, $[M+H]^+$), 523.1292 (found).

N,N'-Dicyanorhodamine NCR1

$H(OEt)_3$ (0.2 mL) was added to a mixture of rhodamine **25a** (1.0 equiv., 0.051 mmol, 29 mg, TFA salt) and NaN_3 (4.3 equiv., 0.22 mmol, 14 mg) in HOAc (0.8 mL) and the resulting mixture was stirred at 90 °C for 17 h. After cooling down, the volatiles were removed by evaporation. The residue was re-suspended in DMSO (0.8 mL) and 1 M aq. KOH (1.60 mL) was added graduately. The resulting mixture was stirred at ambient temperature for 3 h and additionally at 50 °C for 2 h, until complete conversion of tetrazole **26a** was displayed by LCMS analysis. After cooling down, the mixture was diluted with water (10 mL), acidified with HOAc to pH 3, and extracted with EtOAc (3x 10 mL). The combined organic phases were evaporated. The product was purified by preparative HPLC (Interchim PhenC4 250x21.2 mm 5 µm, gradient 30/70 to 60/40 A:B, A = MeCN + 0.1 % formic acid, B = H_2O + 0.1 % formic acid).

N,N'-Dicyanorhodamine **NCR1** was obtained as 14.9 mg pink powder (containing 12 mol% dioxane as remainder) in 67 % yield. The analytical data correspond to the data obtained from **NCR1** prepared by Ullmann coupling (p. 108)

N,N'-Dicyanorhodamine NCR2

To a mixture of tetrazole **26b** (1.0 equiv., 0.03 mmol, 15 mg) in DMSO (0.40 mL), 1 M aq. KOH (0.10 mL) was added. The resulting mixture was stirred at ambient temperature for 2 h. Next, the mixture was diluted with water (10 mL), acidified with 1 M aq. HCl to pH 1, extracted with CH_2Cl_2 (4x 10 mL), and the combined organic phases were evaporated. The product was purified by preparative HPLC (Interchim PhenC4 250x21.2 mm 5 µm, gradient 30/70 to 60/40 A:B, A = MeCN + 0.1 % formic acid, B = H_2O + 0.1 %

formic acid).

N,N'-Dicyanorhodamine **NCR2** was obtained as 12.3 mg light-pink powder (containing 32 mol% dioxane as remainder) in 84 % yield.

^{1}H NMR (400 MHz, DMSO-d_6): δ 10.49 (br s, 2H), 8.20 (d, *J* = 8.0 Hz, 1H), 8.14 (d, *J* = 7.9 Hz, 1H), 7.46 (s, 1H), 7.25 (d, *J* = 2.4 Hz, 2H), 6.85 (dd, *J* = 8.5, 2.3 Hz, 2H), 6.75 (d, *J* = 8.6 Hz, 2H), 1.79 (s, 3H), 1.68 (s, 3H).

^{13}C NMR (101 MHz, DMSO-d_6): δ 168.8, 166.0, 154.7, 146.1, 134.0, 137.7, 130.8, 129.6, 128.5, 125.8, 124.6, 123.8, 114.8, 112.5, 111.7, 85.2, 37.9, 34.4, 33.2.

HRMS (ESI) m/z: 451.1401 (calcd. for $C_{26}H_{19}N_4O_4$, $[M+H]^+$), 451.1401 (found).

N,N'-Dicyanorhodamine NCR3

To a mixture of tetrazole **26c** (1.0 equiv., 0.009 mmol, 4.5 mg) in DMSO (0.4 mL), 1 M aq. KOH (0.1 mL) was added. The resulting mixture was stirred at ambient temperature for 35 min. Next, the mixture was diluted with water (10 mL), acidified with HOAc to pH 3, extracted with EtOAc (3x 10 mL), and the combined organic phases were evaporated. The product was purified by preparative HPLC (Interchim PhenC4 250x21.2 mm 5 µm, gradient 30/70 to 60/40 A:B, A = MeCN + 0.1 % formic acid, B = H_2O + 0.1 % formic acid).

N,N'-Dicyanorhodamine **NCR3** was obtained as 2.1 mg off-white powder (containing 11 mol% dioxane as remainder) in 50 % yield.

^{1}H NMR (400 MHz, DMSO-d_6): δ 8.14 (dd, *J* = 8.0, 1.3 Hz, 1H), 8.06 (d, *J* = 7.9 Hz, 1H), 7.73 (t, *J* = 1.0 Hz, 1H), 7.30 (d, *J* = 2.5 Hz, 2H), 6.99 (d, *J* = 8.7 Hz, 2H), 6.94 (dd, *J* = 8.7, 2.6 Hz, 2H), 0.67 (s, 3H), 0.57 (s, 3H).

^{13}C NMR (101 MHz, DMSO-d_6): δ 130.4, 128.1, 126.5, 124.2, 119.9, 117.3, -0.6, -1.2 (obtained by indirect detection from gHSQC NMR experiment, only proton-coupled carbon nuclei are resolved).

HRMS (ESI) m/z: 467.1170 (calcd. for $C_{25}H_{19}N_4O_4Si$, $[M+H]^+$), 467.1171 (found).

7.1.7 Preparation of *N*-cyanorhodamine conjugates NCR1-Halo, NCR2-Halo, NCR3-Halo and NCR1-SNAP

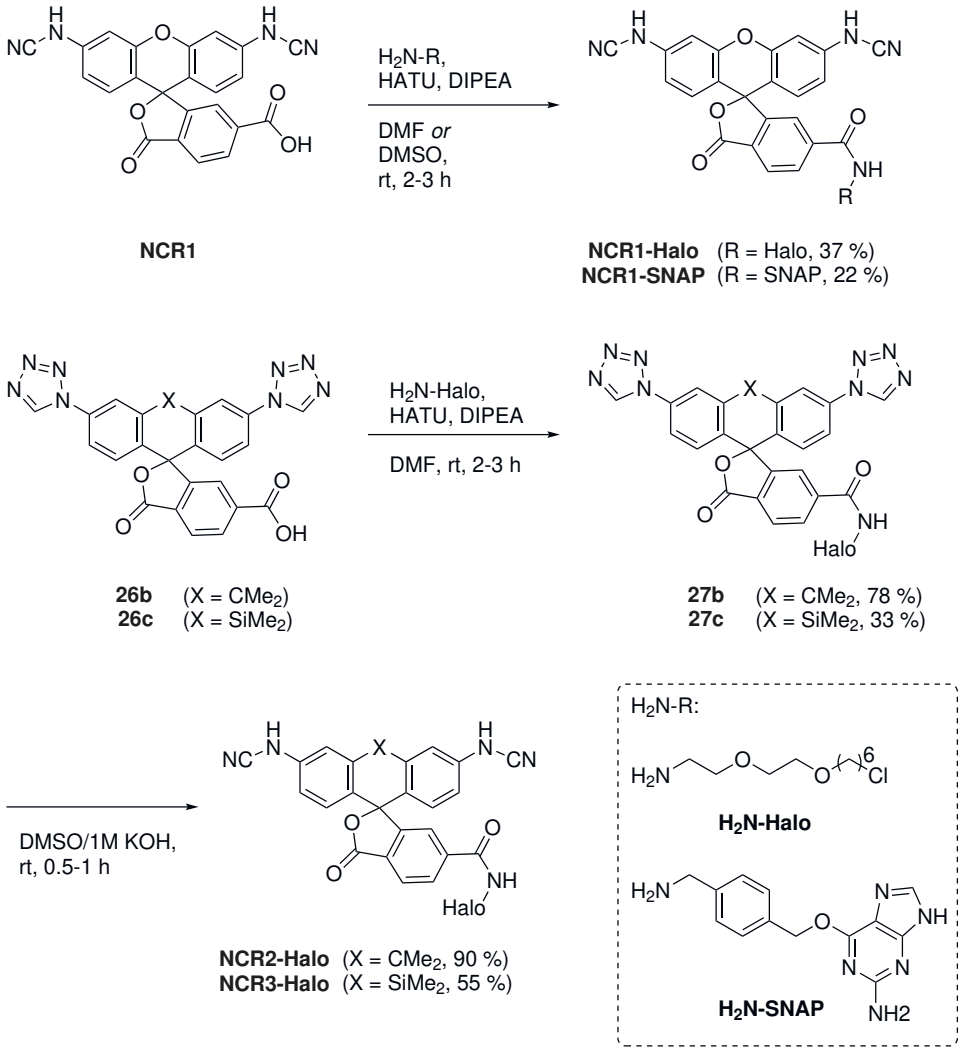

Conjugate NCR1-Halo

Carboxylic acid **NCR1** (1.0 equiv., 0.009 mmol, 3.8 mg) was suspended in DMF (40 µL) and DIPEA (40 µL). HATU in DMF (1.4 equiv., 0.012 mmol, 30 µL of 9.2 mg/100 µL stock solution in DMF) and H_2N-Halo in DMF (1.4 equiv., 0.012 mmol, 30 µL of 15.7 mg/100 µL stock solution in DMF) were added and the resulting mixture was stirred at ambient temperature for 3 h. Next, the volatiles were removed *in vacuo* and the product was isolated by preparative HPLC (Interchim PhenC4 250x21.2 mm 5 µm, gradient 45/55 to 75/25 A:B, A = MeCN + 0.1 % formic acid, B = H_2O + 0.1 % formic acid).

Conjugate **NCR1-Halo** was obtained as 2.1 mg violet powder in 37 % yield.

^{1}H NMR (400 MHz, DMSO-d_6): δ 10.69 (s, 2H), 8.73 (t, *J* = 5.5 Hz, 1H), 8.18 (dd, *J* = 8.0, 1.4 Hz, 1H), 8.12 (d, *J* = 8.0 Hz, 1H), 7.69 (s, 1H), 6.90 (d, *J* = 2.3 Hz, 2H), 6.85 (d, *J* = 8.6 Hz, 2H), 6.76 (dd, *J* = 8.6, 2.3 Hz, 2H), 3.59 (t, *J* = 6.6 Hz, 2H), 3.50 – 3.43 (m, 4H), 3.44 – 3.37 (m, 2H), 3.38 – 3.29 (m, 2H), 3.31 – 3.25 (m, 2H), 1.72 – 1.60 (m, 2H), 1.45 – 1.35 (m, 2H), 1.36 – 1.28 (m, 2H), 1.28 – 1.18 (m, 4H).

^{13}C NMR (101 MHz, DMSO-d_6): δ 130.2, 129.8, 125.3, 122.4, 112.1, 102.4, 70.1, 69.3, 69.2, 45.1, 39.3, 31.9, 28.9, 28.8, 26.2, 24.8 (obtained by indirect detection from gHSQC NMR experiment, only proton-coupled carbon nuclei are resolved).

HRMS (ESI) m/z: 630.2114 (calcd. for $C_{33}H_{33}ClN_5O_6$, $[M+H]^+$), 630.2113 (found).

Conjugate NCR1-SNAP

Carboxylic acid **NCR1** (1.0 equiv., 0.012 mmol, 5.0 mg) and H_2N-SNAP (1.5 equiv., 0.018 mmol, 4.8 mg) were suspended in DMF (70 µL) and DIPEA (40 µL). HATU in DMF (1.5 equiv., 0.018 mmol, 30 µL of 22.6 mg/100 µL stock solution in DMF) was added and the resulting mixture was stirred at ambient temperature for 2 h. Next, the volatiles were removed *in vacuo* and the product was isolated by preparative HPLC (Interchim PhenC4 250x21.2 mm 5 µm, gradient 20/80 to 60/40 A:B, A = MeCN + 0.1 % formic acid, B = H_2O + 0.1 % formic acid).

Conjugate **NCR1-SNAP** was obtained as 1.7 mg violet powder in 22 % yield.

^{1}H NMR (400 MHz, DMSO-d_6): δ 12.40 (br s, 1H), 10.68 (br s, 2H), 9.21 (t, *J* = 5.8 Hz, 1H), 8.22 (dd, *J* = 8.0, 1.4 Hz, 1H), 8.12 (d, *J* = 8.0 Hz, 1H), 7.79 (br s, 1H), 7.73 (s, 1H), 7.43 (d, *J* = 7.8 Hz, 2H), 7.28 (d, *J* = 7.8 Hz, 2H), 6.93 – 6.81 (m, 3H), 6.75 (dd, *J* = 8.6, 2.3 Hz, 2H), 6.25 (br s, 2H), 5.42 (s, 2H), 4.42 (d, *J* = 5.8 Hz, 2H).

^{13}C NMR (101 MHz, DMSO-d_6): δ 130.2, 129.8, 128.6, 127.7, 125.2, 122.4, 112.0, 102.4, 66.5, 42.6 (obtained by indirect detection from gHSQC NMR experiment, only proton-coupled carbon nuclei are resolved).

HRMS (ESI) m/z: 677.2004 (calcd. for $C_{36}H_{25}N_{10}O_5$, $[M+H]^+$), 677.2002 (found).

Tetrazole 27b

Carboxylic acid **26b** (1.0 equiv., 0.011 mmol, 5.5 mg) was suspended in DMF (40 µL) and DIPEA (40 µL). HATU in DMF (1.5 equiv., 0.016 mmol, 30 µL of 20.8 mg/100 µL

stock solution in DMF) and H_2N-Halo in DMF (1.5 equiv., 0.017 mmol, 30 µL of 12.4 mg/100 µL stock solution in DMF) were added and the resulting mixture was stirred at ambient temperature for 3 h. Next, the volatiles were removed *in vacuo* and the product was isolated by preparative HPLC (Interchim PhenC4 250x21.2 mm 5 µm, gradient 45/55 to 75/25 A:B, A = MeCN + 0.1 % formic acid, B = H_2O + 0.1 % formic acid).

Tetrazole **27b** was obtained as 5.8 mg off-white powder in 78 % yield.

^{1}H NMR (400 MHz, DMSO-d_6): δ 10.24 (s, 2H), 8.82 (t, *J* = 5.6 Hz, 1H), 8.45 (d, *J* = 2.3 Hz, 2H), 8.22 (dd, *J* = 8.1, 0.7 Hz, 1H), 8.17 (dd, *J* = 8.1, 1.3 Hz, 1H), 7.80 (dd, *J* = 8.7, 2.2 Hz, 2H), 7.49 (t, *J* = 1.0 Hz, 1H), 7.13 (d, *J* = 8.7 Hz, 2H), 3.57 (t, *J* = 6.6 Hz, 2H), 3.46 – 3.41 (m, 4H), 3.40 – 3.36 (m, 2H), 3.34 – 3.27 (m, 2H), 3.26 (t, *J* = 6.5 Hz, 2H), 2.05 (s, 3H), 1.93 (s, 3H), 1.69 – 1.58 (m, 2H), 1.41 – 1.32 (m, 2H), 1.32 – 1.25 (m, 2H), 1.25 – 1.16 (m, 2H).

^{13}C NMR (101 MHz, DMSO-d_6): δ 168.8, 164.6, 154.4, 146.2, 142.6, 141.2, 134.8, 131.1, 129.8, 129.6, 126.7, 125.9, 121.8, 120.4, 120.0, 83.7, 70.1, 69.5, 69.4, 68.6, 45.4, 38.6, 33.8, 33.6, 32.0, 29.0, 26.1, 24.9.

HRMS (ESI) m/z: 712.2757 (calcd. for $C_{36}H_{39}ClN_9O_5$, $[M+H]^+$), 712.2750 (found).

Tetrazole 27c

Carboxylic acid **26c** (1.0 equiv., 0.014 mmol, 7.6 mg) was suspended in DMF (40 µL) and DIPEA (40 µL). HATU in DMF (1.5 equiv., 0.021 mmol, 30 µL of 26.6 mg/100 µL stock solution in DMF) and H_2N-Halo in DMF (1.2 equiv., 0.017 mmol, 30 µL of 13.0 mg/100 µL stock solution in DMF) were added and the resulting mixture was stirred at ambient temperature for 2 h. Next, the volatiles were removed *in vacuo* and the product was isolated by preparative HPLC (Interchim PhenC4 250x21.2 mm 5 µm, gradient 50/50 to 80/20 A:B, A = MeCN + 0.1 % formic acid, B = H_2O + 0.1 % formic acid).

Tetrazole **27c** was obtained as 3.5 mg off-white powder in 33 % yield.

^{1}H NMR (400 MHz, $CDCl_3$): δ 9.05 (s, 2H), 8.12 – 8.05 (m, 3H), 7.91 (dd, *J* = 8.0, 1.3 Hz, 1H), 7.87 (dd, *J* = 1.3, 0.7 Hz, 1H), 7.65 (dd, *J* = 8.7, 2.4 Hz, 2H), 7.44 (d, *J* = 8.7 Hz, 2H), 6.97 – 6.89 (m, 1H), 3.67 – 3.61 (m, 6H), 3.57 (ddd, *J* = 7.0, 3.2, 1.4 Hz, 2H), 3.50 (t, *J* = 6.6 Hz, 2H), 3.43 (t, *J* = 6.7 Hz, 2H), 1.76 – 1.65 (m, 2H), 1.53 (p, *J* = 6.9 Hz, 2H), 1.45 – 1.35 (m, 2H), 1.35 – 1.21 (m, 2H), 0.91 (s, 3H), 0.77 (s, 3H).

^{13}C NMR (101 MHz, $CDCl_3$): δ 169.0, 165.5, 153.7, 145.5, 141.0, 140.6, 137.8, 133.8,

128.4, 128.0, 127.1, 126.8, 126. 8, 123.7, 122.9, 88. 7, 71.4, 70.3, 70.1, 69.5, 45.2, 40.2, 32.5, 29.5, 26.7, 25.5, 0.2, -0.6.

HRMS (ESI) m/z: 728.2526 (calcd. for $C_{35}H_{39}ClN_9O_5Si$, $[M+H]^+$), 728.2523 (found).

Conjugate NCR2-Halo

To a mixture of tetrazole **27b** (1.0 equiv., 0.008 mmol, 5.8 mg) in DMSO (0.8 mL), 1 M aq. KOH (0.2 mL) was added. The resulting mixture was stirred at ambient temperature for 30 min. Next, the mixture was diluted with water (10 mL, acidified with HOAc to pH 3, extracted with EtOAc (4x 10 mL), and the combined organic phases were evaporated. The product was purified by preparative HPLC (Interchim PhenC4 250x21.2 mm 5 µm, gradient 45/55 to 75/25 A:B, A = MeCN + 0.1 % formic acid, B = H_2O + 0.1 % formic acid).

Conjugate **NCR2-Halo** was obtained as 4.8 mg light-pink powder in 90 % yield.

^{1}H NMR (400 MHz, DMSO-d_6): δ 10.45 (br s, 2H), 8.79 (t, *J* = 5.6 Hz, 1H), 8.14 (dd, *J* = 8.1, 1.4 Hz, 1H), 8.11 (d, *J* = 8.1 Hz, 1H), 7.46 (s, 1H), 7.25 (d, *J* = 2.4 Hz, 2H), 6.83 (dd, *J* = 8.6, 2.4 Hz, 2H), 6.71 (d, *J* = 8.6 Hz, 2H), 3.58 (t, *J* = 6.6 Hz, 2H), 3.51 – 3.42 (m, 4H), 3.43 – 3.36 (m, 2H), 3.28 (t, *J* = 6.5 Hz, 2H), 1.81 (s, 3H), 1.71 – 1.59 (m, 5H), 1.45 – 1.35 (m, 2H), 1.38 – 1.26 (m, 2H), 1.28 – 1.18 (m, 2H).

^{13}C NMR (101 MHz, DMSO-d_6): δ 129.7, 129.3, 125.4, 122.0, 114.8, 112.5, 70.1, 69.4, 69.2, 45.3, 39.3, 34.5, 32.7, 32.0, 28.9, 26.0, 25.2 (obtained by indirect detection from gHSQC NMR experiment, only proton-coupled carbon nuclei are resolved).

HRMS (ESI) m/z: 656.2634 (calcd. for $C_{36}H_{39}ClN_5O_5$, $[M+H]^+$), 656.2630 (found).

Conjugate NCR3-Halo

To a mixture of tetrazole **27c** (1.0 equiv., 0.008 mmol, 3.5 mg) in DMSO (0.4 mL), 1 M aq. KOH (0.1 mL) was added. The resulting mixture was stirred at ambient temperature for 70 min. Next, the mixture was diluted with water (10 mL, acidified with HOAc to pH 3, extracted with EtOAc (3x 10 mL), and the combined organic phases were evaporated. The product was purified by preparative HPLC (Interchim PhenC4 250x21.2 mm 5 µm, gradient 45/55 to 75/245/55 to 75/25 A:B, A = MeCN + 0.1 % formic acid, B = H_2O + 0.1 % formic acid).

Conjugate **NCR3-Halo** was obtained as 1.9 mg violet powder in 55 % yield.

^{1}H NMR (400 MHz, DMSO-d_6): δ 10.41 (s, 2H), 8.81 (t, *J* = 5.6 Hz, 1H), 8.11 (dd, *J* = 8.0, 1.3 Hz, 1H), 8.08 (dd, *J* = 8.0, 0.8 Hz, 1H), 7.72 (t, *J* = 1.1 Hz, 1H), 7.31 (t, *J* = 1.6 Hz, 2H), 6.97 – 6.94 (m, 4H), 3.57 (t, *J* = 6.6 Hz, 2H), 3.53 – 3.47 (m, 4H), 3.45 – 3.41 (m, 2H), 3.40 – 3.36 (m, 2H), 3.31 – 3.27 (m, 2H), 1.69 – 1.60 (m, 2H), 1.44 – 1.34 (m, 2H), 1.34 – 1.27 (m, 2H), 1.26 – 1.19 (m, 2H), 0.68 (s, 3H), 0.57 (s, 3H).

^{13}C NMR (101 MHz, DMSO-d_6): δ 128.8, 128.4, 126.1, 122.8, 119.7, 117.0, 70.0, 69.5, 69.3, 45.3, 39.4, 31.9, 28.8, 26.0, 24.7, -0.5, -1.7 (obtained by indirect detection from gHSQC NMR experiment, only proton-coupled carbon nuclei are resolved).

HRMS (ESI) m/z: 672.2404 (calcd. for $C_{35}H_{39}ClN_5O_5Si$, $[M+H]^+$), 672.2407 (found).

7.1.8 Preparation of *N*-cyanocoumarin 29

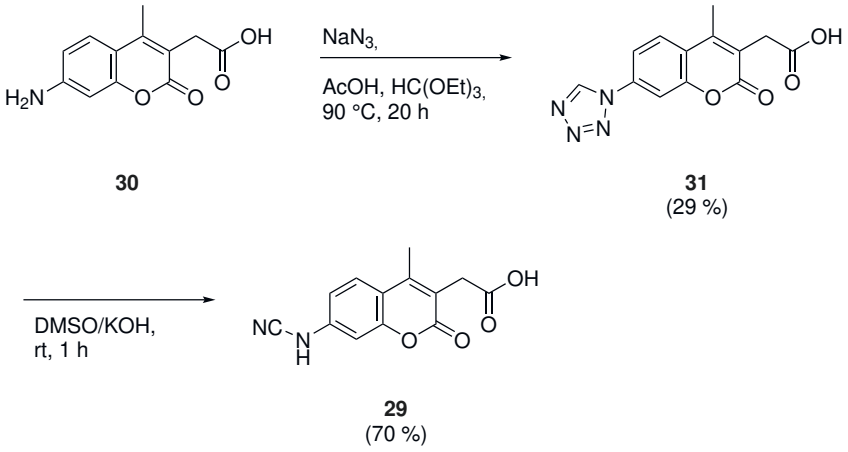

30

31
(29 %)

29
(70 %)

Tetrazole 31

$H(OEt)_3$ (0.2 mL) was added to a mixture of amine **30** (1.0 equiv., 0.085 mmol, 20 mg) and NaN_3 (1.3 equiv., 0.11 mmol, 7.4 mg) in HOAc (0.8 mL). The resulting mixture was stirred at 90 °C for 20 h. Next, it was diluted with water (10 mL, extracted with EtOAc (3x 10 mL), and the combined organic phases were evaporated. The product was purified by preparative HPLC (Interchim PhenC4 250x21.2 mm 5 µm, gradient 10/90 to 50/50 A:B, A = MeCN + 0.1 % formic acid, B = H_2O + 0.1 % formic acid).

Tetrazole **31** was obtained as 7.9 mg off-white powder in 29 % yield.

^{1}H NMR (400 MHz, DMSO-d_6) δ 12.61 (s, 1H), 10.26 (s, 1H), 8.12 (d, J = 8.7 Hz, 1H), 8.08 (d, J = 2.2 Hz, 1H), 7.98 (dd, J = 8.7, 2.3 Hz, 1H), 3.67 (s, 2H), 2.47 (s, 3H).

^{13}C NMR (101 MHz, DMSO-d_6) δ 171.2, 160.2, 152.1, 148.3, 142.6, 135.2, 127.7, 121.1, 120.6, 116.6, 108.7, 33.1, 15.3.

HRMS (ESI) m/z: 287.0775 (calcd. for $C_{13}H_{11}N_4O_4$, $[M+H]^+$), 287.0775 (found).

N-cyanocoumarin 29

To a mixture of tetrazole **29** (1.0 equiv., 0.018 mmol, 5.2 mg) in DMSO (0.8 mL), 1 M aq. KOH (0.2 mL) was added. The resulting mixture was stirred at ambient temperature for 1 h. Next, the mixture was diluted in water (10 mL), adjusted with HOAc to pH 4, extracted with EtOAc (3x 10 mL). The combined organic layer were evaporated and the crude product was purified by preparative HPLC (Interchim PhenC4 250x21.2 mm

5 µm, gradient 10/90 to 50/50 A:B, A = MeCN + 0.1 % formic acid, B = H_2O + 0.1 % formic acid).

N-cyanocoumarin **29** was obtained as 3.1 mg off-white powder (containing 10 mol% dioxane as remainder) in 70 % yield.

^{1}H NMR (400 MHz, DMSO) δ 12.47 (s, 1H), 10.85 (s, 1H), 7.81 (d, *J* = 8.8 Hz, 1H), 6.97 (dd, *J* = 8.7, 2.3 Hz, 1H), 6.84 (d, *J* = 2.3 Hz, 1H), 3.58 (s, 2H), 2.36 (s, 3H).

^{13}C NMR (101 MHz, DMSO) δ 171.6, 160.7, 153.0, 148.9, 127.5, 117.4, 114.7, 112.0, 102.0, 32.8, 15.1.

HRMS (ESI) m/z: 259.0713 (calcd. for $C_{13}H_{11}N_2O_4$, $[M+H]^+$), 259.0713 (found).

7.2 Chapter 5.2

7.2.1 Preparation of *N*-(tetrazinyl)rhodamines 32

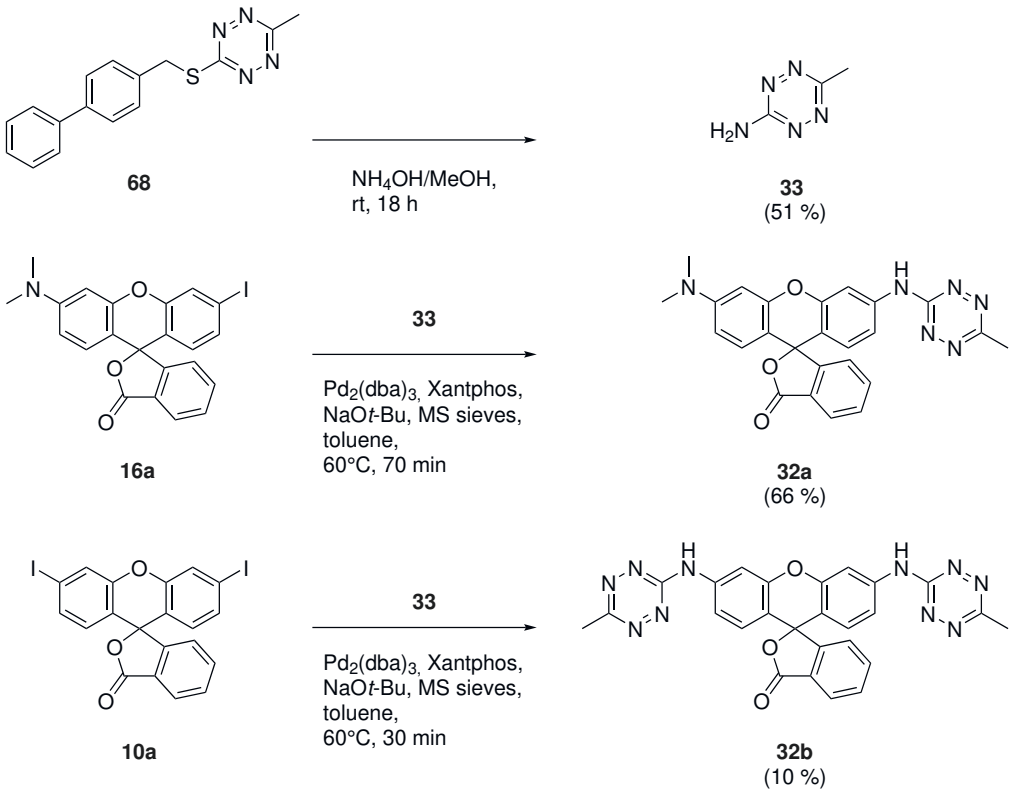

Amino tetrazine 33

Following an adapted procedure,[169] NH_4OH (2.0 mL, 28 to 30 % NH_3 basic) was added to a suspension of thioether **68**[170] (1.0 equiv., 1.02 mmol, 300 mg) in MeOH (3.0 mL). The resulting mixture was stirred at at ambient temperature for 18 h. Next, it was diluted with water/sat. aq. $NaHCO_3$ (40 mL, 1:1) and extracted Et_2O (2x 20 mL) and EtOAc (3x 20 mL). The combined organic phases were washed with brine (50 mL), dried with anhydrous Na_2SO_4, filtered, and evaporated. The crude product was purified by two-fold flash column chromatography (40 g Redisep Rf, 20 % to 100 % EtOAc/hexane; then: 25 g Puriflash 30 µm, 20 % to 80 % EtOAc/hexane).

Amino tetrazine **33** was obtained as 58.1 mg red powder in 51 % yield.

^{1}H NMR (400 MHz, $CDCl_3$) δ 5.65 (br s, 2H), 2.87 (s, 3H).[171]

N-(tetrazinyl)rhodamine 32a

In a 10 mL reaction tube, MS sieves (13.1 mg, 3 Å) were dried under vacuum. Iodide **16a** (1.0 equiv., 0.043 mmol, 24.2 mg), amino tetrazine **33** (1.6 equiv., 0.071 mmol, 7.9 mg), $Pd_2(dba)_3$ (24 mol%, 0.011 mmol, 9.5 mg), and Xantphos (36 mol%, 0.015 mmol, 8.9 mg) NaO*t*-Bu (4.7 equiv., 0.202 mmol, 19.5 mg) were added, and the tube was evacuated and backfilled with argon (3 cycles). Next, toluene (1.0 mL) was added and the resulting mixture was stirred at 60 °C for 70 min. The product was isolated by flash column chromatography (12 g Puriflash 30 µm, 0 % to 80 % EtOAc/CH_2Cl_2).

N-(tetrazinyl)rhodamine **32a** was obtained as 14.5 mg red powder (containing 26 mol% dioxane and 12 mol% EtOAc as remainder) in 66 % yield in mixture with its corresponding dihydrotetrazine form.

^{1}H NMR (400 MHz, DMSO-d_6) δ 11.01 (s, 1H), 8.02 (d, J = 7.6 Hz, 1H), 7.90 (s, 1H), 7.80 (td, J = 7.4, 1.3 Hz, 1H), 7.73 (td, J = 7.5, 1.0 Hz, 1H), 7.40 (dd, J = 8.7, 2.2 Hz, 1H), 7.28 (d, J = 7.6 Hz, 1H), 6.77 (d, J = 8.6 Hz, 1H), 6.62 (s, 1H), 6.53 (s, 2H), 2.96 (s, 6H), 2.82 (s, 3H).

^{13}C NMR (101 MHz, DMSO-d_6) δ 170.3, 168.8, 162.1, 160.8, 135.5, 130.1, 128.6, 128.4, 115.3, 106.2, 98.1, 39.8, 19.9.

HRMS (ESI) m/z: 453.1670 (calcd. for $C_{25}H_{21}N_6O_3$, $[M+H]^+$), 453.1674 (found).

N-(tetrazinyl)rhodamine 32b

In a 10 mL reaction tube, MS sieves (9.7 mg, 3 Å) were dried under vacuum. Iodide **10a** (1.0 equiv., 0.050 mmol, 27.4 mg), amino tetrazine **33** (2.7 equiv., 0.133 mmol, 14.8 mg), $Pd_2(dba)_3$ (25 mol%, 0.013 mmol, 11.6 mg), and Xantphos (40 mol%, 0.020 mmol, 11.7 mg) NaO*t*-Bu (4.1 equiv., 0.203 mmol, 19.5 mg) were added, and the tube was evacuated and backfilled with argon (3 cycles). Toluene (1.0 mL) was added and the resulting mixture was stirred at 60 °C for 30 min. Next, the mixture was diluted with water (10 mL) and extracted with EtOAc (4x 10 mL). The combined organic phases were washed with brine (20 mL), dried with anhydrous Na_2SO_4, and evaporated. The crude product was purified by flash column chromatography (12 g Puriflash 30 µm, 0 % to 100 % EtOAc/hexane) and further purified by preparative HPLC (Interchim PhenC4 250x21.2 mm 5 µm, gradient 45/55 to 75/25 A:B, A = MeCN + 0.1 % formic acid, B = H_2O + 0.1 % formic acid).

N-(tetrazinyl)rhodamine **32b** was obtained as 2.7 mg red powder in 10 % yield.

^{1}H NMR (400 MHz, DMSO-d_6) δ 11.04 (s, 2H), 8.05 (dt, *J* = 7.5, 1.1 Hz, 1H), 7.92 (d, *J* = 2.2 Hz, 2H), 7.81 (td, *J* = 7.5, 1.3 Hz, 1H), 7.75 (td, *J* = 7.5, 1.1 Hz, 1H), 7.45 (dd, *J* = 8.7, 2.2 Hz, 2H), 7.34 (dt, *J* = 7.7, 1.0 Hz, 1H), 6.83 (d, *J* = 8.7 Hz, 2H), 2.82 (s, 6H).

^{13}C NMR (101 MHz, DMSO-d_6) δ 124.9, 106.2, 135.9, 130.2, 115.7, 123.9, 128.6, 19.7 (obtained by indirect detection from gHSQC NMR experiment, only proton-coupled carbon nuclei are resolved).

HRMS (ESI) m/z: 519.1636 (calcd. for $C_{26}H_{19}N_{10}O_3$, $[M+H]^+$), 519.1632 (found).

7.3 Chapter 5.3

7.3.1 Preparation of mercaptofluoran 35

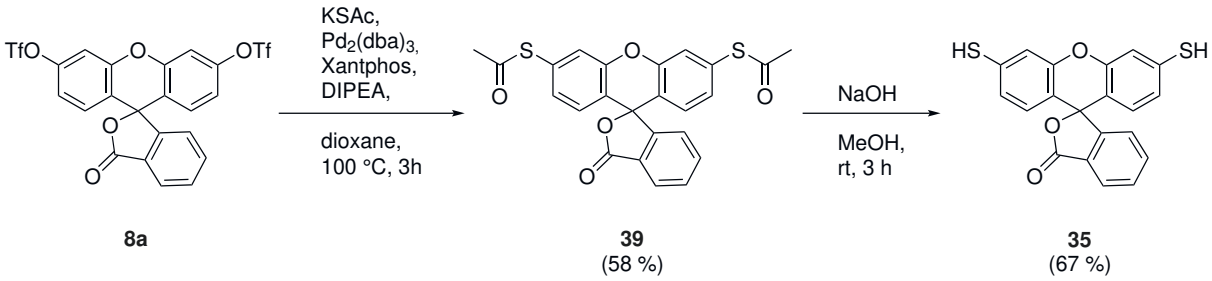

8a | **39** (58 %) | **35** (67 %)

Bis(acetylthio)fluoran 39

In a 10 mL reaction tube, a stirring bar was dried under vacuum. KSAc (4.7 equiv., 0.94 mmol, 107 mg), $Pd_2(dba)_3$ (5 mol%, 0.01 mmol, 9.1 mg), and Xantphos (10 mol%, 0.02 mmol, 11.5 mg) were added, and the tube was evacuated and backfilled with argon (3 cycles). Next, triflate **8a** in dioxane (1.0 equiv., 0.20 mmol, 2.0 µL of 655 mg/11.0 µL stock solution in dioxane) and *N*,*N*-diisopropylethylamine (DIPEA) (3.7 equiv., 0.75 mmol, 0.130 mL) were added and the resulting mixture was stirred at 100 °C for 3 h. The product was isolated by flash column chromatography (25 g Puriflash 30 µm, 0 % to 50 % EtOAc/hexane).

Bis(acetylthio)fluoran **39** was obtained as 53.9 mg yellow powder in 58 % yield.

^{1}H NMR (400 MHz, $CDCl_3$) δ 8.04 (dt, J = 7.2, 0.9 Hz, 1H), 7.73 – 7.59 (m, 2H), 7.42 (d, J = 1.7 Hz, 2H), 7.19 (dt, J = 7.7, 1.0 Hz, 1H), 7.09 (dd, J = 8.2, 1.7 Hz, 2H), 6.88 (d, J = 8.3 Hz, 2H), 2.45 (s, 6H).

^{13}C NMR (101 MHz, $CDCl_3$) δ 192.8, 169.2, 153.0, 151.0, 135.5, 131.1, 130.3, 129.5, 128.6, 125.9, 125.5, 124.1, 122.9, 120.0, 81.4, 30.5.

HRMS (ESI) m/z: 449.0512 (calcd. for $C_{24}H_{17}O_5S_2$, $[M+H]^+$), 449.0514 (found).

Mercaptofluoran 35

To a mixture of bis(acetylthio)fluoran **39** (1.0 equiv., 0.10 mmol, 44.8 mg) in MeOH (1.0 mL), 1 M aq. NaOH (0.50 mL) was added. The resulting mixture was stirred at ambient temperature for 3 h. Next, the mixture was diluted in water/HOAc (6 mL, 1:1),

and extracted with EtOAc (3x 5 mL). The combined organic layer were washed with brine (10 mL), dried with anhydrous Na_2SO_4 and filtered, and evaporated. The residue was lypholized from aq. dioxane.

Mercaptofluoran **35** was obtained as 26.3 mg light-green powder (containing 25 mol% dioxane as remainder) in 67 % yield and used without further purification.

^{1}H NMR (400 MHz, $CDCl_3$) δ 8.02 (dt, *J* = 7.3, 1.0 Hz, 1H), 7.72 – 7.57 (m, 2H), 7.18 (d, *J* = 1.9 Hz, 2H), 7.12 (dt, *J* = 7.7, 0.9 Hz, 1H), 6.90 (dd, *J* = 8.3, 1.9 Hz, 2H), 6.65 (d, *J* = 8.3 Hz, 2H), 3.57 (s, 2H).

^{13}C NMR (101 MHz, $CDCl_3$) δ 169.4, 153.2, 151.2, 135.4, 135.1, 130.1, 128.7, 126.3, 125.4, 124.7, 123.9, 116.9, 116.2, 81.9.

HRMS (ESI) m/z: 365.0301 (calcd. for $C_{20}H_{13}O_3S_2$, $[M+H]^+$), 365.0300 (found).

7.3.2 Preparation of thioacetate 40

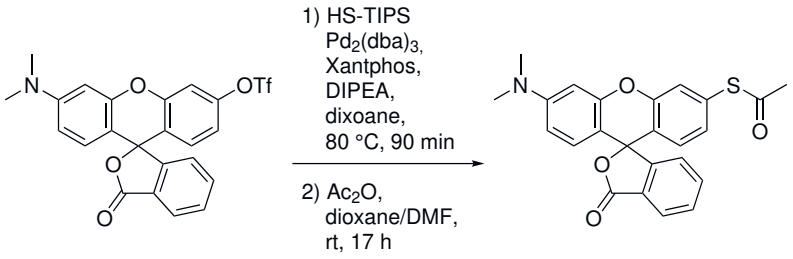

15a **40** (67 %)

In a 10 mL reaction tube, a stirring bar was dried under vacuum. Triflate **15a** (1.0 equiv., 0.20 mmol, 98.7 mg), $Pd_2(dba)_3$ (10 mol%, 0.02 mmol, 18.4 mg), and Xantphos (20 mol%, 0.04 mmol, 23.2 mg) were added, and the tube was evacuated and back-filled with argon (3 cycles). Dioxane (1.0 mL), HS-TIPS (2.1 equiv., 0.42 mmol, 90 µL), and and DIPEA (3.0 equiv., 0.60 mmol, 105 µL) were added and the resulting mixture was stirred at 80 °C for 1.5 h. Next, the mixture was allowed to cool down, Ac_2O (5.3 equiv., 1.06 mmol, 0.100 mL)in DMF (0.5 mL) was added, and the resulting mixture was stirred for 17 h. Then, it was diluted with water (5 mL) and extracted with CH_2Cl_2 (3x 5 mL). The combined organic phases were dried with anhydrous Na_2SO_4, filtered and evaporated. The product was purified by flash column chromatography (12 g Puriflash 30 µm, 0 % to 50 % EtOAc/hexane).

Thioacetate **40** was obtained as 58.0 mg yellow powder in 67 % yield.

^{1}H NMR (400 MHz, $CDCl_3$) δ 8.05 – 7.99 (m, 1H), 7.66 (td, *J* = 7.4, 1.3 Hz, 1H), 7.61 (td, *J* = 7.4, 1.2 Hz, 1H), 7.37 (d, *J* = 1.7 Hz, 1H), 7.19 (dt, *J* = 7.6, 1.0 Hz, 1H), 7.03 (dd, *J* = 8.2, 1.8 Hz, 1H), 6.81 (d, *J* = 8.2 Hz, 1H), 6.63 (d, *J* = 8.9 Hz, 1H), 6.52 (d, *J* = 2.6 Hz, 1H), 6.44 (dd, *J* = 8.8, 2.6 Hz, 1H), 3.00 (s, 6H), 2.44 (s, 3H).

^{13}C NMR (101 MHz, $CDCl_3$) δ 193.2, 169.6, 153.2, 152.4, 152.3, 151.9, 135.1, 130.4, 129.9, 128.8, 128.8, 127.0, 125.2, 124.2, 122.8, 120.7, 109.4, 98.8, 83.3, 40.5, 30.5.

HRMS (ESI) m/z: 418.1108 (calcd. for $C_{24}H_{20}NO_4S$, $[M+H]^+$), 418.1109 (found).

7.3.3 Preparation of rhodol analog 43

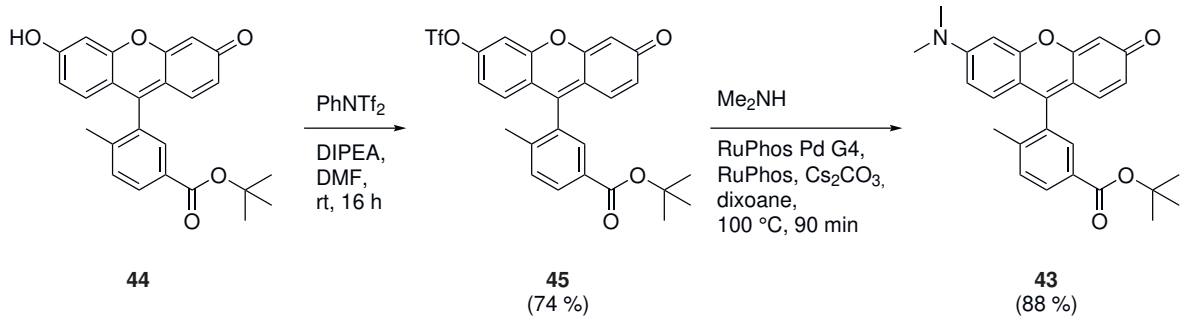

44 **45** (74 %) **43** (88 %)

Triflate 45

Following an adapted procedure,[164] DIPEA (3.1 equiv., 0.41 mmol, 0.18 mL) was added to a mixture of compound **44**[172] (1.0 equiv., 0.33 mmol, 134 mg) and $PhNTf_2$ (1.2 equiv., 0.42 mmol, 148 mg) in DMF (6.0 mL). The mixture was stirred at at ambient temperature for 16 h, before it was diluted with water (60 mL) and extracted with EtOAc (4x 25 mL). The combined organic phases were washed with brine (50 mL), dried with anhydrous Na_2SO_4, filtered, and evaporated. The crude product was purified by flash column chromatography (12 g Puriflash 30 µm, 0 % to 60 % EtOAc/hexane).

Triflate **45** was obtained as 139 mg yellow powder in 74 % yield and used without further purification.

^{1}H NMR (400 MHz, $CDCl_3$) δ 8.10 (dd, *J* = 8.1, 1.8 Hz, 1H), 7.78 (d, *J* = 1.8 Hz, 1H), 7.49 (d, *J* = 8.0 Hz, 1H), 7.42 (d, *J* = 2.0 Hz, 1H), 7.10 (dd, *J* = 8.9, 2.2 Hz, 1H), 7.07 (dd, *J* = 8.9, 0.6 Hz, 1H), 6.93 (d, *J* = 9.8 Hz, 1H), 6.61 (dd, *J* = 9.7, 1.9 Hz, 1H), 6.48 (d, *J* = 1.9 Hz, 1H), 2.15 (s, 3H), 1.59 (s, 9H).

^{19}F NMR (376 MHz, $CDCl_3$) δ -72.52.

^{13}C NMR (101 MHz, $CDCl_3$) δ 186.0, 164.9, 158.0, 153.0, 151.7, 145.7, 141.2, 132.0, 131.8, 131.1, 131.1, 130.8, 130.5, 130.1, 129.8, 122.1, 120.6, 118.8 (q, *J* = 321.0 Hz), 117.9, 110.6, 107.1, 82.0, 28.3, 20.0.

HRMS (ESI) m/z: 535.1033 (calcd. for $C_{26}H_{22}F_3O_7S$, $[M+H]^+$), 535.1032 (found).

Rhodol analog 43

In a 10 mL reaction tube, Cs_2CO_3 (5.0 equiv., 0.50 mmol, 164 mg) was dried under vacuum. Triflate **45** (1.0 equiv., 0.10 mmol, 53.7 mg), RuPhos Pd G4 (20 mol%, 0.02 mmol, 18.9 mg), and RuPhos (10 mol%, 0.01 mmol, 4.6 mg) were added, and the tube was evacuated and backfilled with argon (3 cycles). Next, dioxane (1.2 mL) and $HNMe_2$ in THF (5.0 equiv., 0.50 mmol, 0.25 mL of a 5 M stock solution) were added and the resulting mixture was stirred at 100 °C for 90 min. The product was isolated by flash column chromatography (12 g Puriflash 30 µm, 0 % to 10 % EtOAc/CH_2Cl_2).

Rhodol analog **43** was obtained as 37.8 mg red powder in 88 % yield and used without further purification.

^{1}H NMR (400 MHz, $CDCl_3$) δ 8.06 (dd, *J* = 8.0, 1.9 Hz, 1H), 7.78 (d, *J* = 1.8 Hz, 1H), 7.44 (d, *J* = 8.0 Hz, 1H), 6.85 (d, *J* = 1.8 Hz, 1H), 6.83 (d, *J* = 2.3 Hz, 1H), 6.64 (d, *J* = 2.5 Hz, 1H), 6.61 – 6.53 (m, 2H), 6.48 (d, *J* = 2.0 Hz, 1H), 3.14 (s, 6H), 2.13 (s, 3H), 1.59 (s, 9H).

^{13}C NMR (101 MHz, $CDCl_3$) δ 185.2, 165.2, 159.2, 155.5, 154.5, 149.6, 141.3, 133.3, 130.6, 130.3, 130.3, 130.1, 129.4, 128.7, 115.8, 110.8, 110.4, 105.6, 97.4, 81.6, 40.4, 28.3, 19.9.

HRMS (ESI) m/z: 430.2013 (calcd. for $C_{27}H_{28}NO_4$, $[M+H]^+$), 430.2011 (found).

7.4 Chapter 5.4

7.4.1 Preparation of protected xanthones 46

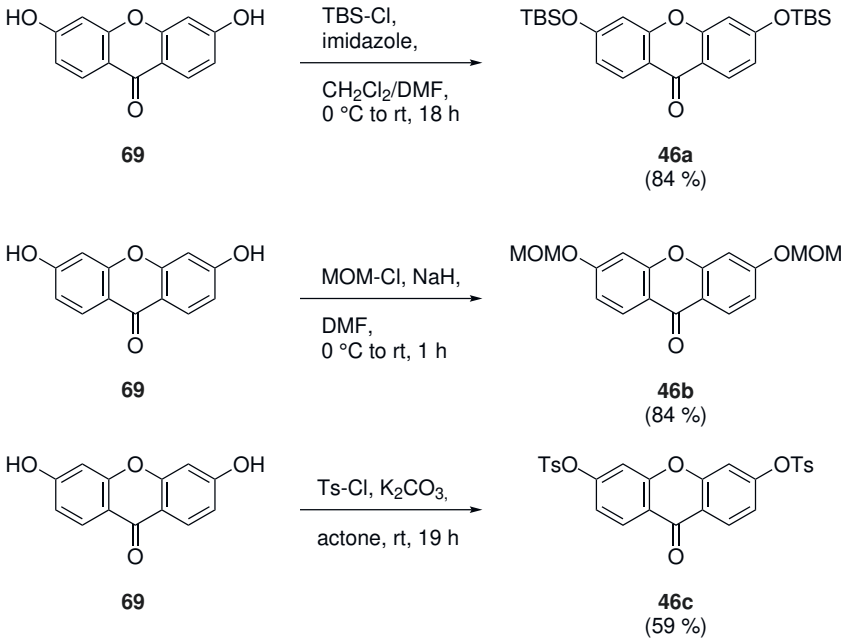

Tert-butyldimethyl(aryl)silylxanthone 46a

Following an adapted procedure,[173] TBS-Cl (3.1 equiv., 13.8 mmol, 2.08 mg) in CH_2Cl_2 (10 mL) was added slowing to a suspension of xanthone **69**[174] (1.0 equiv., 4.4 mmol, 1.00 g) and imidazole (3.0 equiv., 13.8 mmol, 2.08 g) in CH_2Cl_2 (10 mL) and DMF (2.0 mL) cooled at 0 °C. The resulting mixture was stirred at 0 °C for 10 min, then allowed to warm up and stirred at ambient temperature for 18 h. Next, the reaction was quenched with water (40 mL), and extracted with CH_2Cl_2 (3x 20 mL). The combined organic phases were washed with water/brine (40 mL, 1:1) and brine (40 mL), dried with anhydrous Na_2SO_4, filtered, and evaporated. The crude product was purified by flash column chromatography (220 g Redisep Rf, 0 % to 50 % A/hexane, A = hexane + 25 % EtOAc).

Tert-butyldimethyl(aryl)silane **46a** was obtained as 1.70 g off-white powder in 84 % yield.

^{1}H NMR (400 MHz, $CDCl_3$) δ 8.20 (dt, J = 9.0, 1.1 Hz, 2H), 6.91 – 6.72 (m, 4H), 1.01 (s, 18H), 0.28 (s, 12H).

The analytical data correspond to the literature.[173]

Methoxymethoxyxanthone 46b

Following an adapted procedure,[175] NaH (2.6 equiv., 2.6 mmol, 104 mg of 60 % in parafin) was added slowing to a suspension of xanthone **69**[174] (1.0 equiv., 1.0 mmol, 226 mg) in DMF (5.0 mL) cooled at 0 °C. The resulting mixture was stirred at 0 °C for 10 min, then chlormethyl methylether (2.2 equiv., 2.2 mmol, 0.17 mL) was added slowly. The resulting mixutre was stirred at 0 °C for 20 min, allowed to warm up and at ambient temperature for 1 h. Next, the reaction was quenched with water (50 mL), and extracted with EtOAc/hexane (3x 50 mL, 1:4). The combined organic phases were washed with water/brine (50 mL, 1:1) and brine (50 mL), dried with anhydrous Na_2SO_4, filtered, and evaporated. The crude product was purified by flash column chromatography (25 g Puriflash 30 µm, 0 % to 100 % EtOAc/hexane).

Methoxymethoxyxanthone **46b** was obtained as 262 mg off-white powder in 84 % yield.

^{1}H NMR (400 MHz, $CDCl_3$) δ 8.24 (d, J = 8.8 Hz, 2H), 7.07 (d, J = 2.3 Hz, 2H), 7.02 (dd, J = 8.8, 2.3 Hz, 2H), 5.29 (s, 4H), 3.52 (s, 6H).

The analytical data correspond to the literature.[175]

Tosylxanthone 46c

Following an adapted procedure,[176] Ts-Cl (2.5 equiv., 2.5 mmol, 476 mg) in acetone (4.0 mL) xanthone **69**[174] (1.0 equiv., 1.0 mmol, 225 mg) and K_2CO_3 (3.1 equiv., 3.0 mmol, 416 mg) in acetone (4.0 mL). The resulting mixture was stirred at ambient temperature for 19 h. Next, it was filtered through a pad on Celite, the pad was washed with EtOAc (3x 10 mL), and the combined organic phases were evaporated. The crude product was purified by flash column chromatography (40 g Redisep Rf, 0 % to 100 % EtOAc/hexane).

Tosyl **46c** was obtained as 314 mg beige-colored powder in 59 % yield.

^{1}H NMR (400 MHz, $CDCl_3$) δ 8.22 (d, J = 8.7 Hz, 2H), 7.76 (d, J = 8.3 Hz, 4H), 7.35 (d, J = 8.1 Hz, 4H), 7.25 (d, J = 2.2 Hz, 2H), 6.98 (dd, J = 8.8, 2.2 Hz, 2H), 2.47 (s, 6H).

^{13}C NMR (101 MHz, $CDCl_3$) δ 175.4, 156.7, 154.3, 146.3, 132.1, 130.2, 128.7, 128.6, 120.5, 119.0, 111.9, 21.9.

HRMS (ESI) m/z: 537.0672 (calcd. for $C_{27}H_{21}O_8S_2$, $[M+H]^+$), 537.0670 (found).

7.4.2 Preparation of PaX(–)1

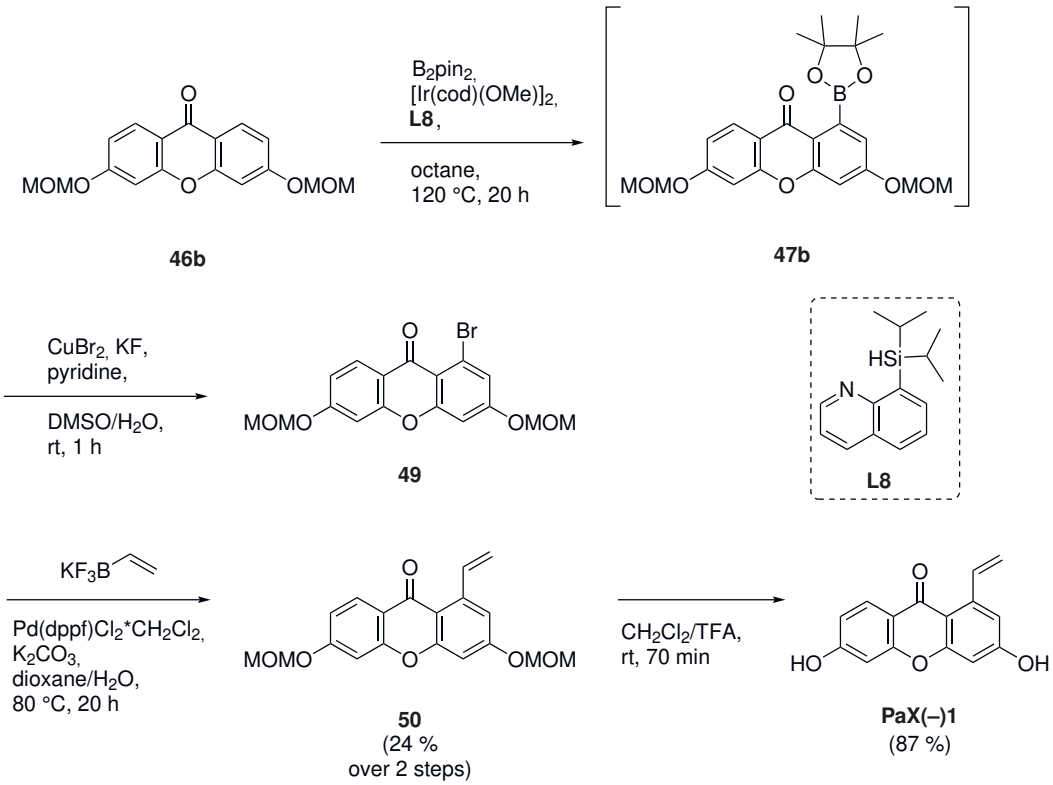

Bromide 49

In a 10 mL reaction tube, xanthone **46b** (1.0 equiv., 0.20 mmol, 64.2 mg), B_2pin_2 (1.0 equiv., 0.21 mmol, 52.7 mg), $[Ir(cod)(OMe)]_2$ (10 mol%, 0.02 mmol, 13.2 mg), and **L8** (20 mol%, 0.04 mmol, 9.8 mg) were added, and the tube was evacuated and backfilled with argon (3 cycles). Next, octane (1.0 mL) was added and the resulting mixture was stirred light-protected at 120 °C for 20 h. The mixture was filtered through a pad of Celite, the pad was washed with EtOAc (3x 10 mL), and the combined organic phases were evaporated.

The residue with crude **70** was re-suspended in DMSO (1.0 mL) and water (0.10 mL). $CuBr_2$ (3.0 equiv., 0.61 mmol, 137 mg), KF (4.0 equiv., 0.80 mmol, 46.6 mg), and pyridine (20 equiv., 3.97 mmol, 0.32 mL) were added and the resulting mixture was stirred light-protected at ambient temperature for 1 h. Next, the mixture was diluted with water (20 mL), and extracted with EtOAc (4x 10 mL). The combined organic phases were washed with water/brine (20 mL, 1:1) and brine (20 mL), dried with anhydrous Na_2SO_4, filtered, and evaporated. The product was isolated by flash column chromatography (12 g Puriflash 30 µm, 20 % to 80 % EtOAc/hexane).

Bromide **49** was obtained as 50.6 mg yellow powder used without further purification in the next step.

^{1}H NMR (400 MHz, $CDCl_3$) δ 8.25 – 8.17 (m, 1H), 7.30 (d, *J* = 2.4 Hz, 1H), 7.05 (d, *J* = 2.4 Hz, 1H), 7.04 – 6.95 (m, 2H), 5.31 – 5.23 (m, 4H), 3.54 – 3.46 (m, 6H).

^{13}C NMR (101 MHz, $CDCl_3$) δ 129.0, 121.1, 103.8, 114.4, 102.8, 94.8, 56.7 (obtained by indirect detection from gHSQC NMR experiment, only proton-coupled carbon nuclei are resolved).

HRMS (ESI) m/z: 395.0125 (calcd. for $C_{17}H_{16}BrO_6$, $[M+H]^+$), 395.0124 (found).

Vinyl 50

In a 10 mL reaction tube, crude bromide **49** (19.5 mg), potassium trifluoro(vinyl)borate (0.08 mmol, 10.1 mg), $Pd(dppf)Cl_2{\cdot}CH_2Cl_2$ (0.01 mmol, 8.2 mg), and K_2CO_3 (0.015 mmol, 20.9 mg), dioxane (1.0 mL) and water (0.40 mL) were added, and the tube was flushed with argon (15 min). The resulting mixture was stirred light-protected at 80 °C for 20 h. Next, the mixture was diluted with water (10 mL), and extracted with EtOAc (4x 10 mL). The combined organic phases were washed with brine (20 mL), dried with anhydrous Na_2SO_4, filtered, and evaporated. The product was isolated by flash column chromatography (12 g Puriflash 30 µm, 0 % to 80 % EtOAc/hexane).

Vinyl **50** was obtained as 7.0 mg off-white powder (containing 7 mol% of bis-vinyl by-product) in 24 % yield over two steps.

^{1}H NMR (400 MHz, $CDCl_3$) δ 8.19 (d, *J* = 8.8 Hz, 1H), 8.10 (dd, *J* = 17.3, 10.9 Hz, 1H), 7.08 – 6.94 (m, 4H), 5.61 (dd, *J* = 17.3, 1.6 Hz, 1H), 5.42 (dd, *J* = 10.9, 1.6 Hz, 1H), 5.29 (s, 2H), 5.28 (s, 2H), 3.52 (s, 4H), 3.51 (s, 4H).

^{13}C NMR (101 MHz, $CDCl_3$) δ 177.2, 162.2, 161.1, 159.0, 157.0, 143.5, 137.6, 128.5, 117.6, 116.9, 114.0, 113.9, 112.9, 103.0, 102.6, 94.5, 94.4, 56.6, 56.6.

HRMS (ESI) m/z: 343.1176 (calcd. for $C_{19}H_{19}O_6$, $[M+H]^+$), 343.1170 (found).

PaX(–)1

TFA (0.10 mL) was added to a light-protected solution of **50** (1.0 equiv., 0.016 mmol, 6.0 mg) in CH_2Cl_2 (0.50 mL). The resulting mixture was stirred at ambient temperature for 70 min and then diluted and evaporated to dryness from toluene (3 cycles).

The crude product was purified by preparative HPLC (Interchim PhenC4 250x21.2 mm 5 µm, gradient 30/70 to 60/40 A:B, A = MeCN + 0.1 % formic acid, B = H_2O + 0.1 % formic acid).

PaX(–)1 was obtained as 4.1 mg light-yellow powder in 87 % yield.

^{1}H NMR (400 MHz, DMSO-d_6) δ 10.84 (s, 1H), 10.78 (s, 1H), 8.03 (dd, *J* = 17.4, 10.9 Hz, 1H), 7.93 (d, *J* = 8.7 Hz, 1H), 6.90 (d, *J* = 2.4 Hz, 1H), 6.84 (dd, *J* = 8.7, 2.2 Hz, 1H), 6.79 (d, *J* = 2.4 Hz, 1H), 6.77 (d, *J* = 2.2 Hz, 1H), 5.60 (dd, *J* = 17.4, 1.6 Hz, 1H), 5.34 (dd, *J* = 10.8, 1.6 Hz, 1H).

^{13}C NMR (101 MHz, DMSO-d_6) δ 175.6, 163.2, 162.0, 158.6, 156.5, 142.1, 137.1, 127.9, 116.5, 114.8, 113.6, 111.6, 111.1, 102.4, 101.5.

HRMS (ESI) m/z: 255.0652 (calcd. for $C_{15}H_{11}O_4$, $[M+H]^+$), 255.0661 (found).

7.4.3 Preparation of PaX(–)2

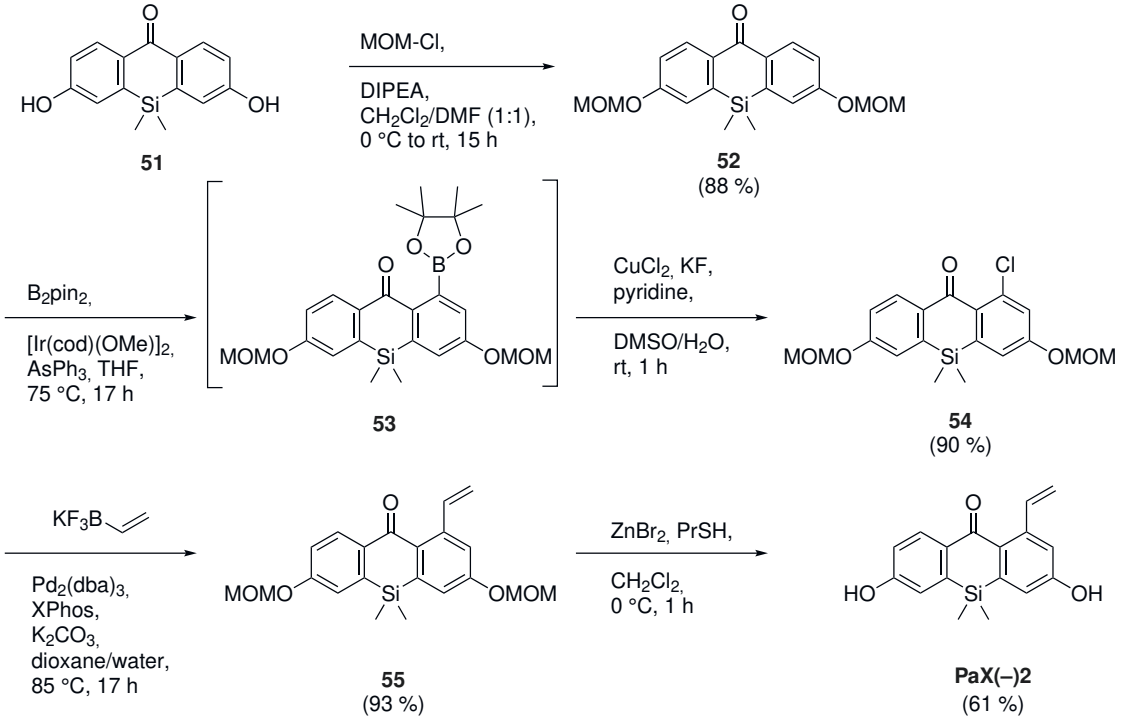

Methoxymethoxyxanthone 52

Following an adapted procedure,[177] chlormethyl methylether (4.0 equiv., 6.02 mmol, 0.46 mL) was added to a suspension of xanthone **71** (1.0 equiv., 1.51 mmol, 406 mg)

and DIPEA (6.1 equiv., 9.20 mmol, 1.60 mL) in CH_2Cl_2 (10 mL) and DMF (2.0 mL) cooled at 0 °C. The resulting mixture was stirred at 0 °C for 10 min, allowed to warm up and stirred at ambient temperature for 15 h. Next, the reaction was quenched with water (20 mL), and extracted with CH_2Cl_2 (3x 10 mL). The combined organic phases were washed with water/brine (20 mL, 1:1) and brine (20 mL), dried with anhydrous Na_2SO_4, filtered, and evaporated. The crude product was purified by flash column chromatography (40 g Redisep Rf, 0 % to 50 % EtOAc/hexane).

Methoxymethoxyxanthone **52** was obtained as 467 mg off-white powder in 88 % yield.

^{1}H NMR (400 MHz, $CDCl_3$) δ 8.43 (dd, *J* = 8.7, 0.5 Hz, 2H), 7.23 (d, *J* = 2.4 Hz, 2H), 7.20 (dd, *J* = 8.8, 2.7 Hz, 2H), 5.28 (s, 4H), 3.52 (s, 6H), 0.48 (s, 6H).

^{13}C NMR (101 MHz, $CDCl_3$) δ 185.9, 159.9, 141.4, 135.0, 132.5, 119.8, 117.6, 94.3, 56.5, -1.3.

HRMS (ESI) m/z: 359.1309 (calcd. for $C_{19}H_{23}O_5Si$, $[M+H]^+$), 359.1311 (found).

Chloride 54

In a 10 mL flask, xanthone **52** (1.0 equiv., 0.80 mmol, 286 mg), B_2pin_2 (1.3 equiv., 1.05 mmol, 267 mg), $[Ir(cod)(OMe)]_2$ (5 mol%, 0.04 mmol, 26.5 mg), and $AsPh_3$ (10 mol%, 0.08 mmol, 24.8 mg) were added, and the tube was evacuated and backfilled with argon (3 cycles). Next, THF (8.0 mL) was added and the resulting mixture was stirred light-protected at 75 °C for 17 h. The mixture was filtered through a pad of Celite, the pad was washed with EtOAc (3x 20 mL), and the combined organic phases were evaporated.

The residue was re-suspended in DMSO (8.0 mL) and water (0.80 mL). $CuCl_2$ (3.1 equiv., 2.47 mmol, 334 mg), KF (4.0 equiv., 3.21 mmol, 186 mg), and pyridine (20 equiv., 16.1 mmol, 1.30 mL) were added and the resulting mixture was stirred light-protected at ambient temperature for 1 h. Next, the mixture was diluted with water (100 mL), and extracted with EtOAc (3x 100 mL). The combined organic phases were washed with water/brine (100 mL, 1:1) and brine (100 mL), dried with anhydrous Na_2SO_4, filtered, and evaporated. The product was isolated by flash column chromatography (40 g Redisep Rf, 0 % to 50 % EtOAc/hexane).

Chloride **54** was obtained as 283 mg yellow oil in 90 % yield.

^{1}H NMR (400 MHz, $CDCl_3$) δ 8.19 – 8.10 (m, 1H), 7.24 (d, *J* = 2.5 Hz, 1H), 7.22 – 7.15

(m, 2H), 7.14 (d, *J* = 2.5 Hz, 1H), 5.26 (s, 2H), 5.24 (s, 2H), 3.50 (s, 6H), 0.48 (s, 6H).

^{13}C NMR (101 MHz, $CDCl_3$) δ 187.6 159.4, 158.7, 142.9, 139.0, 138.0, 136.6, 133.0, 131.8, 120.9, 119.1, 118.8, 117.8, 94.4, 94.3, 56.6, 56.4, -1.6.

HRMS (ESI) m/z: 393.0920 (calcd. for $C_{19}H_{22}ClO_5Si$, $[M+H]^+$), 393.0920 (found).

Vinyl 55

A flask was charged with potassium trifluoro(vinyl)borate (1.5 equiv., 0.92 mmol, 123 mg), $Pd_2(dba)_3$ (5 mol%, 0.03 mmol, 28.6 mg), XPhos (10 mol%, 0.06 mmol, 29.3 mg), and K_2CO_3 (1.9 equiv., 1.19 mmol, 159 mg). Chloride **54** in dixoane (1.0 equiv., 0.80 mmol, 6.0 mL of a 39.9 mg/mL stock solution in dioxane), and water (1.2 mL) were added, and the flash was flushed with argon (15 min). The resulting mixture was stirred light-protected at 85 °C for 16 h. Next, the mixture was diluted with water (50 mL), and extracted with EtOAc (3x 20 mL). The combined organic phases were washed with brine (50 mL), dried with anhydrous Na_2SO_4, filtered, and evaporated. The product was purified by two-fold flash column chromatography (25 g Puriflash 30 µm, 0 % to 40 % EtOAc/hexane).

Vinyl **55** was obtained as 217 mg color-less oil in 93 % yield.

^{1}H NMR (400 MHz, $CDCl_3$) δ 8.20 (dd, *J* = 8.4, 0.7 Hz, 1H), 7.40 (dd, *J* = 17.3, 10.9 Hz, 1H), 7.24 (dd, *J* = 2.7, 0.6 Hz, 1H), 7.22 – 7.15 (m, 3H), 5.55 (dd, *J* = 17.2, 1.4 Hz, 1H), 5.32 (dd, *J* = 10.8, 1.4 Hz, 1H), 5.28 (s, 2H), 5.26 (s, 2H), 3.52 (s, 3H), 3.51 (s, 3H), 0.48 (s, 6H).

^{13}C NMR (101 MHz, $CDCl_3$) δ 189.3, 159.4, 158.9, 144.2, 141.9, 139.8, 139.3, 137.8, 134.0, 131.8, 119.5, 119.2, 117.7, 117.7, 114.8, 94.3, 56.5, 56.4, -1.4.

HRMS (ESI) m/z: 385.1466 (calcd. for $C_{21}H_{25}O_5Si$, $[M+H]^+$), 385.1461 (found).

PaX(–)2

To a solution of $ZnBr_2$ (3.0 equiv., 0.30 mmol, 67.1 mg) in CH_2Cl_2 (1.0 mL) cooled at 0 °C, a solution of **55** in CH_2Cl_2 (1.0 equiv., 0.10 mmol, 1.00 mL of a 38.4 mg/mL stock solution) was added. Next, PrSH (6.0 equiv., 0.61 mmol, 55 µL) was added, and the resulting mixture was stirred light-protected at 0 °C for 2 h. The volatiles were removed by evaporation and the product was isolated by flash column chromatography (12 g

Puriflash 30 µm, 20 % to 100 % EtOAc/hexane).

PaX(–)2 was obtained as 19.8 mg beige-colored powder (containing 26 mol% dioxane as remainder) in 61 % yield.

^{1}H NMR (400 MHz, CD_3CN) δ 8.03 (d, J = 8.7 Hz, 1H), 7.34 (dd, J = 17.3, 10.9 Hz, 1H), 7.08 (d, J = 2.6 Hz, 2H), 7.04 (dd, J = 2.7, 0.6 Hz, 1H), 6.96 (dd, J = 8.7, 2.6 Hz, 1H), 5.51 (dd, J = 17.3, 1.6 Hz, 1H), 5.23 (dd, J = 10.9, 1.5 Hz, 1H), 0.44 (s, 6H).

^{13}C NMR (101 MHz, CD_3CN) δ 189.5, 160.4, 159.8, 144.8, 143.2, 140.9, 140.4, 137.0, 133.2, 132.5, 120.0, 119.3, 118.2, 117.8, 114.5, -1.6.

HRMS (ESI) m/z: 297.0941 (calcd. for $C_{17}H_{17}O_3Si$, $[M+H]^+$), 297.0940 (found).

7.4.4 Preparation of PaX(–)2-OAc

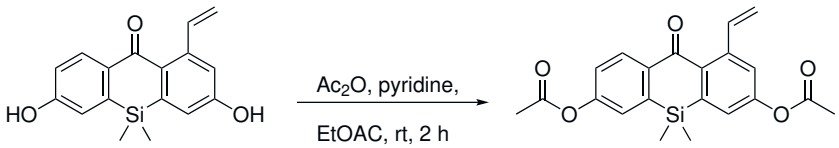

PaX(–)2 **PaX(–)2-OAc** (73 %)

To a solution of **PaX(–)2** (1.0 equiv., 0.03 mmol, 8.7 mg) in EtOAc (100 µL), pyridine (10 equiv., 0.30 mmol, 24 µL), and acetic anhydride in EtOAc (2.6 equiv., 0.08 mmol, 200 µL of 3.9 mg/100 µL stock solution in EtOAc), were added. The resulting mixture was stirred light-protected at ambient temperature for 2 h. The volatiles were removed by evaporation and the product was isolated by flash column chromatography (12 g Puriflash 30 µm, 0 % to 60 % EtOAc/hexane).

PaX(–)2-OAc was obtained as 8.1 mg pale yellow solid in 73 % yield.

^{1}H NMR (400 MHz, $CDCl_3$) δ 8.21 (d, J = 8.6 Hz, 1H), 7.38 – 7.29 (m, 4H), 7.27 (dd, J = 8.6, 2.4 Hz, 1H), 5.59 (dd, J = 17.3, 1.3 Hz, 1H), 5.37 (dd, J = 10.9, 1.2 Hz, 1H), 2.35 (s, 3H), 2.34 (s, 3H), 0.50 (s, 6H).

^{13}C NMR (101 MHz, $CDCl_3$) δ 189.9, 169.1, 169.0, 153.0, 152.5, 143.6, 141.4, 141.4, 139.4, 137.9, 137.3, 131.3, 125.1, 125.0, 123.7, 123.4, 116.0, 21.4, 21.3, -1.6.

HRMS (ESI) m/z: 381.1153 (calcd. for $C_{21}H_{21}O_5Si$, $[M+H]^+$), 381.1156 (found).

7.4.5 Preparation of PaX(–)2-Halo

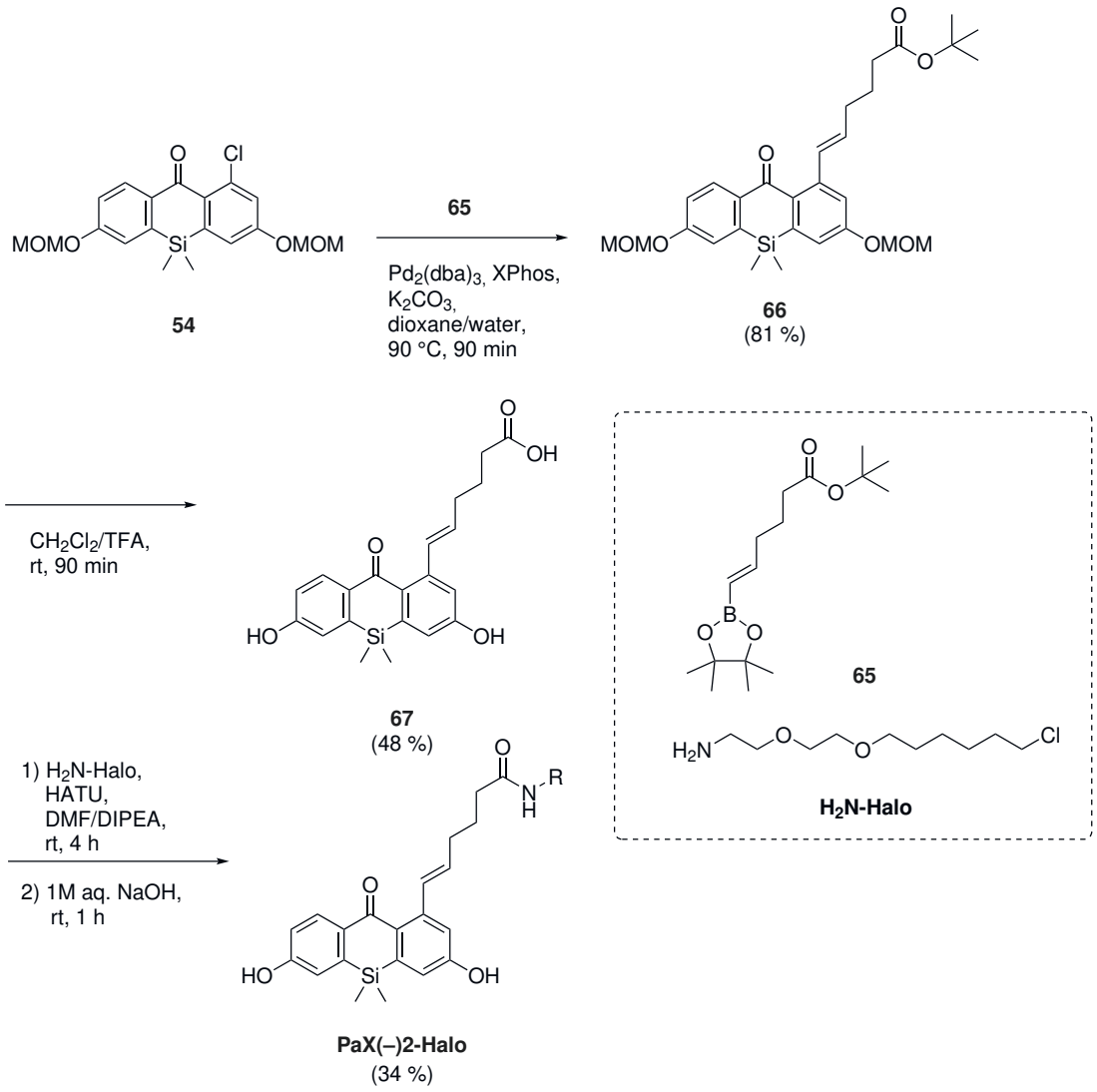

Compound 66

In a 10 mL reaction tube, borate **65** (1.5 equiv., 0.06 mmol, 17.8 mg), $Pd_2(dba)_3$ (5 mol%, 0.002 mmol, 1.8 mg), XPhos (10 mol%, 0.004 mmol, 1.9 mg), and K_2CO_3 (2.0 equiv., 0.08 mmol, 10.5 mg) were placed. Chloride **54** in dioxane (1.0 equiv., 0.04 mmol, 400 µL of a 39.3 mg/mL stock solution in dioxane), and water (80 µL) were added, and the tube was flushed with argon (15 min). The resulting mixture was stirred light-protected at 90 °C for 90 min. Next, the mixture was diluted with water (10 mL), and extracted with EtOAc (3x 10 mL). The combined organic phases were washed with brine (20 mL), dried with anhydrous Na_2SO_4, filtered, and evaporated. The product was isolated by flash column chromatography (12 g Puriflash 30 µm, 0 % to 60 % EtOAc/hexane).

Compound **66** was obtained as 17.1 mg pale yellow powder in 81 % yield.

^{1}H NMR (400 MHz, $CDCl_3$) δ 8.18 (d, *J* = 8.5 Hz, 1H), 7.22 – 7.08 (m, 5H), 6.01 (dt, *J* = 15.5, 6.9 Hz, 1H), 5.27 (s, 2H), 5.26 (s, 2H), 3.51 (s, 3H), 3.50 (s, 3H), 2.38 – 2.23 (m, 4H), 1.82 (p, *J* = 7.5 Hz, 2H), 1.46 (s, 9H), 0.47 (s, 6H).

^{13}C NMR (101 MHz, $CDCl_3$) δ 189.6, 173.3, 159.3, 158.7, 143.7, 141.8, 139.6, 138.2, 133.7, 132.5, 131.7, 131.3, 119.1, 118.9, 117.6, 117.4, 94.3, 94.3, 80.2, 56.4, 56.4, 35.2, 32.6, 28.3, 25.0, -1.4.

HRMS (ESI) m/z: 549.2279 (calcd. for $C_{29}H_{39}O_7Si$, $[M+H]^+$), 549.2275 (found).

Carboxylic acid 67

TFA (0.10 mL) was added to a light-protected solution of *tert*-butyl ester **66** (1.0 equiv., 0.024 mmol, 12.7 mg) in CH_2Cl_2 (0.50 mL). The resulting mixture was stirred at at ambient temperature for 90 min and then diluted and evaporated to dryness from toluene (3 cycles). The crude product was purified by preparative HPLC (Interchim PhenC4 250x21.2 mm 5 µm, gradient 30/70 to 60/40 A:B, A = MeCN + 0.1 % formic acid, B = H_2O + 0.1 % formic acid).

Carboxylic acid **67** was obtained as 4.9 mg light-yellow powder (containing 27 mol% dioxane as remainder) in 48 % yield.

^{1}H NMR (400 MHz, DMSO-d_6) δ 12.00 (br s, 1H), 10.20 (s, 1H), 10.20 (s, 1H), 7.95 (d, *J* = 8.7 Hz, 1H), 7.03 (d, *J* = 2.7 Hz, 1H), 7.00 (d, *J* = 2.5 Hz, 1H), 6.95 (d, *J* = 2.5 Hz, 1H), 6.93 (dd, *J* = 8.7, 2.6 Hz, 1H), 5.88 (dt, *J* = 15.5, 6.9 Hz, 1H), 2.31 (t, *J* = 7.4 Hz, 2H), 2.29 – 2.15 (m, 2H), 1.70 (p, *J* = 7.4 Hz, 2H), 0.40 (s, 6H).

^{13}C NMR (101 MHz, DMSO-d_6) δ 187.9, 174.5, 159.8, 159.2, 143.1, 141.5, 139.2, 134.9, 132.4, 131.4, 130.6, 129.9, 118.6, 118.3, 117.3, 116.7, 33.0, 31.8, 24.2, -1.6.

HRMS (ESI) m/z: 383.1309 (calcd. for $C_{21}H_{23}O_5Si$, $[M+H]^+$), 383.1307 (found).

Conjugate PaX(–)2-Halo

Carboxylic acid **67** (1.0 equiv., 0.009 mmol, 3.5 mg) and HATU (1.5 equiv., 0.013 mmol, 5.1 mg) were stirred light-protected in DMF (100 µL) and DIPEA (40 µL). H_2N-Halo in DMF (1.2 equiv., 0.011 mmol, 100 µL of 2.4 mg/100 µL stock solution in DMF) was added and the resulting mixture was stirred at ambient temperature for 4 h. Next,

20 µL 1 M NaOH was added to hydrolyse HATU-adducts observed by LCMS analysis, and the resulting mixture was stirred at ambient temperature for 1 h. The volatiles were removed *in vacuo* and the product was isolated by preparative HPLC (Interchim PhenC4 250x21.2 mm 5 µm, gradient 45/55 to 75/25 A:B, A = MeCN + 0.1 % formic acid, B = H_2O + 0.1 % formic acid).

Conjugate **PaX(–)2-Halo** was obtained as 1.8 mg yellow powder in 34 % yield.

^{1}H NMR (400 MHz, DMSO-d_6) δ 10.20 (s, 1H), 10.20 (s, 1H), 7.95 (d, *J* = 8.6 Hz, 1H), 7.86 (t, *J* = 5.7 Hz, 1H), 7.10 – 6.97 (m, 3H), 6.96 – 6.89 (m, 2H), 6.18 – 5.69 (m, 1H), 3.58 (t, *J* = 6.6 Hz, 2H), 3.51 – 3.45 (m, 2H), 3.45 – 3.37 (m, 2H), 3.22 (q, *J* = 5.8 Hz, 2H), 2.22 – 2.12 (m, 4H), 1.76 – 1.58 (m, 4H), 1.51 – 1.39 (m, 2H), 1.35 – 1.29 (m, 2H), 1.28 – 1.15 (m, 4H), 0.40 (s, 6H).

^{13}C NMR (101 MHz, DMSO-d_6) δ 131.4, 118.3, 132.5, 118.6, 116.8, 116.8, 117.3, 130.1, 45.2, 69.4, 69.4, 70.0, 38.4, 31.8, 34.5, 24.9, 31.8, 28.9, 26.0, 24.7, 28.7, -1.8.

HRMS (ESI) m/z: 588.2543 (calcd. for $C_{31}H_{43}ClNO_6Si$, $[M+H]^+$), 588.2540 (found).

Chapter 8

Bibliography

[1] L. Heynck, J. Matthias, M. L. Bossi, A. N. Butkevich, S. W. Hell, *Chem. Sci.* **2022**, *13*, 8297–8306.

[2] S. W. Hell, S. J. Sahl, M. Bates, X. W. Zhuang, R. Heintzmann, M. J. Booth, J. Bewersdorf, G. Shtengel, H. Hess, P. Tinnefeld, A. Honigmann, S. Jakobs, I. Testa, L. Cognet, B. Lounis, H. Ewers, S. J. Davis, C. Eggeling, D. Klenerman, K. I. Willig, G. Vicidomini, M. Castello, A. Diaspro, T. Cordes, *J. Phys. D: Appl. Phys.* **2015**, *48*, DOI 10.1088/0022-3727/48/44/443001.

[3] Z. Yang, S. Samanta, W. Yan, B. Yu, J. Qu in *Optical Imaging in Human Disease and Biological Research*, (Eds.: X. Wei, B. Gu), Springer Singapore, Singapore, **2021**, pp. 23–43.

[4] F. Rost in *Encyclopedia of Spectroscopy and Spectrometry (Third Edition)*, (Eds.: J. C. Lindon, G. E. Tranter, D. W. Koppenaal), Academic Press, Oxford, **2017**, pp. 627–631.

[5] L. Schermelleh, R. Heintzmann, H. Leonhardt, *J. Cell Biol.* **2010**, *190*, 165–175.

[6] M. Lelek, M. T. Gyparaki, G. Beliu, F. Schueder, J. Griffié, S. Manley, R. Jungmann, M. Sauer, M. Lakadamyali, C. Zimmer, *Nat. Rev. Methods Primers* **2021**, *1*, 39.

[7] S. van de Linde, M. Heilemann, M. Sauer, *Annu. Rev. Phys. Chem.* **2012**, *63*, 519–540.

[8] E. V. Orlova, H. R. Saibil, *Chem. Rev.* **2011**, *111*, 7710–7748.

[9] L. F. Kourkoutis, J. M. Plitzko, W. Baumeister, *Annu. Rev. Mater. Res.* **2012**, *42*, 33–58.

[10] A. T. Wassie, Y. Zhao, E. S. Boyden, *Nat. Methods* **2019**, *16*, 33–41.

[11] B. R. Gallagher, Y. Zhao, *Neurobiol. Dis.* **2021**, *154*, 105362.

[12] T. A. Klar, S. W. Hell, *Opt. Lett.* **1999**, *24*, 954–956.

[13] S. T. Hess, T. P. Girirajan, M. D. Mason, *Biophys. J.* **2006**, *91*, 4258–4272.

[14] F. Balzarotti, Y. Eilers, K. C. Gwosch, A. H. Gynnå, V. Westphal, F. D. Stefani, J. Elf, S. W. Hell, *Science* **2017**, *355*, 606–612.

[15] L. Wang, M. S. Frei, A. Salim, K. Johnsson, *J. Am. Chem. Soc.* **2019**, *141*, 2770–2781.

[16] Z. Liu, L. D. Lavis, E. Betzig, *Molecular Cell* **2015**, *58*, 644–659.

[17] B. L. Oliveira, Z. Guo, G. J. L. Bernardes, *Chem. Soc. Rev.* **2017**, *46 16*, 4895–4950.

[18] C. A. Hoelzel, X. Zhang, *ChemBioChem* **2020**, *21*, 1935–1946.

[19] J. B. Grimm, L. D. Lavis, *Nat. Methods* **2022**, *19*, 149–158.

[20] L. Wang, W. Du, Z. Hu, K. Uvdal, L. Li, W. Huang, *Angew. Chem. Int. Ed.* **2019**, *58*, 14026–14043.

[21] M. Beija, C. A. M. Afonso, J. M. G. Martinho, *Chem. Soc. Rev.* **2009**, *38*, 2410–2433.

[22] Y. M. Poronik, K. V. Vygranenko, D. Gryko, D. T. Gryko, *Chem. Soc. Rev.* **2019**, *48*, 5242–5265.

[23] L. D. Lavis, *Annu. Rev. Biochem.* **2017**, *86*, 825–843.

[24] A. P. Demchenko, *Methods Appl. Fluoresc.* **2020**, *8*, 022001.

[25] S. A. Hilderbrand, R. Weissleder, *Curr. Opin. Chem. Biol.* **2010**, *14*, 71–79.

[26] L. V. Johnson, M. L. Walsh, B. J. Bockus, L. B. Chen, *J. Cell Biol.* **1981**, *88*, 526–535.

[27] J. S. Modica-Napolitano, J. R. Aprille, *Cancer Res* **1987**, *47*, 4361–5.

[28] P. K. S. Magut, S. Das, V. E. Fernand, J. Losso, K. McDonough, B. M. Naylor, S. Aggarwal, I. M. Warner, *J. Am. Chem. Soc.* **2013**, *135*, 15873–15879.

[29] S. Hauke, A. von Appen, T. Quidwai, J. Ries, R. Wombacher, *Chem. Sci.* **2017**, *8*, 559–566.

[30] J. B. Grimm, T. Klein, B. G. Kopek, G. Shtengel, H. F. Hess, M. Sauer, L. D. Lavis, *Angew. Chem. Int. Ed.* **2016**, *55*, 1723–1727.

[31] V. N. Belov, C. A. Wurm, V. P. Boyarskiy, S. Jakobs, S. W. Hell, *Angew. Chem. Int. Ed.* **2010**, *49*, 3520–3523.

[32] A. Baeyer, *Ber. Dtsch. Chem. Ges.* **1871**, *4*, 555–558.

[33] J. B. Grimm, A. J. Sung, W. R. Legant, P. Hulamm, S. M. Matlosz, E. Betzig, L. D. Lavis, *ACS Chem. Biol.* **2013**, *8*, 1303–1310.

[34] N. Saruyama, Y. Sakakura, T. Asano, T. Nishiuchi, H. Sasamoto, H. Kodama, *Anal. Biochem.* **2013**, *441*, 58–62.

[35] W.-C. Sun, K. R. Gee, D. H. Klaubert, R. P. Haugland, *J. Org. Chem.* **1997**, *62*, 6469–6475.

[36] T. D. Gruber, C. Krishnamurthy, J. B. Grimm, M. R. Tadross, L. M. Wysocki, Z. J. Gartner, L. D. Lavis, *ACS Chem. Biol.* **2018**, *13*, 2888–2896.

[37] L. D. Lavis, T.-Y. Chao, R. T. Raines, *Chem. Sci.* **2011**, *2*, 521–530.

[38] B. Rotman, B. W. Papermaster, *PNAS* **1966**, *55*, 134–141.

[39] R. Lincoln, M. L. Bossi, M. Remmel, E. D'Este, A. N. Butkevich, S. W. Hell, *Nat. Chem.* **2022**, *14*, 1013–1020.

[40] L. Lin, P. Jiang, Z. Bao, W. Pang, S. Ding, M.-J. Yin, P. Li, B. Gu in *Optical Imaging in Human Disease and Biological Research*, (Eds.: X. Wei, B. Gu), Springer Singapore, Singapore, **2021**, pp. 1–22.

[41] V. Ntziachristos, *Nat. Methods* **2010**, *7*, 603–614.

[42] S. P. Singh, S. Siddhanta in *Modern Techniques of Spectroscopy: Basics, Instrumentation, and Applications*, (Eds.: D. K. Singh, M. Pradhan, A. Materny), Springer Singapore, Singapore, **2021**, pp. 637–660.

[43] S. Manohar, D. Razansky, *Adv. Opt. Photon.* **2016**, *8*, 586–617.

[44] In *Principles of Fluorescence Spectroscopy*, (Ed.: J. R. Lakowicz), Springer US, Boston, MA, **2006**, pp. 623–673.

[45] M. Minsky, *Scanning* **1988**, *10*, 128–138.

[46] M. Minsky, Microscopy apparatus, Patent US 3013467A, **1961**.

[47] S. Inoué in *Handbook Of Biological Confocal Microscopy*, (Ed.: J. B. Pawley), Springer US, Boston, MA, **2006**, pp. 1–19.

[48] S. K. Saka in *Super-Resolution Microscopy Techniques in the Neurosciences*, (Eds.: E. F. Fornasiero, S. O. Rizzoli), Humana Press, Totowa, NJ, **2014**, pp. 1–11.

[49] S. Dunst, P. Tomancak, *Genetics* **2019**, *211*, 15–34.

[50] Y. Zhang, F. M. Raymo, *Methods Appl. Fluoresc.* **2020**, *8*, 032002.

[51] N. P. Outreach, The Nobel Prize in Chemistry 2014, can be found under https://www.nobelprize.org/prizes/chemistry/2014/summary/ (accessed September 2022), **2014**.

[52] S. W. Hell, J. Wichmann, *Opt. Lett.* **1994**, *19*, 780–782.

[53] M. A. Lauterbach, C. Eggeling in *Super-Resolution Microscopy Techniques in the Neurosciences*, (Eds.: E. F. Fornasiero, S. O. Rizzoli), Humana Press, Totowa, NJ, **2014**, pp. 41–71.

[54] S. Jeong, J. Widengren, J.-C. Lee, *Nanomaterials* **2022**, *12*, DOI 10.3390/nano12010021.

[55] C. A. Wurm, K. Kolmakov, F. Göttfert, H. Ta, M. Bossi, H. Schill, S. Berning, S. Jakobs, G. Donnert, V. N. Belov, S. W. Hell, *Optical Nanoscopy* **2012**, *1*, 7.

[56] M. J. Rust, M. Bates, X. Zhuang, *Nat. Methods* **2006**, *3*, 793–796.

[57] G. T. Dempsey, J. C. Vaughan, K. H. Chen, M. Bates, X. Zhuang, *Nat. Methods* **2011**, *8*, 1027–1036.

[58] M. Heilemann, S. van de Linde, M. Schüttpelz, R. Kasper, B. Seefeldt, A. Mukherjee, P. Tinnefeld, M. Sauer, *Angew. Chem. Int. Ed.* **2008**, *47*, 6172–6176.

[59] H. Takakura, Y. Zhang, R. S. Erdmann, A. D. Thompson, Y. Lin, B. McNellis, F. Rivera-Molina, S.-n. Uno, M. Kamiya, Y. Urano, J. E. Rothman, J. Bewersdorf, A. Schepartz, D. Toomre, *Nat. Biotechnol.* **2017**, *35*, 773–780.

[60] W.-h. Li, G. Zheng, *Photochem. Photobiol. Sci.* **2012**, *11*, 460–471.

[61] C. Brieke, F. Rohrbach, A. Gottschalk, G. Mayer, A. Heckel, *Angew. Chem. Int. Ed.* **2012**, *51*, 8446–8476.

[62] F. Balzarotti, Y. Eilers, K. C. Gwosch, A. H. Gynnå, V. Westphal, F. D. Stefani, J. Elf, S. W. Hell, *Science* **2017**, *355*, 606–612.

[63] R. Schmidt, T. Weihs, C. A. Wurm, I. Jansen, J. Rehman, S. J. Sahl, S. W. Hell, *Nat. Commun.* **2021**, *12*, 1478.

[64] M. Remmel, L. Scheiderer, A. N. Butkevich, M. L. Bossi, S. W. Hell, *bioRxiv* **2022**, DOI 10.1101/2022.08.29.505670.

[65] Y. Chu, J. Park, E. Kim, S. Lee, *Materials* **2021**, *14*, DOI 10.3390/ma14154180.

[66] Cole, Davies, Hyde, Ashford, *J. Microsc.* **2000**, *197*, 239–249.

[67] J. Kapuscinski, *Biotech. Histochem.* **1995**, *70*, 220–233.

[68] S. A. Latt, G. Stetten, *J. Histochem. Cytochem.* **1976**, *24*, 24–33.

[69] A. C. Schmit, A. M. Lambert, *The Plant Cell* **1990**, *2*, 129–138.

[70] J. Riedl, A. H. Crevenna, K. Kessenbrock, J. H. Yu, D. Neukirchen, M. Bista, F. Bradke, D. Jenne, T. A. Holak, Z. Werb, M. Sixt, R. Wedlich-Soldner, *Nat. Methods* **2008**, *5*, 605–607.

[71] W. Chi, L. Huang, C. Wang, D. Tan, Z. Xu, X. Liu, *Mater. Chem. Front.* **2021**, *5*, 7012–7021.

[72] G. Beliu, A. J. Kurz, A. C. Kuhlemann, L. Behringer-Pliess, M. Meub, N. Wolf, J. Seibel, Z.-D. Shi, M. Schnermann, J. B. Grimm, L. D. Lavis, S. Doose, M. Sauer, *Commun. Biol.* **2019**, *2*, 261.

[73] G. Knorr, E. Kozma, J. M. Schaart, K. Németh, G. Török, P. Kele, *Bioconjugate Chem.* **2018**, *29*, 1312–1318.

[74] L. Liu, D. Zhang, M. Johnson, N. K. Devaraj, *Nat. Chem.* **2022**, *14*, 1078–1085.

[75] G. S. Kumar, Q. Lin, *ChemBioChem* **2022**, *23*, e202200175.

[76] *Chemistry & Biology* **2003**, *10*, 313–317.

[77] G. V. Los, L. P. Encell, M. G. McDougall, D. D. Hartzell, N. Karassina, C. Zimprich, M. G. Wood, R. Learish, R. F. Ohana, M. Urh, D. Simpson, J. Mendez, K. Zimmerman, P. Otto, G. Vidugiris, J. Zhu, A. Darzins, D. H. Klaubert, R. F. Bulleit, K. V. Wood, *ACS Chem. Biol.* **2008**, *3*, 373–382.

[78] J. Wilhelm, S. Kühn, M. Tarnawski, G. Gotthard, J. Tünnermann, T. Tänzer, J. Karpenko, N. Mertes, L. Xue, U. Uhrig, J. Reinstein, J. Hiblot, K. Johnsson, *Biochemistry* **2021**, *60*, 2560–2575.

[79] D. R. Dempsey, H. Jiang, J. H. Kalin, Z. Chen, P. A. Cole, *J. Am. Chem. Soc.* **2018**, *140*, 9374–9378.

[80] E. A. Specht, E. Braselmann, A. E. Palmer, *Annu. Rev. Physiol.* **2017**, *79*, 93–117.

[81] A. P. Demchenko in *Introduction to Fluorescence Sensing*, Springer International Publishing, Cham, **2015**, pp. 1–37.

[82] K. P. Carter, A. M. Young, A. E. Palmer, *Chem. Rev.* **2014**, *114*, 4564–4601.

[83] L. Li, J. Wang, S. Xu, C. Li, B. Dong, *Front. Chem.* **2022**, *10*, 875241.

[84] J.-T. Hou, W. X. Ren, K. Li, J. Seo, A. Sharma, X.-Q. Yu, J. S. Kim, *Chem. Soc. Rev.* **2017**, *46*, 2076–2090.

[85] X. Luo, H. Yang, H. Wang, Z. Ye, Z. Zhou, L. Gu, J. Chen, Y. Xiao, X. Liang, X. Qian, Y. Yang, *Anal. Chem.* **2018**, *90*, 5803–5809.

[86] J. B. Grimm, T. D. Gruber, G. Ortiz, T. A. Brown, L. D. Lavis, *Bioconjugate Chem.* **2016**, *27*, 474–480.

[87] J. Chan, S. C. Dodani, C. J. Chang, *Nat. Chem.* **2012**, *4*, 973–984.

[88] E. A. Halabi, Z. Thiel, N. Trapp, D. Pinotsi, P. Rivera-Fuentes, *J. Am. Chem. Soc.* **2017**, *139*, PMID: 28820941, 13200–13207.

[89] Z. Thiel, P. Rivera-Fuentes, *Angew. Chem. Int. Ed.* **2019**, *58*, 11474–11478.

[90] T. Gessner, U. Mayer in *Ullmann's Encyclopedia of Industrial Chemistry*, John Wiley & Sons, Ltd, **2000**.

[91] Y. Hatano in *Chemistry and Applications of Leuco Dyes*, (Ed.: R. Muthyala), Springer US, Boston, MA, **2002**, pp. 159–205.

[92] J. B. Grimm, T. A. Brown, A. N. Tkachuk, L. D. Lavis, *ACS Cent. Sci.* **2017**, *3*, 975–985.

[93] Y. Koide, Y. Urano, K. Hanaoka, T. Terai, T. Nagano, *ACS Chem. Biol.* **2011**, *6*, 600–608.

[94] F. Deng, Z. Xu, *Chin. Chem. Lett.* **2019**, *30*, 1667–1681.

[95] J. B. Grimm, A. K. Muthusamy, Y. Liang, T. A. Brown, W. C. Lemon, R. Patel, R. Lu, J. J. Macklin, P. J. Keller, N. Ji, L. D. Lavis, *Nat. Methods* **2017**, *14*, 987–994.

[96] A. N. Butkevich, G. Y. Mitronova, S. C. Sidenstein, J. L. Klocke, D. Kamin, D. N. H. Meineke, E. D'Este, P.-T. Kraemer, J. G. Danzl, V. N. Belov, S. W. Hell, *Angew. Chem. Int. Ed.* **2016**, *55*, 3290–3294.

[97] L. Wang, M. Tran, E. D'Este, J. Roberti, B. Koch, L. Xue, K. Johnsson, *Nat. Chem.* **2020**, *12*, 165–172.

[98] E. Azuma, N. Nakamura, K. Kuramochi, T. Sasamori, N. Tokitoh, I. Sagami, K. Tsubaki, *J. Org. Chem.* **2012**, *77*, 3492–3500.

[99] X.-F. Zhang, I. Zhang, L. Liu, *Photochem Photobiol.* **2010**, *86*, 492–498.

[100] L. D. Lavis, T. J. Rutkoski, R. T. Raines, *Anal. Chem.* **2007**, *79*, 6775–6782.

[101] S.-n. Uno, M. Kamiya, T. Yoshihara, K. Sugawara, K. Okabe, M. C. Tarhan, H. Fujita, T. Funatsu, Y. Okada, S. Tobita, Y. Urano, *Nat. Chem.* **2014**, *6*, 681–689.

[102] K. N. More, S.-K. Mun, J. Kang, J.-J. Kim, S.-T. Yee, D.-J. Chang, *Dyes Pigm.* **2021**, *184*, 108785.

[103] J. R. Casey, S. Grinstein, J. Orlowski, *Nat. Rev. Mol. Cell Biol.* **2010**, *11*, 50–61.

[104] L. D. Lavis, *Biochemistry* **2021**, *60*, 3539–3546.

[105] J. E. Whitaker, R. P. Haugland, D. Ryan, P. C. Hewitt, R. P. Haugland, F. G. Prendergast, *Anal. Biochem.* **1992**, *207*, 267–279.

[106] T. Kobayashi, Y. Urano, M. Kamiya, T. Ueno, H. Kojima, T. Nagano, *J. Am. Chem. Soc.* **2007**, *129*, 6696–6697.

[107] D. Puliti, D. Warther, C. Orange, A. Specht, M. Goeldner, *Bioorg. Med. Chem.* **2011**, *19*, 1023–1029.

[108] P. Wang, *Asian J. Org. Chem.* **2013**, *2*, 452–464.

[109] I. Aujard, C. Benbrahim, M. Gouget, O. Ruel, J.-B. Baudin, P. Neveu, L. Jullien, *Chem. Eur. J.* **2006**, *12*, 6865–6879.

[110] J. Kohl-Landgraf, F. Buhr, D. Lefrancois, J.-M. Mewes, H. Schwalbe, A. Dreuw, J. Wachtveitl, *J. Am. Chem. Soc.* **2014**, *136*, 3430–3438.

[111] M. Weber, T. A. Khan, L. J. Patalag, M. Bossi, M. Leutenegger, V. N. Belov, S. W. Hell, *Chem. Eur. J.* **2021**, *27*, 451–458.

[112] A. N. Butkevich, M. Weber, A. R. Cereceda Delgado, L. M. Ostersehlt, E. D'Este, S. W. Hell, *J. Am. Chem. Soc.* **2021**, *143*, 18388–18393.

[113] R. M. LoPachin, T. Gavin, *Chem. Res. Toxicol.* **2014**, *27*, 1081–1091.

[114] S. Moumtaz, B. C. Percival, D. Parmar, K. L. Grootveld, P. Jansson, M. Grootveld, *Sci Rep* **2019**, *9*, 4125.

[115] A. A. Laskar, H. Younus, *Drug Metab. Rev.* **2019**, *51*, 42–64.

[116] V. N. Belov, G. Y. Mitronova, M. L. Bossi, V. P. Boyarskiy, E. Hebisch, C. Geisler, K. Kolmakov, C. A. Wurm, K. I. Willig, S. W. Hell, *Chem. Eur. J.* **2014**, *20*, 13162–13173.

[117] J. B. Grimm, B. P. English, J. Chen, J. P. Slaughter, Z. Zhang, A. Revyakin, R. Patel, J. J. Macklin, D. Normanno, R. H. Singer, T. Lionnet, L. D. Lavis, *Nat. Methods* **2015**, *12*, 244–250.

[118] A. N. Butkevich, *Org. Lett.* **2021**, *23*, 2604–2609.

[119] J. B. Grimm, L. D. Lavis, *Org. Lett.* **2011**, *13*, 6354–6357.

[120] Y. Imazaki, E. Shirakawa, R. Ueno, T. Hayashi, *J. Am. Chem. Soc.* **2012**, *134*, 14760–14763.

[121] A. N. Butkevich, M. L. Bossi, G. Lukinavičius, S. W. Hell, *J. Am. Chem. Soc.* **2019**, *141*, 981–989.

[122] J. Bergman, B. Pettersson, V. Hasimbegovic, P. H. Svensson, *J. Org. Chem.* **2011**, *76*, 1546–1553.

[123] B. Ghaffari, S. M. Preshlock, D. L. Plattner, R. J. Staples, P. E. Maligres, S. W. Krska, R. E. Maleczka, M. R. Smith, *J. Am. Chem. Soc.* **2014**, *136*, 14345–14348.

[124] G. R. Fulmer, A. J. M. Miller, N. H. Sherden, H. E. Gottlieb, A. Nudelman, B. M. Stoltz, J. E. Bercaw, K. I. Goldberg, *Organometallics* **2010**, *29*, 2176–2179.

[125] S. Budavari, M. J. O'Neil, A. Smith, P. E. Heckelman, *The Merck index: an encyclopedia of chemicals, drugs, and biologicals*, 7th ed., Merck, Rahway, N.J., U.S.A., **1989**.

[126] L. Porrès, A. Holland, L.-O. Pålsson, A. P. Monkman, C. Kemp, A. Beeby, *J. Fluoresc.* **2006**, *16*, 267–273.

[127] K. Uno, M. L. Bossi, T. Konen, V. N. Belov, M. Irie, S. W. Hell, *Adv. Opt. Mater.* **2019**, *7*, 1801746.

[128] M. H. Deniel, D. Lavabre, J. C. Micheau in *Vol. 2*, (Eds.: J. C. Crano, R. J. Guglielmetti), Springer, New York, NY, **2002**, pp. 167–209.

[129] Y. Koide, R. Kojima, K. Hanaoka, K. Numasawa, T. Komatsu, T. Nagano, H. Kobayashi, Y. Urano, *Commun. Chem.* **2019**, *2*, 94.

[130] F. E. Critchfield, J. A. Gibson, J. L. Hall, *J. Am. Chem. Soc.* **1953**, *75*, 1991–1992.

[131] J. V. Thevathasan, M. Kahnwald, K. Cieśliński, P. Hoess, S. K. Peneti, M. Reitberger, D. Heid, K. C. Kasuba, S. J. Hoerner, Y. Li, Y.-L. Wu, M. Mund, U. Matti, P. M. Pereira, R. Henriques, B. Nijmeijer, M. Kueblbeck, V. J. Sabinina, J. Ellenberg, J. Ries, *Nat. Methods* **2019**, *16*, 1045–1053.

[132] T. Jegou, I. Chung, G. Heuvelman, M. Wachsmuth, S. M. Gorisch, K. M. Greulich-Bode, P. Boukamp, P. Lichter, K. Rippe, *Mol. Biol. Cell* **2009**, *20*, 2070–2082.

[133] S. Bolte, F. P. Cordelieres, *Journal of Microscopy* **2006**, *224*, 213–232.

[134] C. A. Schneider, W. S. Rasband, K. W. Eliceiri, *Nat. Methods* **2012**, *9*, 671–675.

[135] D. K. Sharma, S. T. Adams, K. L. Liebmann, A. Choi, S. C. Miller, *Org. Lett.* **2019**, *21*, 1641–1644.

[136] B. C. Dickinson, C. Huynh, C. J. Chang, *J. Am. Chem. Soc.* **2010**, *132*, 5906–5915.

[137] R. M. Stolley, W. Guo, J. Louie, *Org. Lett.* **2012**, *14*, 322–325.

[138] A. N. Butkevich, H. Ta, M. Ratz, S. Stoldt, S. Jakobs, V. N. Belov, S. W. Hell, *ACS Chem. Biol.* **2018**, *13*, 475–480.

[139] D. D. Nekrasov, *Russ. J. Org. Chem.* **2004**, *40*, 1387–1402.

[140] L. M. Baumgartner, J. M. Dennis, N. A. White, S. L. Buchwald, K. F. Jensen, *Org. Process Res. Dev.* **2019**, *23*, 1594–1601.

[141] S. N. M. Boddapati, N. Polam, B. R. Mutchu, H. B. Bollikolla, *New J. Chem.* **2018**, *42*, 918–922.

[142] X. Ding, M. Huang, Z. Yi, D. Du, X. Zhu, Y. Wan, *J. Org. Chem.* **2017**, *82*, 5416–5423.

[143] S. V. Voitekhovich, A. N. Vorob'ev, P. N. Gaponik, O. A. Ivashkevich, *Chem. Heterocycl. Compd.* **2005**, *41*, 999–1004.

[144] G. Aridoss, K. K. Laali, *Eur. J. Org. Chem.* **2011**, *2011*, 2827–2835.

[145] S. N. Dighe, K. S. Jain, K. V. Srinivasan, *Tetrahedron Lett.* **2009**, *50*, 6139–6142.

[146] M. Martineau, A. Somasundaram, J. B. Grimm, T. D. Gruber, D. Choquet, J. W. Taraska, L. D. Lavis, D. Perrais, *Nat. Commun.* **2017**, *8*, 1412.

[147] F. Hu, Y. Huang, Y. Xiao, Y. Li, X. Luo, X. Qian, Y. Yang, *Anal. Methods* **2021**, *13*, 3012–3016.

[148] G. Y. Mitronova, G. Lukinavičius, A. N. Butkevich, T. Kohl, V. N. Belov, S. E. Lehnart, S. W. Hell, *Sci Rep* **2017**, *7*, 12319.

[149] T. L. Riss, R. A. Moravec, A. L. Niles, S. Duellman, H. A. Benink, T. J. Worzella, L. Minor., Cell Viability Assays, can be found under https://www.ncbi.nlm.nih.gov/books/NBK144065/ (accessed September 2022), **2013**.

[150] G. Lukinavičius, C. Blaukopf, E. Pershagen, A. Schena, L. Reymond, E. Derivery, M. Gonzalez-Gaitan, E. D'Este, S. W. Hell, D. Wolfram Gerlich, K. Johnsson, *Nat. Commun.* **2015**, *6*, 8497.

[151] S. P. Brown, A. B. Smith, *J. Am. Chem. Soc.* **2015**, *137*, 4034–4037.

[152] M. J. Tucker, J. R. Courter, J. Chen, O. Atasoylu, A. B. Smith III, R. M. Hochstrasser, *Angew. Chem. Int. Ed.* **2010**, *49*, 3612–3616.

[153] A. Loredo, J. Tang, L. Wang, K.-L. Wu, Z. Peng, H. Xiao, *Chem. Sci.* **2020**, *11*, 4410–4415.

[154] J. Maes, L. Verlooy, O. E. Buenafe, P. A. M. de Witte, C. V. Esguerra, A. D. Crawford, *PLOS ONE* **2012**, *7*, 1–9.

[155] J. Tang, M. A. Robichaux, K.-L. Wu, J. Pei, N. T. Nguyen, Y. Zhou, T. G. Wensel, H. Xiao, *J. Am. Chem. Soc.* **2019**, *141*, 14699–14706.

[156] A. Corsaro, V. Pistarà, *Tetrahedron* **1998**, *54*, 15027–15062.

[157] J. W. Shaw, D. H. Grayson, I. Rozas, *Eur. J. Org. Chem.* **2014**, *2014*, 3565–3569.

[158] L. Gattermann, *Ber. Dtsch. Chem. Ges.* **1899**, *32*, 1127–1135.

[159] M. Wroński, *Talanta* **1977**, *24*, 347–354.

[160] V. V. Russkikh, A. V. Konstantinova, V. N. Berezhnaya, T. N. Gerasimova, V. V. Shelkovnikov, *Russ. J. Org. Chem.* **2005**, *41*, 57–60.

[161] N. O. McHedlov-Petrosyan, N. A. Vodolazkaya, V. P. Martynova, D. V. Samoilov, A. V. El'tsov, *Russ. J. Gen. Chem.* **2002**, *72*, 785–792.

[162] C. Lai, B. J. Backes, *Tetrahedron Lett.* **2007**, *48*, 3033–3037.

[163] M. Kreis, S. Bräse, *Adv. Synth. Catal.* **2005**, *347*, 313–319.

[164] E. W. Miller, O. Tulyathan, E. Y. Isacoff, C. J. Chang, *Nat. Chem. Biol.* **2007**, *3*, 263–267.

[165] J. H. Han, Y. E. Kwon, J.-H. Sohn, D. H. Ryu, *Tetrahedron* **2010**, *66*, 1673–1677.

[166] T. Peng, D. Yang, *Org. Lett.* **2010**, *12*, 496–499.

[167] Y. Wang, Y. Zhou, Q. Song, *Chem. Commun.* **2020**, *56*, 6106–6109.

[168] K. Škoch, I. Císařová, P. Štěpnička, *Chem. Eur. J.* **2018**, *24*, 13788–13791.

[169] S. C. Fields, M. H. Parker, W. R. Erickson, *J. Org. Chem.* **1994**, *59*, 8284–8287.

[170] W. D. Lambert, Y. Fang, S. Mahapatra, Z. Huang, C. W. am Ende, J. M. Fox, *J. Am. Chem. Soc.* **2019**, *141*, 17068–17074.

[171] S. Kronister, D. Svatunek, C. Denk, H. Mikula, *Synlett* **2018**, *29*, 1297–1302.

[172] T. Mineno, T. Ueno, Y. Urano, H. Kojima, T. Nagano, *Org. Lett.* **2006**, *8*, 5963–5966.

[173] A. M. Christianson, F. P. Gabbaï, *Inorg. Chem.* **2016**, *55*, 5828–5835.

[174] W. Piao, S. Tsuda, Y. Tanaka, S. Maeda, F. Liu, S. Takahashi, Y. Kushida, T. Komatsu, T. Ueno, T. Terai, T. Nakazawa, M. Uchiyama, K. Morokuma, T. Nagano, K. Hanaoka, *Angew. Chem. Int. Ed.* **2013**, *52*, 13028–13032.

[175] A. Katori, E. Azuma, H. Ishimura, K. Kuramochi, K. Tsubaki, *J. Org. Chem.* **2015**, *80*, 4603–4610.

[176] P. Sudta, P. Jiarawapi, A. Suksamrarn, P. Hongmanee, S. Suksamrarn, *Chem. Pharm. Bull.* **2013**, *61*, 194–203.

[177] Y. Dong, N. Du, X. Li, L. Zheng, G. Liu, *Org. Lett.* **2015**, *17*, 4110–4113.

[178] A. N. Butkevich, V. N. Belov, K. Kolmakov, V. V. Sokolov, H. Shojaei, S. C. Sidenstein, D. Kamin, J. Matthias, R. Vlijm, J. Engelhardt, S. W. Hell, *Chem. Eur. J.* **2017**, *23*, 12114–12119.

Chapter 9

Appendix

Table 9.1–Table 9.5, Table 9.7, Figure 9.1–Figure 9.14, and NMR spectra of compounds **NCR1**, **NCR2**, **NCR3**, **NCR1-Halo**, **NCR2-Halo**, **NCR3-Halo**, **NCR1-SNAP**, **10**, **13**, **14**, **15**, **16**, **18**, **24**, **25**, **26** and **27** have been previously reported and are reproduced from Ref.[1] with permission from the Royal Society of Chemistry.

9.1 Supplementary Tables

9.1.1 Chapter 4

Table 9.1 – Optical parameters of the fluorescence intensity changes upon addition of detergent (Figure 4.5B, p. 61)

Dye	TMR-Halo	NCR1-Halo	NCR2-Halo	NCR3-Halo	6-SiR-Halo	1a-Halo
Excitation wavelength [nm]	500	500	580	600	600	450

Excitation wavelengths for recording the full emission spectra of dyes in presence of SDS, CTAB, *or* no detergent.

Table 9.2 – Optical parameters of the fluorescence intensity changes upon addition of HaloTag®7 protein (Figure 4.5C, p. 61).

Dye	TMR-Halo	NCR1-Halo	NCR2-Halo	NCR3-Halo	6-SiR-Halo	1a-Halo
Excitation wavelength [nm]	540	540	610	640	640	490
Emission wavelength [nm]	580	580	650	680	680	530

Excitation and emission wavelengths for recording fluorescence intensities of dyes in presence of HaloTag7 protein *or* no protein.

Table 9.3 – Optical parameters of HaloTag7 labeling kinetics (Figure 4.6, p. 62).

Dye	TMR-HALO	NCR1-Halo	NCR2-Halo	NCR3-Halo	1a-Halo
Excitation wavelength [nm]	540-20	540-20	590-50	590-50	482-16
Dichromic filter	LP 566	LP 566	LP 639	LP 639	LP 504
Emission wavelength [nm]	590-20	590-20	675-50	675-50	530-40
Gain	1500	1400	1200	1000	1000

Excitation and emission filter - bandwidth, dichronic mirror and gain for recording FP changes of dyes binding to HaloTag7 protein.

Table 9.4 – Statistical information on CellTiter-Blue cell viability assay.

Fig.	condition	concentration	N_{exp}	$\mathbf{INT_{fl,norm}}$		p-value
				mean	SD	
Figure 4.8	control	—	630	1.000	0.091	—
	13a	1 µM	63	1.081	0.039	$8 \cdot 10^{-12}$
	13a	5 µM	63	1.058	0.040	$6 \cdot 10^{-7}$
	13a	10 µM	63	1.091	0.017	$1 \cdot 10^{-14}$
	13a	33 µM	63	1.066	0.056	$3 \cdot 10^{-8}$
	13a	100 µM	63	0.890	0.023	$2 \cdot 10^{-20}$
	13a	333 µM	63	0.150	0.019	$< 10^{-308}$
	14a	1 µM	63	0.992	0.077	$5 \cdot 10^{-1}$
	14a	5 µM	63	1.079	0.014	$2 \cdot 10^{-11}$
	14a	10 µM	63	1.008	0.048	$5 \cdot 10^{-1}$
	14a	33 µM	63	1.045	0.102	$2 \cdot 10^{-4}$
	14a	100 µM	63	0.932	0.048	$8 \cdot 10^{-9}$
	14a	333 µM	63	0.095	0.013	$< 10^{-308}$
	TMR	1 µM	63	1.048	0.052	$5 \cdot 10^{-5}$
	TMR	5 µM	63	1.113	0.028	$4 \cdot 10^{-21}$
	TMR	10 µM	63	1.149	0.030	$4 \cdot 10^{-34}$
	TMR	33 µM	63	1.143	0.048	$3 \cdot 10^{-31}$
	TMR	100 µM	63	0.830	0.025	$6 \cdot 10^{-43}$
	TMR	333 µM	63	0.119	0.024	$< 10^{-308}$
	DMSO	0.02%	63	0.995	0.039	$6 \cdot 10^{-1}$
	DMSO	0.2%	63	1.004	0.057	$8 \cdot 10^{-1}$
	DMSO	0.66%	63	1.075	0.022	$2 \cdot 10^{-10}$
	DMSO	2.00%	63	0.816	0.021	$4 \cdot 10^{-49}$
	DMSO	6.60%	63	0.087	0.005	$< 10^{-308}$
	DMSO	20.0%	63	0.000	0.001	$< 10^{-308}$
Figure 9.10	control	—	504	1.000	0.084	—
	TX100	1.00%	63	0.000	0.001	$< 10^{-308}$

NCR1-Halo	5 µM	63	1.076	0.042	$7 \cdot 10^{-12}$
NCR1-SNAP	5 µM	63	1.068	0.051	$1 \cdot 10^{-9}$
NCR2-Halo	5 µM	63	1.033	0.050	$2 \cdot 10^{-3}$
NCR3-Halo	5 µM	63	0.964	0.100	$2 \cdot 10^{-3}$
13a	5 µM	63	1.058	0.040	$9 \cdot 10^{-8}$
14a	5 µM	63	1.079	0.014	$5 \cdot 10^{-13}$
2a	5 µM	63	1.086	0.081	$1 \cdot 10^{-13}$
TMR-Halo	5 µM	63	1.030	0.061	$2 \cdot 10^{-13}$
JF_{549}-Halo	5 µM	63	0.984	0.031	$3 \cdot 10^{-117}$
JF_{585}-Halo	5 µM	63	0.918	0.050	$7 \cdot 10^{-39}$
TMR	5 µM	63	0.679	0.044	$1 \cdot 10^{-23}$
JF_{549}	5 µM	63	0.848	0.037	$8 \cdot 10^{-48}$

with: N_{exp} = number of experiments; $\mathbf{INT_{fl,norm}}$ = normalized fluorescence intensity; p-value = significance of difference to control; Tx100 - Triton X100.

Table 9.5 – Statistical information to holographic imaging.

Fig.	condition	conc.	N_{exp}	N_{cells}	mean [A]	SD [A]	p-value
Figure 4.8	control	—	19	22713	364	32	—
	NCR1-Halo	5 µM	15	18196	374	26	$4 \cdot 10^{-1}$
	NCR1-SNAP	5 µM	18	23642	392	26	$6 \cdot 10^{-3}$
	NCR2-Halo	5 µM	19	23117	376	26	$2 \cdot 10^{-1}$
	NCR3-Halo	5 µM	19	23790	397	28	$2 \cdot 10^{-3}$
	13a	5 µM	18	23882	401	26	$7 \cdot 10^{-4}$
	14a	5 µM	18	20932	382	36	$1 \cdot 10^{-1}$
	2a	5 µM	16	17873	363	34	$9 \cdot 10^{-1}$
	TMR-Halo	5 µM	20	23532	384	30	$5 \cdot 10^{-2}$
	JF_{549}-Halo	5 µM	18	11254	237	32	$1 \cdot 10^{-13}$
	JF_{585}-Halo	5 µM	19	24520	379	30	$1 \cdot 10^{-1}$
	TMR	5 µM	17	21461	383	27	$7 \cdot 10^{-2}$
	JF_{549}	5 µM	19	20955	354	48	$5 \cdot 10^{-1}$
Figure 9.11	control	—	19	22713	2.80	0.43	—
	NCR1-Halo	5 µM	15	18196	3.34	0.62	0.297 ± 0.289
	NCR1-SNAP	5 µM	18	23642	2.99	0.65	0.480 ± 0.285
	NCR2-Halo	5 µM	19	23117	3.42	0.37	0.060 ± 0.156
	NCR3-Halo	5 µM	19	23790	3.26	0.59	0.247 ± 0.303
	13a	5 µM	18	23882	2.97	0.52	0.492 ± 0.266
	14a	5 µM	18	20932	3.30	0.44	0.267 ± 0.306
	2a	5 µM	16	17873	3.40	0.46	0.122 ± 0.210
	TMR-Halo	5 µM	20	23532	2.65	0.45	0.309 ± 0.254
	JF_{549}-Halo	5 µM	18	11254	1.02	0.17	0.009 ± 0.060
	JF_{585}-Halo	5 µM	19	24520	3.22	0.75	0.209 ± 0.225
	TMR	5 µM	17	21461	3.13	0.67	0.306 ± 0.278
	JF_{549}	5 µM	19	20955	2.86	0.38	0.554 ± 0.275

with: N_{exp} = number of experiments; $\mathbf{N_{cells}}$ = number of cells analyzed; p-value = significance of difference to control. with: N_{exp} = number of experiments; $\mathbf{INT_{fl,norm}}$ = normalized fluorescence intensity; p-value = significance of difference to control. [A] Measured values: Cell cyle lengths in minutes (for Figure 4.89 and increase of cell count after 48 h in fold change (for Figure 9.11).

Table 9.6 – Photophysical data of *N*-cyanocoumarine **29** compared to hydroxy coumarin **28** and AMCA (**30**)

Dye	$\lambda_{\mathbf{abs}}$ **[nm]**	$\epsilon(\lambda_{\mathbf{abs}})$ $[\cdot\mathbf{10^3}$ $\mathbf{M^{-1}cm^{-1}}]$	$\lambda_{\mathbf{em}}$ **[nm]**	$\mathbf{\Phi_{fl}}$	$\tau_{\mathbf{fl}}$ **[ns]**
Coumarines					
30	342 (348)	18 (20)	447 (428)	0.83[A,B]	4.61[A]
28	361 (327, 372)	20 (n.d)	447 (384, 444)	0.88[A,B]	5.27[A]
29	361 (373)	23 (25)	481(478)	0.70[A,B]	4.46[A]

Absorption maxima λ_{abs}, extinction coefficient $\epsilon(\lambda_{abs})$, emission maxima λ_{em} fluorescence quantum yields, and Φ_{fl} fluorescence lifetimes τ_{fl} were determined in 0.1 M phosphate buffer at pH 10 and EtOH + 1 % NEt_3 (in brackets), unless stated otherwise. n.d. = not determined. [A] Measured at pH 11. [B] Relative Φ_{fl} measurement using quinine sulfate dihydrate (1 mM in 0.1 Molar H_2SO_4). Conducted by Dr. Mariano Bossi.

9.1.2 Imaging parameters for Chapter 4 and Chapter 5.4

Table 9.7 – Imaging parameters for the acquisition of confocal and STED imaging.

Fig.	dye	excitation (wavelength, power)	STED (wavelength, power)	delay [ns]	gate [ns]	detection window [nm]	pixel size [nm]	dwell time [µs]	line repetition	multi-plexing
Figure 4.7A	**14a**	561nm, 62µW	—	—	—	570-640	80	10	1	frame
	TMR	561nm, 62µW	—	—	—	570-640	80	10	1	frame
	NCR1-Halo	561nm, 62µW	—	—	—	570-640	80	10	1	frame
	TMR-Halo	561nm, 62µW	—	—	—	570-640	80	10	1	frame
	Hoechst	405nm, 1µW	—	—	—	420-475	80	10	2	frame
Figure 4.7B	TMR-Halo	561nm, 62µW	—	—	—	570-640	80	10	1	frame
	ER-Tracker	405nm, 50µW	—	—	—	420-475	80	10	2	frame
Figure 4.9A	**NCR1-Halo**	561nm, 7µW	—	—	—	575-630	80	5	4	pixel
	SiR-Hoechst	640nm, 13µW	—	—	—	655-757	80	5	4	pixel
	LIVE 510	485nm, 33µW	—	—	—	500-545	80	5	4	frame
	ER-Tracker	405nm, 92µW	—	—	—	410-700	80	5	4	frame
Figure 4.9B	**NCR1-Halo**	561nm, 11µW	775nm, 368mW	0.75	8	570-630	25	3	40	line
	NCR1-Halo	561nm, 18µW	—	—	—	570-630	25	5	4	pixel
	SiR-Hoechst	640nm, 9µW	775nm, 220mW	0.75	8	650-757	25	3	40	line
	SiR-Hoechst	640nm, 3µW	—	—	—	650-757	25	5	4	pixel
Figure 9.12	**NCR2-Halo**	640nm, 37µW	775nm, 146mW	0.75	8	650-757	25	20	4	line

Table 9.7 – Imaging parameters for the acquisition of confocal and STED imaging.

Fig.	dye	excitation (wavelength, power)	STED (wavelength, power)	delay [ns]	gate [ns]	detection window [nm]	pixel size [nm]	dwell time [µs]	line repetition	multi-plexing
	LIVE 550	561nm, 17µW	775nm, 368mW	0.75	8	575-645	25	20	4	line
	Hoechst	405nm, 5µW	—	—	—	420-475	25	10	2	frame
	NCR2-Halo	640nm, 37µW	775nm, 146mW	0.75	8	650-757	25	20	4	line
	NCR2-Halo	640nm, 33µW	—	—	—	650-757	25	10	1	pixel
	LIVE 550	561nm, 17µW	775nm, 368mW	0.75	8	575-645	25	20	4	line
	LIVE 550	561nm, 15µW	—	—	—	575-645	25	10	1	pixel
Figure 9.13	**NCR1-SNAP**	561nm, 7µW	—	—	—	575-630	80	10	1	frame
	GeR-tubulin	640nm, 6µW	—	—	—	650-750	80	10	1	frame
	Mito-Tracker	485nm, 6µW	—	—	—	500-550	80	10	1	frame
	Hoechst	405nm, 1µW	—	—	—	420-475	80	10	1	frame
	NCR1-SNAP	561nm, 23µW	775nm, 750mW	1	10	570-630	25	3	5	frame
	NCR1-SNAP	561nm, 7µW	—	—	—	570-630	25	3	3	frame
	GeR-tubulin	640nm, 6µW	775nm, 146mW	0.85	10	650-757	25	3	20	line
	GeR-tubulin	640nm, 6µW	—	—	—	650-757	25	3	3	line
Figure 9.14	**NCR3-Halo**	640nm, 33µW	—	—	—	650-757	80	10	1	—
	NCR3-Halo	640nm, 136µW	775nm, 73mW	0.75	8	650-757	40	10	8	line

Table 9.7 – Imaging parameters for the acquisition of confocal and STED imaging.

Fig.	dye	excitation (wavelength, power)	STED (wavelength, power)	delay [ns]	gate [ns]	detection window [nm]	pixel size [nm]	dwell time [µs]	line repetition	multi-plexing
	NCR3-Halo	640nm, 67µW	—	—	—	650-763	40	10	1	line
Figure 5.3	**PaX(–)2-Halo**[A]	485nm, 26µW	—	—	—	500-600	70	20	2	—
	Hoechst	405nm, 53µW	—	—	—	420-470	70	20	2	line

Laser powers are measured in back focal apperatus. Abbreviations: delay = delay between excitation and STED pulse; gate = gated detection time; Hoechst = Hoechst 33342; ER Tracker = ER-Tracker Blue-White DPX; LIVE 510 = abberious LIVE 550 tubulin; LIVE 550 = abberious LIVE 550 tubulin; MitoTracker = MitoTracker Green FM. [A] Preactivated with 405 nm excitation laser (53 µW).

9.2 Supplementary Figures

9.2.1 Chapter 4

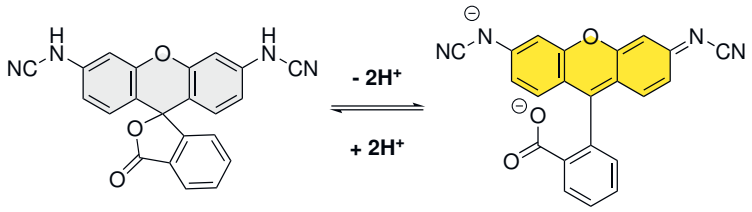

non-fluoroecent spirolactone

fluorescent form

a) Simplified equilibrium of **14a**.

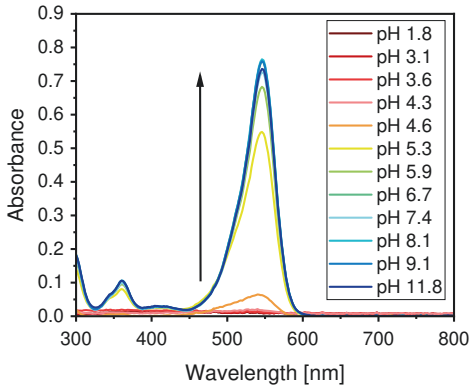

b) Absorption spectra at different pH.

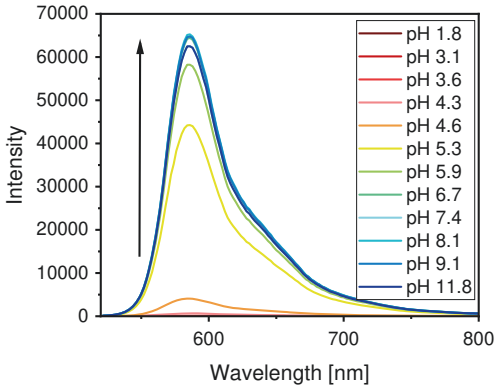

c) Emission spectra at different pH.

Figure 9.1 – Acid-base behavior of **14a**. (a) Simplified open-close equilibrium and non-fluorescent and fluorescent form of **14a**. (b) Absorption and (c) emission spectra (fluorescence excitation at 490 nm) of **14a** (10 µM) in phosphate buffers (0.1 M) with different pH values.

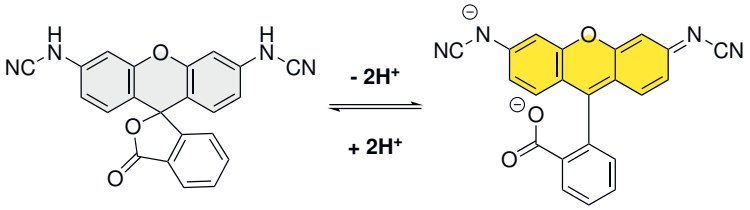

non-fluoroecent spirolactone

fluorescent form

a) Simplified equilibrium of **14a**.

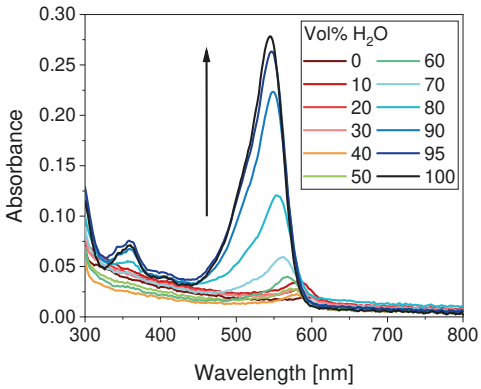

b) Absorption spectra at different Vol% H_2O.

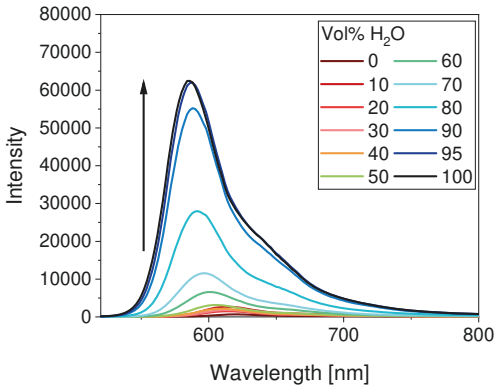

c) Emission spectra at different Vol% H_2O.

Figure 9.2 – Polarity dependency of **14a**. (a) Simplified open-close equilibrium and non-fluorescent and fluorescent form of **14a**. (b) Absorption and (c) emission spectra (fluorescence excitation at 490 nm) of **14a** (10 µM) in aqueous dioxane solutions with different Vol% H_2O.

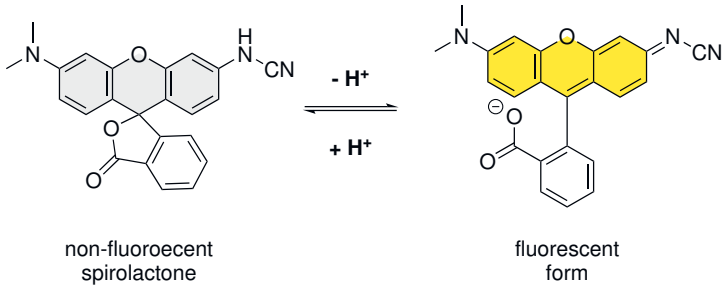

a) Simplified equilibrium of **13a**.

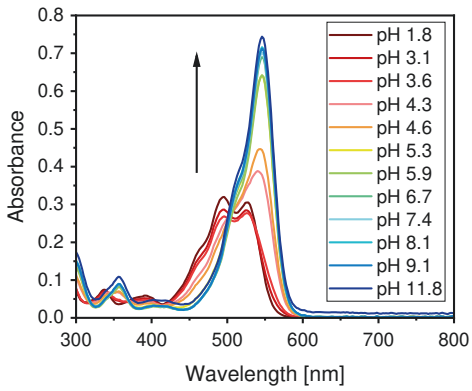

b) Absorption spectra at different pH.

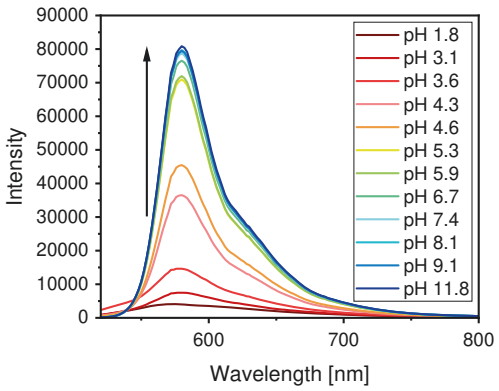

c) Emission spectra at different pH.

Figure 9.3 – Acid-base behavior of **13a**. (a) Simplified open-close equilibrium and non-fluorescent and fluorescent form of **13a**. (b) Absorption and (c) emission spectra (fluorescence excitation at 490 nm) of **13a** (10 µM) in phosphate buffers (0.1 M) with different pH values.

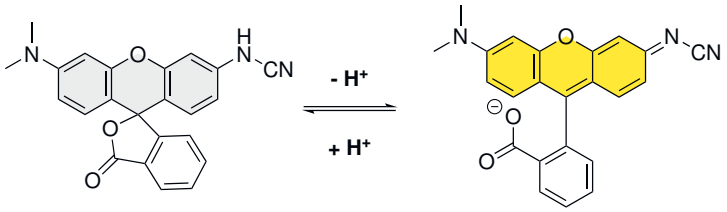

a) Simplified equilibrium of **13a**.

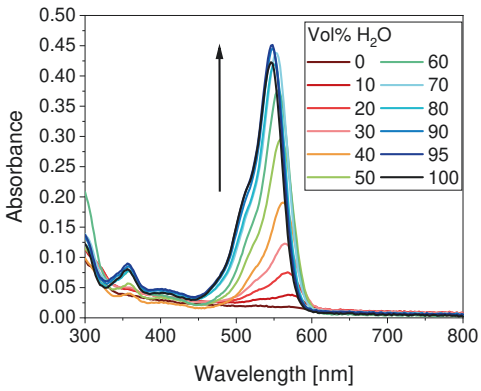

b) Absorption spectra at different Vol% H_2O.

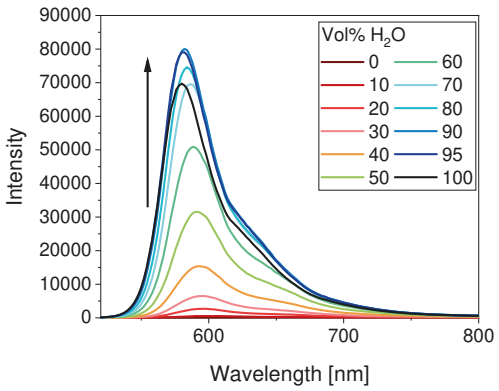

c) Emission spectra at different Vol% H_2O.

Figure 9.4 – Polarity dependency of **13a**. (a) Simplified open-close equilibrium and non-fluorescent and fluorescent form of **13a**. (b) Absorption and (c) emission spectra (fluorescence excitation at 490 nm) of **13a** (10 µM) in aqueous dioxane solutions with different Vol% H_2O.

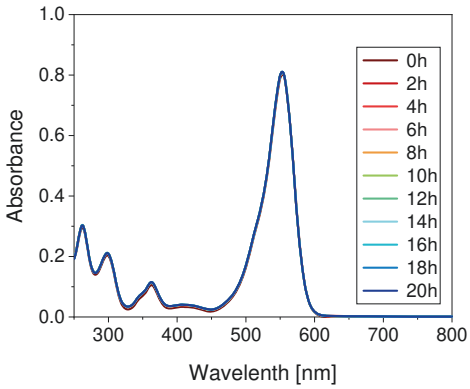

a) Absorption spectra in pH 5 over time.

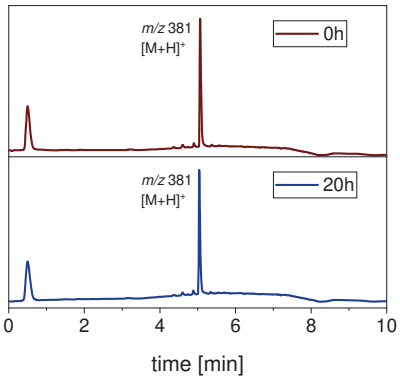

b) LCMS analysis of samples (pH 5).

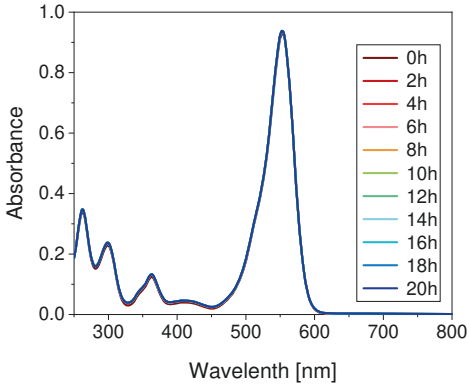

c) Absorption spectra in pH 7 over time.

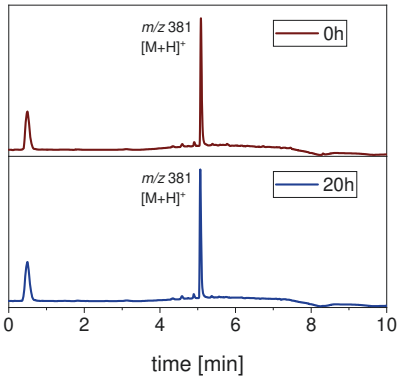

d) LCMS analysis of samples (pH 7).

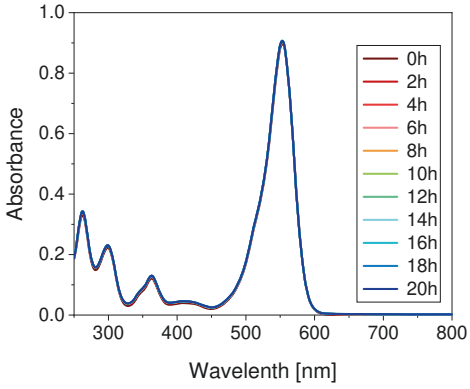

e) Absorption spectra in pH 10 over time.

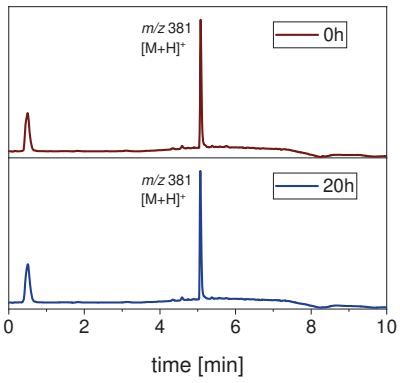

f) LCMS analysis of samples (pH 10).

Figure 9.5 – Stability of **14a** in 0.1 M phosphate buffer + 20 % DMSO of indicated pH over time. (A,C,E) Evolution of absorption spectra over 20 h. (B,D,F) LCMS traces (absorption at 254 nm) at 0 h and 20 h with obtained *m/z* values.

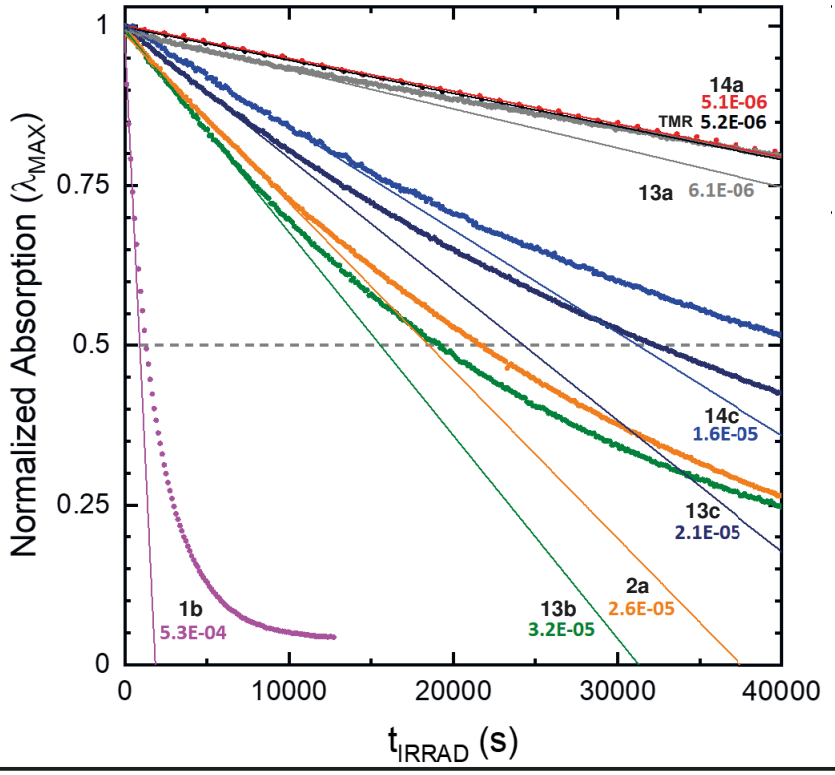

Compound	ϵ_{530}	slope, normalized	$\epsilon_{530} \cdot \Phi_{bl}$	Φ_{bl}
	$[\cdot 10^{-3} M^{-1} cm^{-1}]$	$[s-1]$	$[M^{-1} cm^{-1}]$	$[10^{-6}]$
1b	52	$5.3 \cdot 10^{-4}$	1.8	35
13b	32	$3.2 \cdot 10^{-5}$	0.82	2.5
2a	41	$2.6 \cdot 10^{-5}$	0.77	1.9
13c	36	$1.6 \cdot 10^{-5}$	0.43	1.2
14c	58	$2.1 \cdot 10^{-5}$	0.58	0.99
13a	28	$6.1 \cdot 10^{-6}$	0.18	0.63
TMR	48	$5.2 \cdot 10^{-6}$	0.14	0.3
14a	93	$5.1 \cdot 10^{-6}$	0.15	0.16

Figure 9.6 – Photobleaching kinetics (rates and Φ_{fl}) of *N*-cyanorhodamine dyes in borate buffer (0.1 M, pH 9.9) irradiated with a 530 nm LED.

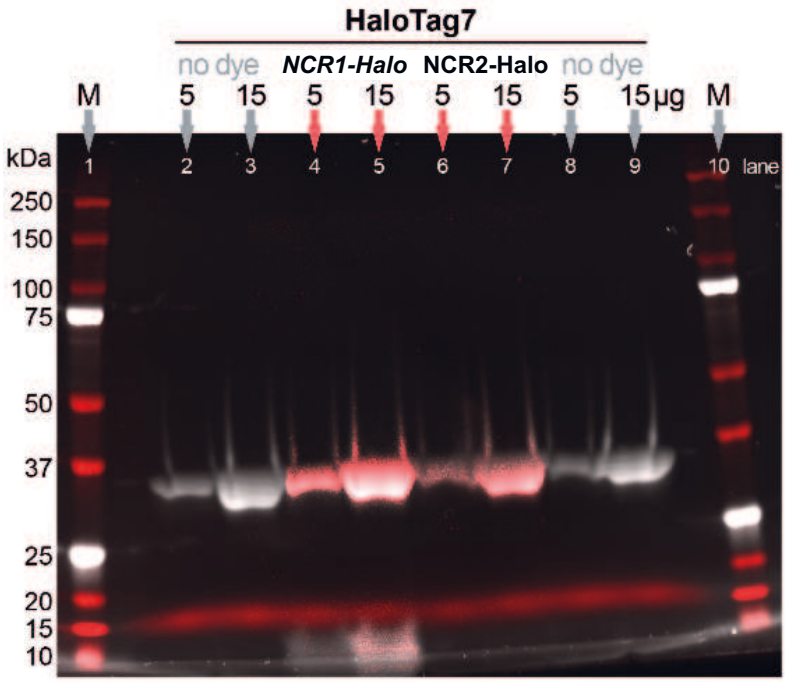

Figure 9.7 – SDS PAGE of HaloTag7 (in PBS (pH 7.4) + 0.1 % CHAPS) labeled at ambient temperature of 1 h without or with **NCR1-Halo** or **NCR2-Halo**: Markers in lane 1/10; HaloTag7 protein in lane 2/3/8/9; HaloTag7 protein and 1.1 equiv. **NCR1-Halo** in lane 4/5; *and* HaloTag7 protein and 1.1 equiv. **NCR2-Halo** in lane 6/7. lanes were loaded with 5 µg HaloTag7 protein and odd lane with 15 µg, respectively. **NCR1-Halo** and **NCR2-Halo** were detected by their own fluorescence ($\lambda_{em} = 610nm$ and $\lambda_{em} = 650nm$) HaloTag7 protein was visualized with trihalo compounds (UV activation, $\lambda_{em} = 535/45nm$). The corresponding protein bad matches the expected size of the HaloTag7 protein (35 kDa). The experiment was conducted by Dr. Jessica Matthias.

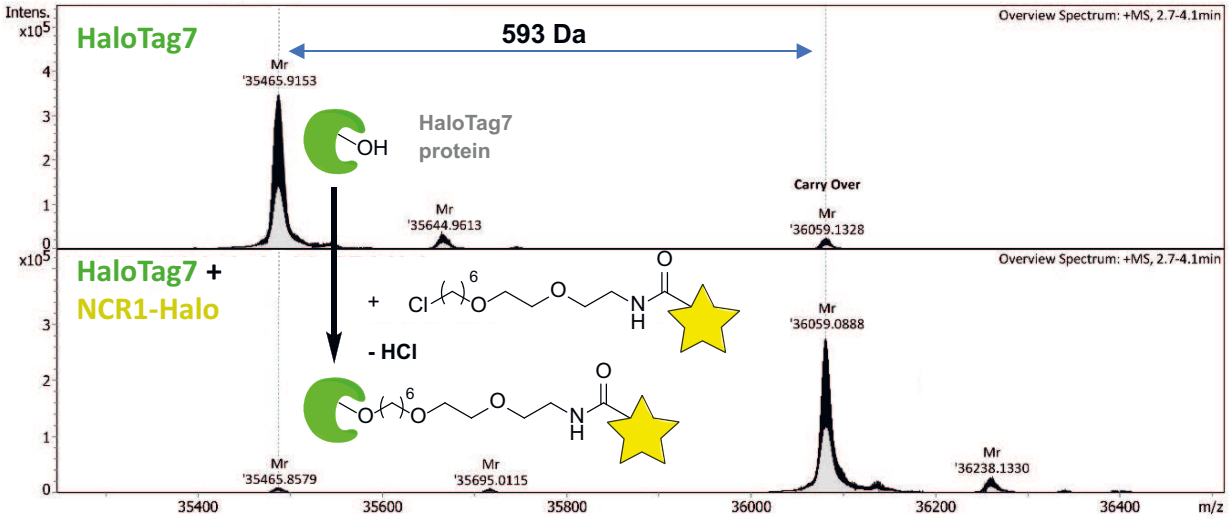

Figure 9.8 – Mass spectrometry of HaloTag7 (in PBS (pH 7.4) + 0.1 % CHAPS) labeled at ambient temperature of 1 h without (top) or with **NCR1-Halo** (bottom), before diluted to $\sim$ 1 mg/mL in 13 mM ammonium acetate. The difference in the ESI MS spectra corresponds to the expected increase in mass of 593 Da of the HaloTag7 protein after the covalent binding of conjugate **NCR1-Halo**. The experiment was conducted by Dr. Jessica Matthias.

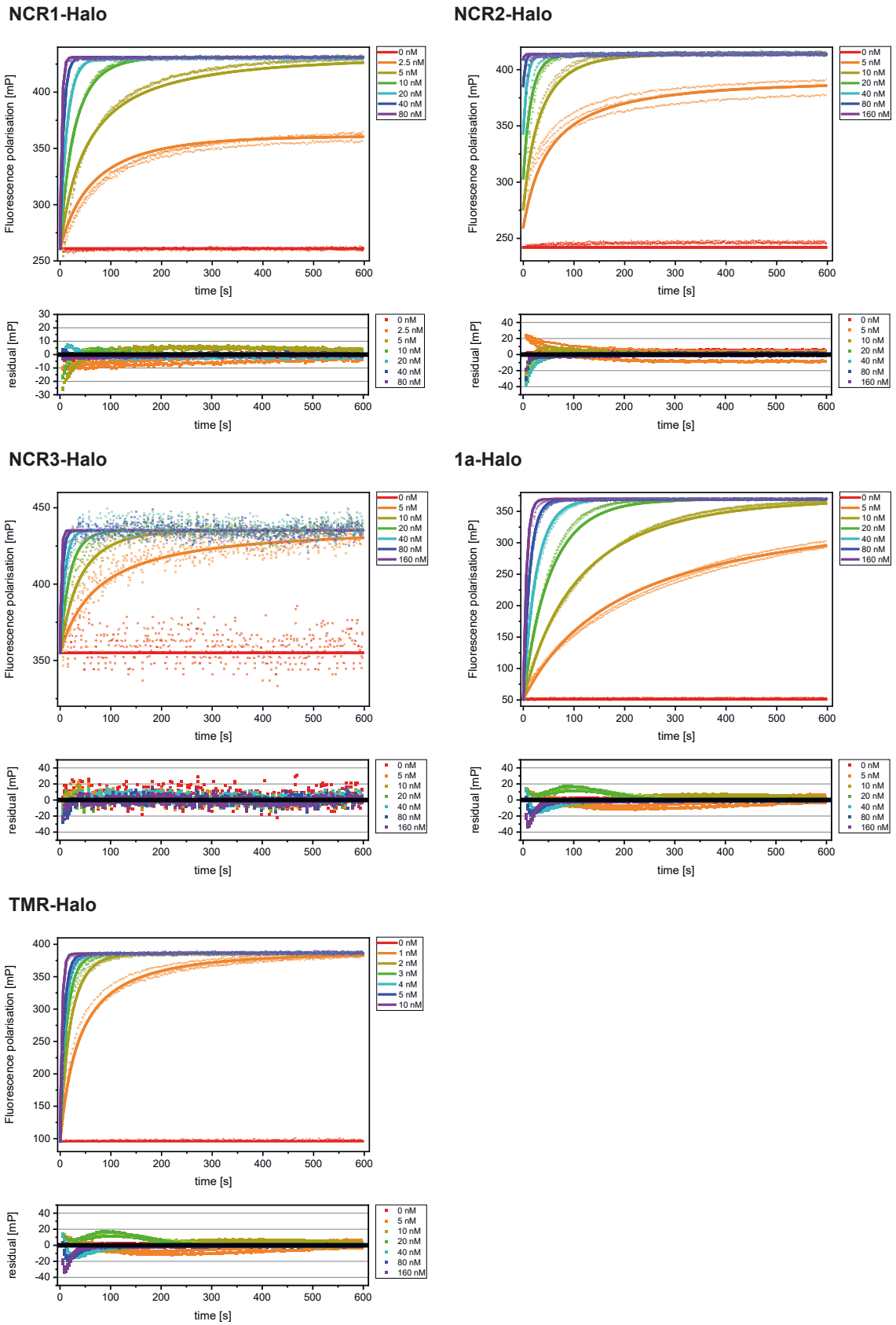

Figure 9.9 – Labeling kinetics of HaloTag ligand conjugates (5 nM; **TMR-Halo**: 1 nM) to HaloTag7 protein (indicated concentrations). Top: Fluorescence polarization traces (dots) and fitted values (lines). Bottom: Residuals of the fits.

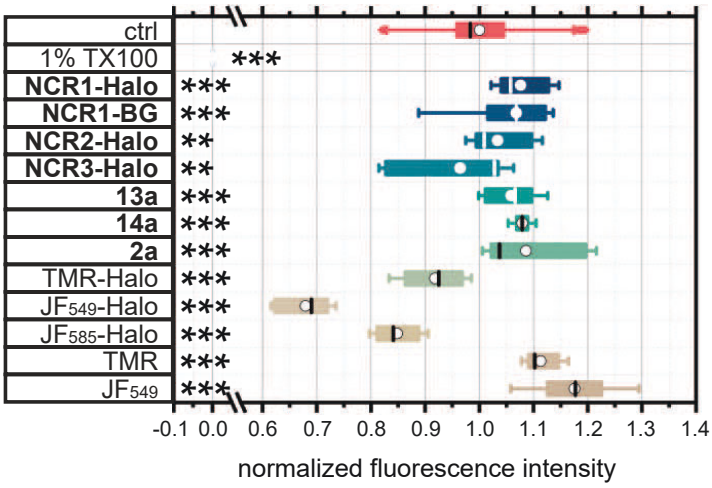

Figure 9.10 – Toxicity studies of dyes via CellTiter-Blue cell viability assay with 1 % TX100 as positive control. U-2 OS cells were exposed to 5 µM of various dyes or TX100 over 24 h. Statistical significance: ns: no significant difference to control, $*p < 0.05, **p < 0.005, ***p < 0.0005$ The experiment was conducted by Dr. Jessica Matthias. Statistic information are provided in the appendix (Table 9.4, p. 19)

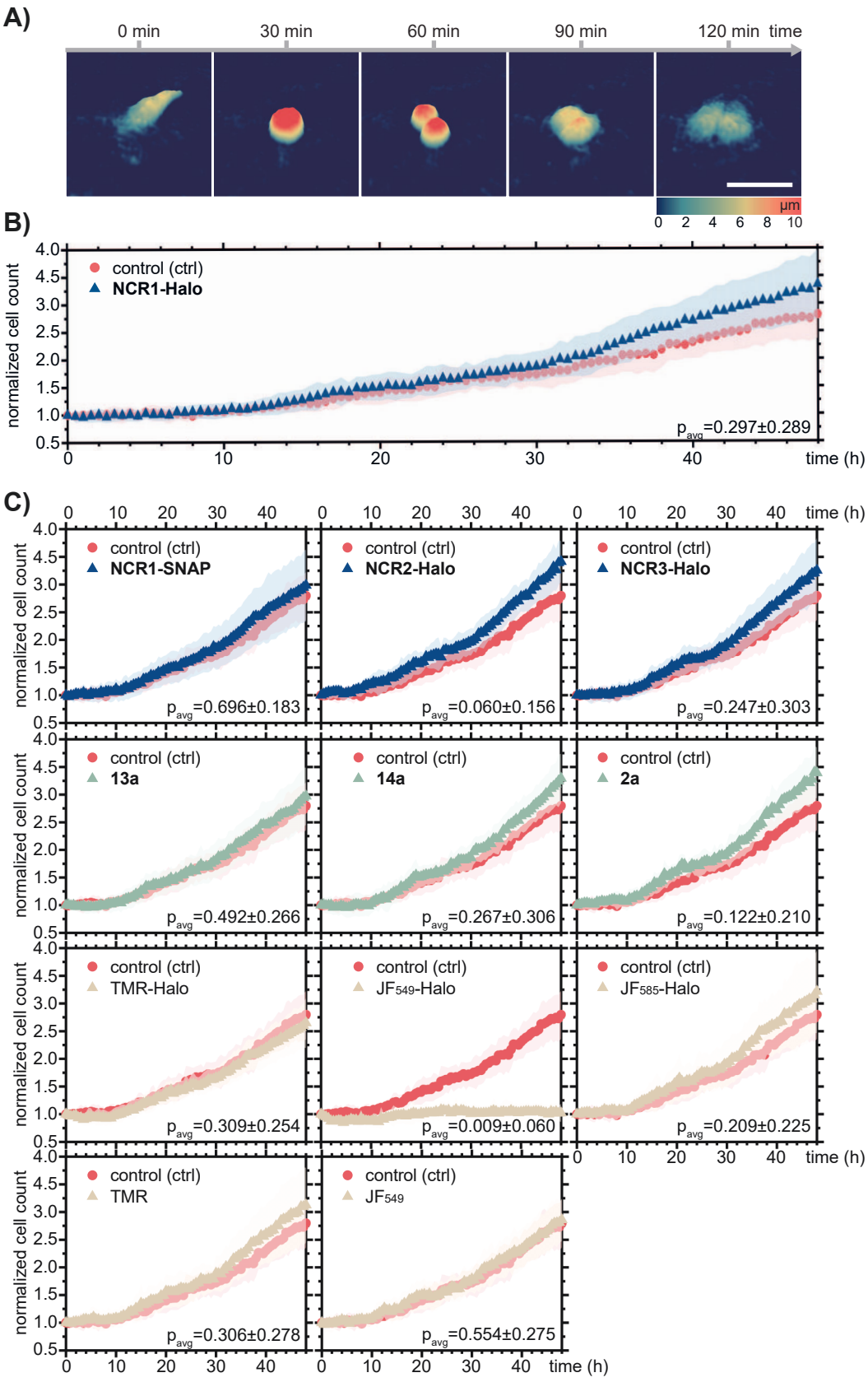

Figure 9.11 – (a) A normal cell division and (b) normalized cell count of U-2 OS cells during exposure to 5 mM **NCR1-Halo** visualized via holographic time-lapse imaging cytometry. Scale bar: 50 µm (c) Normalized cell counts over 48 h pf U-2 OS cells during exposure to 5 mM dye. Statistic information are provided in the appendix (Table 9.5, p. 21) The experiment was conducted by Dr. Jessica Matthias.

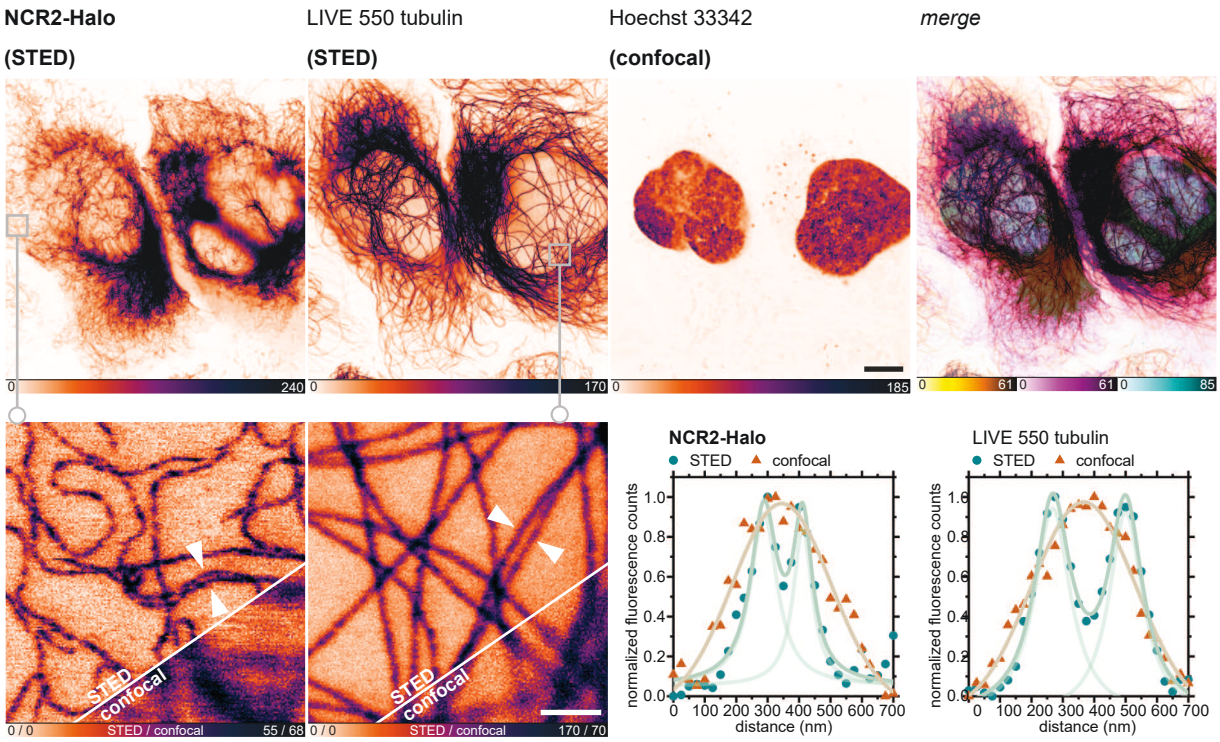

Figure 9.12 – Multi-color live-cell super-resolution imaging with N-cyanorhodamine probe **NCR2-Halo**. Confocal and STED imaging of living U-2 OS Vim-Halo cells labeled over 5 h with **NCR2-Halo** (1 µM, for Vimentin), abberior LIVE 510 tubulin (0.5 µM, for b-tubulin), and Hoechst 33354 (8 µM, for DNA for 10 min). Scale bars: 10 µm (top), 1 µm (bottom). Intensity profiles along the marked regions (arrows) are plotted for STED imaging. Imaging parameters are provided in the appendix (Table 9.7, p. 27). The experiment was conducted by Dr. Jessica Matthias.

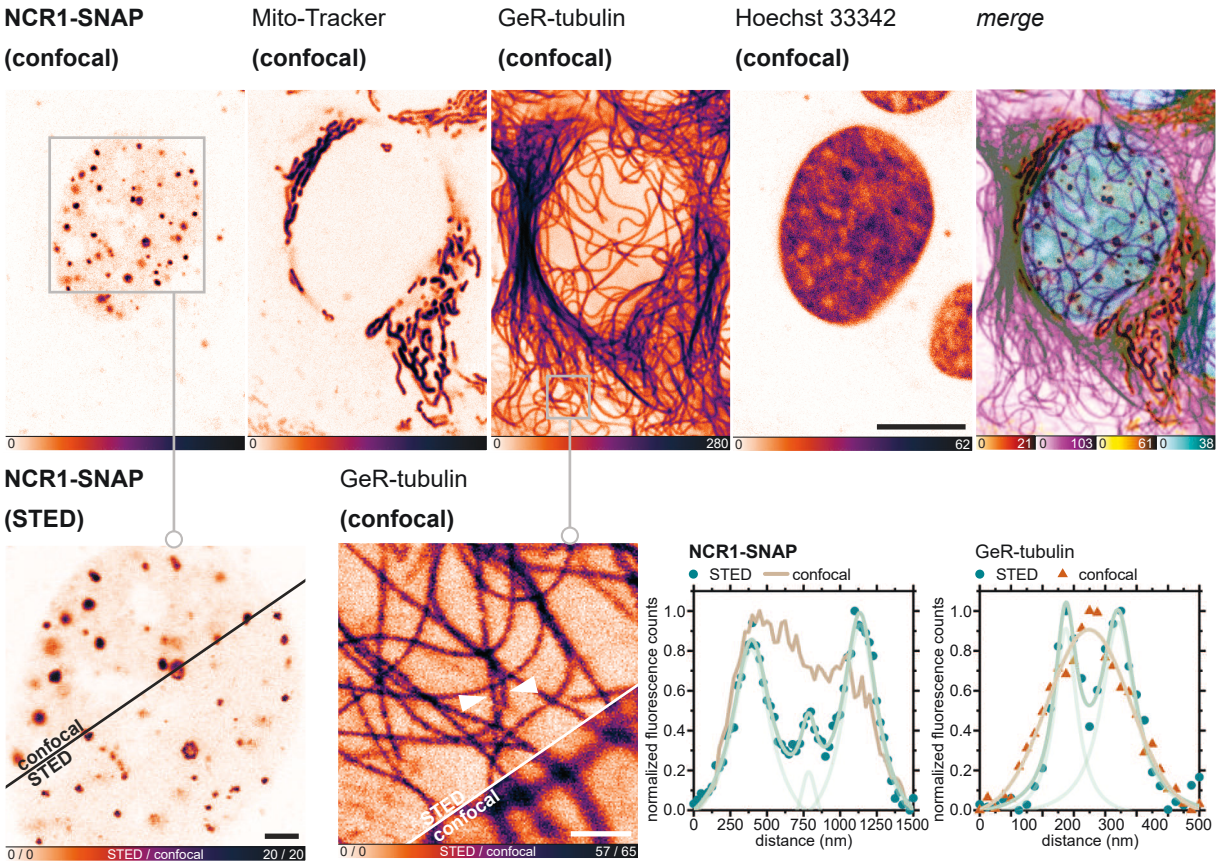

Figure 9.13 – Multi-color live-cell super-resolution imaging with N-cyanorhodamine probe **NCR1-SNAP**. Confocal and STED imaging of living U-2 OS cells transiently expressing PMLIII-SNAP labeled over 5 h with **NCR1-SNAP** (5 µM, for PML-nuclear bodies), MitoTracker Green FM (2 µM, for mitochondria), GeR-tubulin [2] (1 µM, for b-tubulin), and Hoechst 33354 (8 µM, for DNA for 10 min). Scale bars: 10 µm (top), 2 µm (bottom, left), 1 µm (bottom, right). Intensity profiles along the marked regions (arrows) are plotted for STED imaging. Imaging parameters are provided in the appendix (Table 9.7, p. 27). The experiment was conducted by Dr. Jessica Matthias.

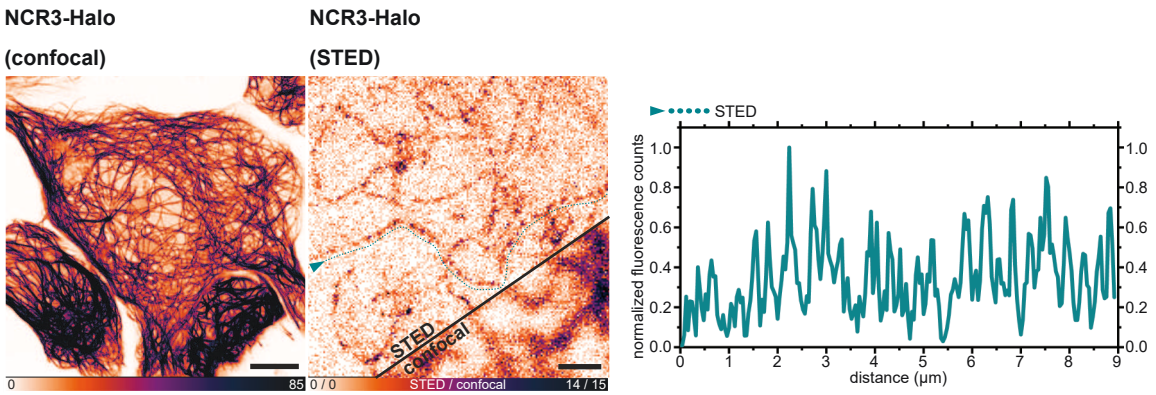

Figure 9.14 – Caption Exemplary confocal and STED imaging of the vimentin network in U-2 OS Vim-Halo cells labeled with **NCR3-Halo** (5 µM). Line profile highlights the insufficient STED signal along the vimentin structure. Imaging parameters are provided in the appendix (Table 9.7, p. 27). The experiment was conducted by Dr. Jessica Matthias.

9.2.2 Chapter 5.2

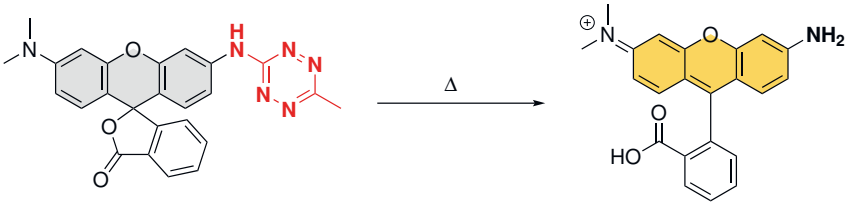

32a
Exact Mass: 452

34a
Exact Mass: 359

a) Conversion of **32a**.

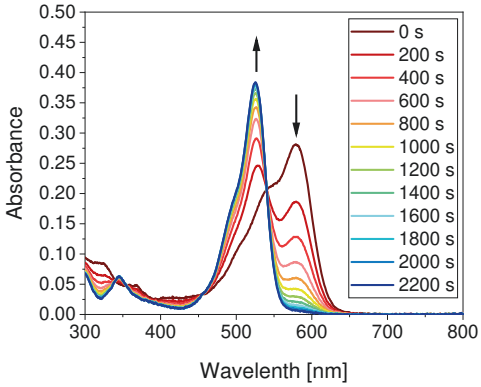

b) Temporal evolution of absorption spectra.

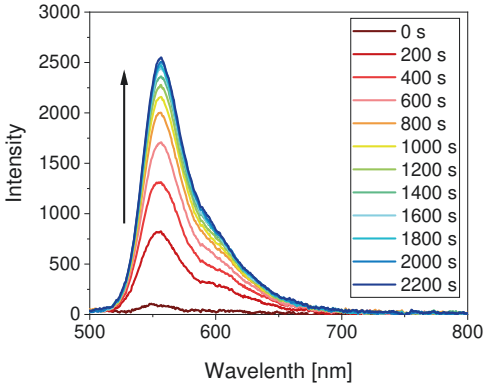

c) Temporal evolution of emission spectra.

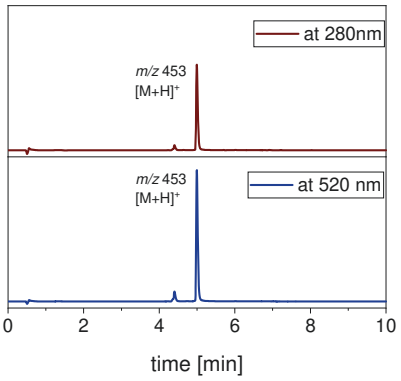

d) LCMS analysis before irradiation.

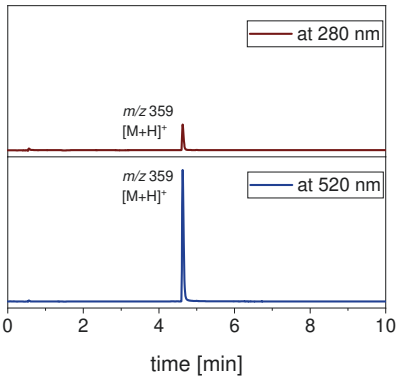

e) LCMS analysis after irradiation.

Figure 9.15 – Conversion of **32a** (5 µM) in borate buffer (0.1 M, pH 11) without irradiation. (a) Reaction scheme and exact masses of compounds involved. Temporal evolution of (b) absorption and (c) emission spectra (fluorescence excitation at 505 nm). LCMS traces (absorption at indicated wavelengths) and *m/z* values are shown (d) before and (e) after irradiation. The experiment was conducted by Dr. Mariano Bossi.

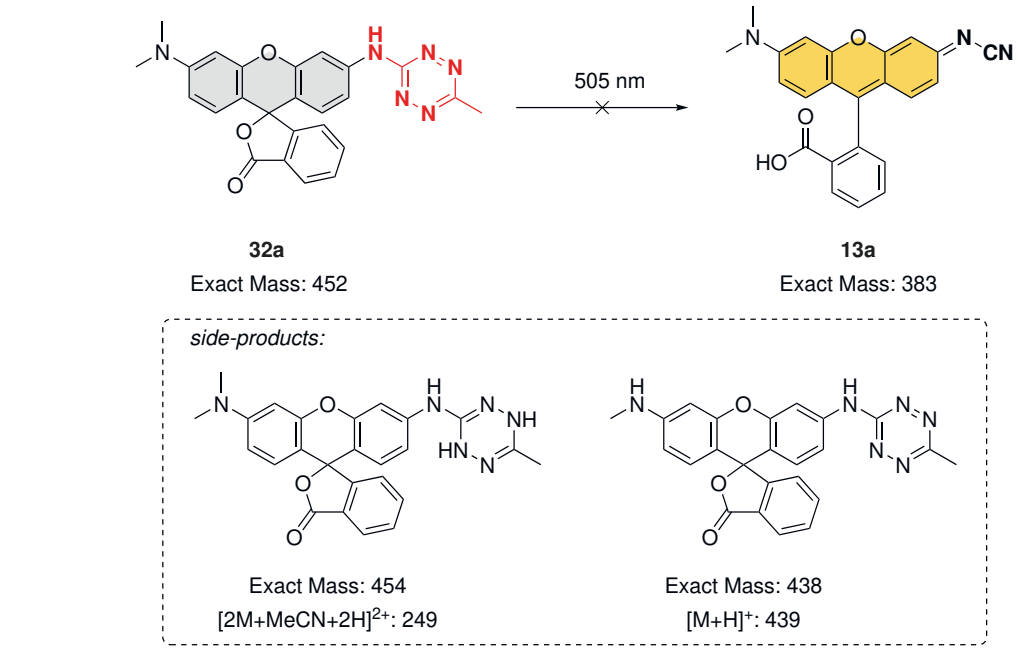

a) Unsuccessful photoactivation of **32a**.

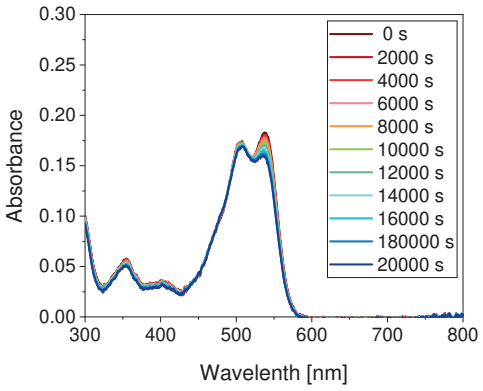

b) Temporal evolution of absorption spectra.

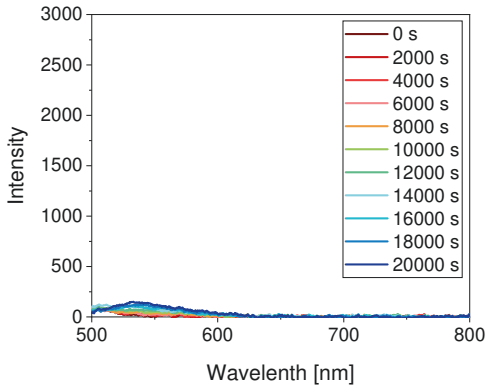

c) Temporal evolution of emission spectra.

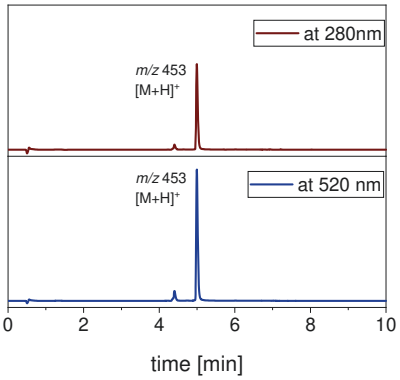

d) LCMS analysis before irradiation.

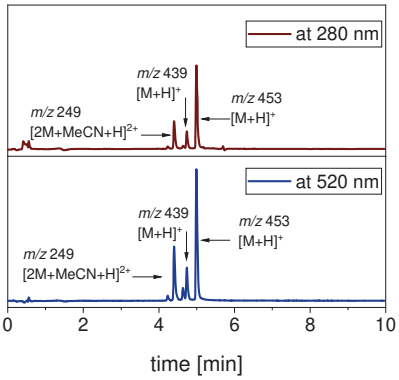

e) LCMS analysis after irradiation.

Figure 9.16 – Unsuccessful photoactivation of **32a** (5 µM) in phosphate buffer (0.1 M, pH 7) upon irradiation (505 nm). (a) Reaction scheme and exact masses of compounds involved. Temporal evolution of (b) absorption and (c) emission spectra (fluorescence excitation at 505 nm). LCMS traces (absorption at indicated wavelengths) and *m/z* values are shown (d) before and (e) after irradiation. The experiment was conducted by Dr. Mariano Bossi.

9.2.3 Chapter 5.3

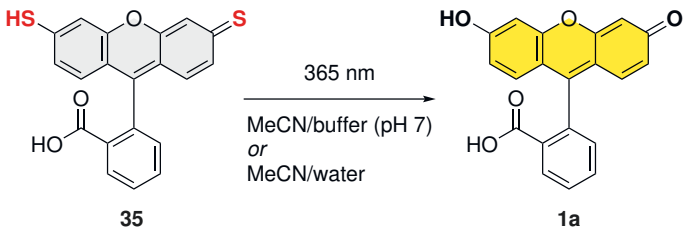

35 **1a**

Exact Mass: 364 Exact Mass: 332

a) Proposed photoactivation of **35**.

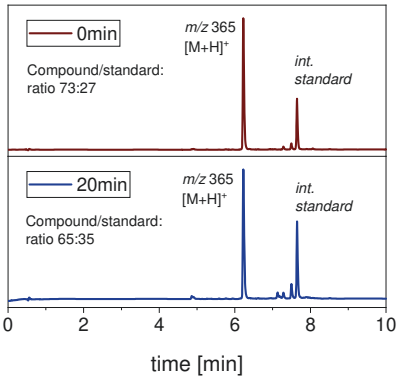

b) LCMS analysis of photolysis of **35** in MeCN/buffer.

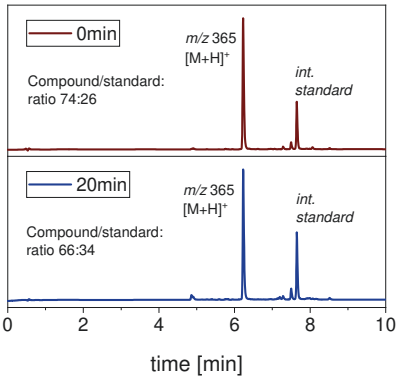

c) LCMS analysis of photolysis of **35** in MeCN/water.

Figure 9.17 – Photolysis of **35** with a 365 nm LED (10 % power) for 20 min (0.3 mg/mL 4,4'-di(tert-butyl)biphenyl were added as internal standard). LCMS traces and observed *m/z* values are shown at 254 nm absorption. (a) Reaction scheme and exact masses of compounds involved. (b) 0.6 mg/mL **35** in MeCN/phosphate buffer (5:1, pH 7). (c) 0.7 mg/mL **35** in MeCN/water (5:1).

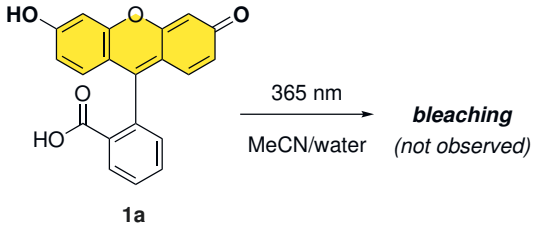

1a

Exact Mass: 332

a) Proposed photobleaching of **1a**.

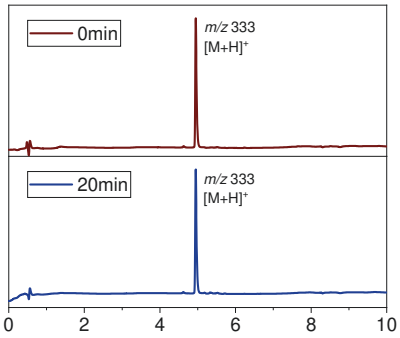

b) LCMS analysis of photolysis of **1a**.

Figure 9.18 – Photolysis of **1a** with a 365 nm LED (10 % power) for 20 min. LCMS traces and observed *m/z* values are shown at 254 nm absorption. (a) Reaction scheme and exact masses of compounds involved. (b) 0.8 mg/mL of **1a** in MeCN/water (5:1).

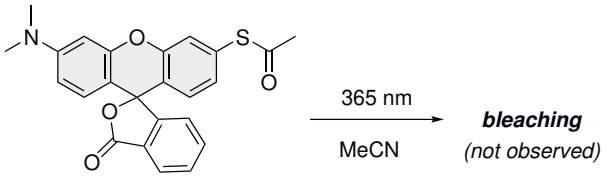

40

Exact Mass: 417

a) Proposed photobleaching of **40**.

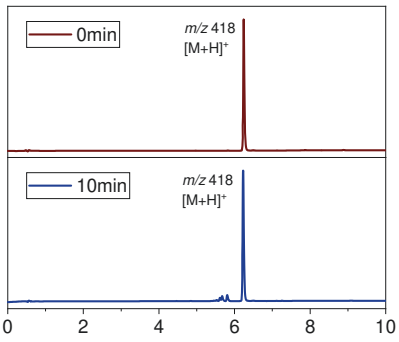

b) LCMS analysis of photolysis of **40**.

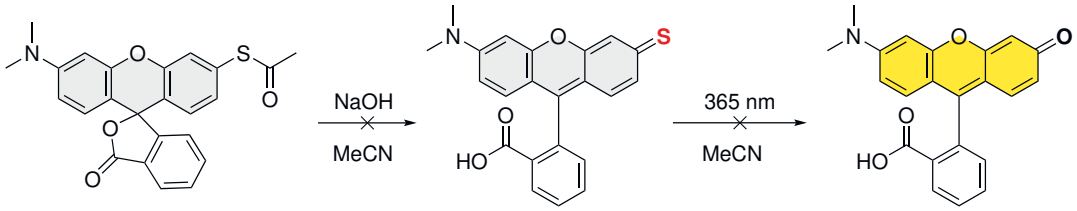

40

Exact Mass: 417

37

Exact Mass: 375

2a

Exact Mass: 359

c) Proposed photoactivation of **40**.

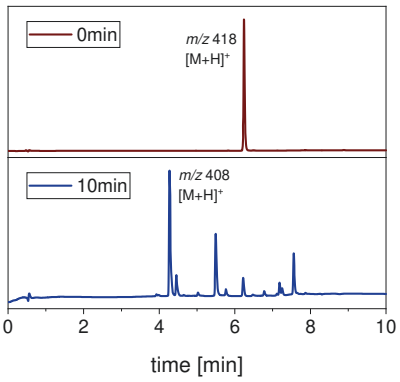

d) LCMS analysis of basic hydrolysis of **40**.

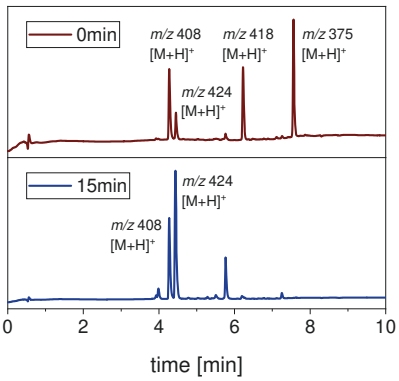

e) LCMS analysis of basic hydrolysis and photolysis **40**.

Figure 9.19 – Photolysis studies of **40** with a 365 nm LED (50 % power) LCMS traces and observed *m/z* values are shown at 254 nm absorption. (A,C) Reaction schemes and exact masses of compounds involved. (b) **40** in MeCN (2.0 mg/mL, 1.0 mL) irradiated for 10 min. (d) To **40** in MeCN (2.0 mg/mL, 1.0 mL), 0.2 mL 1 M aq. NaOH were added. The mixture was stirred at ambient temperature for 10 min. (e) To **40** in MeCN (2.0 mg/mL, 1.0 mL), 0.2 mL 1 M aq. NaOH were added. The mixture was irradiated for 15 min.

9.2.4 Chapter 5.4

PaX(–)1
Exact Mass: 254

PaX(–)1-CF
Exact Mass: 254

a) Photoactivation of **PaX(–)1**.

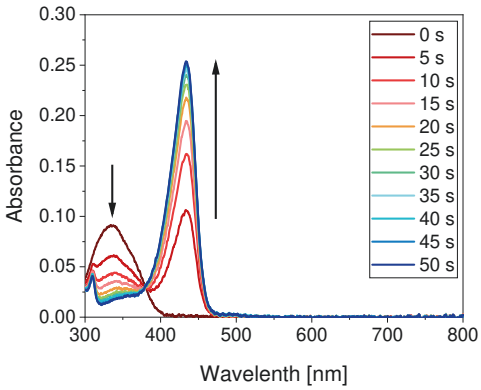

b) Temporal evolution of absorption spectra.

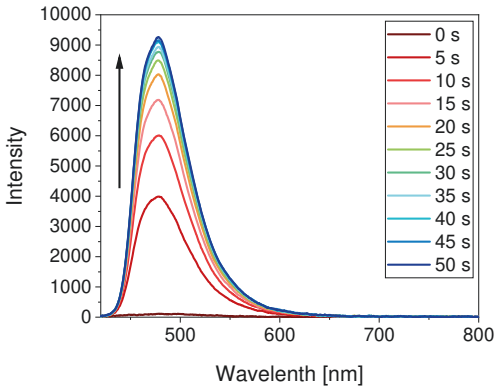

c) Temporal evolution of emission spectra.

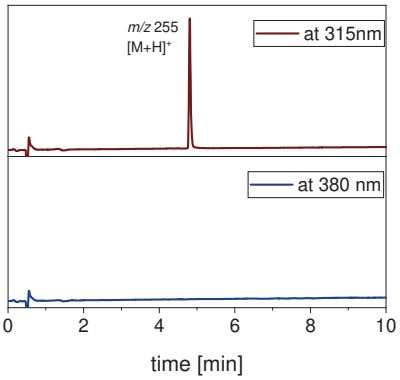

d) LCMS analysis before irradiation.

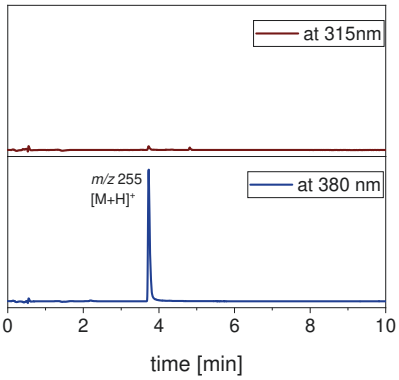

e) LCMS analysis after irradiation.

Figure 9.20 – Photoactivation of **PaX(–)1** (6.5 µM) in phosphate buffer (0.1 M, pH 7) upon irradiation (365 nm). (a) Reaction scheme and exact masses of compounds involved. Temporal evolution of (b) absorption and (c) emission spectra (fluorescence excitation at 405 nm). LCMS traces (absorption at indicated wavelengths) and *m/z* values are shown (d) before and (e) after irradiation.

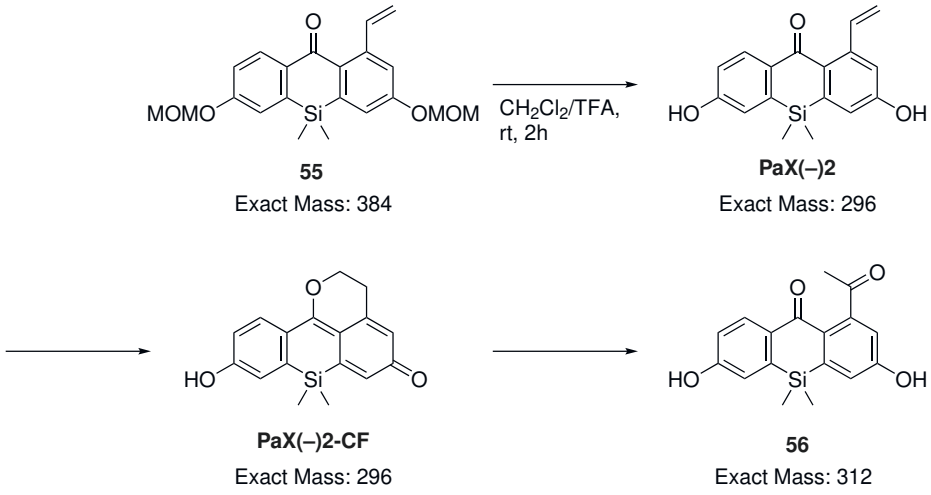

a) Proposed conversion of **55** to **56**.

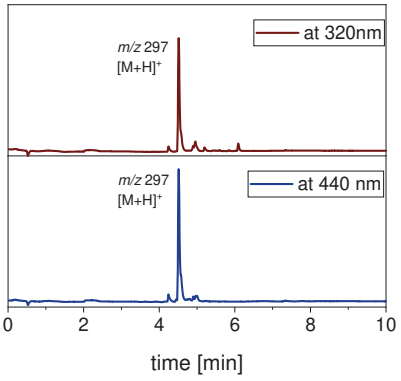

b) LCMS analysis of the reaction mixture (after 90 min).

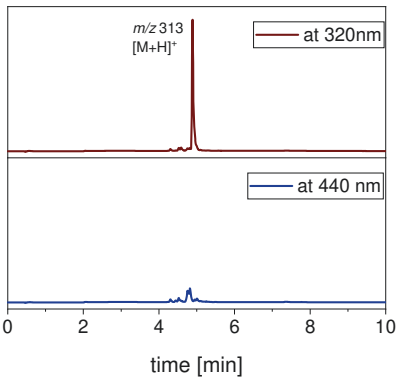

c) LCMS analysis after isolation.

^{1}H NMR (400 MHz, DMSO-d_6) δ 8.09 (d, J = 8.8 Hz, 1H), 7.15 (d, J = 2.5 Hz, 1H), 7.11 (d, J = 2.6 Hz, 1H), 6.98 (dd, J = 8.7, 2.6 Hz, 1H), 6.68 (d, J = 2.5 Hz, 1H), 2.32 (s, 3H), 0.44 (s, 6H).

^{13}C NMR (101 MHz, DMSO-d_6)) δ 203.4, 184.5, 160.9, 160.3, 149.2, 142.7, 141.0, 132.0, 131.3, 128.8, 119.8, 119.2, 117.6, 114.5, 30.6, -1.6.

HRMS (ESI) m/z: 313.0891 (calcd. for $C_{17}H_{17}O_4Si$, $[M+H]^+$), 313.0891 (found).

d) Analytical data indication the formation of **56**.

Figure 9.21 – Unsuccessful acidic deprotection of **55** to **PaX(–)2** dye. **55** (30.3 mg) was stirred in CH_2Cl_2 (1.0 mL) and TFA (0.20 mL) at rt for 2 h. After evaporation from toluene (3x 20 mL), the crude mixture was purified by preparative HPLC (Interchim PhenC4 250x21.2 mm 5 µm, gradient 25/75 to 55/45 A:B, A = MeCN + 0.1 % formic acid, B = H_2O + 0.1 % formic acid), affording a yellow powder (19.4 mg). (a) Reaction scheme and exact masses of compounds involved. LCMS traces (absorption at indicated wavelengths) and *m/z* values are shown (b) of the reaction mixture and (c) of the afforded yellow powder. (d) Analytical data of the afforded yellow powder (NMR spectra are provided on p. 233).

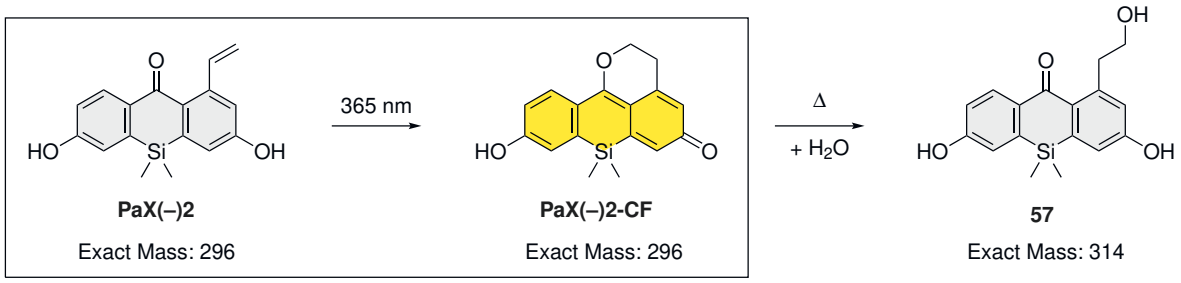

a) Photoactivation of **PaX(–)2**.

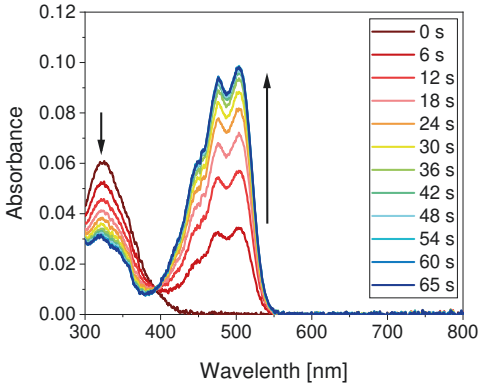

b) Temporal evolution of absorption spectra.

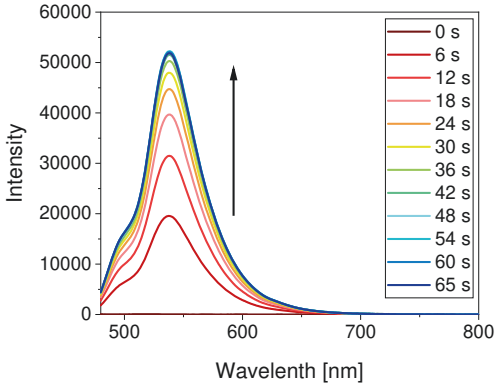

c) Temporal evolution of emission spectra.

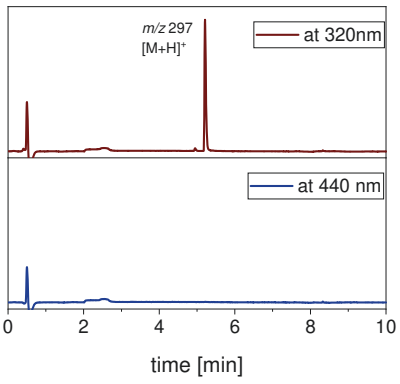

d) LCMS analysis before irradiation.

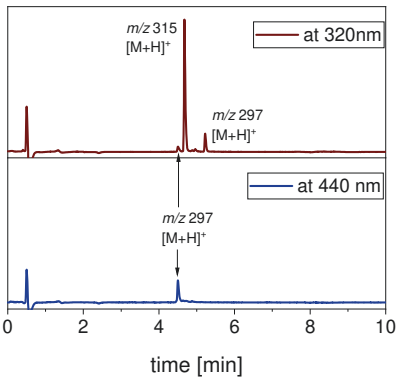

e) LCMS analysis after irradiation.

Figure 9.22 – Photoactivation of **PaX(–)2** (5.6 µM) in phosphate buffer (0.1 M, pH 7) upon irradiation (365 nm). (a) Reaction scheme and exact masses of compounds involved. Temporal evolution of (b) absorption and (c) emission spectra (fluorescence excitation at 455 nm). LCMS traces (absorption at indicated wavelengths) and *m/z* values are shown (d) before and (e) after irradiation. The experiment was conducted by Dr. Mariano Bossi.

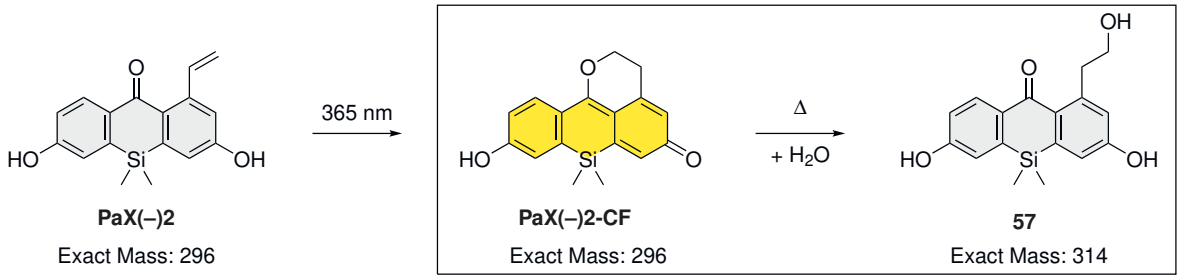

a) Photoactivation of **PaX(–)2**.

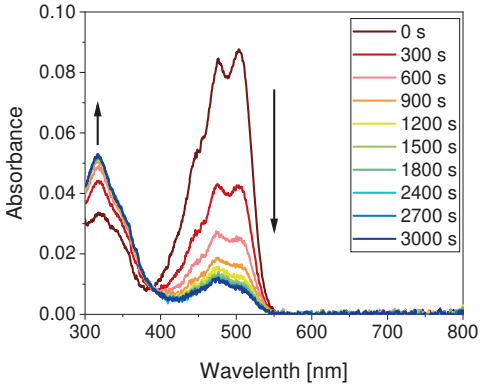

b) Temporal evolution of absorption spectra.

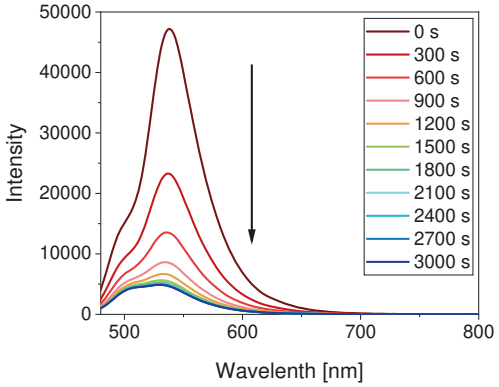

c) Temporal evolution of emission spectra.

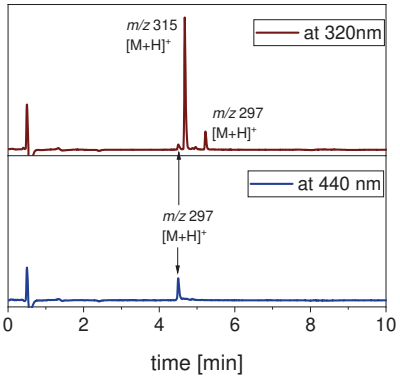

d) LCMS analysis after irradiation.

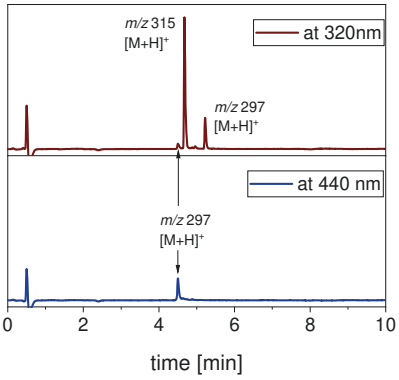

e) LCMS analysis after thermal hydrolysis.

Figure 9.23 – Thermal hydrolysis of **PaX(–)2-CF** to **57** after irradiation (Appendix Figure 9.22, p. 183) (a) Reaction scheme and exact masses of compounds involved. Temporal evolution of (b) absorption and (c) emission spectra (fluorescence excitation at 455 nm). LCMS traces (absorption at indicated wavelengths) and *m/z* values are shown (d) after irradiation and (e) after thermal hydrolysis. The experiment was conducted by Dr. Mariano Bossi.

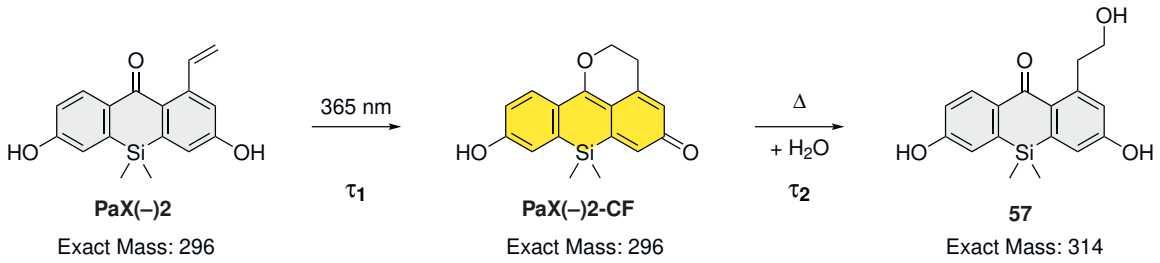

a) Photoactivation and thermal hydrolysis of **PaX(–)2**.

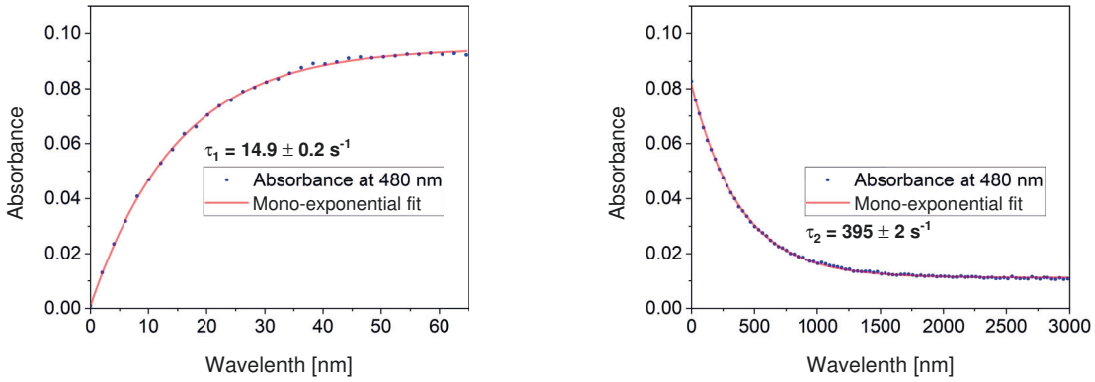

b) During irradiation.

c) After irradiation.

Figure 9.24 – Photoactivation of **PaX(–)2** (5.6 µM) in phosphate buffer (0.1 M, pH 7) upon irradiation (365 nm) and thermal reaction of **PaX(–)2-CF** after irradiation. (a) Reaction scheme and exact masses of compounds involved. (B, C) Absorbance at 480 nm plotted vs time. Data (dots) were fits (line) based on mono-exponential decay are shown. The experiment was conducted by Dr. Mariano Bossi.

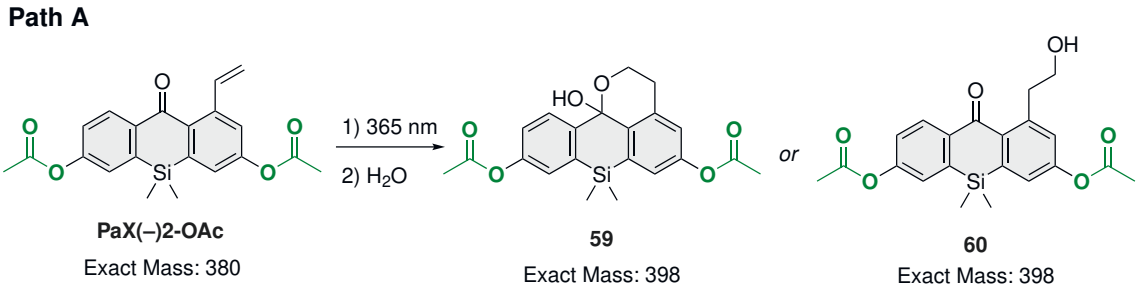

a) Photoconversion of **PaX(–)2-OAc**.

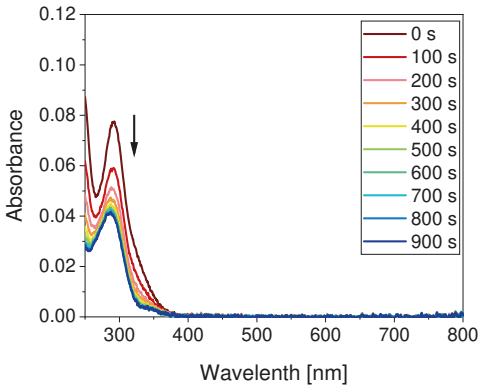

b) Temporal evolution of absorption spectra.

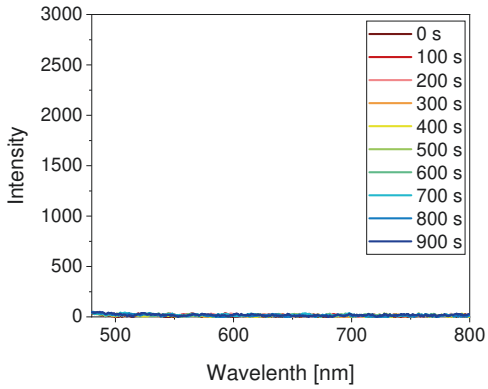

c) Temporal evolution of emission spectra.

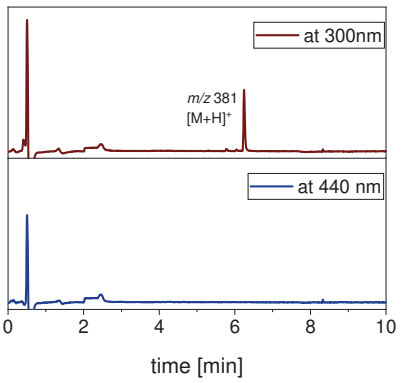

d) LCMS analysis before irradiation.

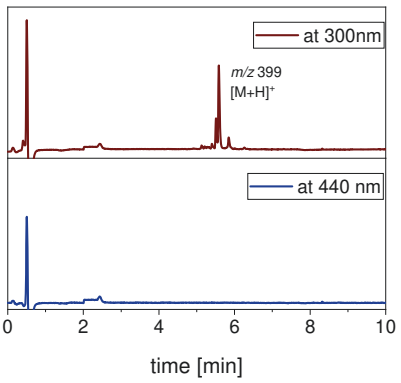

e) LCMS analysis after irradiation.

Figure 9.25 – Photoconversion of of **PaX(–)2-OAc** (5.6 µM) in phosphate buffer (0.1 M, pH 7) upon irradiation (365 nm). (a) Reaction scheme and exact masses of compounds involved. Temporal evolution of (b) absorption and (c) emission spectra (fluorescence excitation at 455 nm). LCMS traces (absorption at indicated wavelengths) and *m/z* values are shown (d) after irradiation and (e) after thermal hydrolysis. The experiment was conducted by Dr. Mariano Bossi.

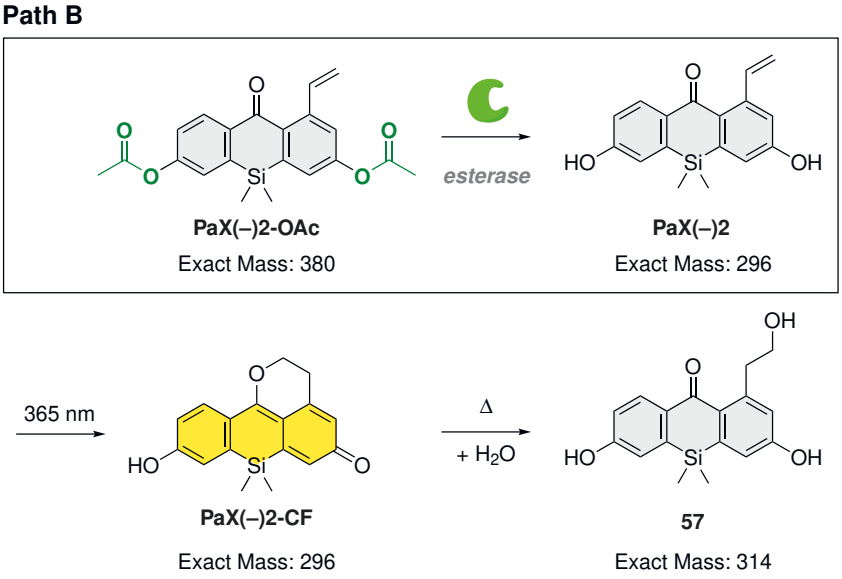

a) Enzymatic cleavage and photoactivation of **PaX(–)2-OAc**.

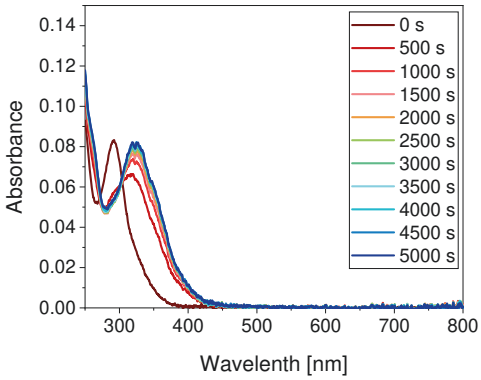

b) Temporal evolution of absorption spectra.

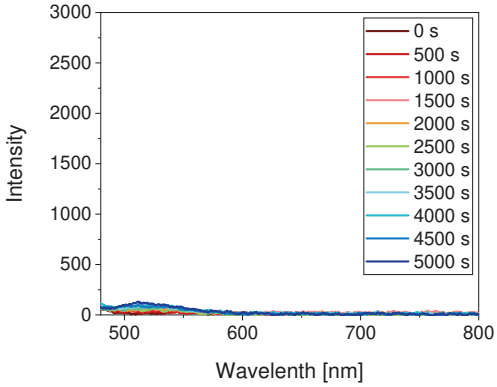

c) Temporal evolution of emission spectra.

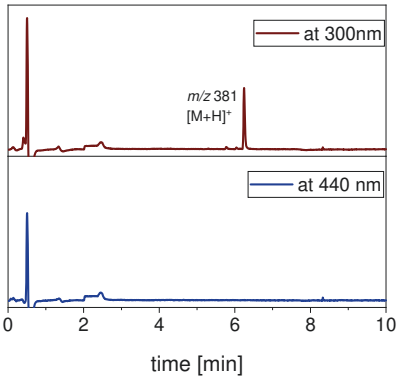

d) LCMS analysis before addition of esterase.

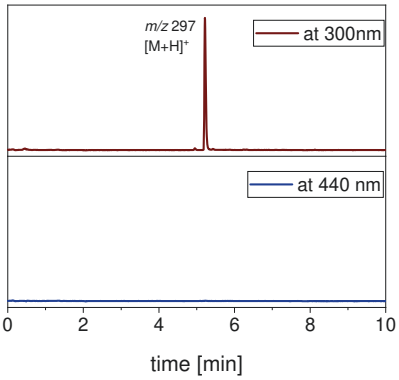

e) LCMS analysis after addition of esterase.

Figure 9.26 – Enzymatic cleavage (2 µg/mL PLE) **PaX(–)2-OAc** (5.6 µM) in phosphate buffer (0.1 M, pH 7) before irradiation (365 nm). (a) Reaction scheme and exact masses of compounds involved. Temporal evolution of (b) absorption and (c) emission spectra (fluorescence excitation at 455 nm). LCMS traces (absorption at indicated wavelengths) and *m/z* values are shown (d) before and (e) after addition of PLE. The experiment was conducted by Dr. Mariano Bossi.

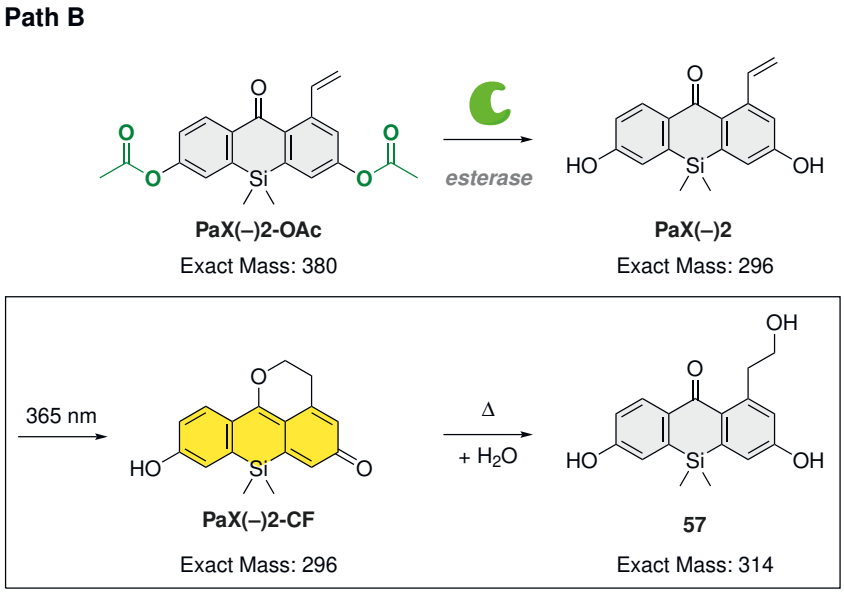

a) Enzymatic cleavage and photoactivation of **PaX(–)2-OAc**.

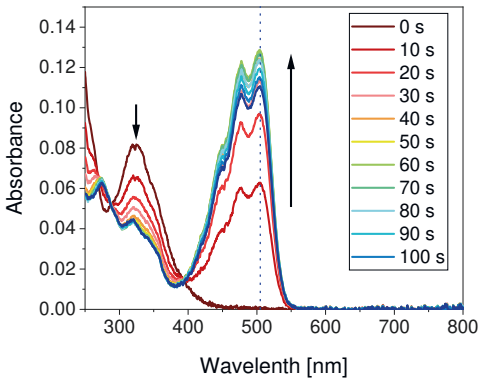

b) Temporal evolution of absorption spectra.

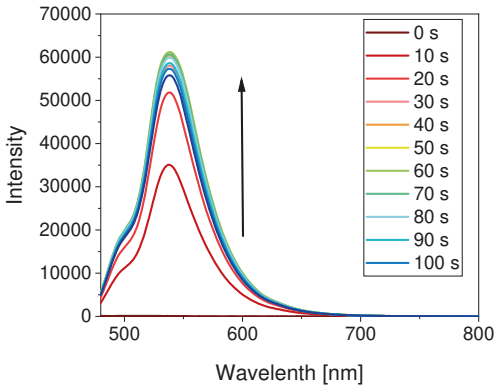

c) Temporal evolution of emission spectra.

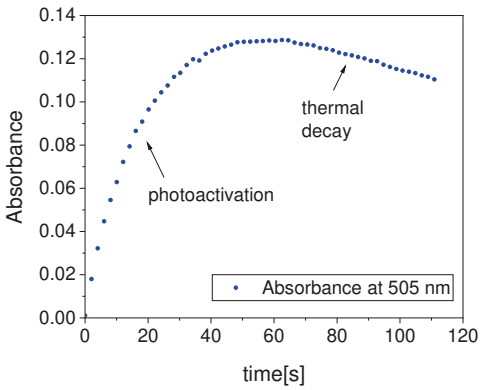

d) Absorbance vs time.

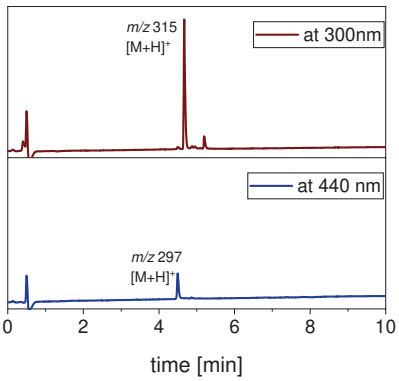

e) LCMS analysis after irradiation.

Figure 9.27 – Photoactivation of **PaX(–)2-OAc** (5.6 µM) in phosphate buffer (0.1 M, pH 7) upon irradiation (365 nm) after enzymatic cleavage (with PLE, see Appendix Figure 9.26, p. 187). (a) Reaction scheme and exact masses of compounds involved. Temporal evolution of (b) absorption and (c) emission spectra (fluorescence excitation at 455 nm) and (d) absorbance at 505 nm plotted vs time. (e) LCMS traces (absorption at indicated wavelengths) and *m/z* values are shown after irradiation. The experiment was conducted by Dr. Mariano Bossi.

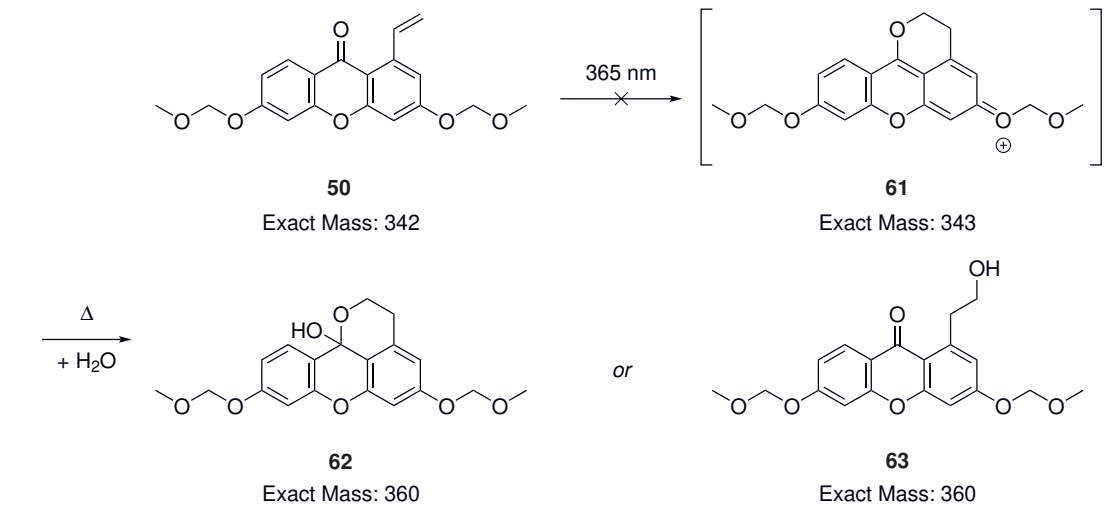

a) Proposed photoconversion of **50**.

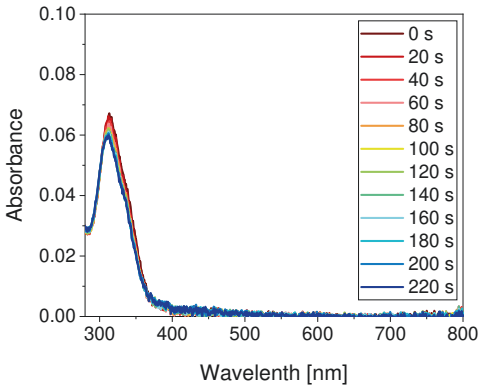

b) Temporal evolution of absorption spectra.

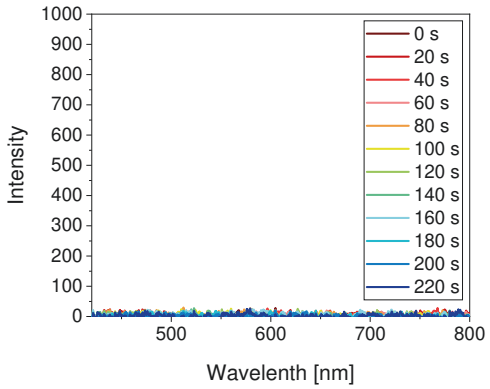

c) Temporal evolution of emission spectra.

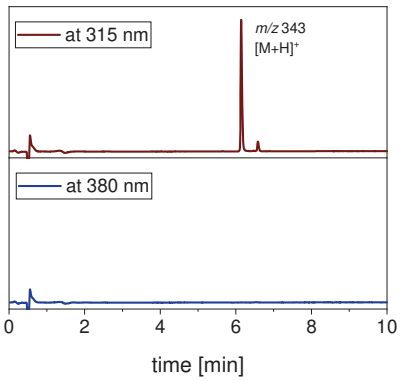

d) LCMS analysis before irradiation.

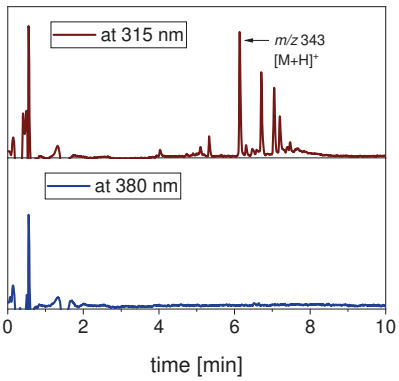

e) LCMS analysis after irradiation.

Figure 9.28 – Attempted photoconversion of **50** (5.0 µM) in phosphate buffer (0.1 M, pH 7) upon irradiation (365 nm). (a) Reaction scheme and exact masses of compounds involved. Temporal evolution of (b) absorption and (c) emission spectra (fluorescence excitation at 405 nm). LCMS traces (absorption at indicated wavelengths) and *m/z* values are shown (d) before and (e) after irradiation. The experiment was conducted by Dr. Mariano Bossi.

9.3 NMR spectra

9.3.1 Chapter 4

Compound 15a

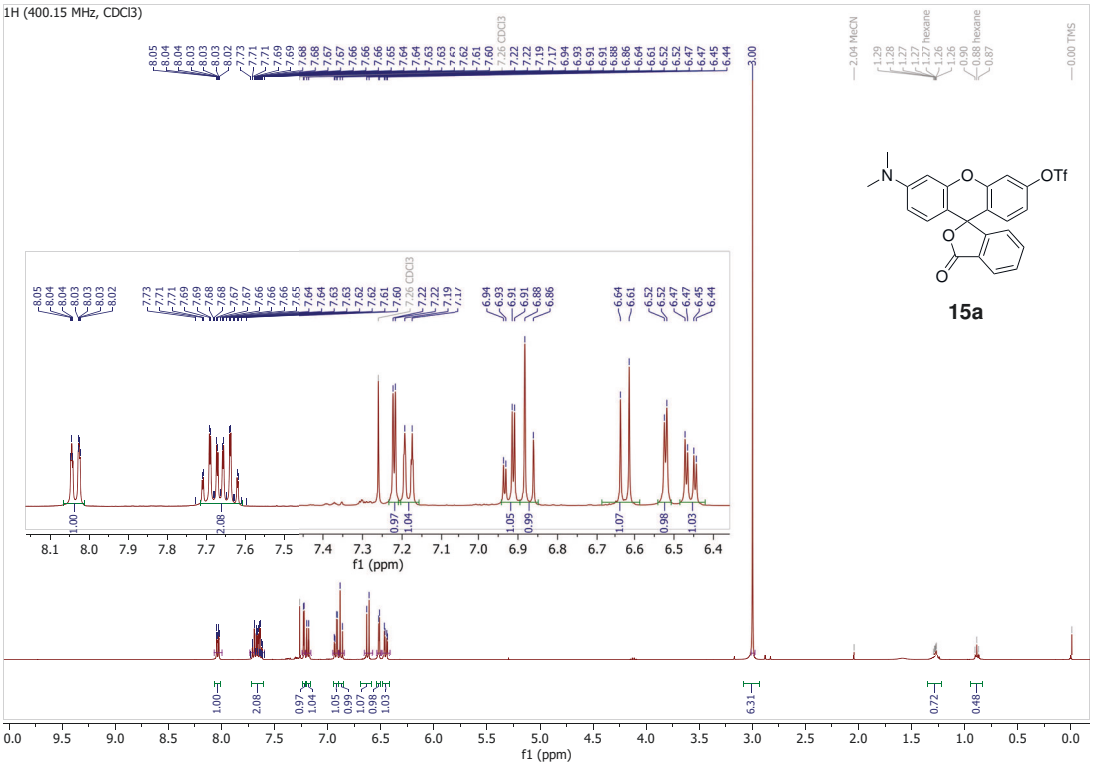

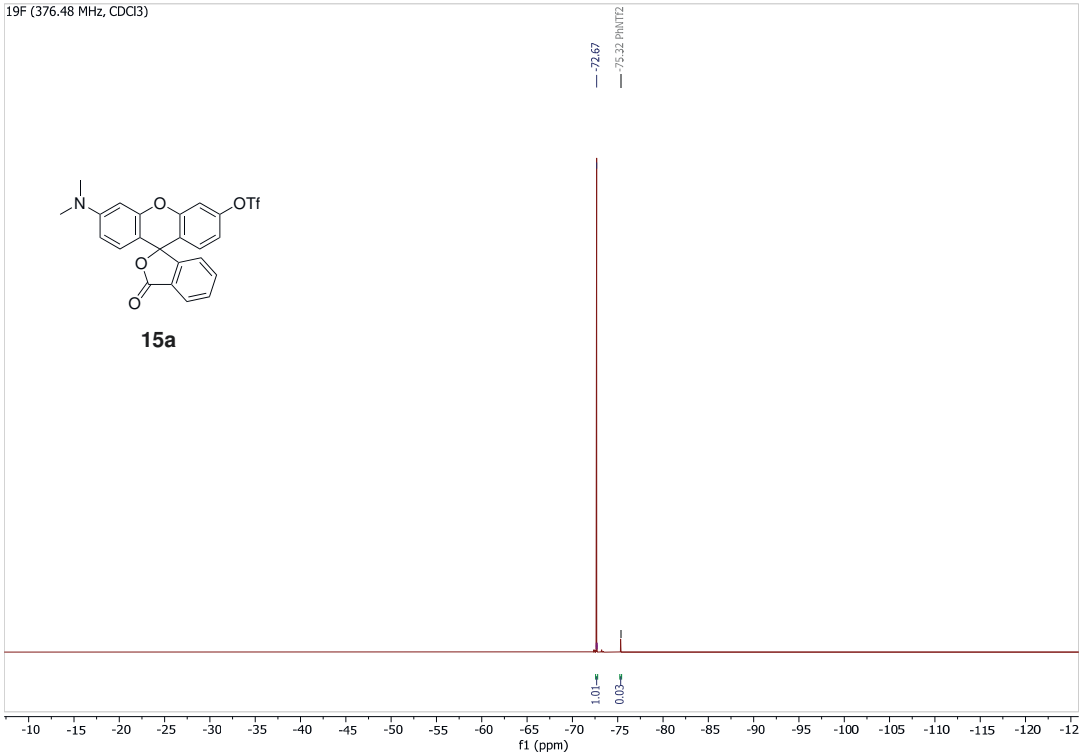
19F (376.48 MHz, CDCl3)
-72.67
-75.32 PhNTf2
OTf
15a
1.01
0.03
f1 (ppm)

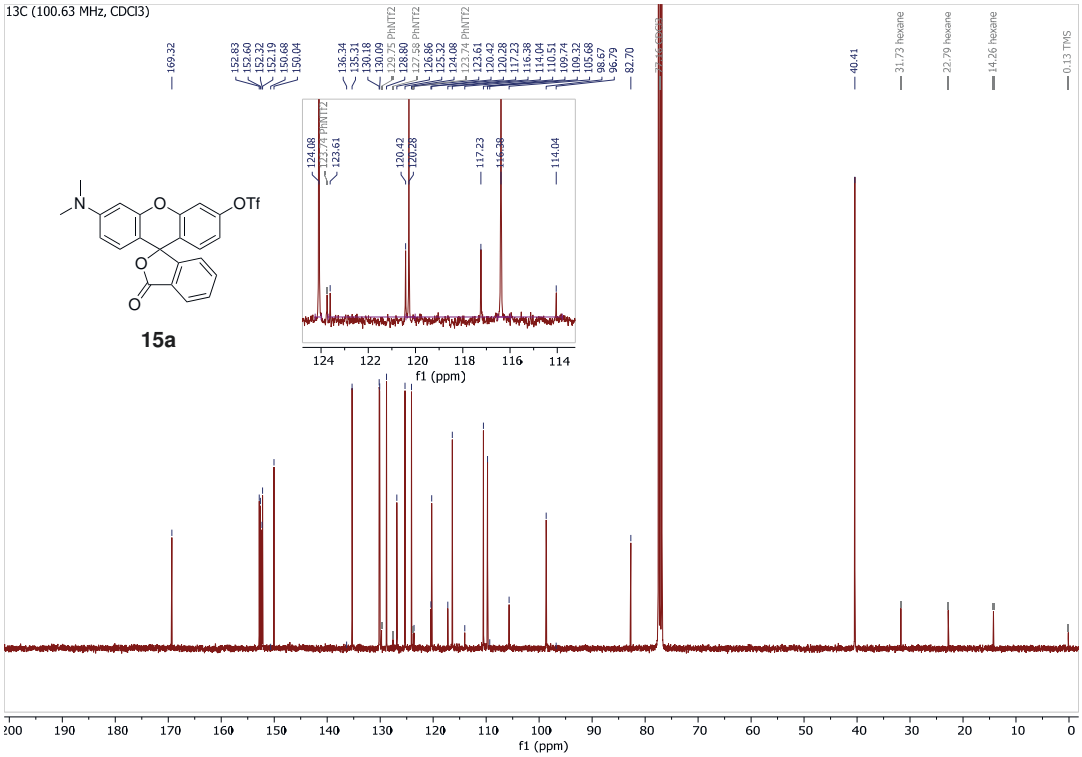
13C (100.63 MHz, CDCl3)
169.32
152.83
152.60
152.32
152.19
150.68
150.04
136.34
135.31
130.18
130.09
129.75 PhNTf2
128.80
127.58 PhNTf2
126.86
125.32
124.08
123.74 PhNTf2
123.61
120.42
120.28
117.23
116.38
114.04
110.51
109.74
109.23
105.68
98.67
96.79
82.70
40.41
31.73 hexane
22.79 hexane
14.26 hexane
0.13 TMS
OTf
15a
f1 (ppm)

Compound 16a

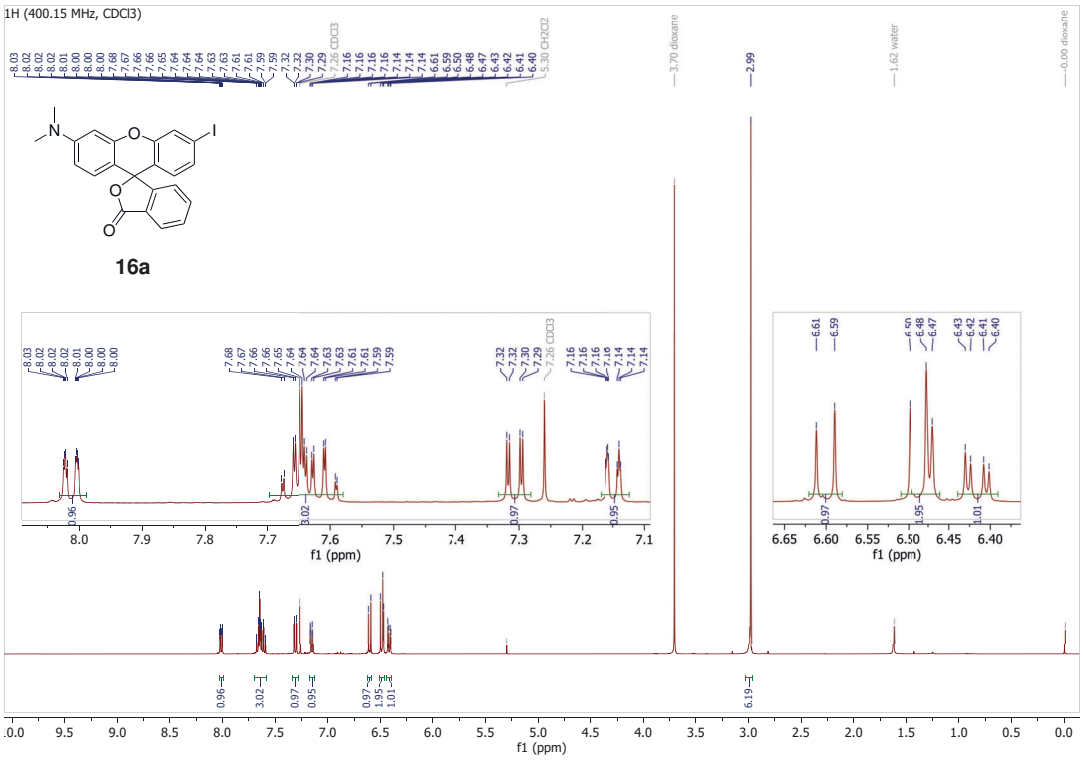

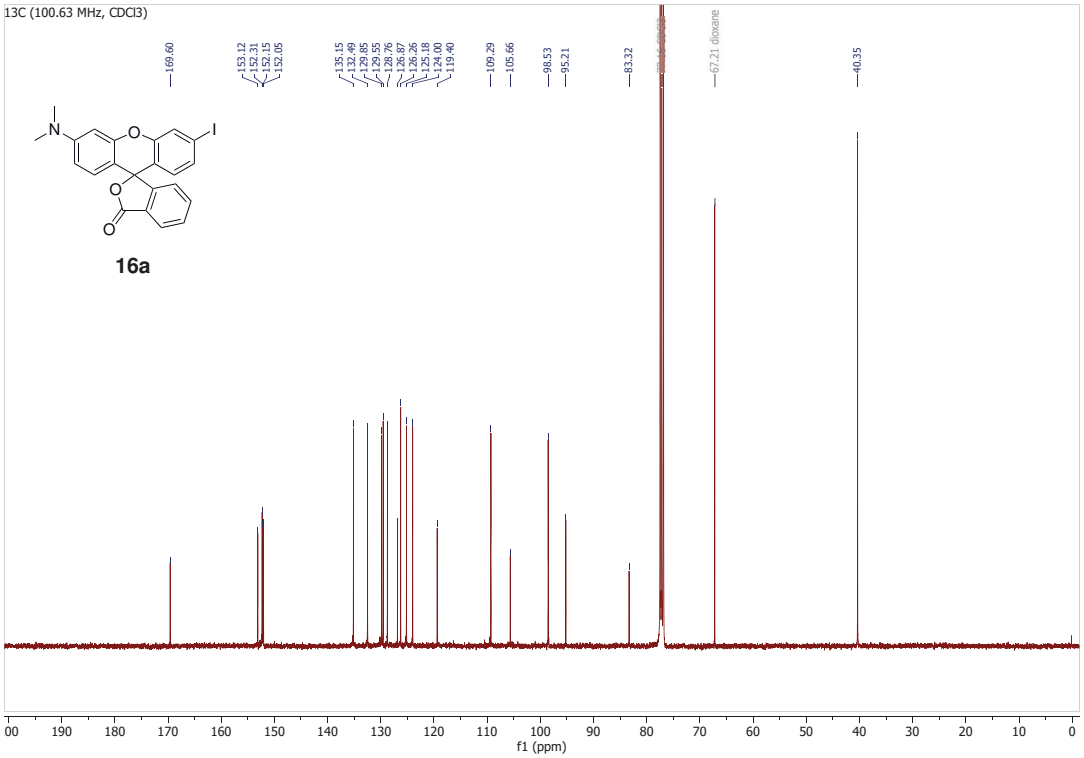

Compound 10d

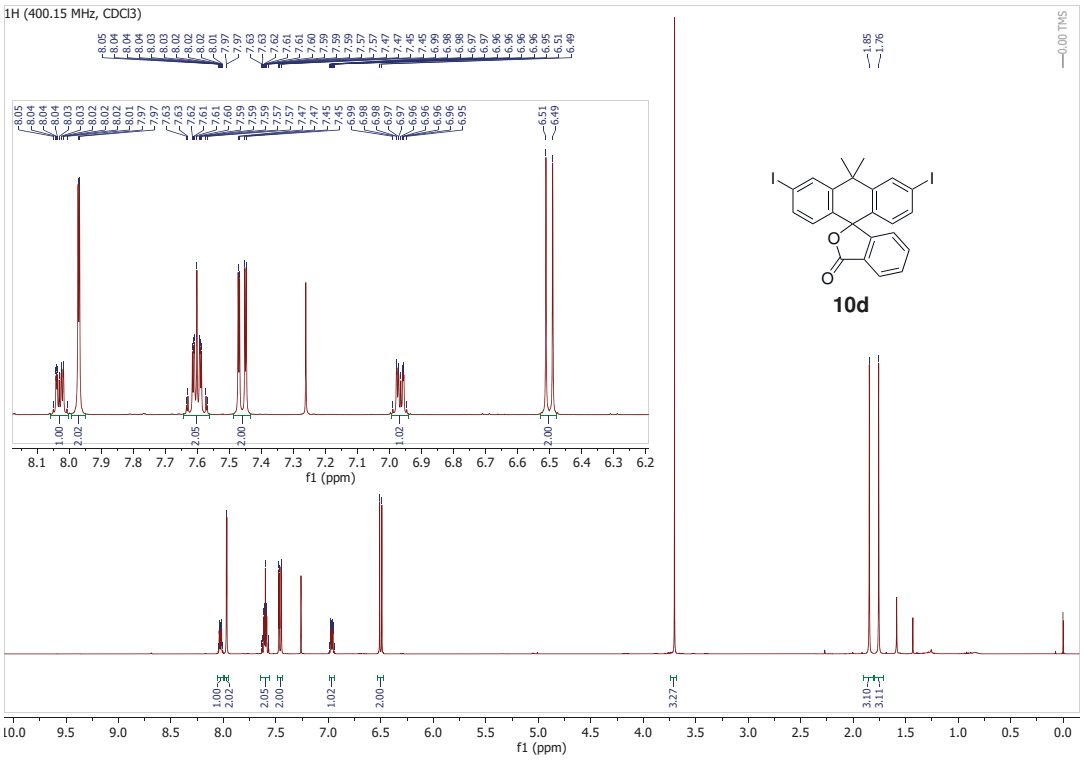

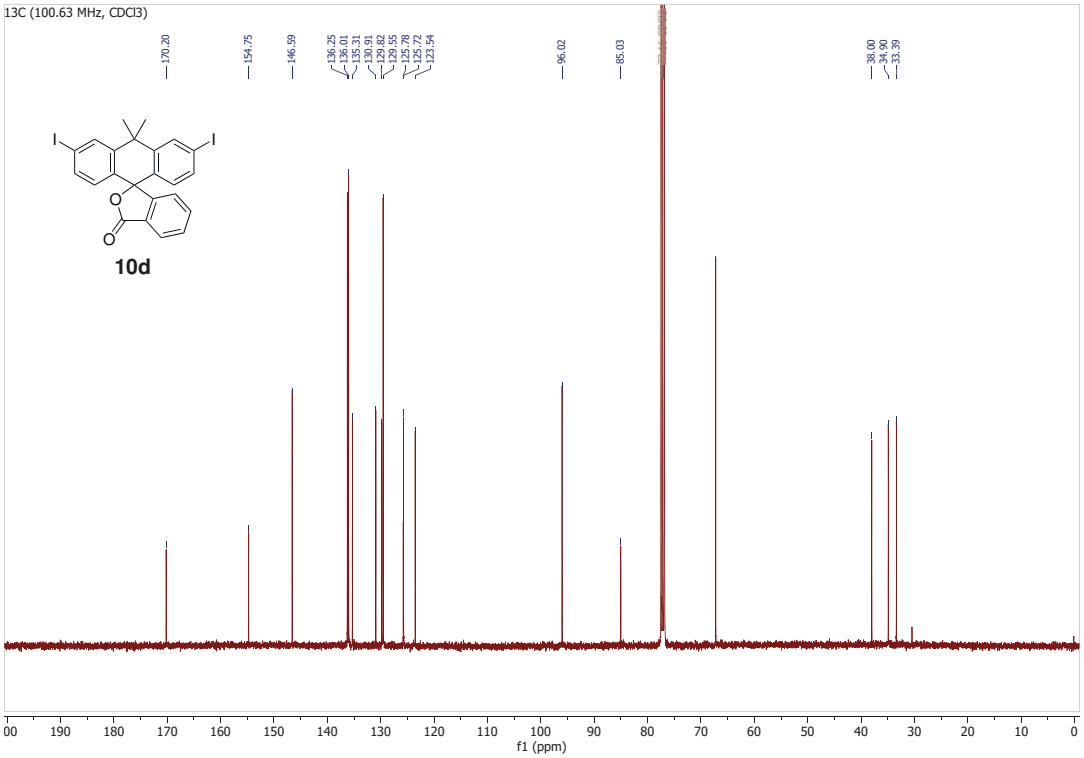

Compound 10f

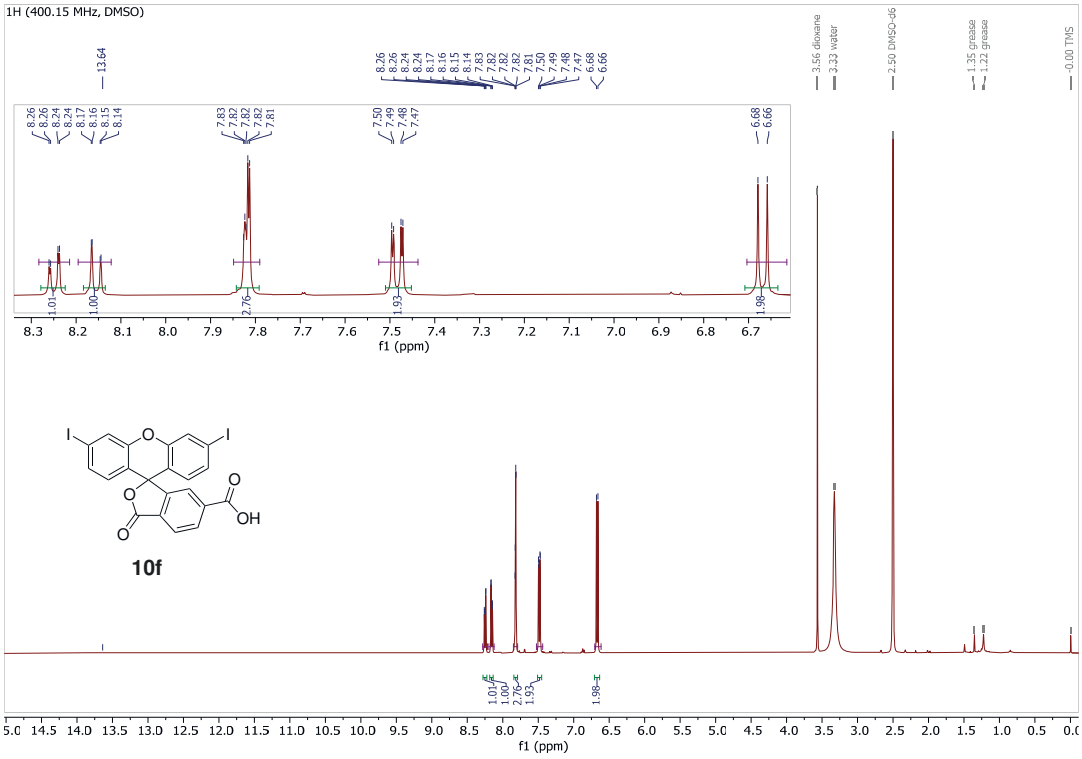

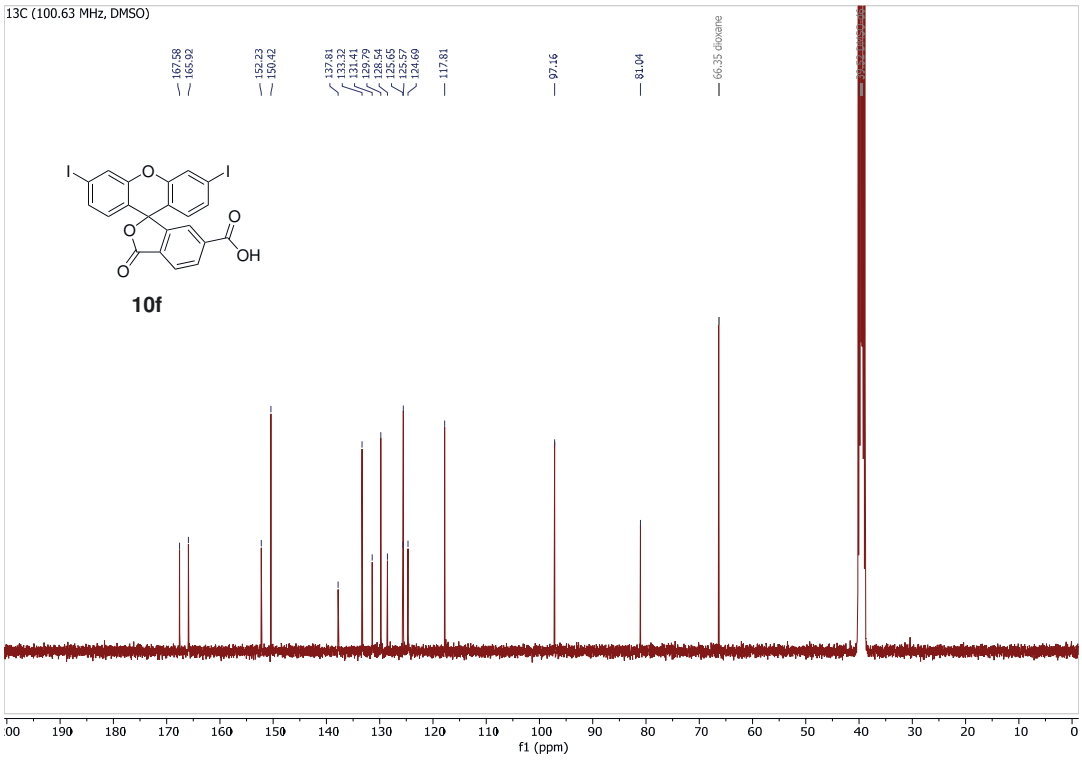

Compound 13a

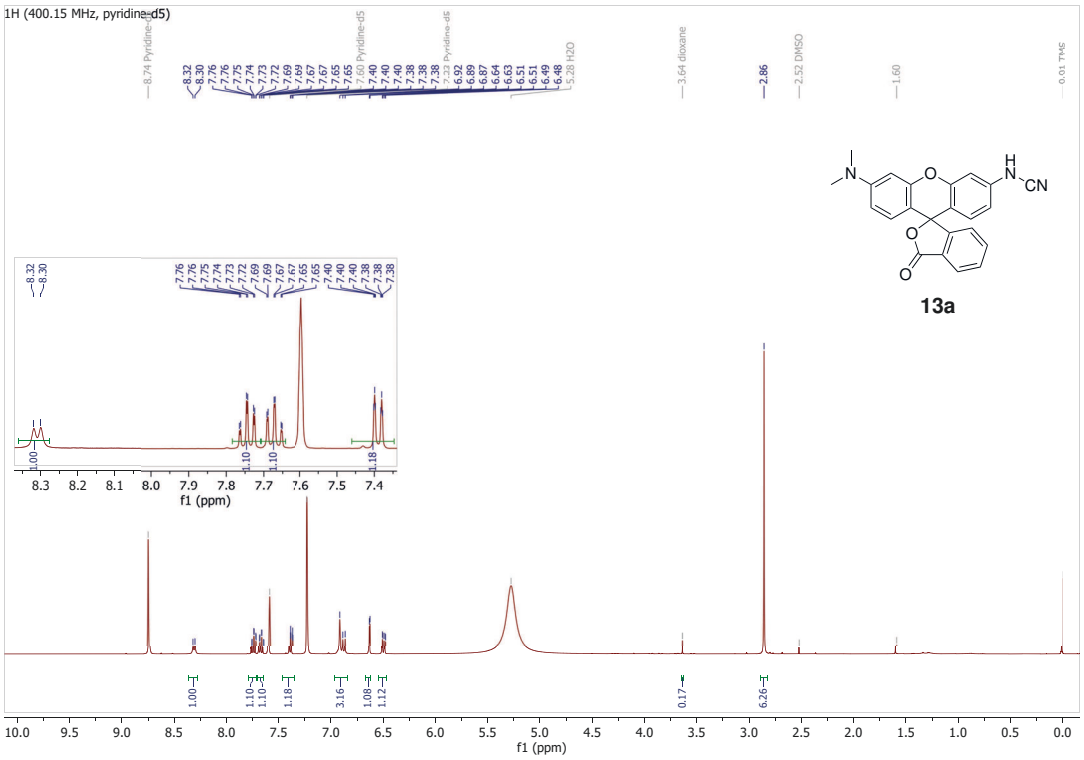

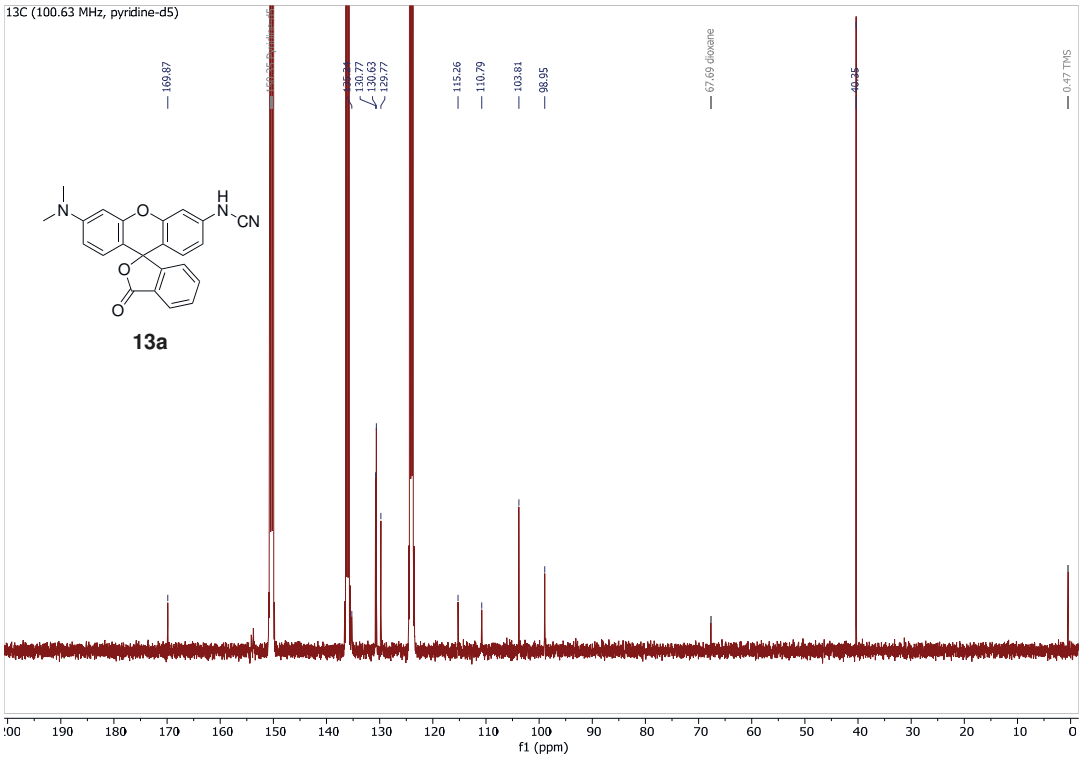

Compound 13b

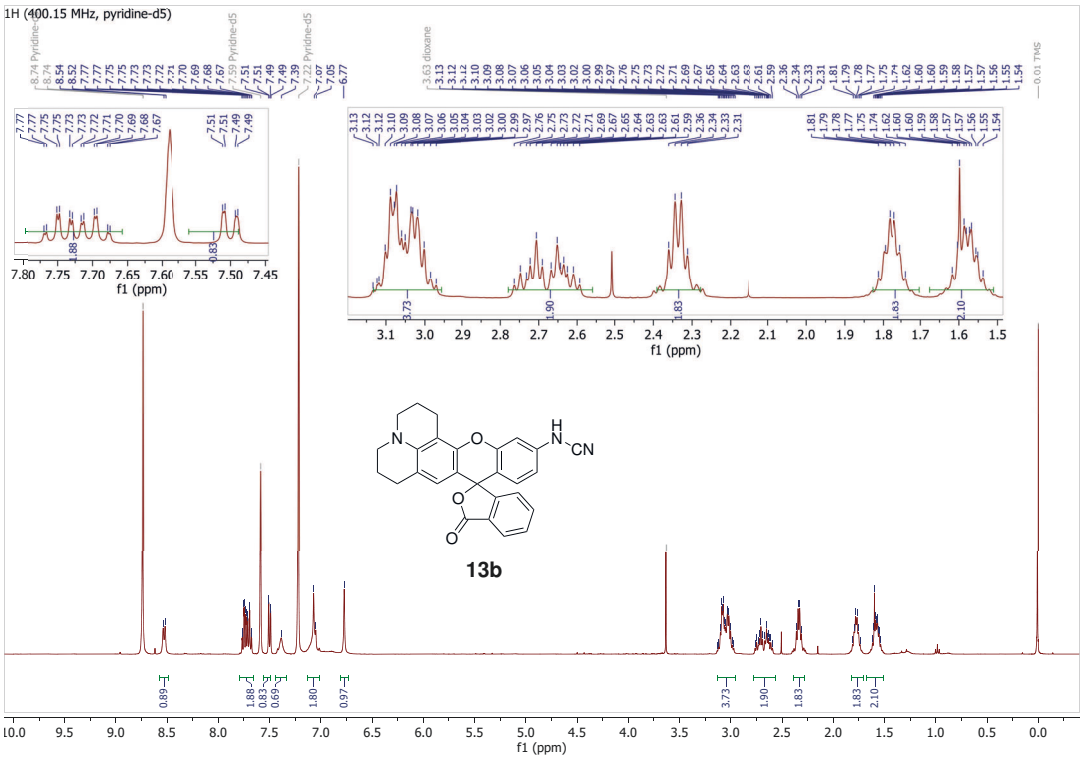

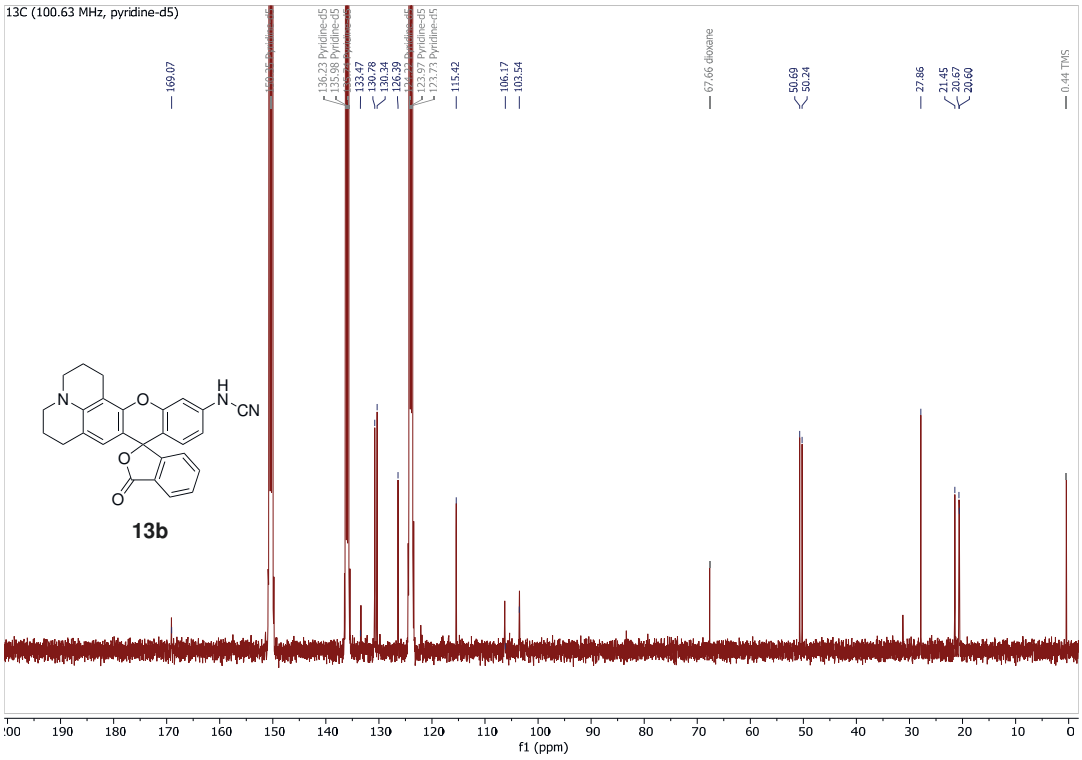

Compound 13c

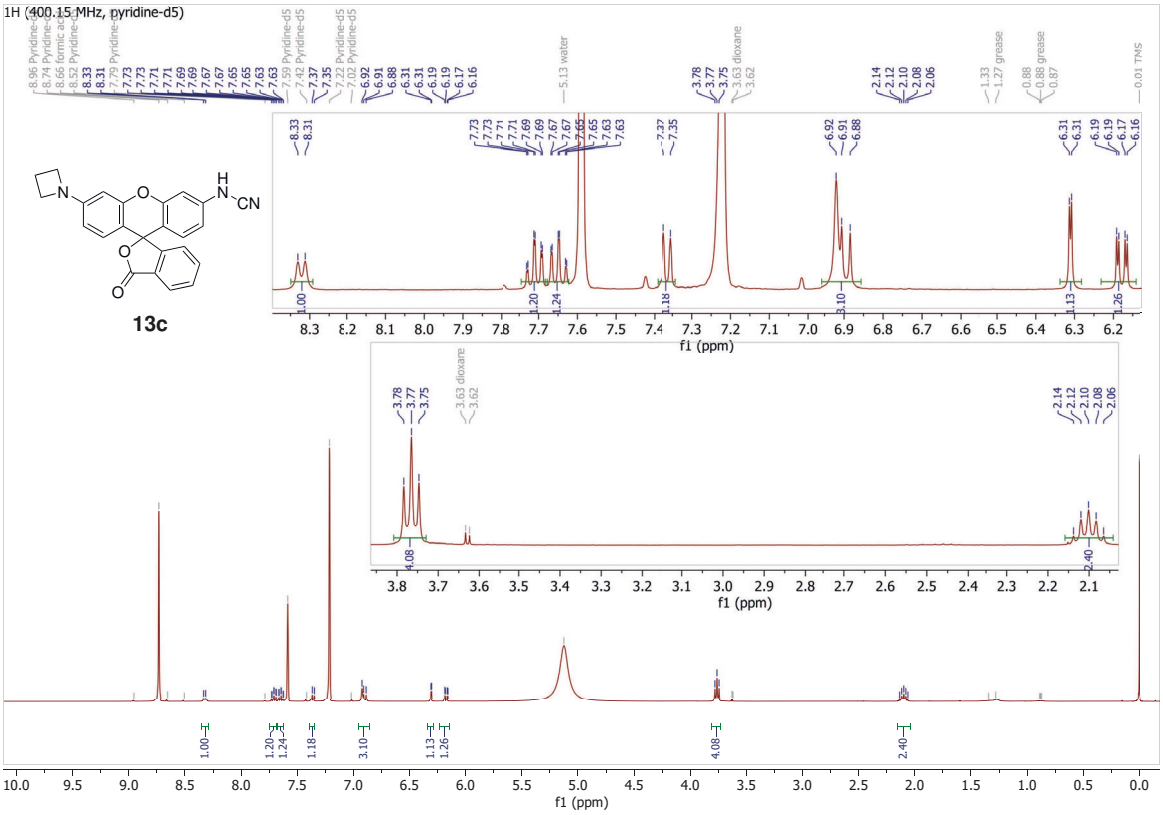

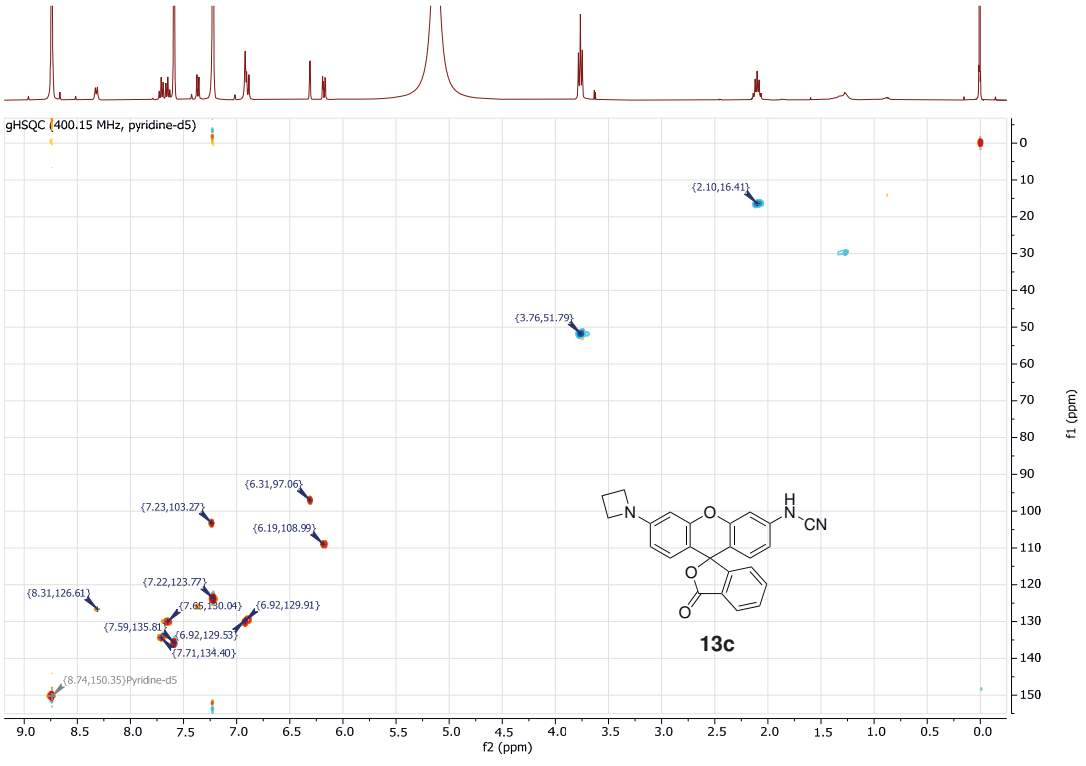

Compound 17

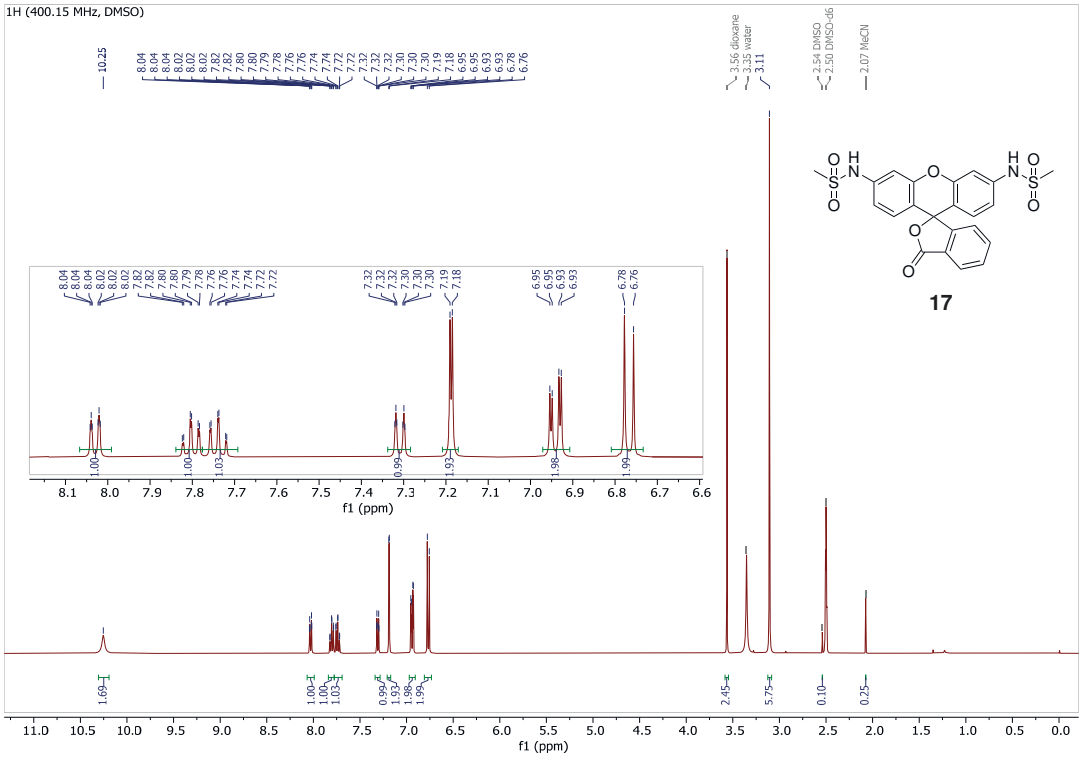

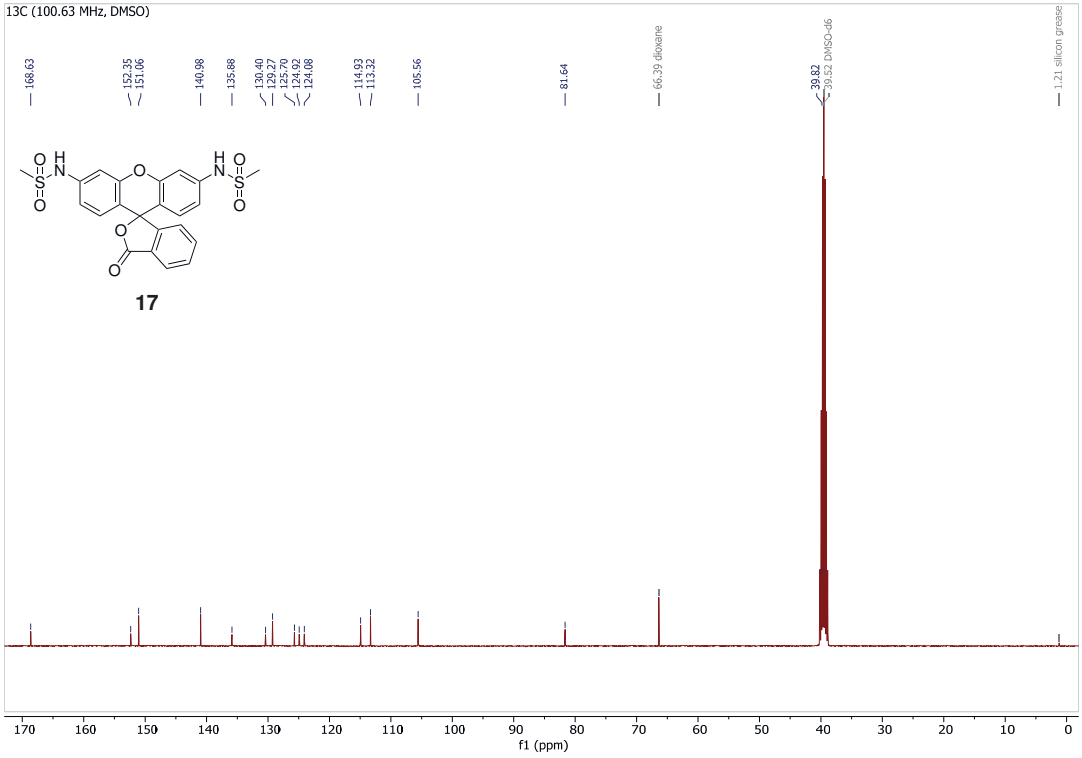

Compound 14a

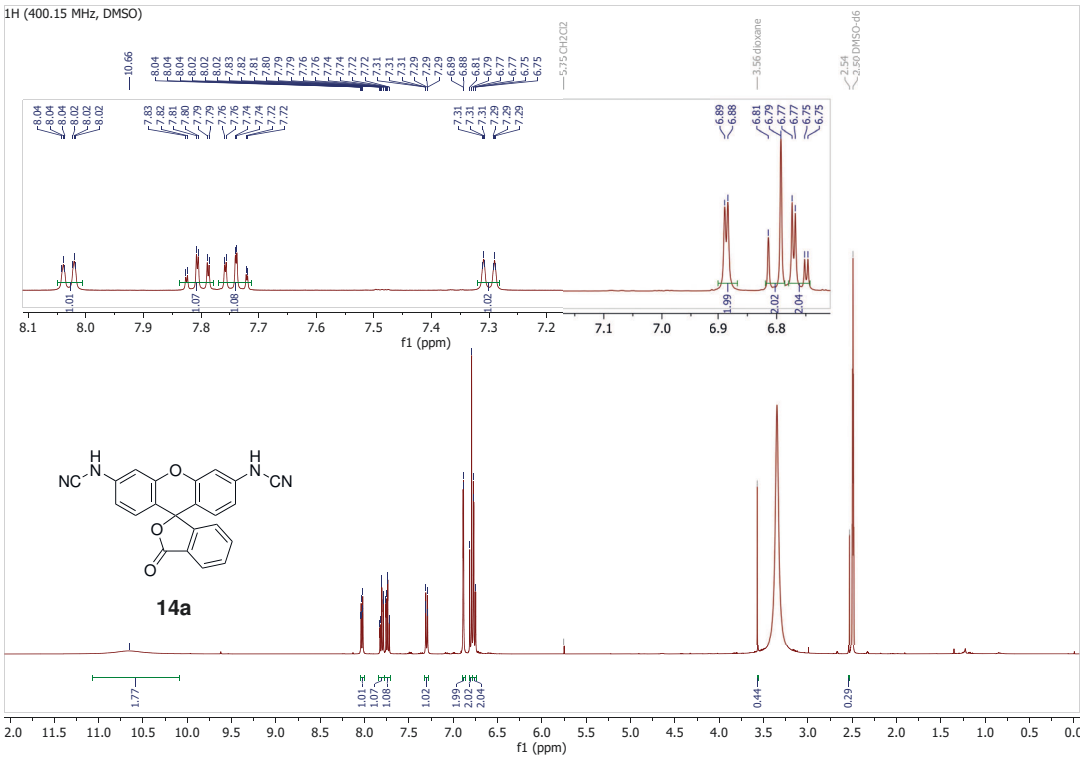

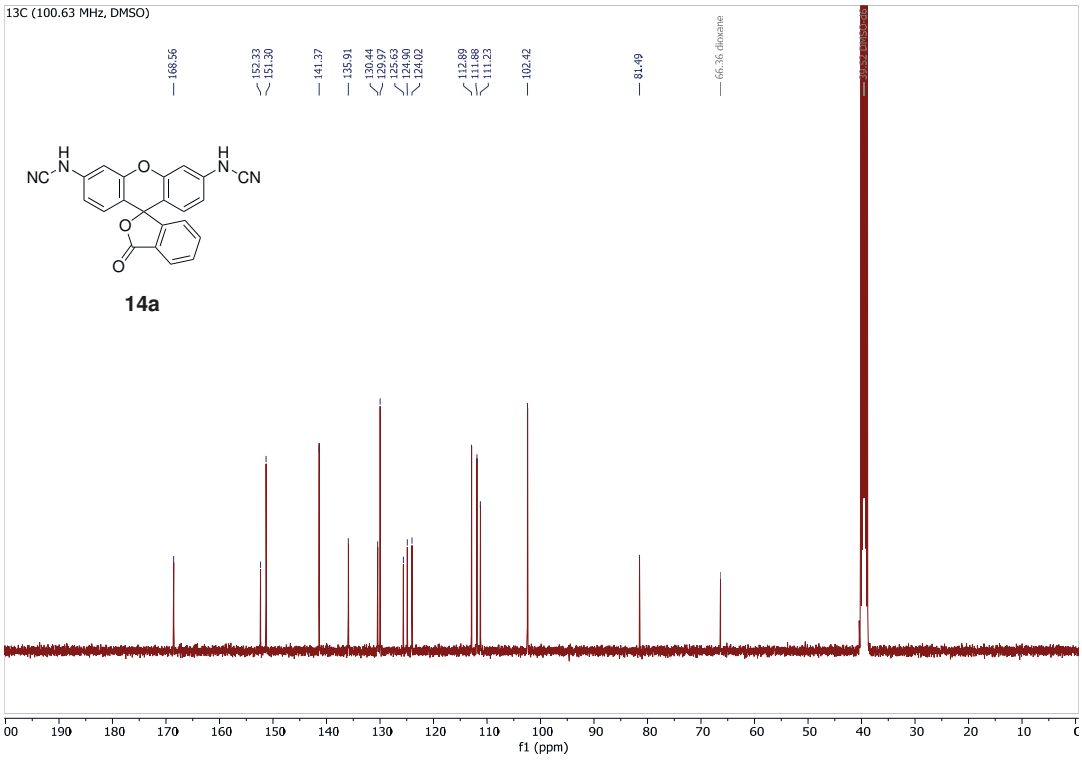

Compound 14c

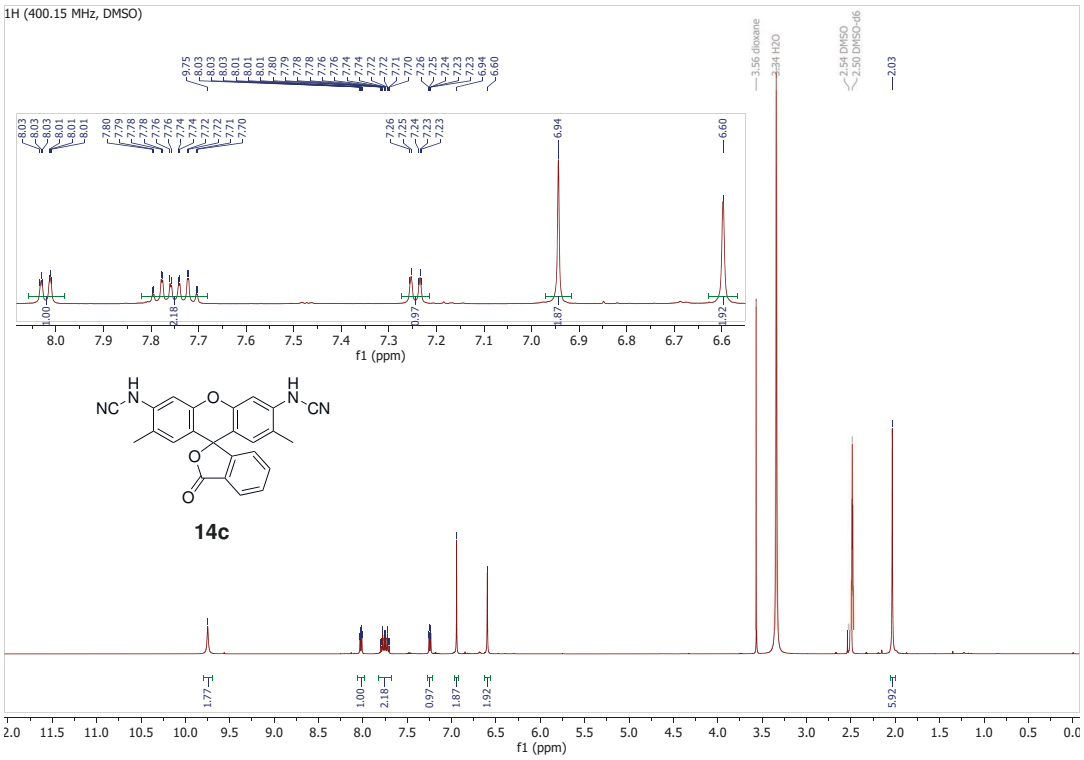

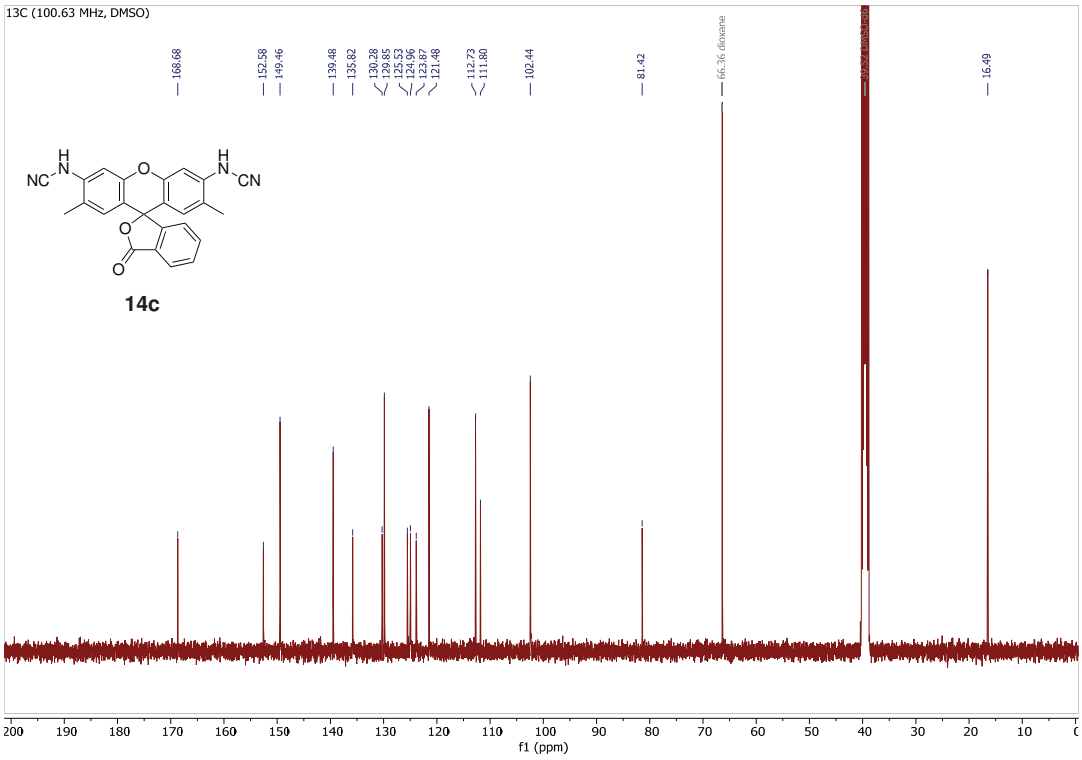

Compound 14d

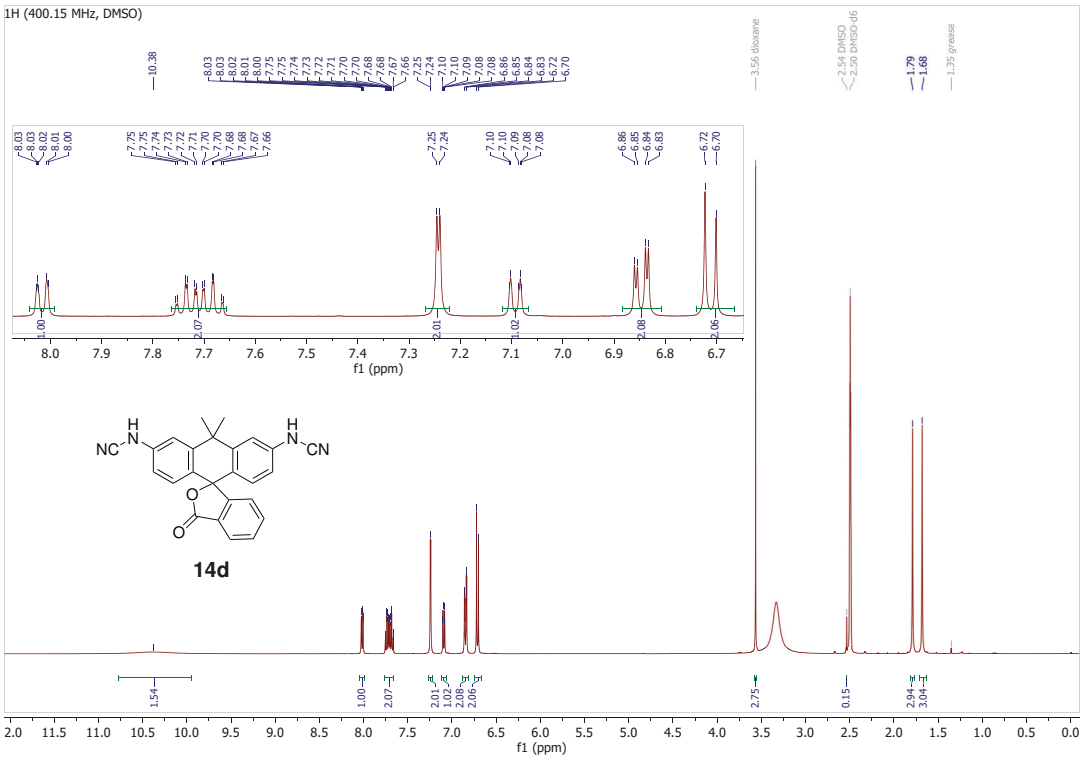

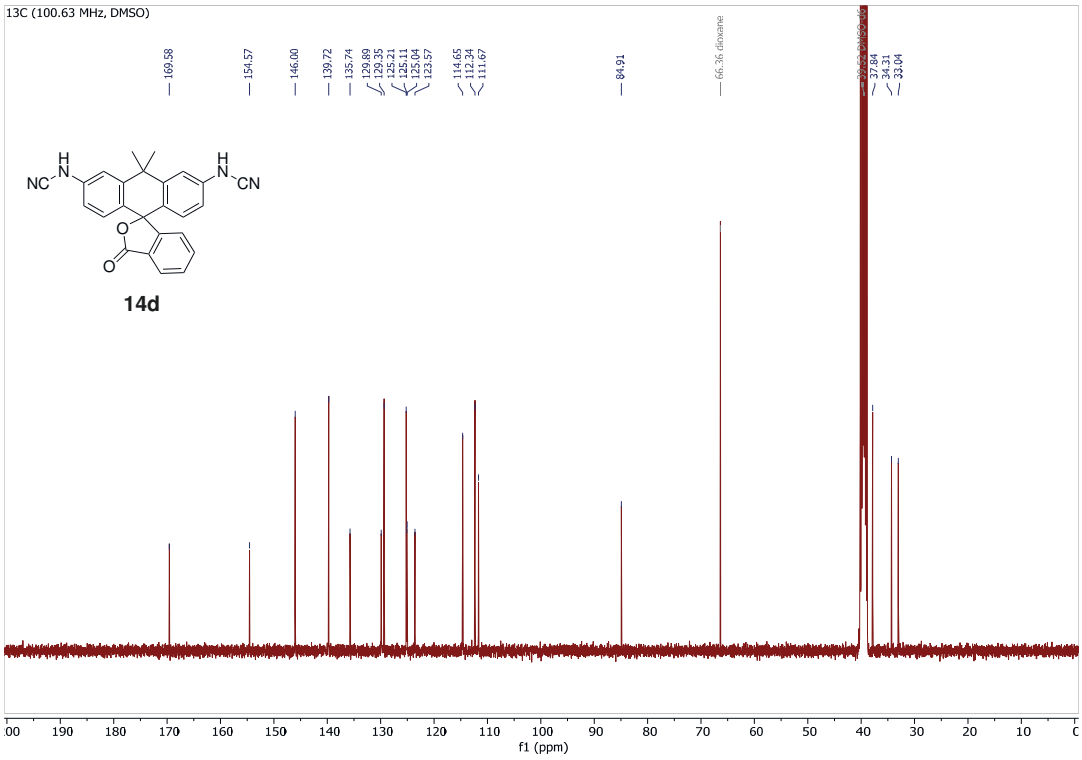

Compound NCR1

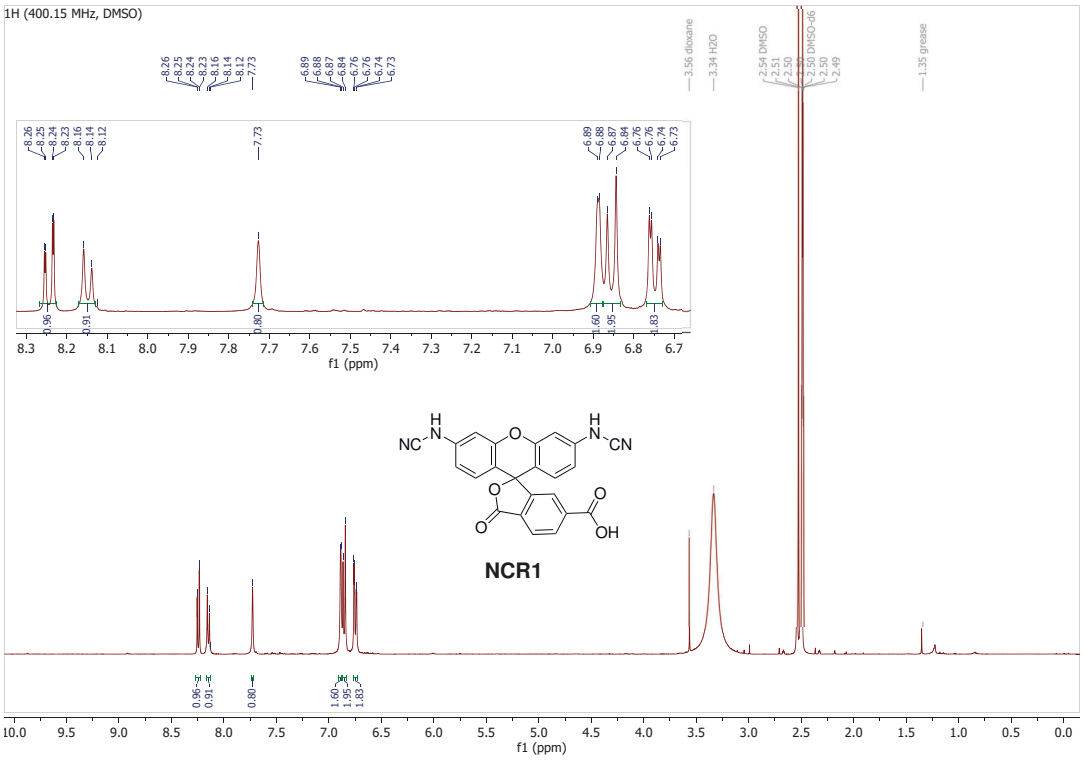

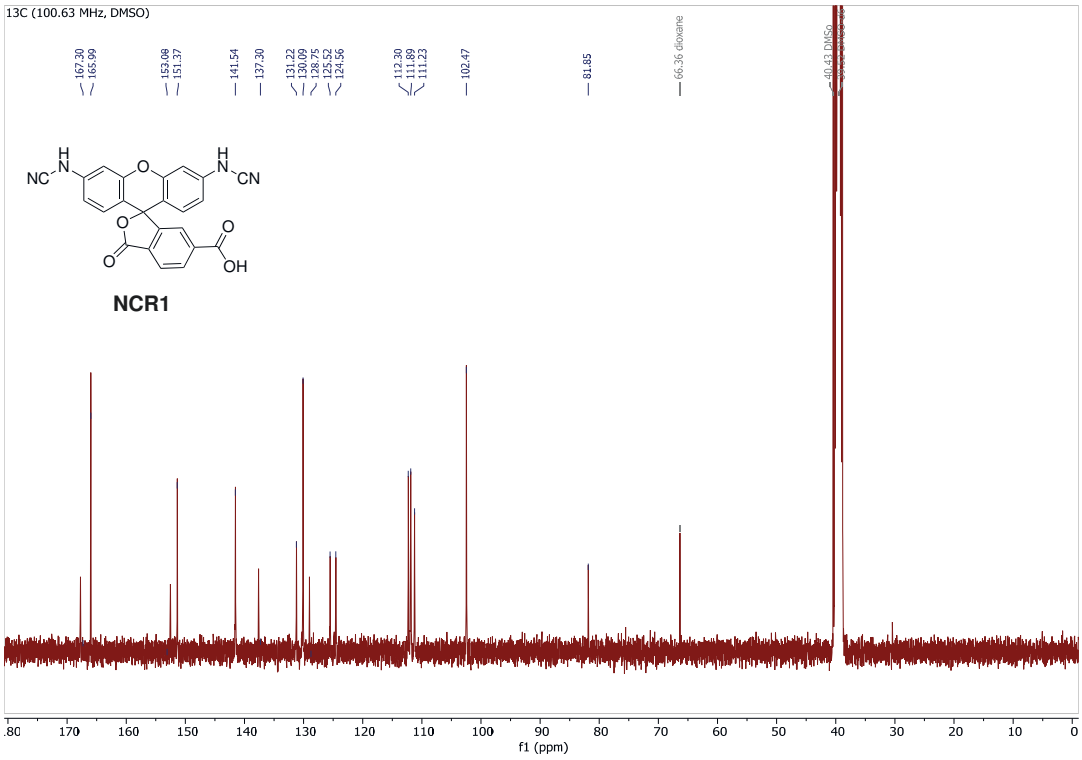

Compound 18

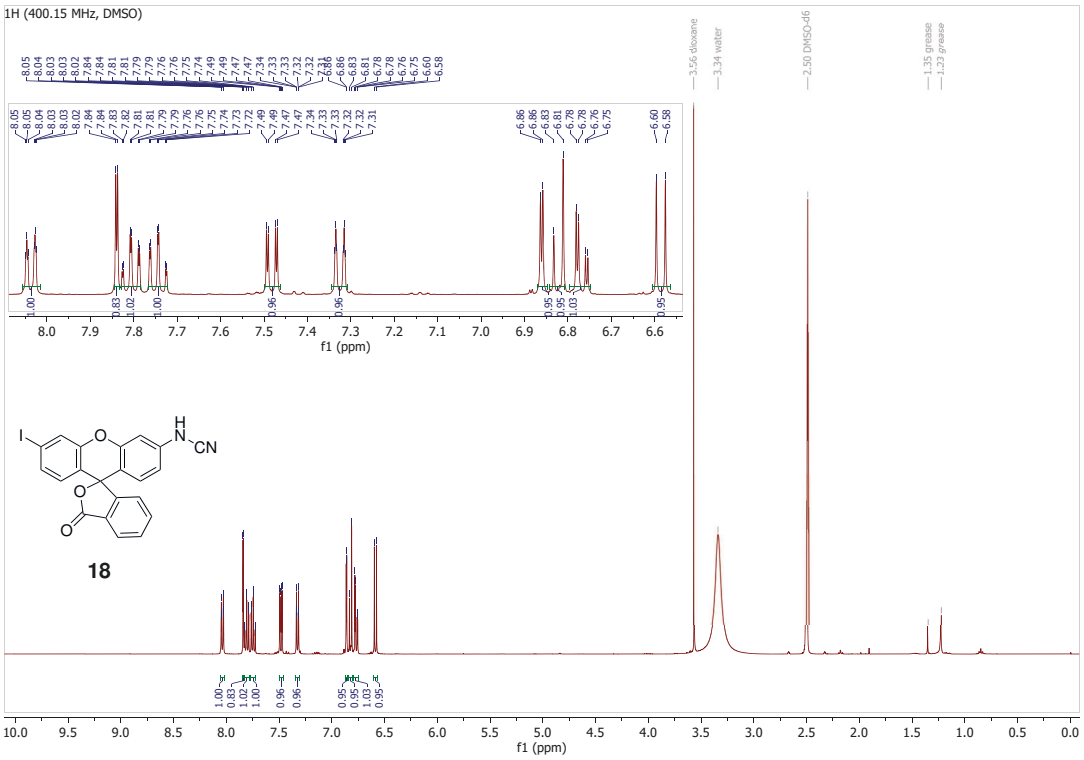
1H (400.15 MHz, DMSO)
3.56 dioxane
3.34 water
2.50 DMSO-d6
1.35 grease
1.23 grease
f1 (ppm)
18

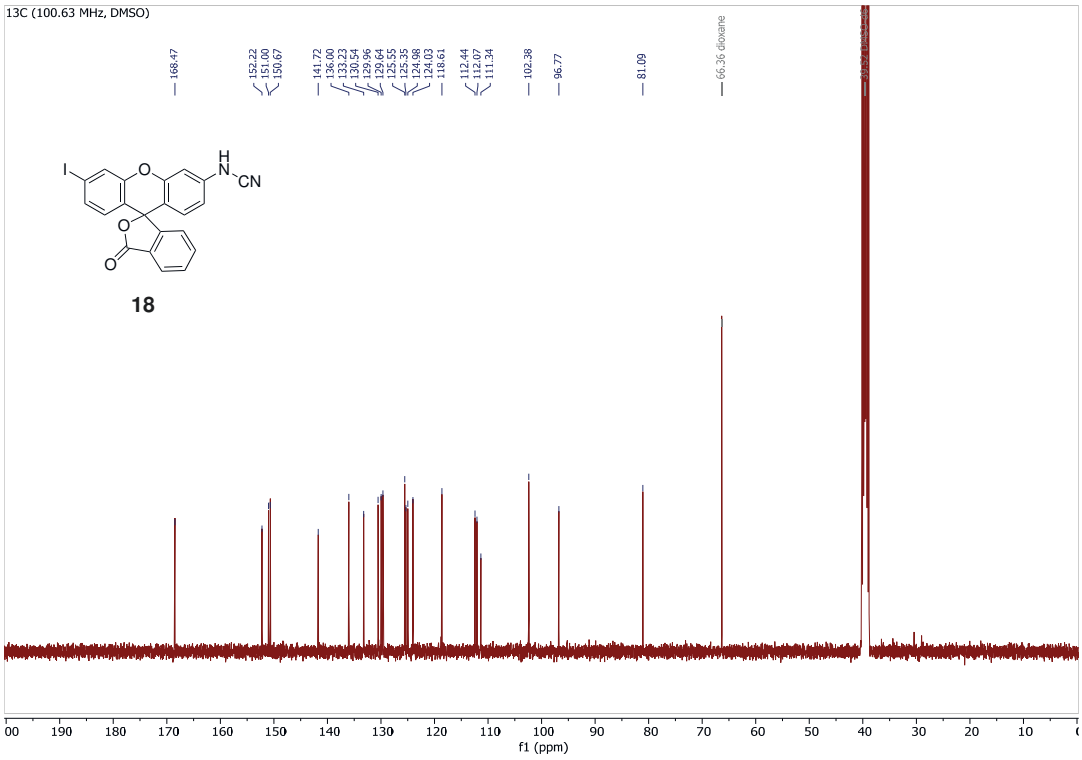
13C (100.63 MHz, DMSO)
168.47
152.22
151.00
150.67
141.72
136.00
133.23
130.54
129.96
129.64
125.55
125.35
124.98
124.03
118.61
112.44
112.07
111.34
102.38
96.77
81.09
66.36 dioxane
f1 (ppm)
18

Compound 24a

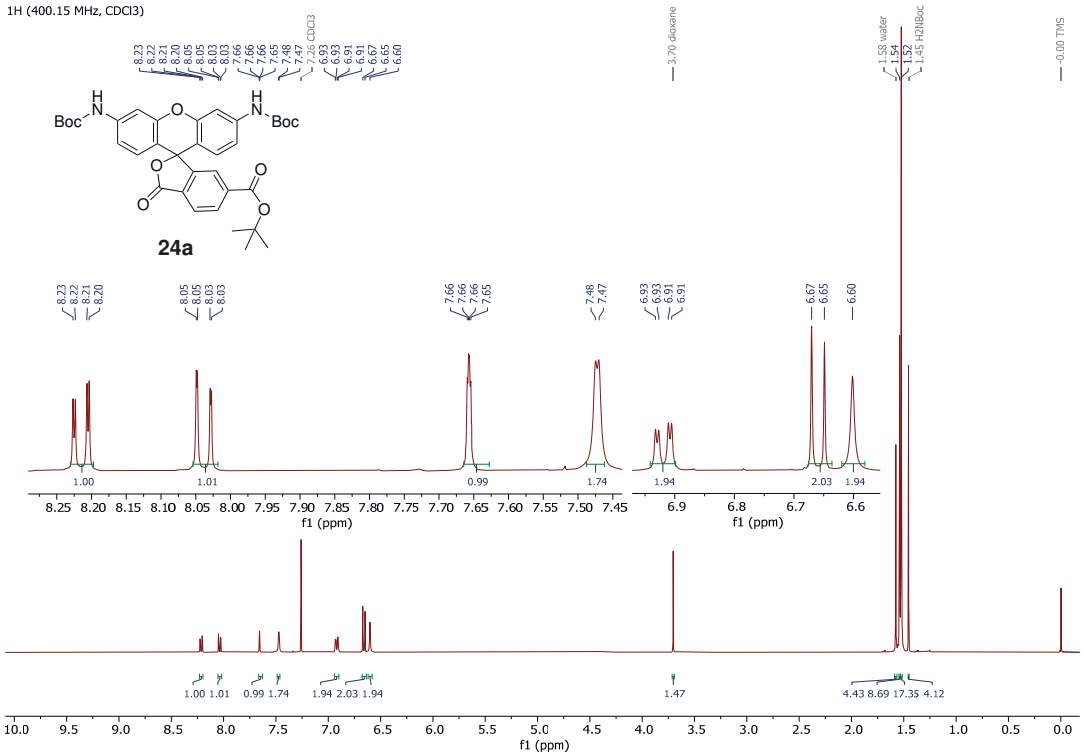

Compound 24b

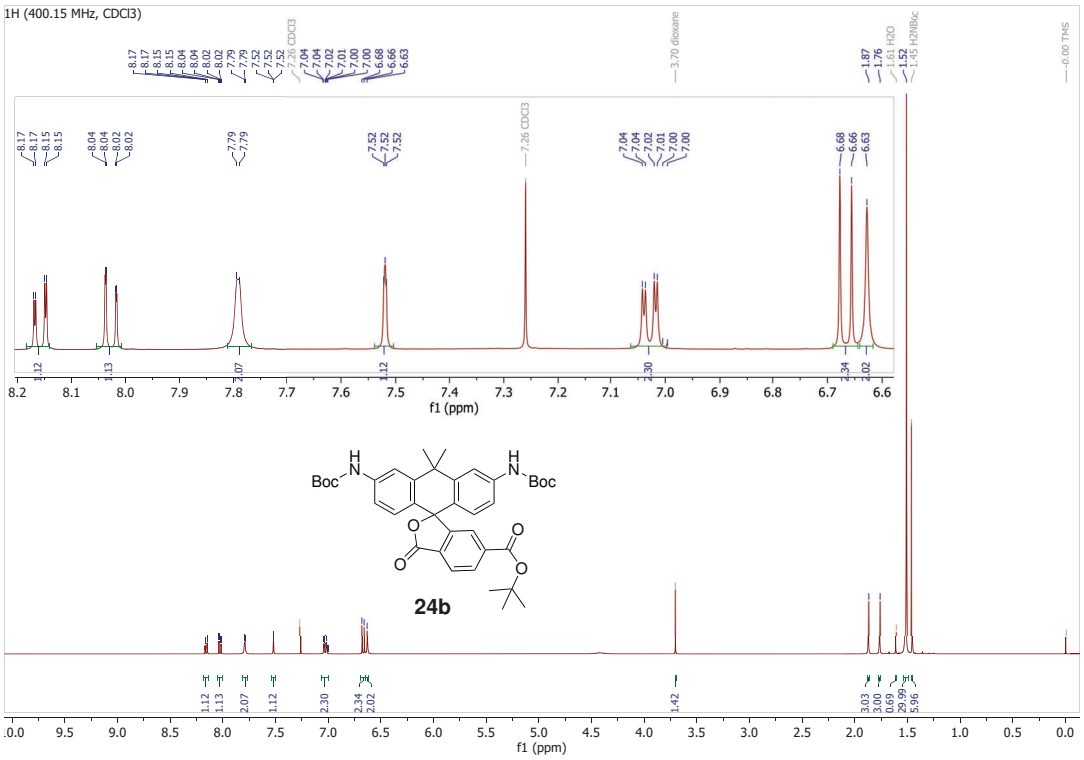

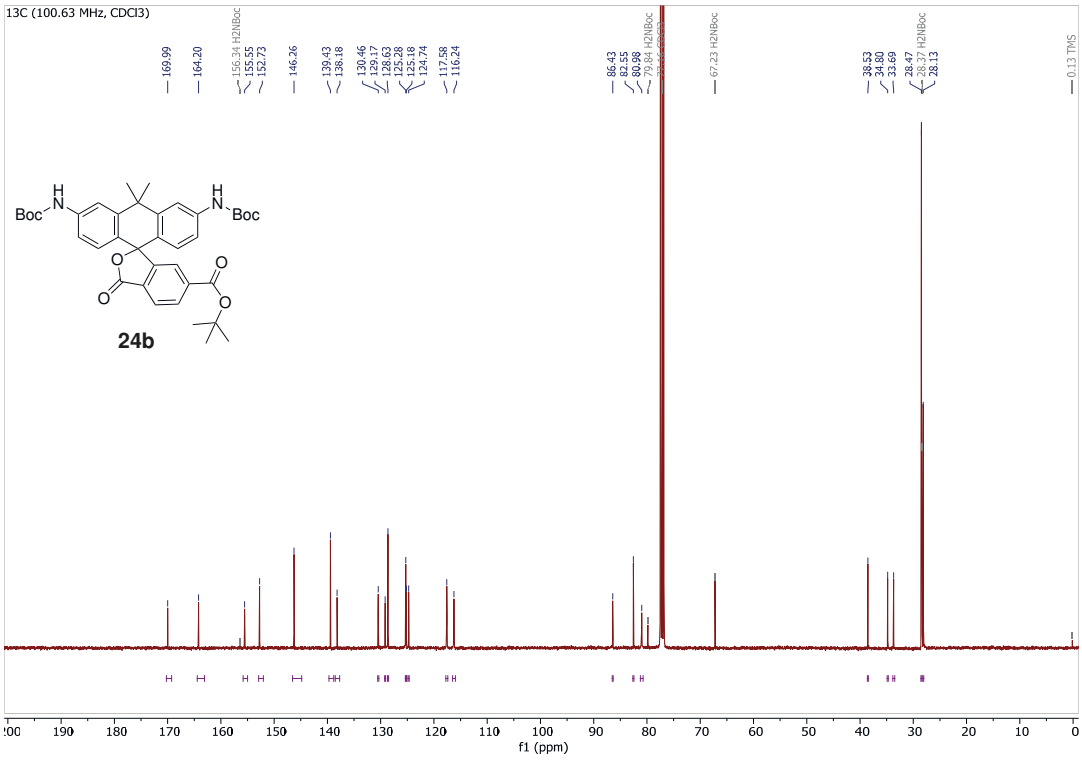

Compound 25a

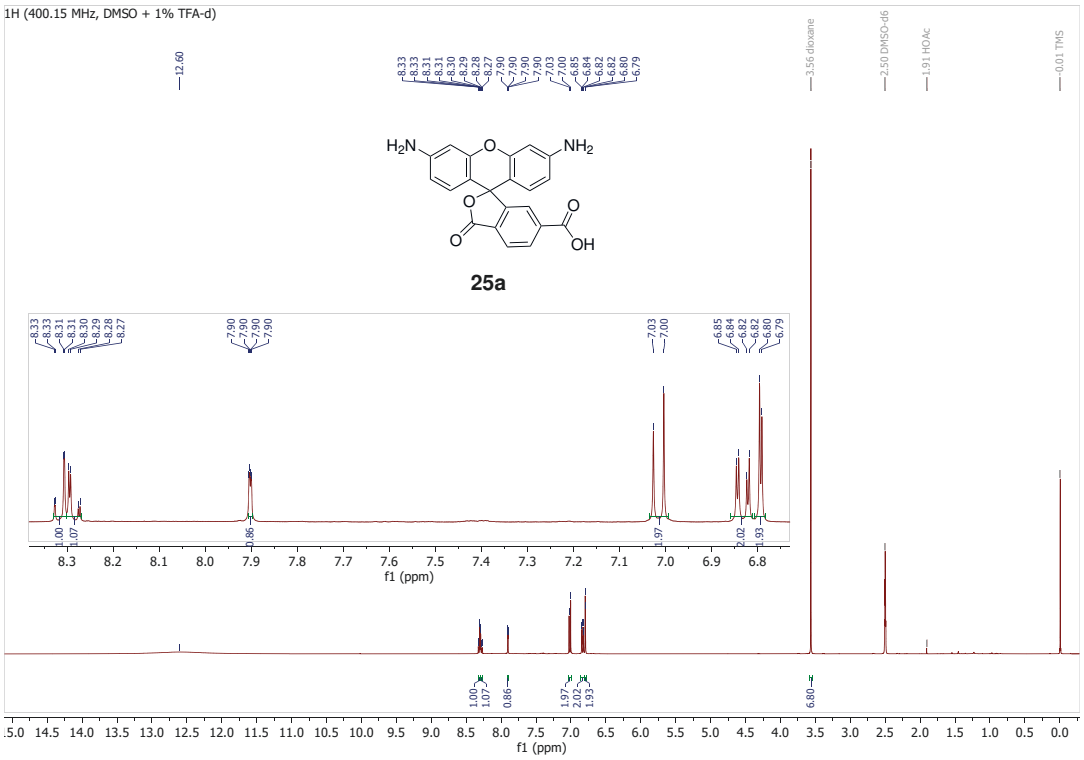

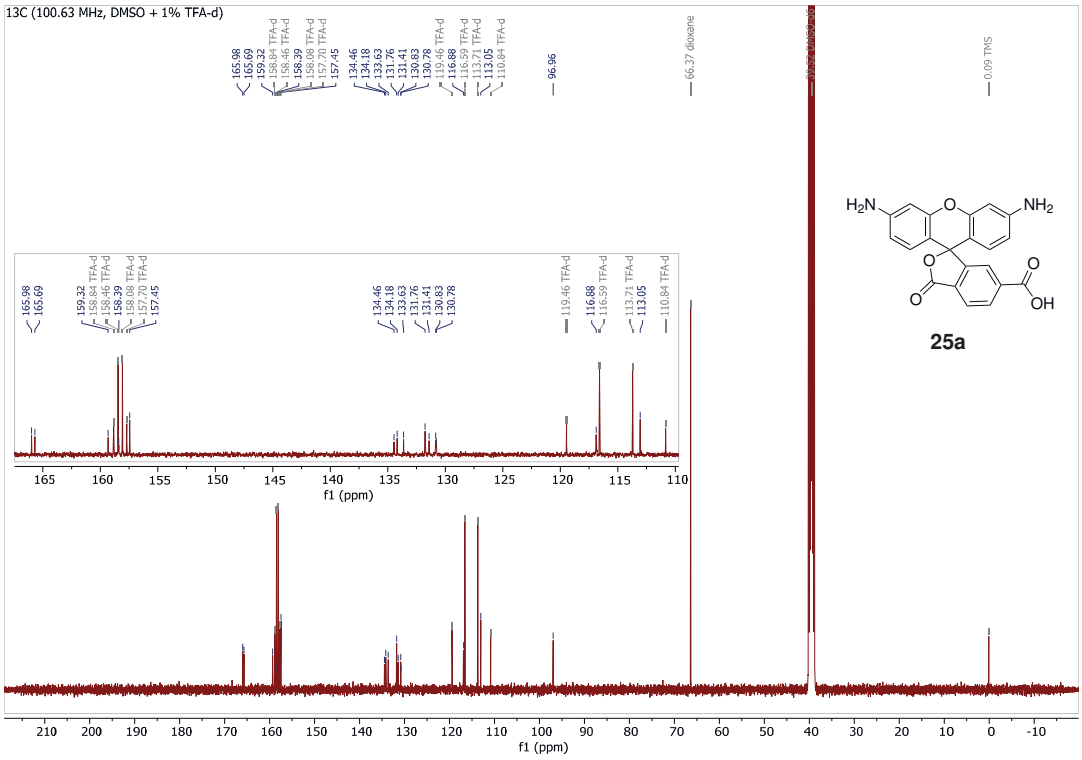

Compound 25b

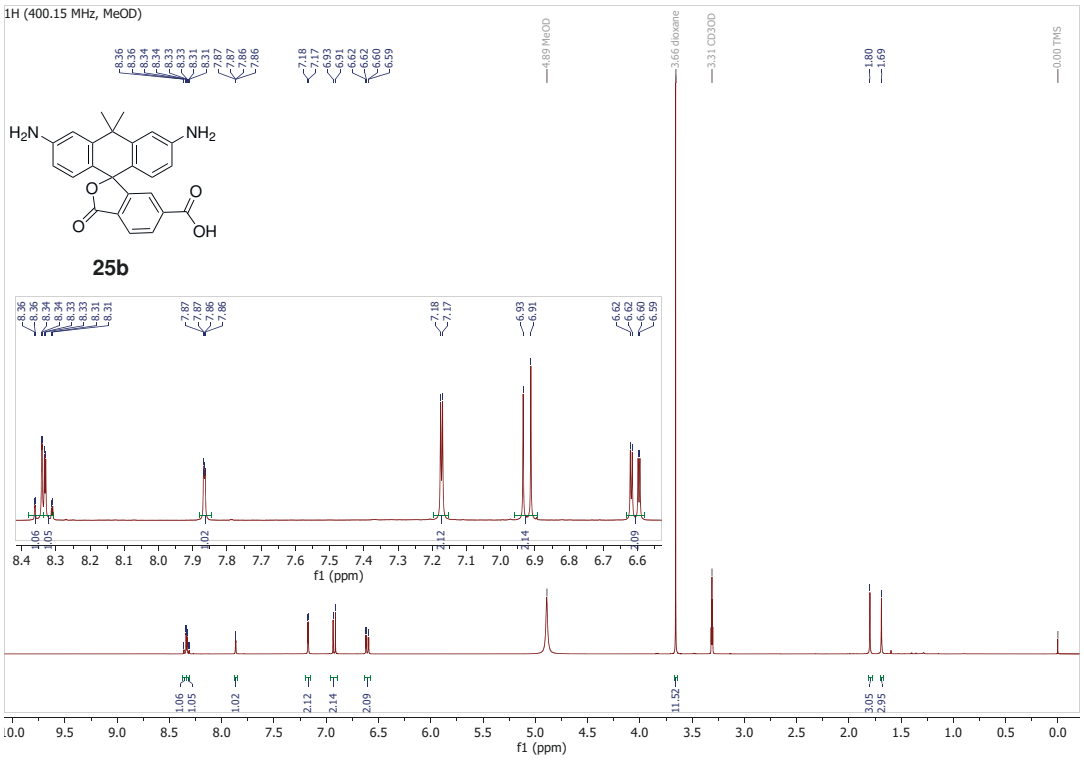

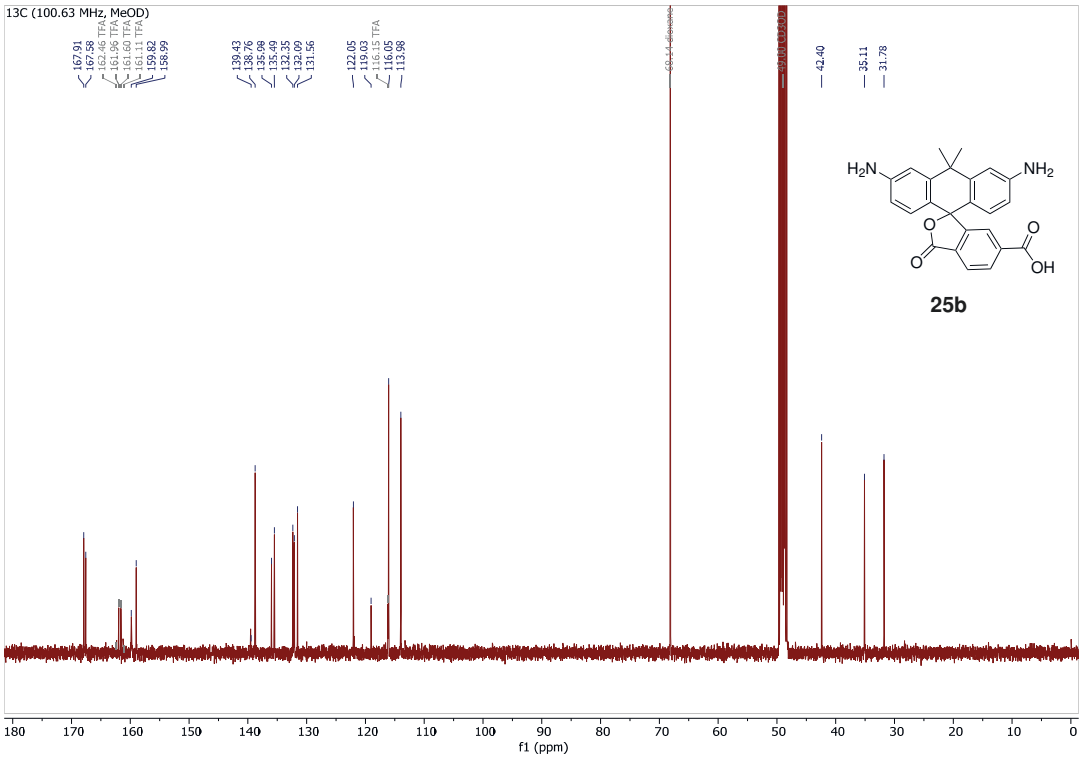

Compound 26a

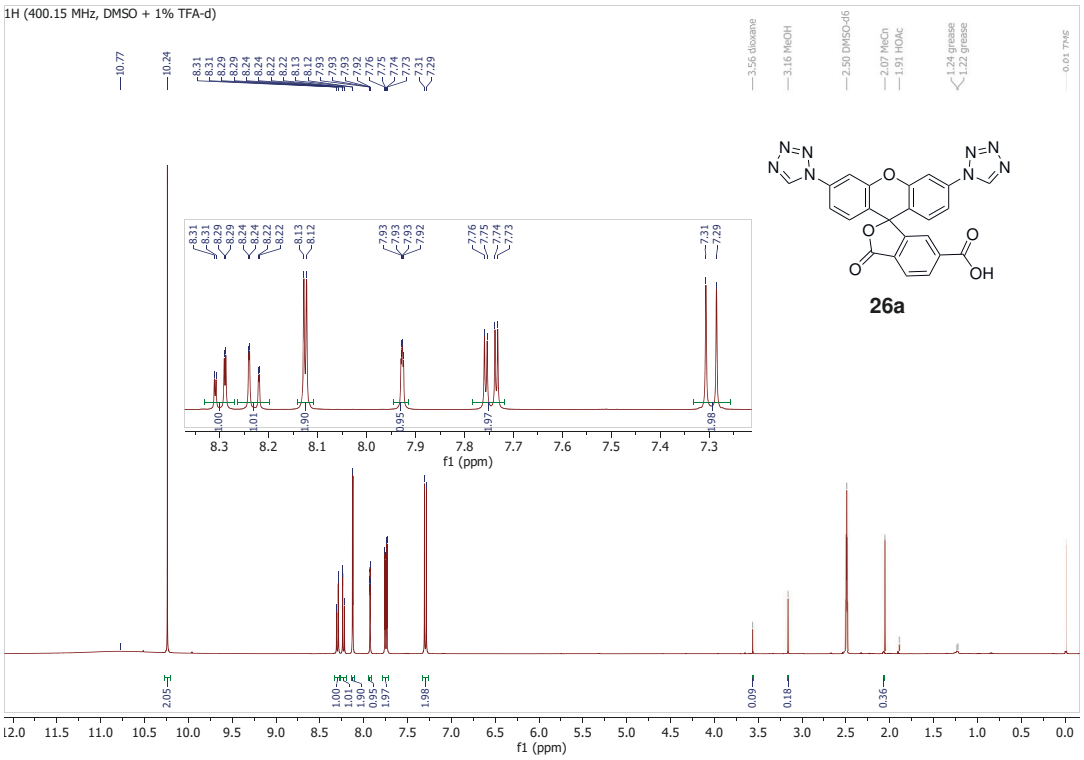

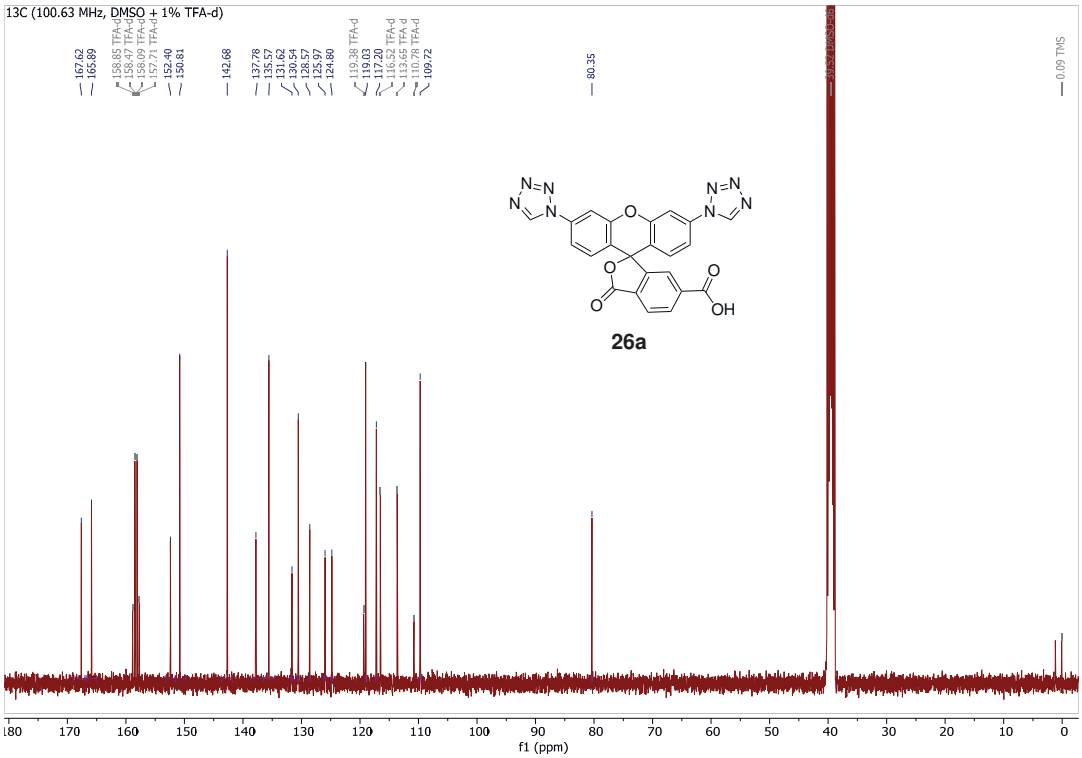

Compound 26b

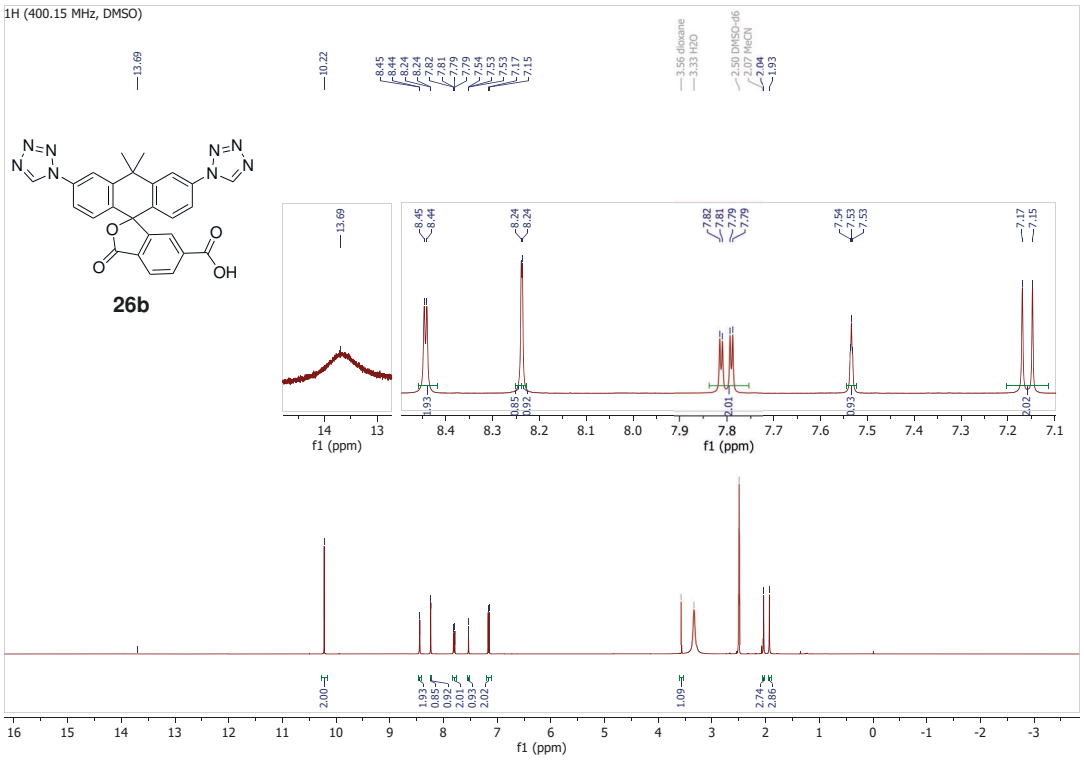

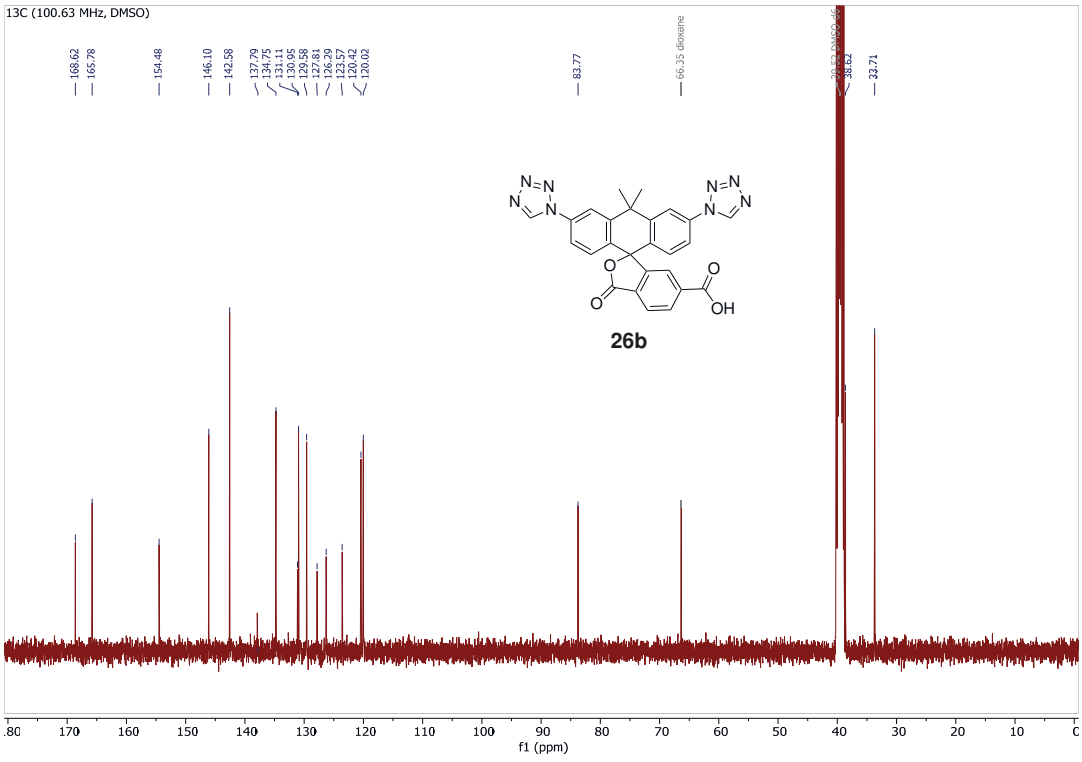

Compound 26c

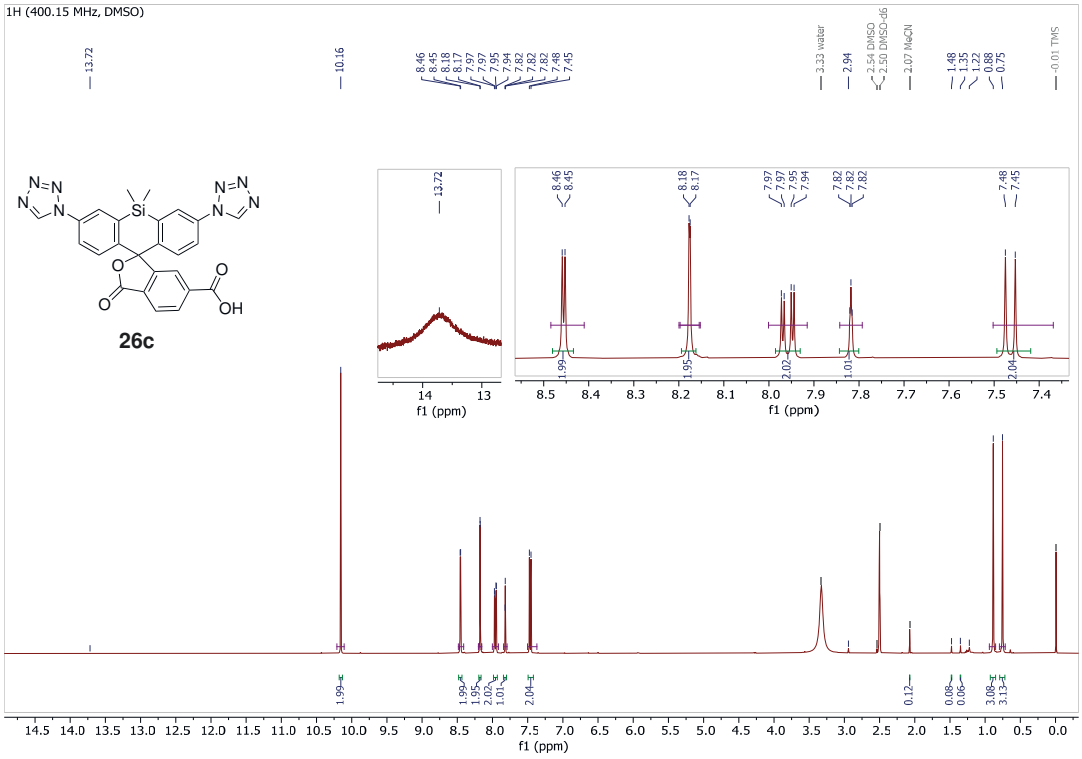

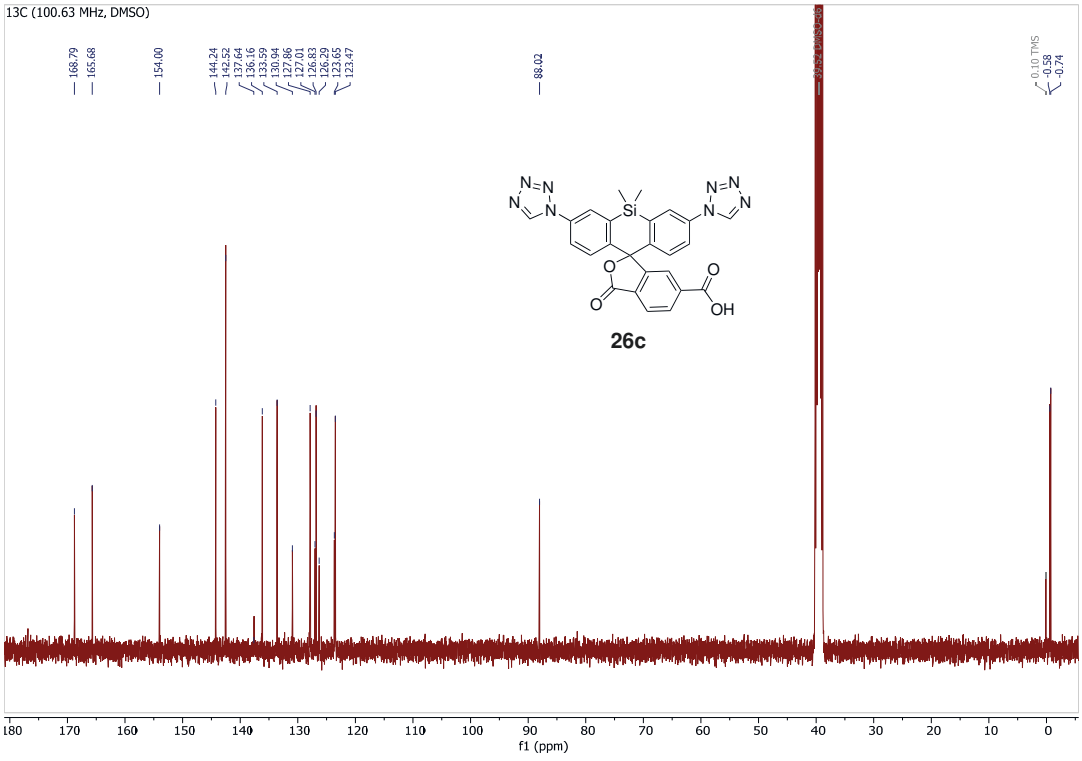

Compound NCR2

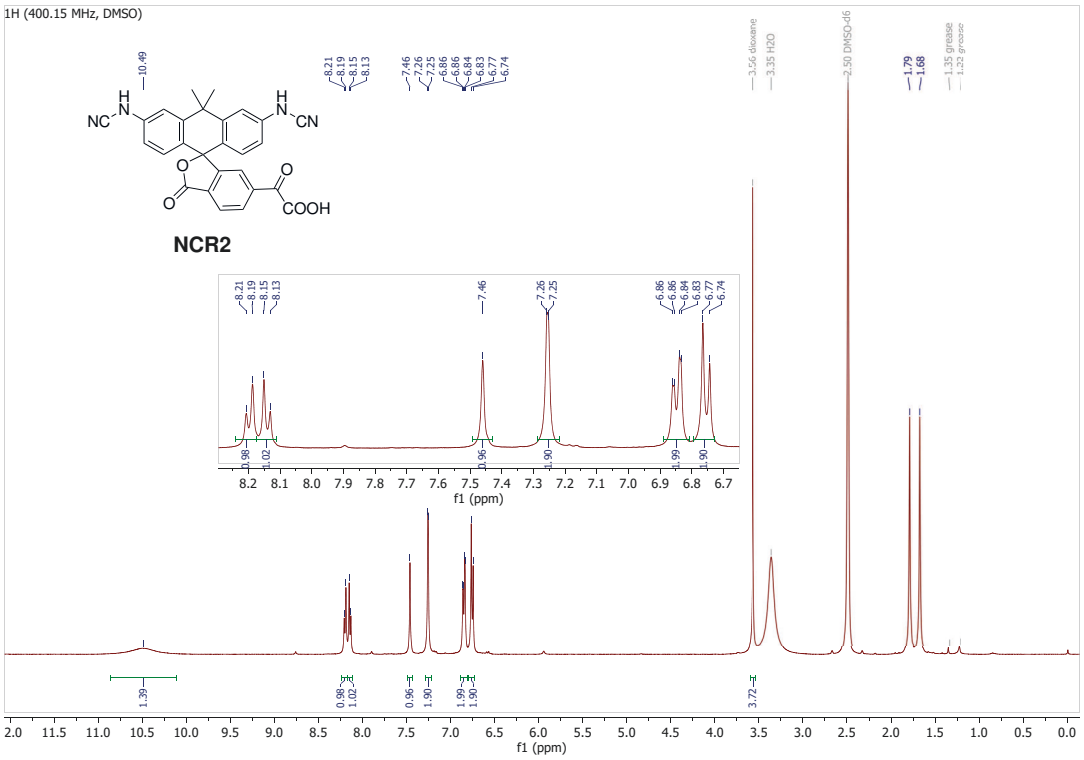

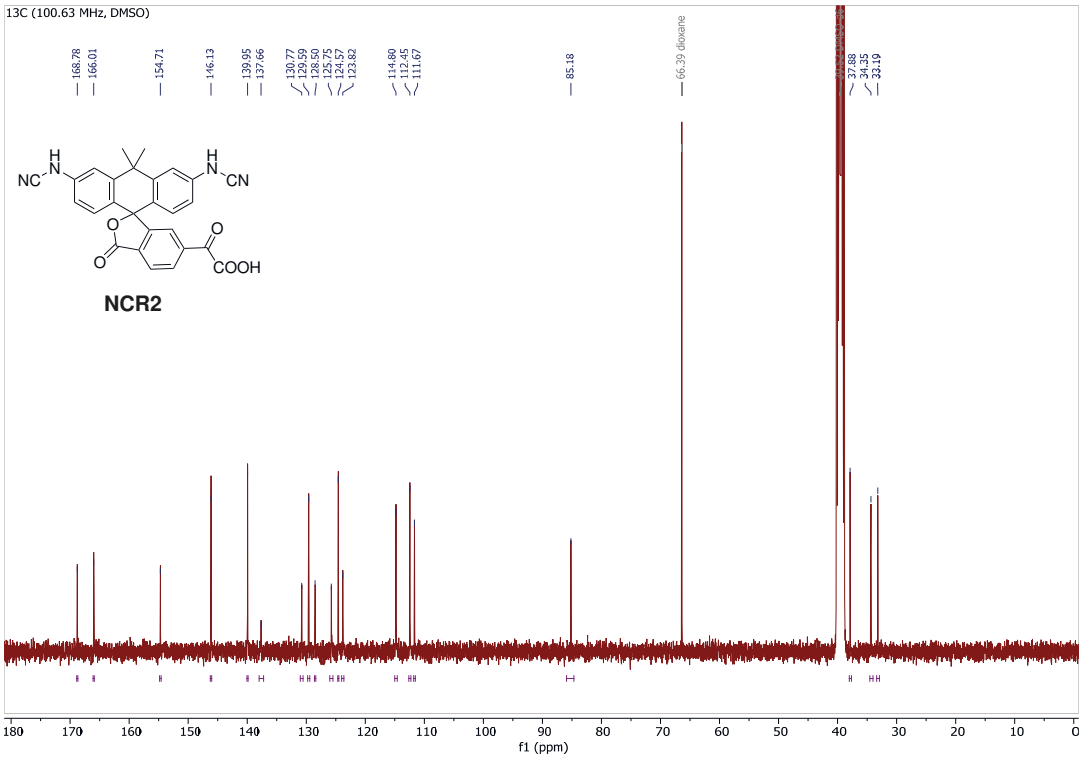

Compound NCR3

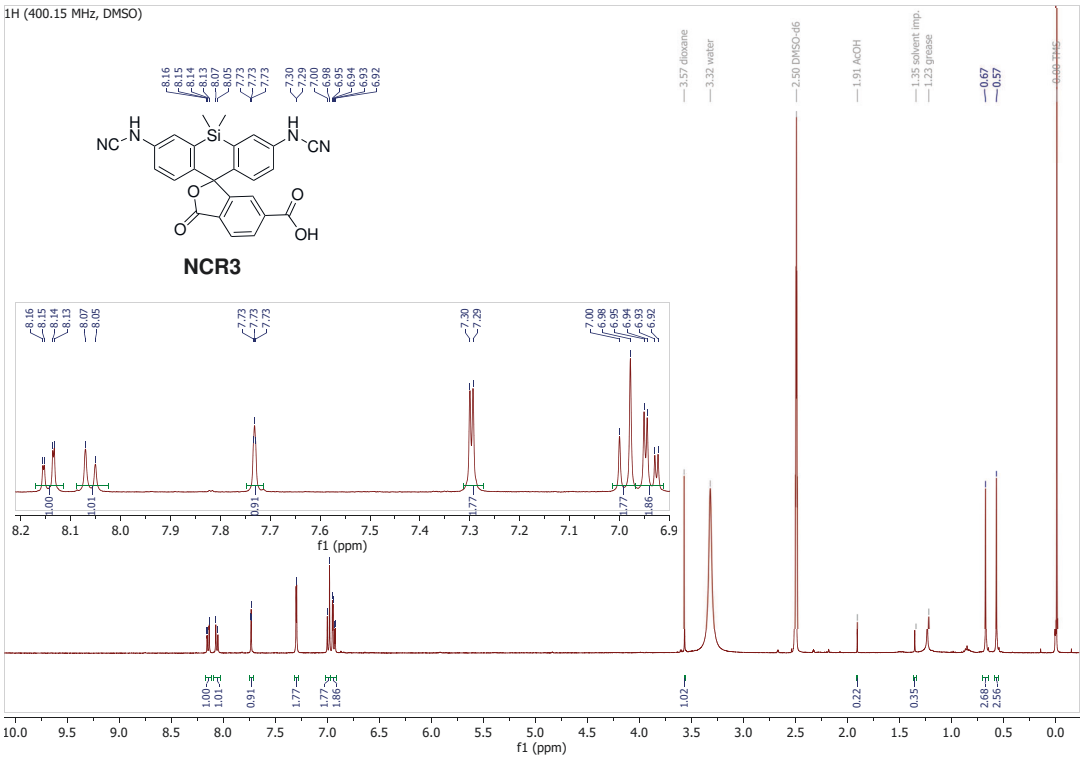

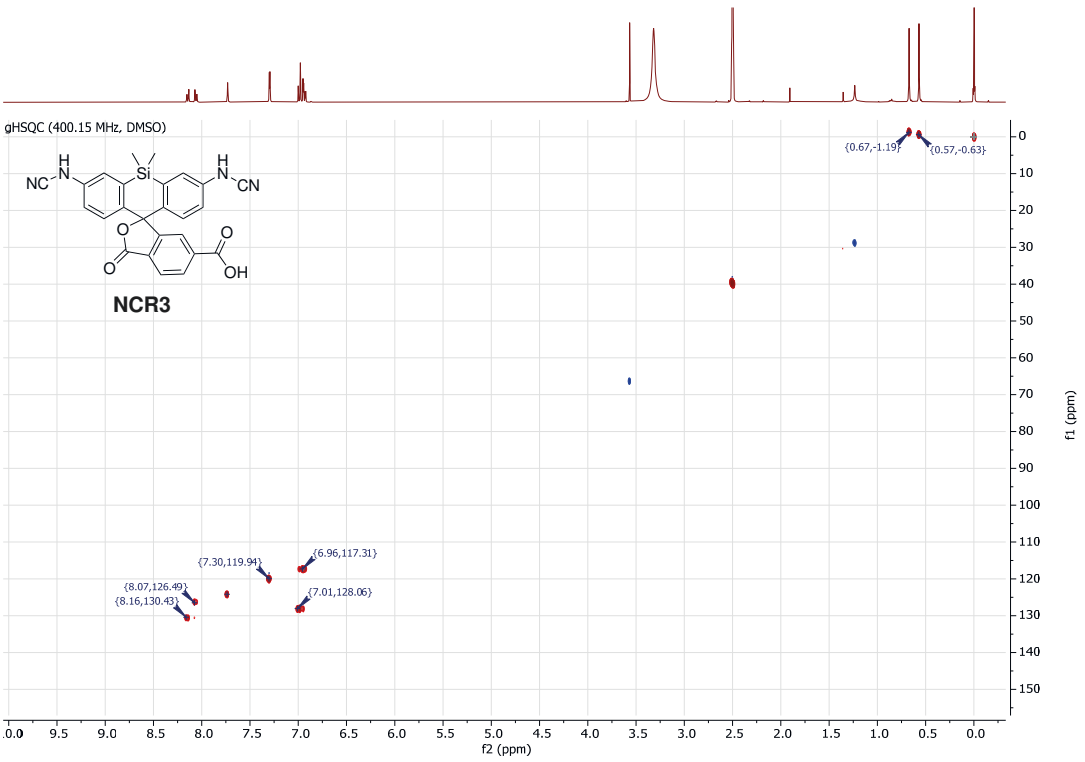

Compound NCR1-Halo

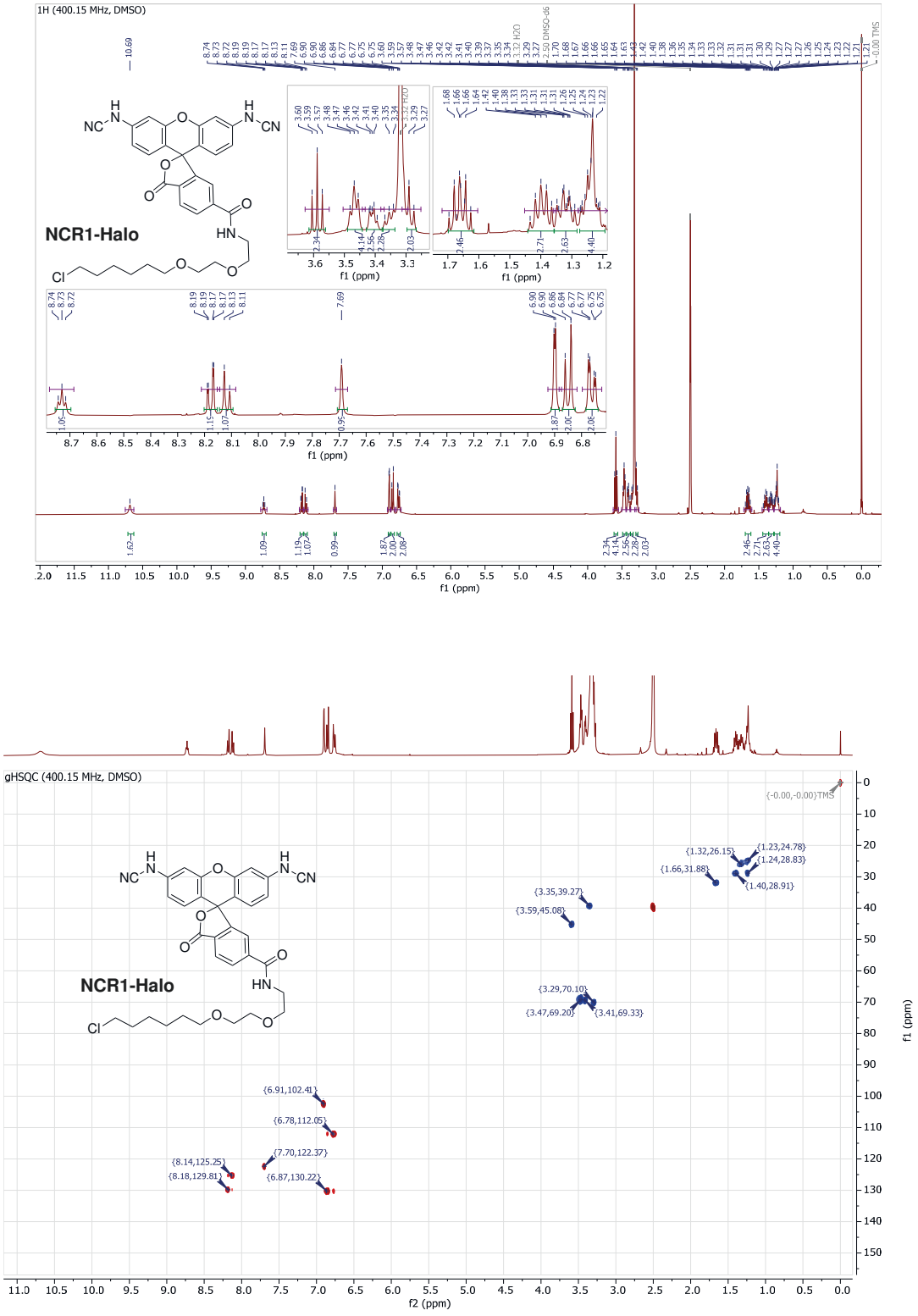

Compound NCR1-SNAP

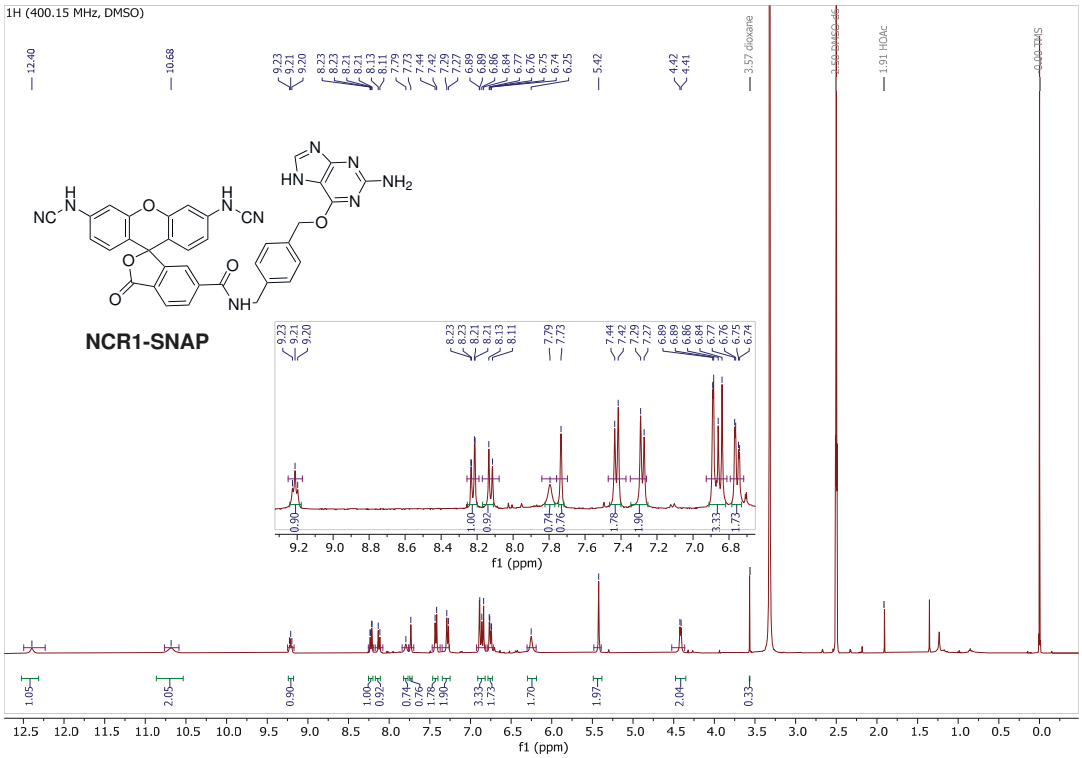

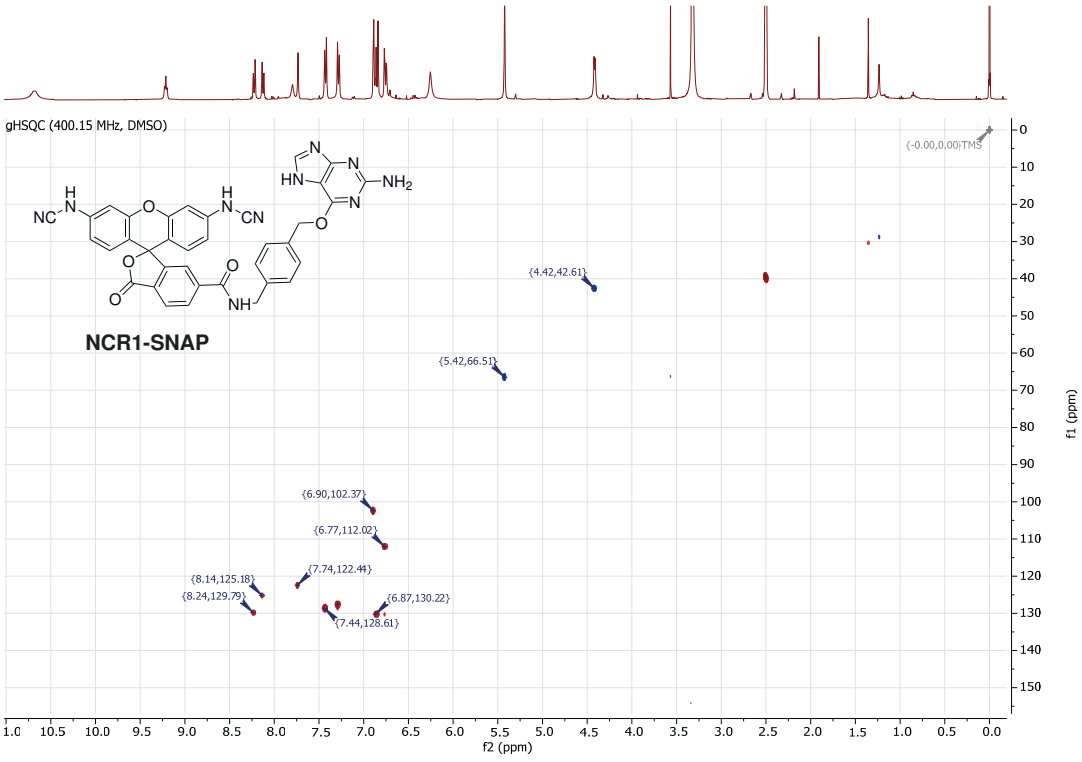

Compound 27b

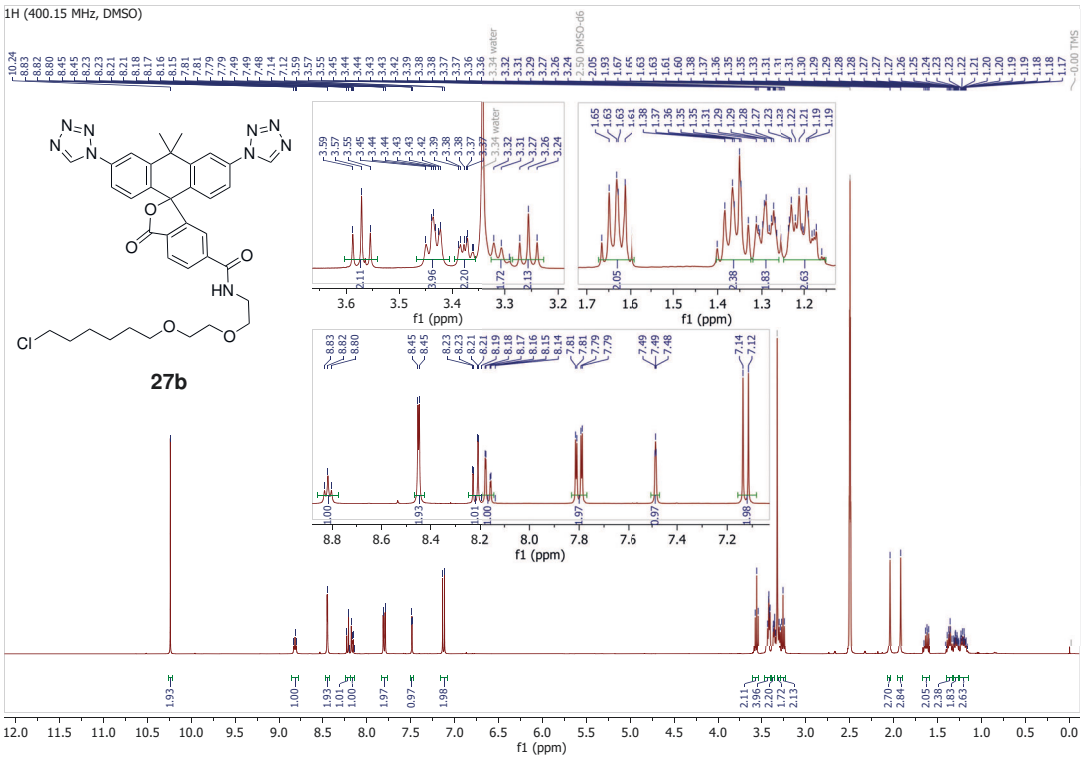

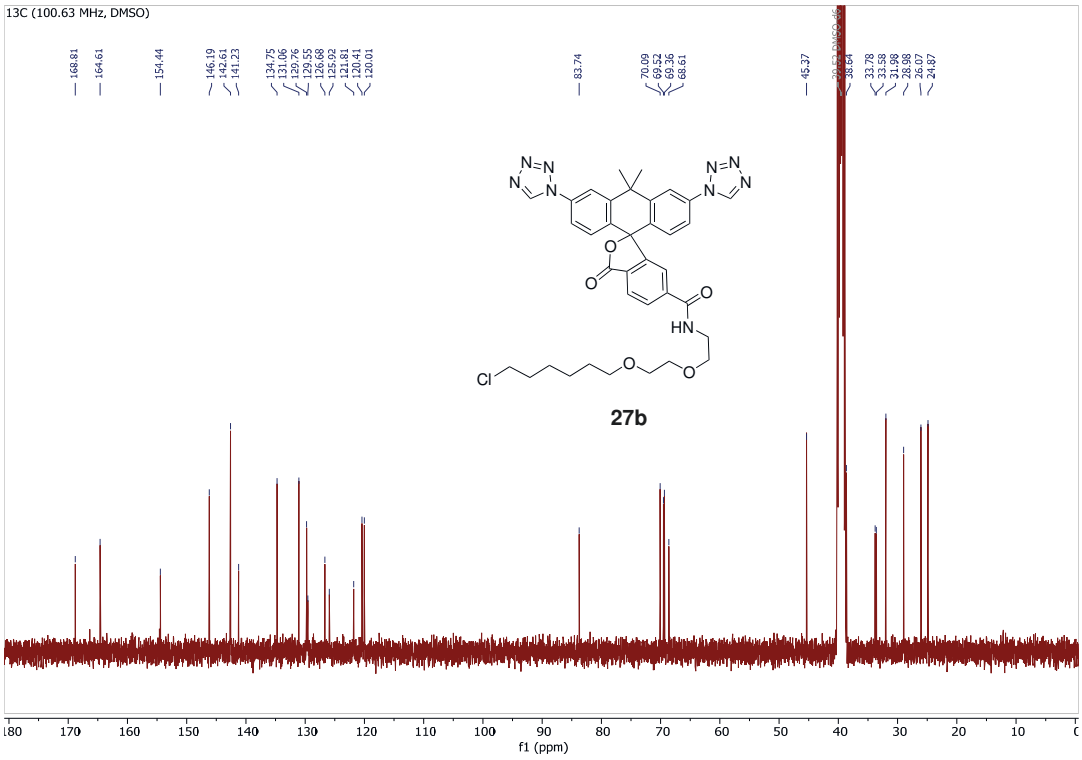

Compound 27c

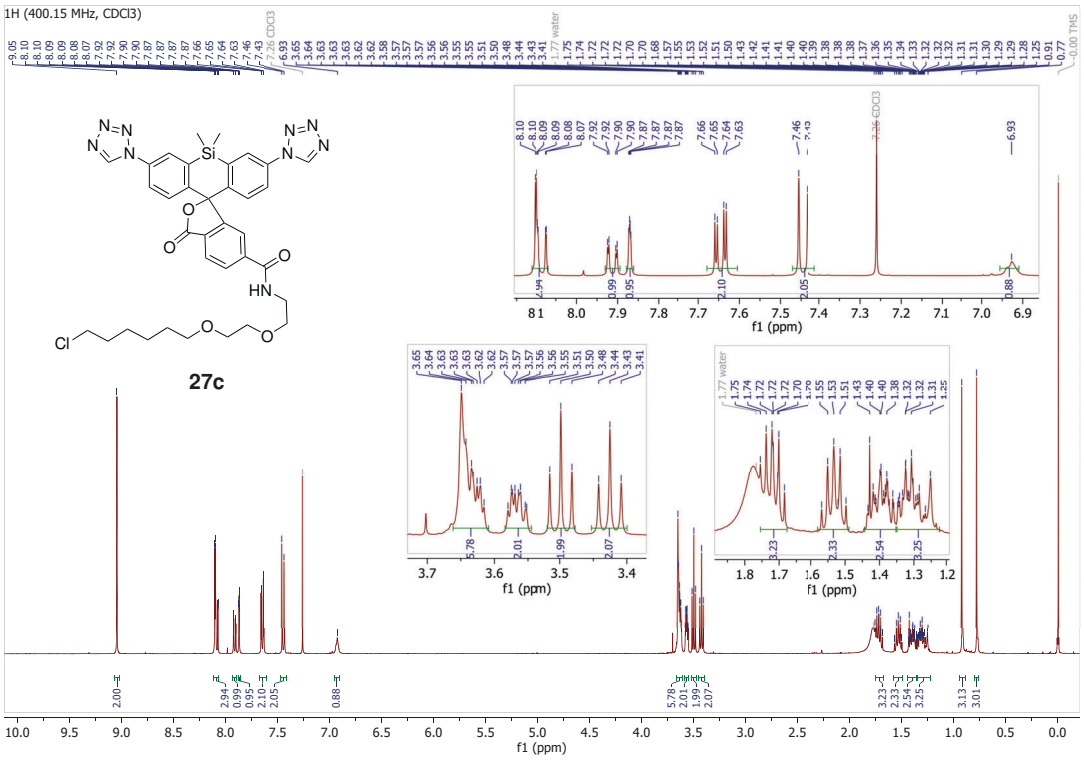

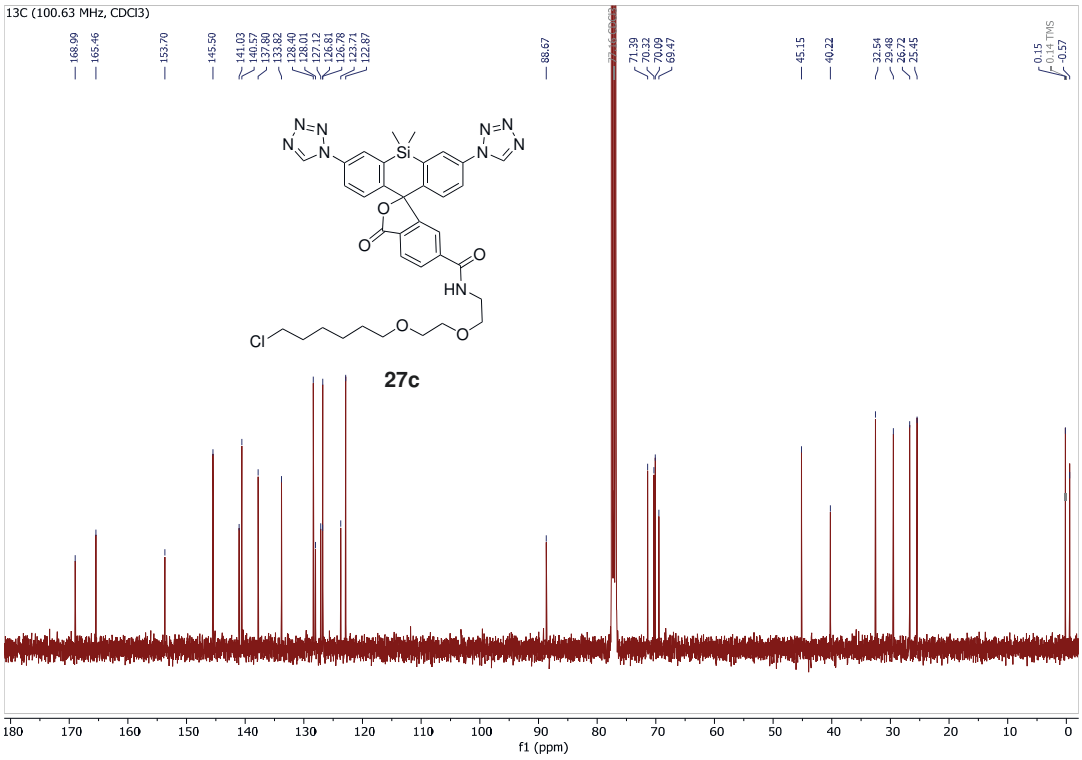

Compound NCR2-Halo

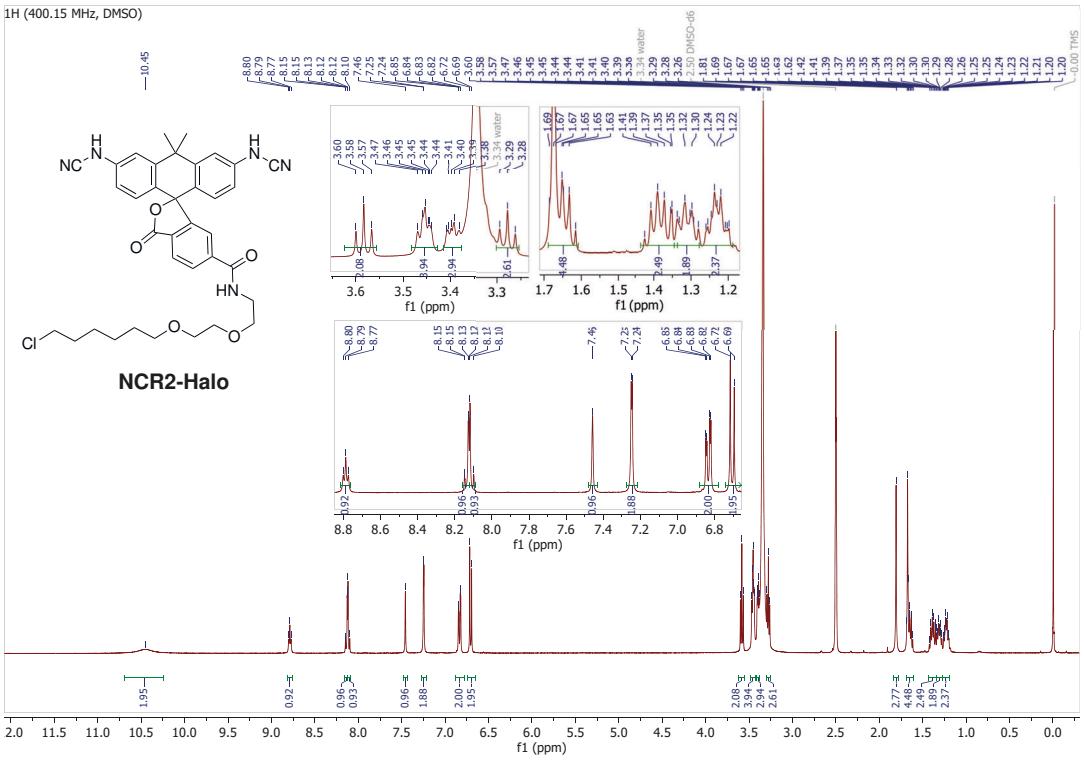

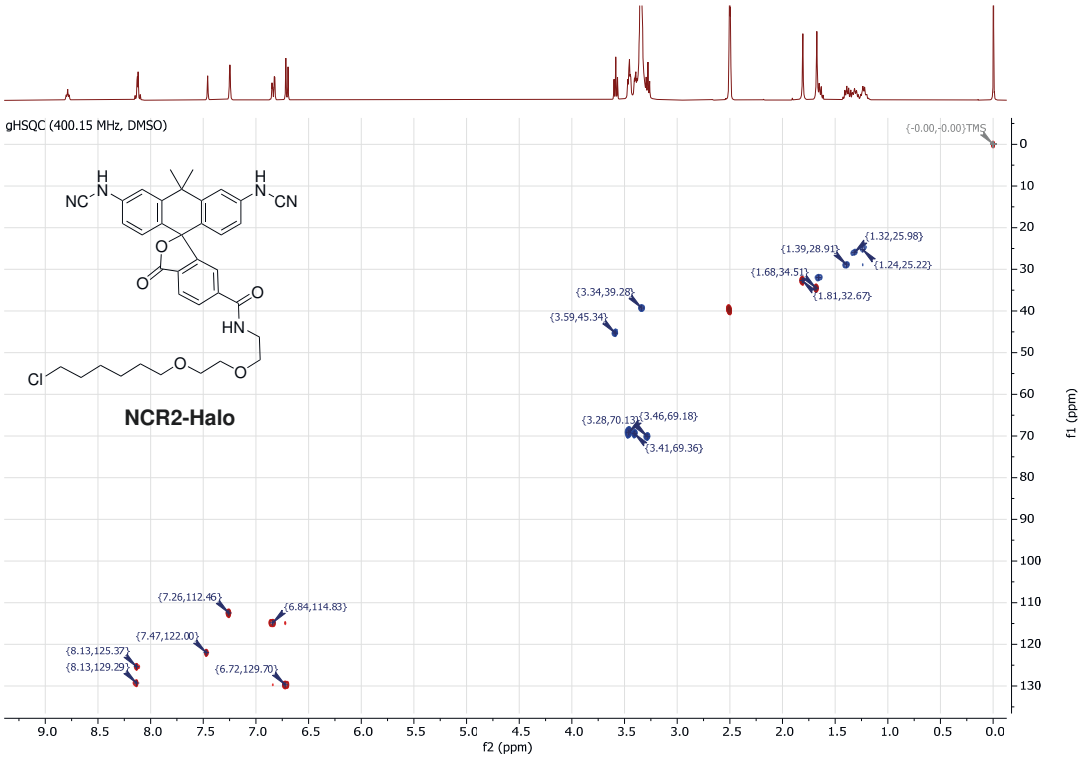

Compound NCR3-Halo

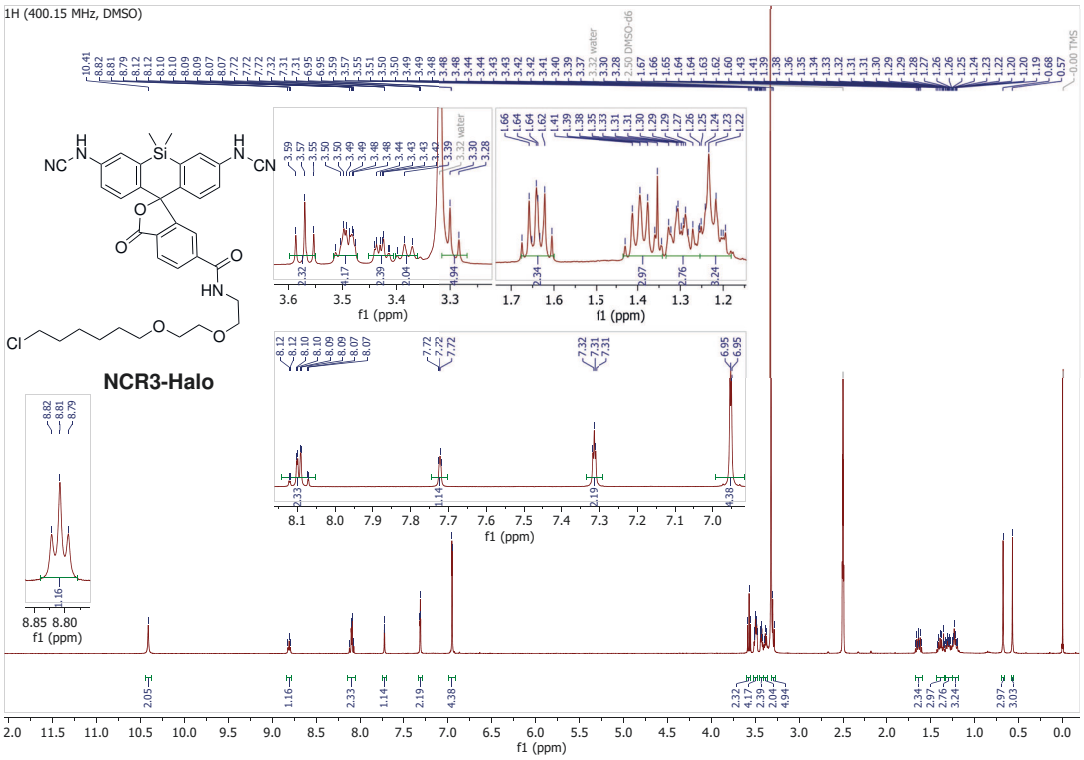

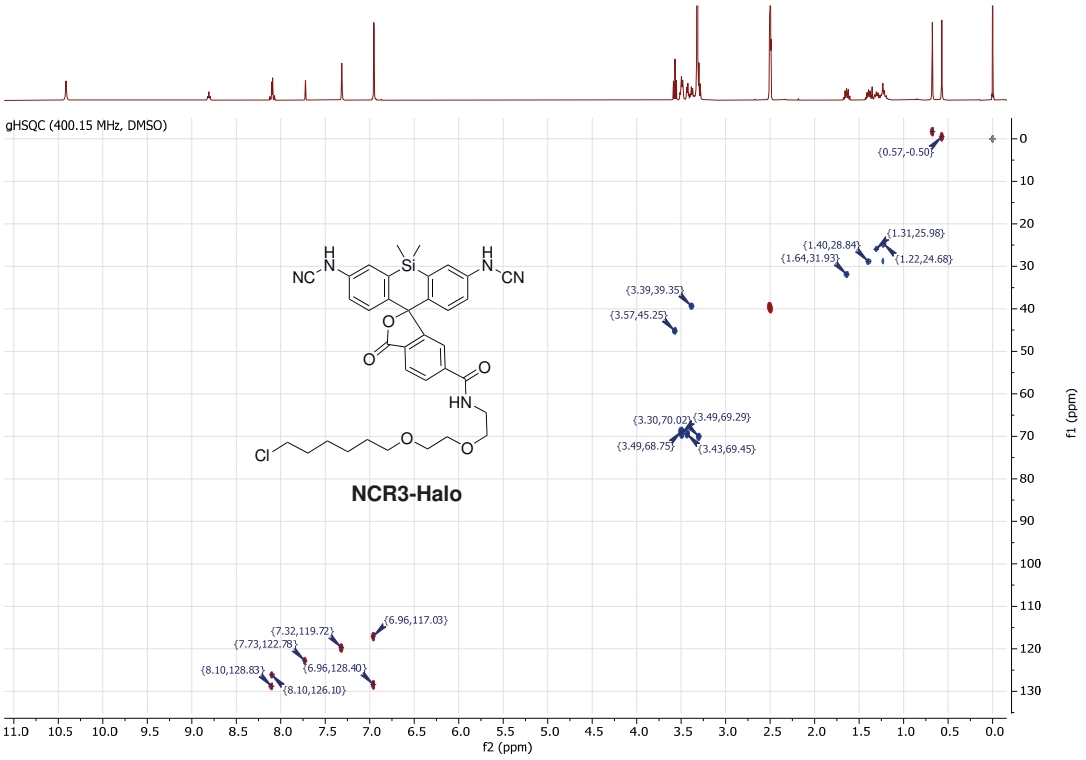

Compound 31

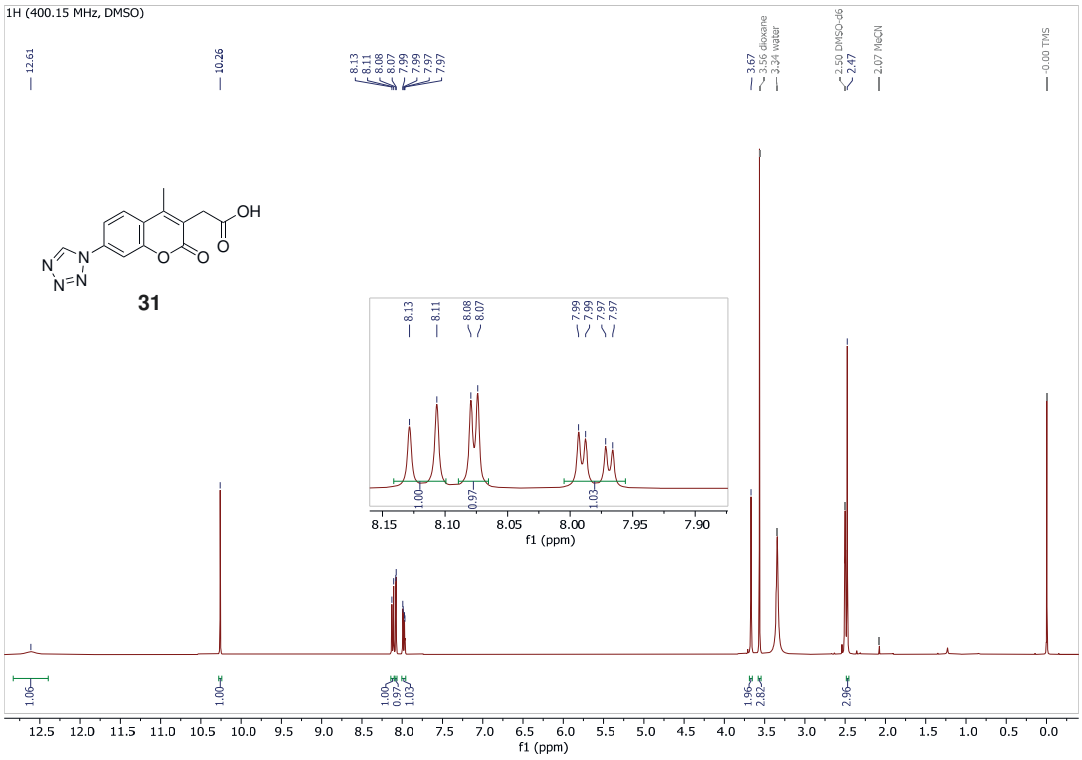
1H (400.15 MHz, DMSO)
12.61
10.26
8.13
8.11
8.08
8.07
7.99
7.99
7.97
7.97
3.67
3.56 dioxane
3.34 water
2.50 DMSO-d6
2.47
2.07 MeCN
0.00 TMS
OH
O
O
N
N
N
31
f1 (ppm)

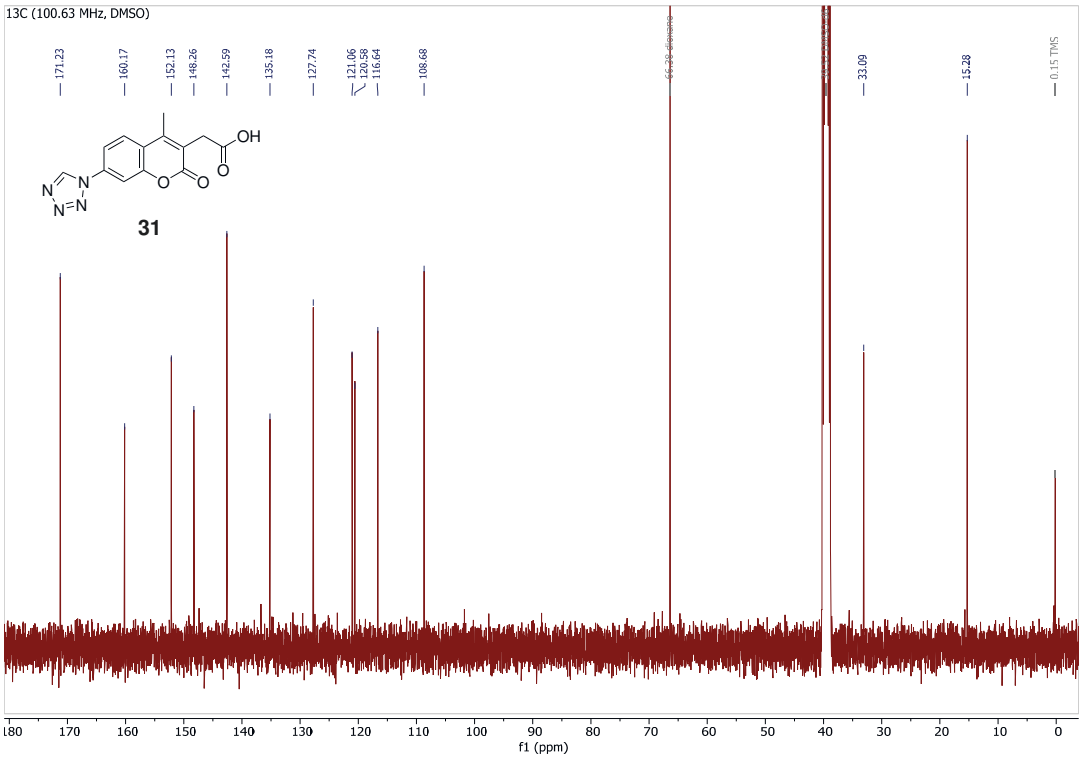
13C (100.63 MHz, DMSO)
171.23
160.17
152.13
148.26
142.59
135.18
127.74
121.06
120.58
116.64
108.68
66.28 dioxane
39.50 DMSO-d6
33.09
15.28
0.15 TMS
OH
O
O
N
N
N
31
f1 (ppm)

Compound 29

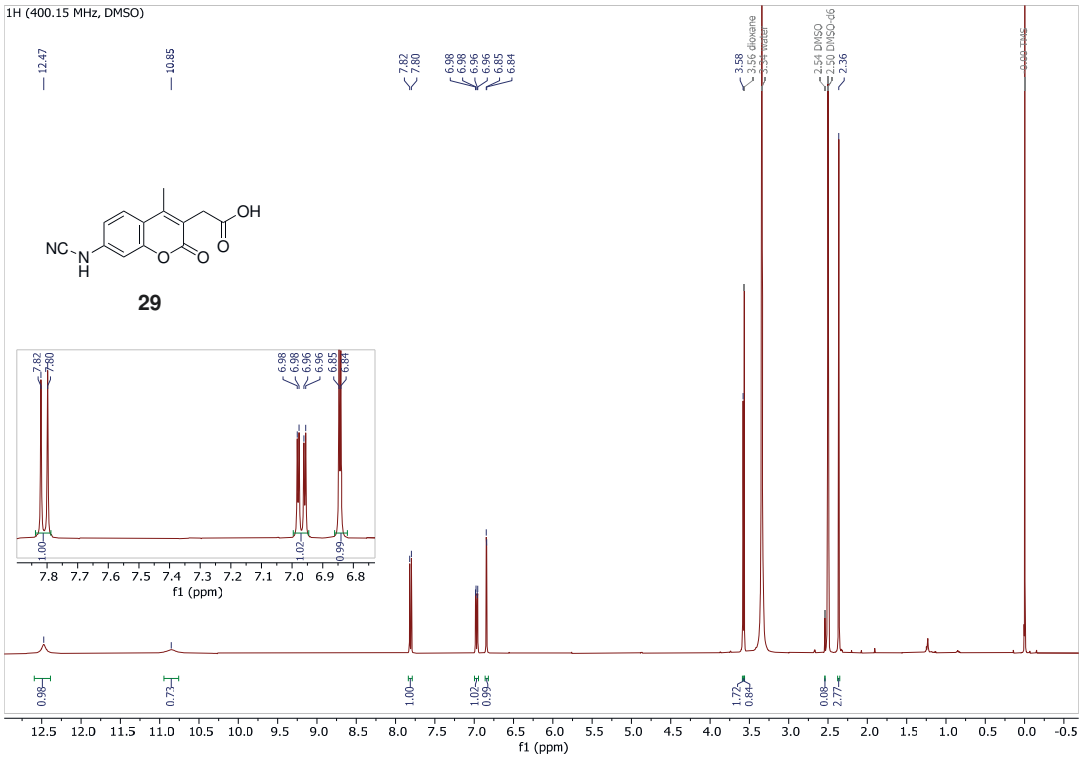
1H (400.15 MHz, DMSO)
12.47
10.85
7.82
7.80
6.98
6.98
6.96
6.96
6.85
6.84
3.58
3.56 dioxane
3.34 water
2.54 DMSO
2.50 DMSO-d6
2.36
0.00 TMS
OH
NC
N
H
O
O
O
29
f1 (ppm)

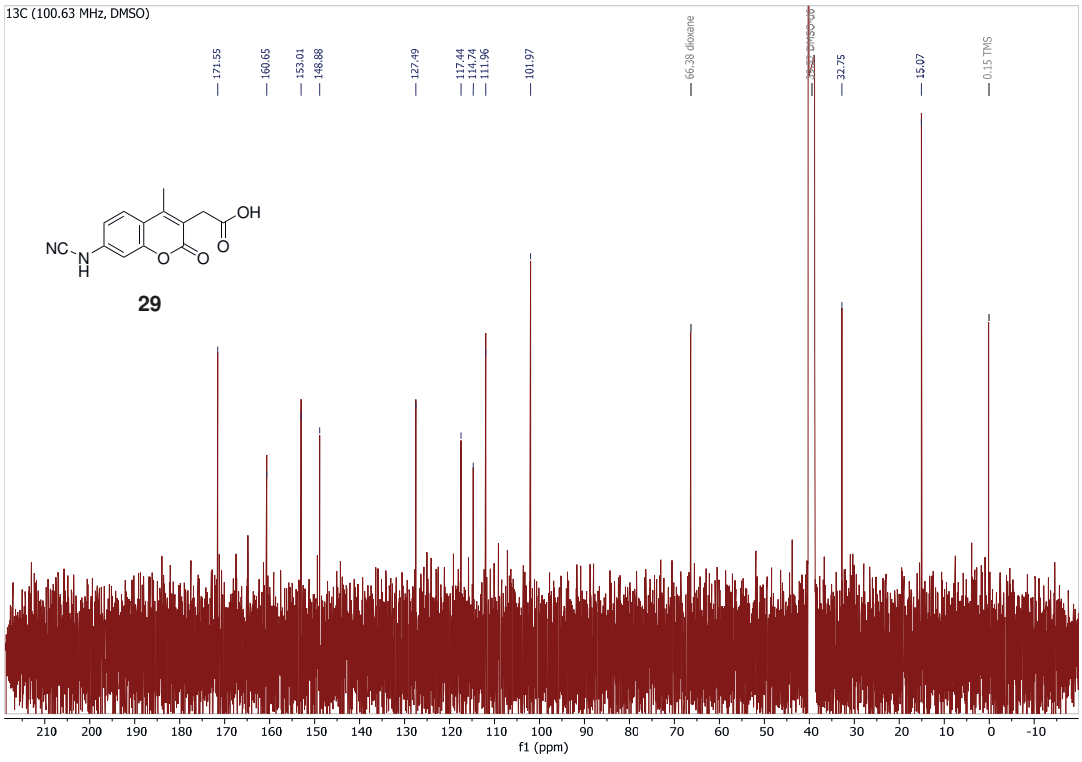
13C (100.63 MHz, DMSO)
171.55
160.65
153.01
148.88
127.49
117.44
114.74
111.96
101.97
66.38 dioxane
32.75
15.07
0.15 TMS
OH
NC
N
H
O
O
O
29
f1 (ppm)

9.3.2 Chapter 5.2

Compound 32a

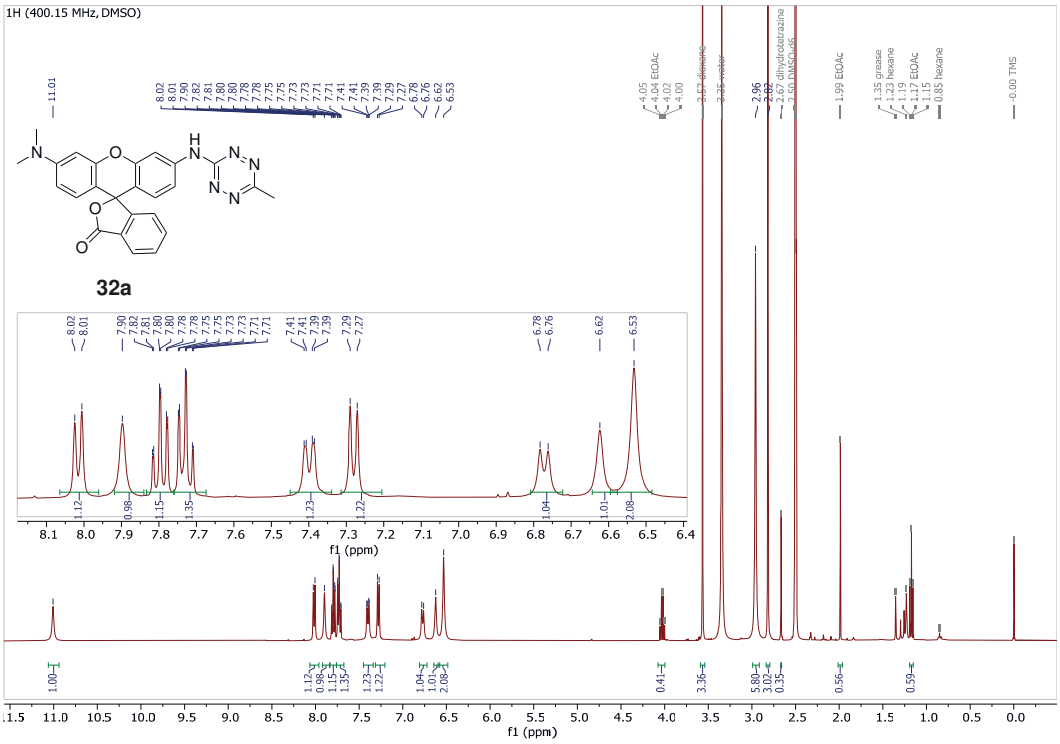

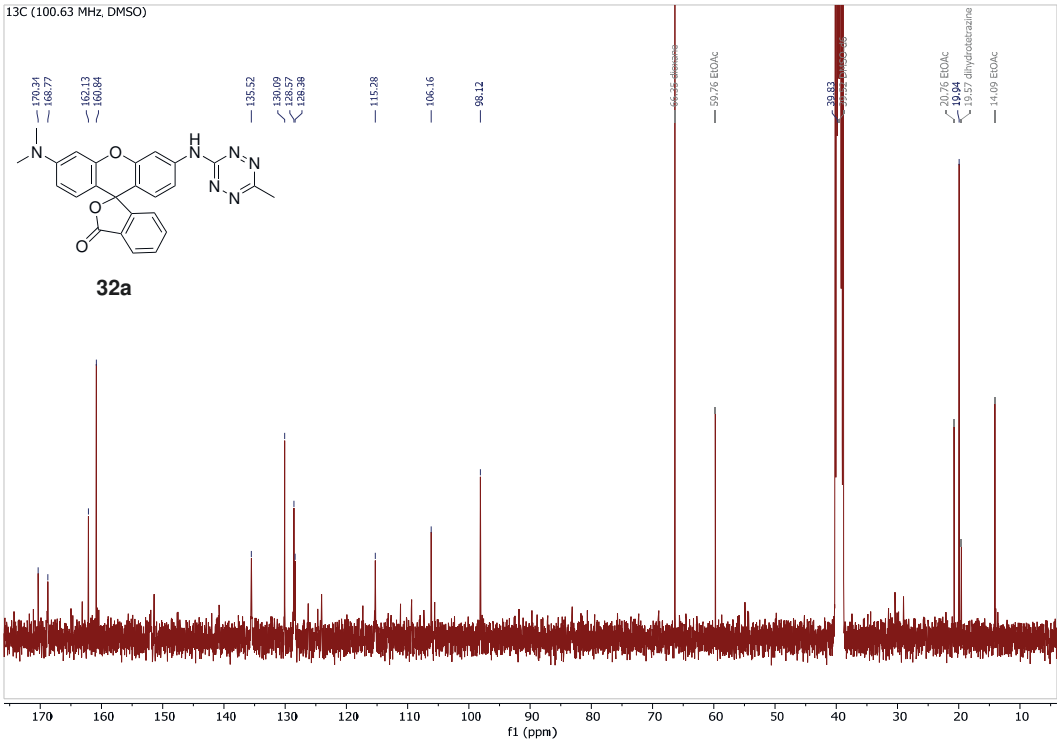

Compound 32b

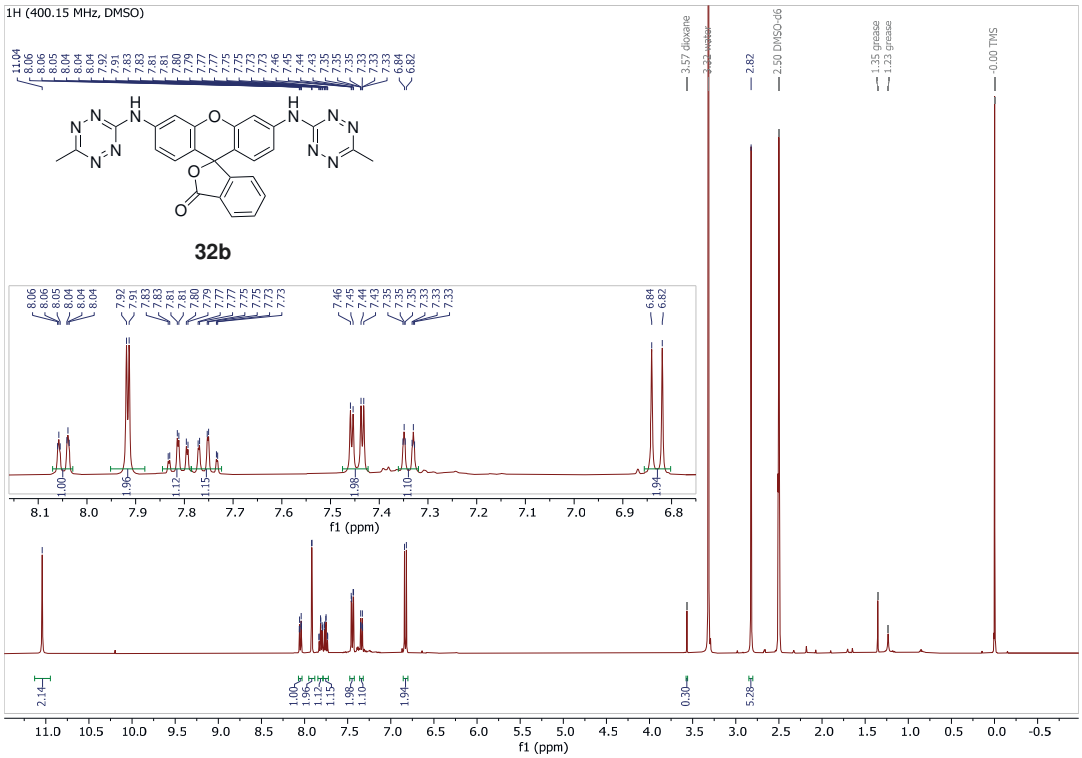

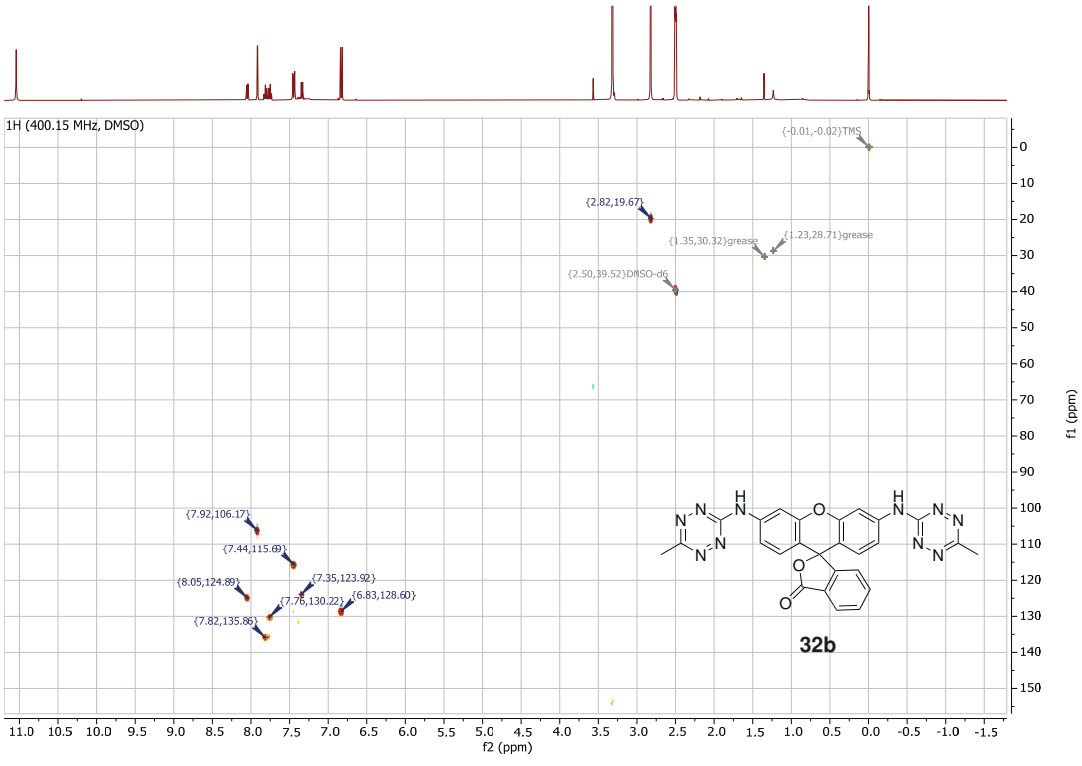

9.3.3 Chapter 5.3

Compound 39

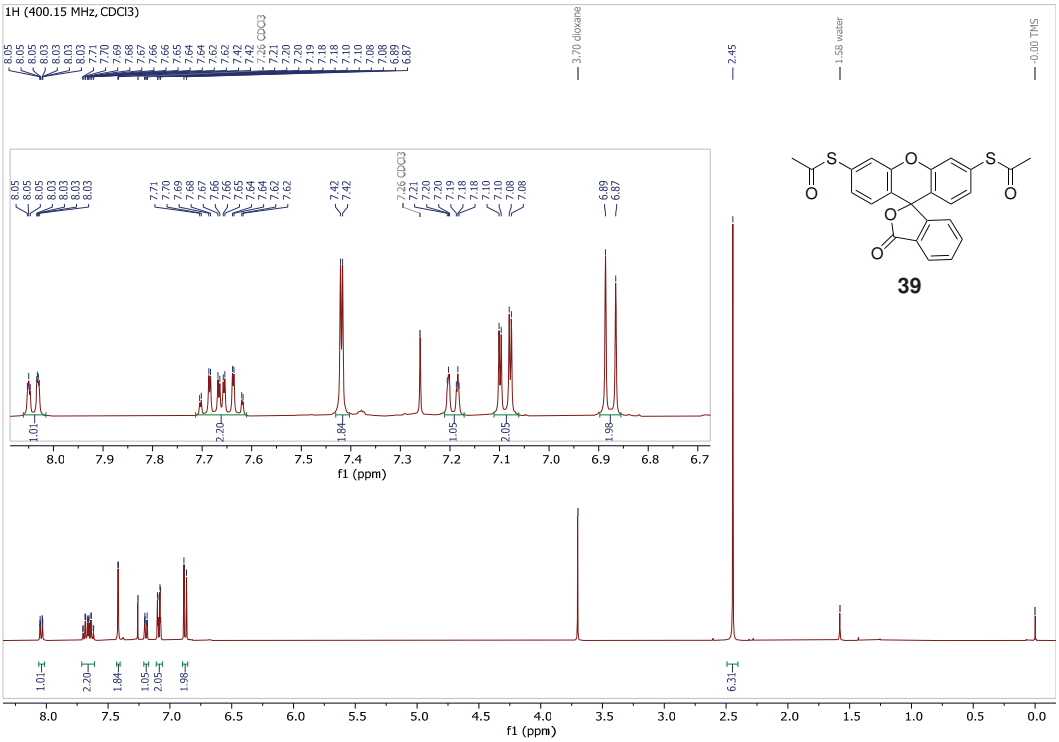

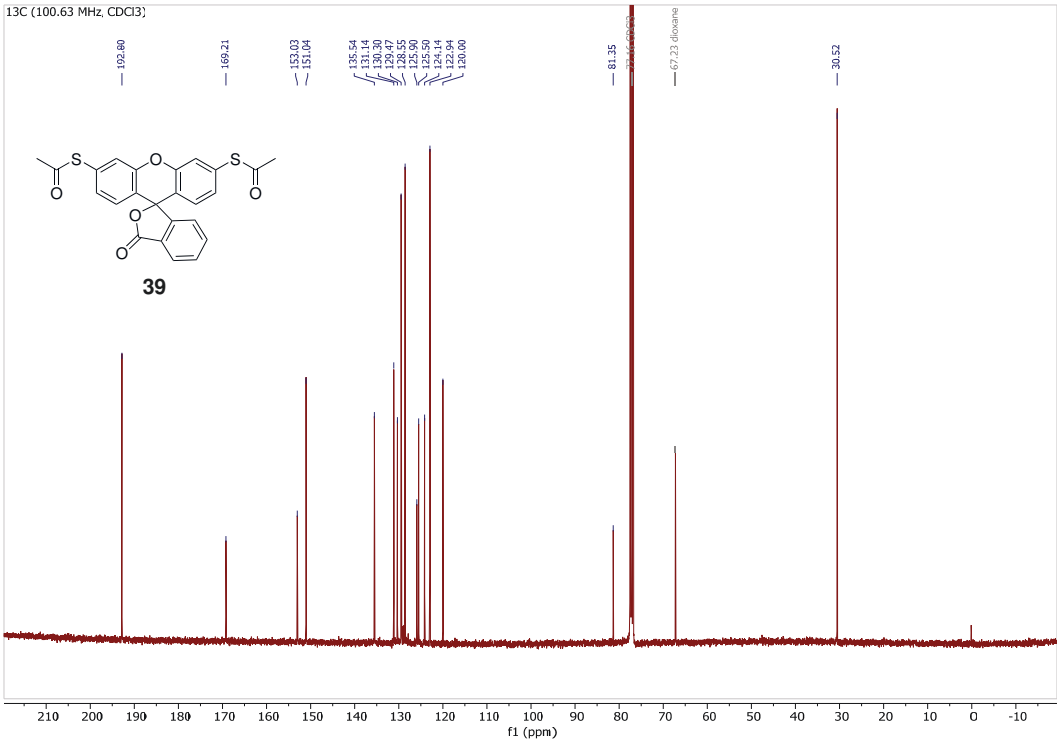

Compound 35

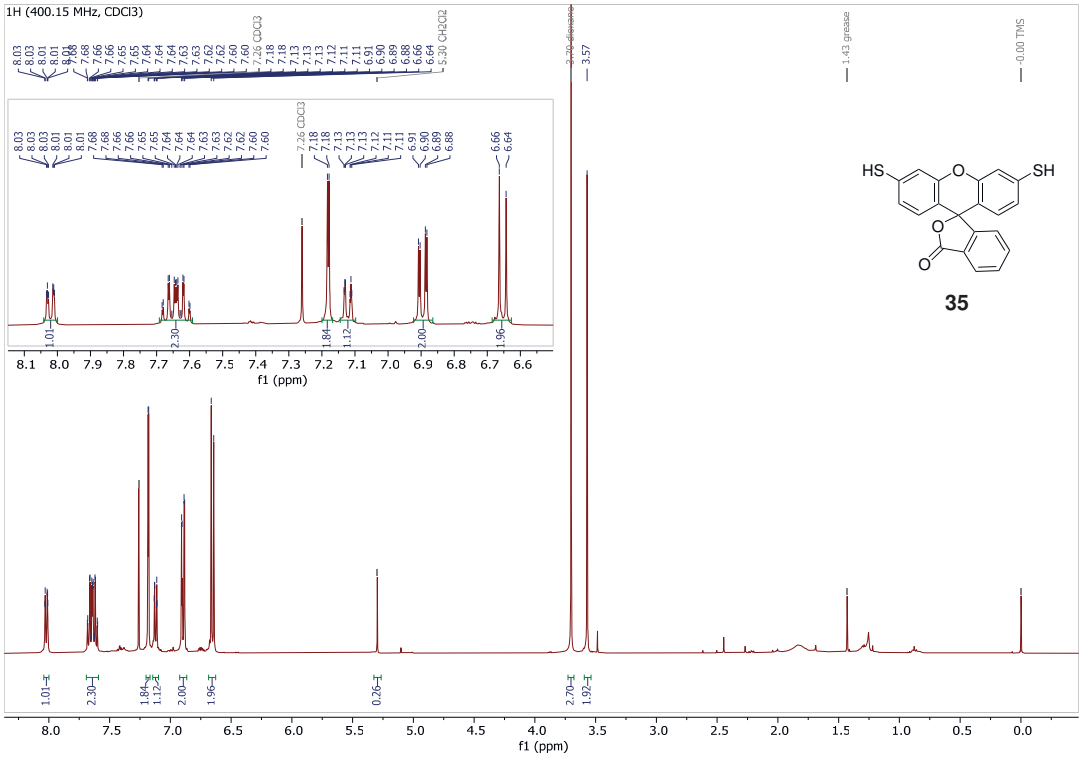
1H (400.15 MHz, CDCl3)
HS
SH
O
O
O
35
f1 (ppm)

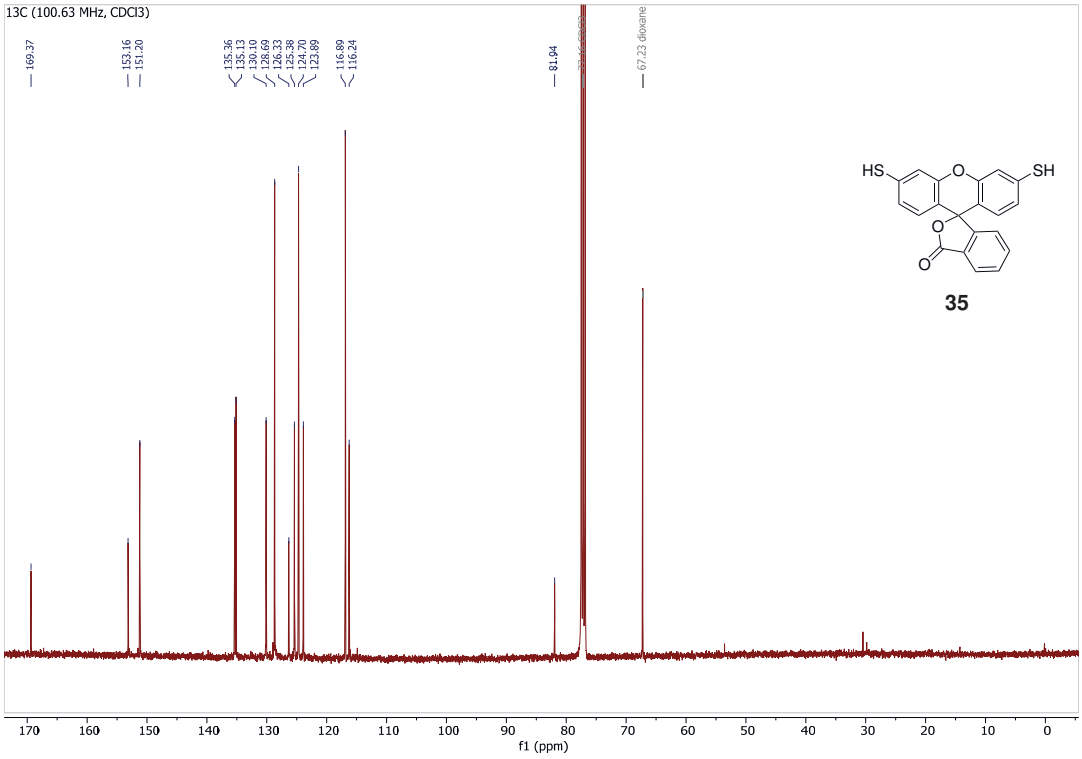
13C (100.63 MHz, CDCl3)
HS
SH
O
O
O
35
f1 (ppm)

Compound 40

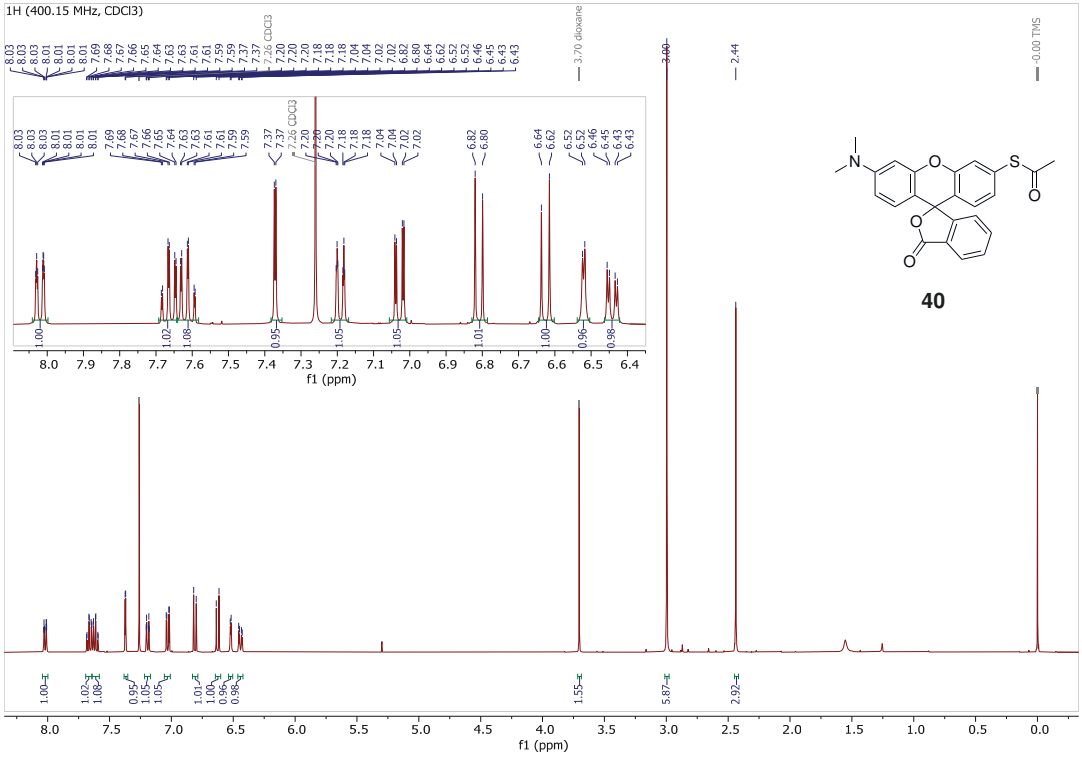

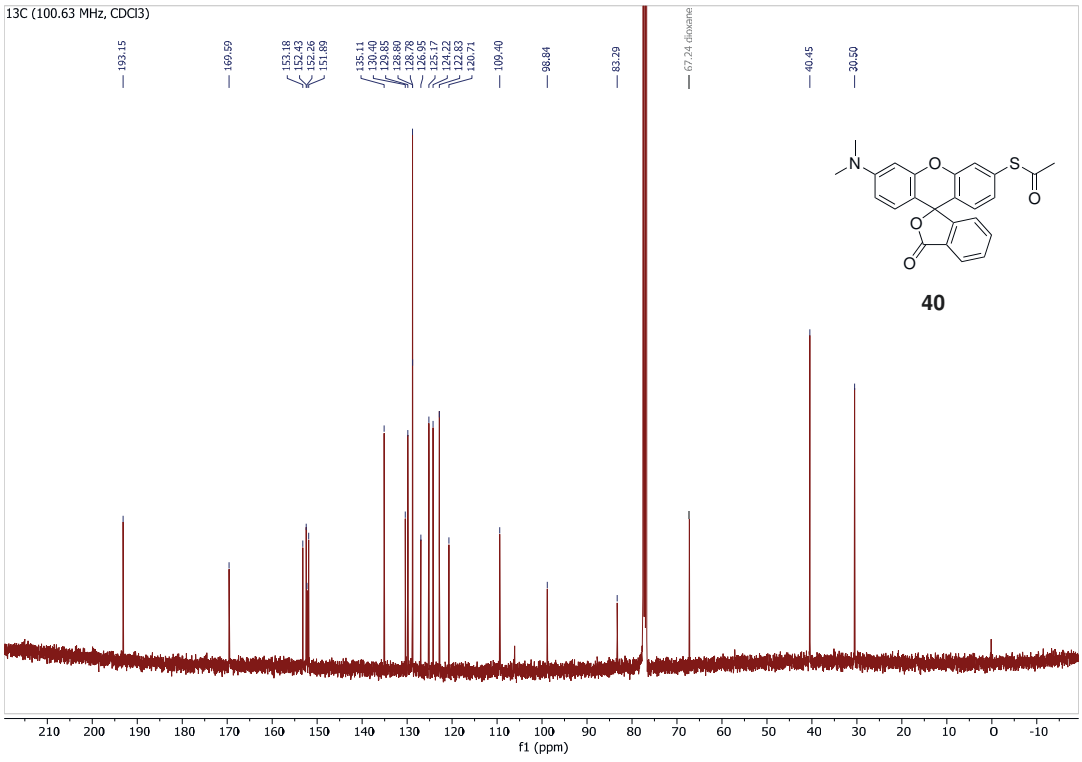

Compound 45

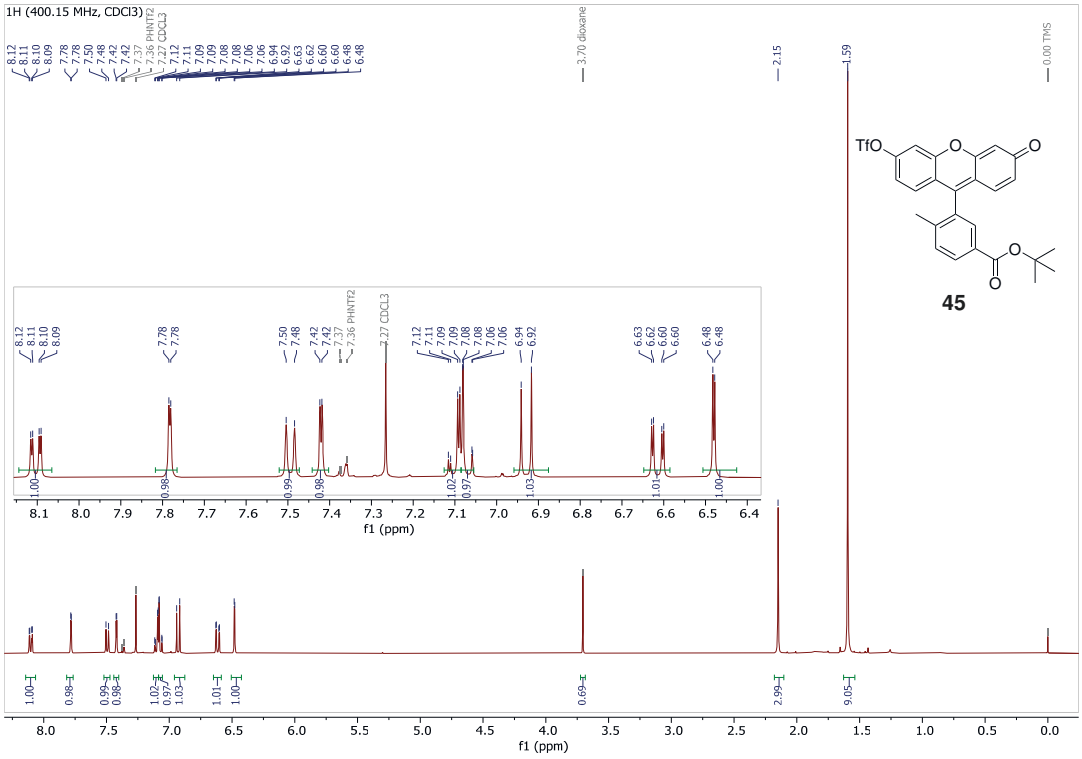
1H (400.15 MHz, CDCl3)
3.70 dioxane
2.15
1.59
0.00 TMS
TfO
O
O
O
O
45
f1 (ppm)

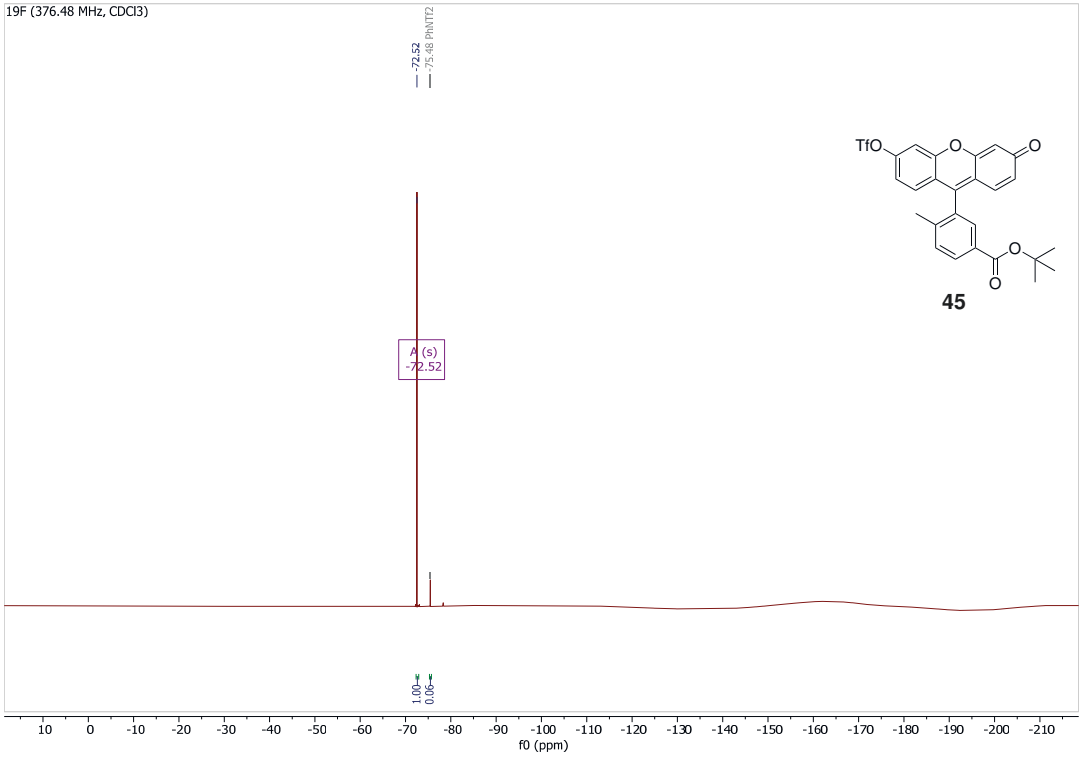
19F (376.48 MHz, CDCl3)
-72.52
-75.48 PhNTf2
TfO
O
O
O
O
45
A (s)
-72.52
f0 (ppm)

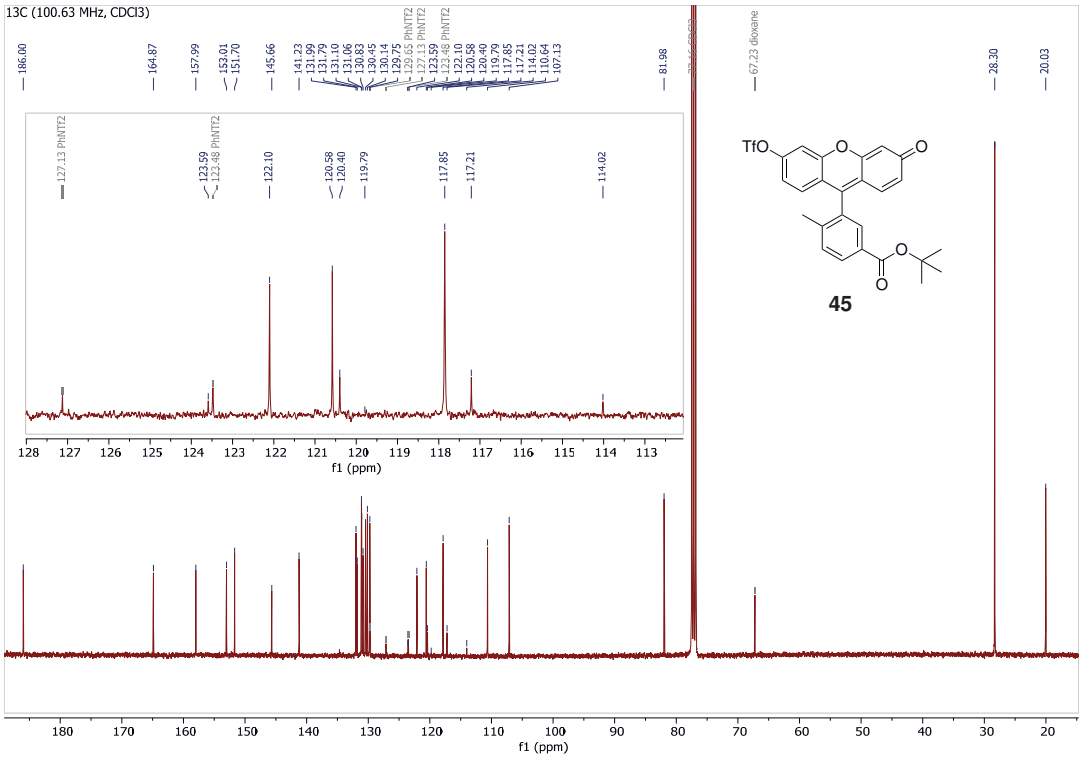
13C (100.63 MHz, CDCl3)
186.00
164.87
157.99
153.01
151.70
145.66
141.23
131.99
131.79
131.10
131.06
130.83
130.45
130.14
129.75
129.65 PhNTT2
129.23 PhNTT2
123.59 PhNTT2
122.48 PhNTT2
122.10
120.58
120.40
119.79
117.85
117.21
114.02
110.64
107.13
81.98
67.23 dioxane
28.30
20.03
127.13 PhNTT2
123.59
123.48 PhNTT2
122.10
120.58
120.40
119.79
117.85
117.21
114.02
f1 (ppm)
TfO
O
O
O
O
O
45
f1 (ppm)

Compound 43

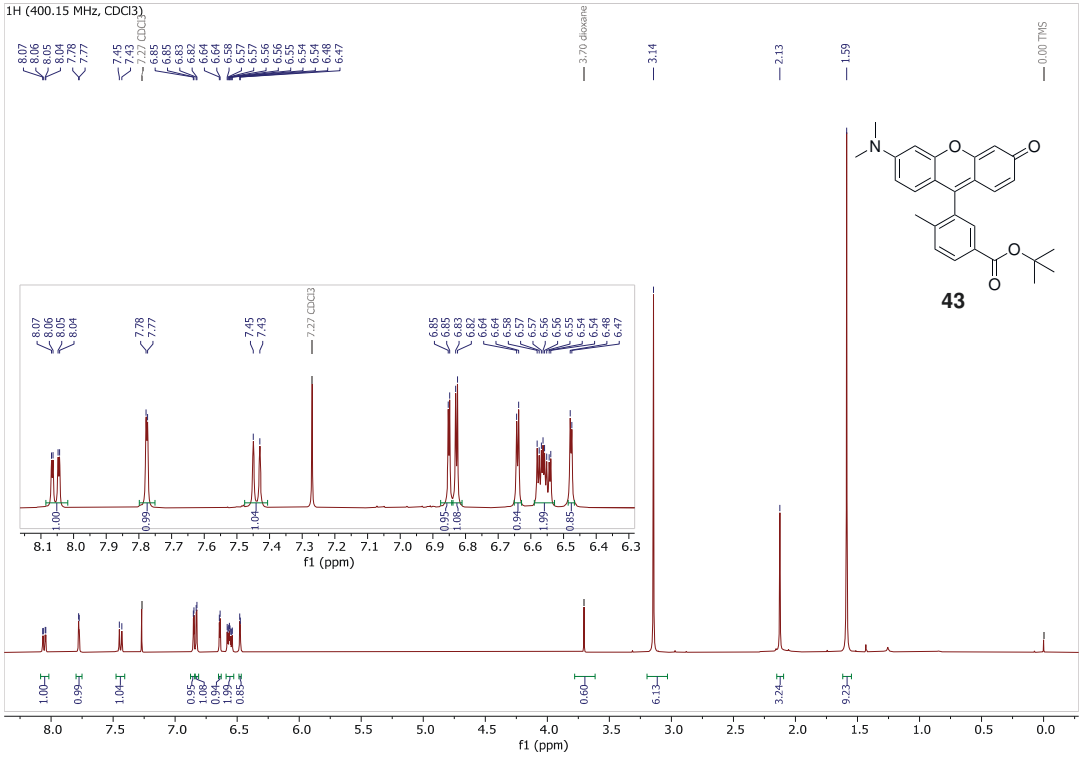
1H (400.15 MHz, CDCl3)
3.70 dioxane
3.14
2.13
1.59
0.00 TMS
7.27 CDCl3
43
f1 (ppm)

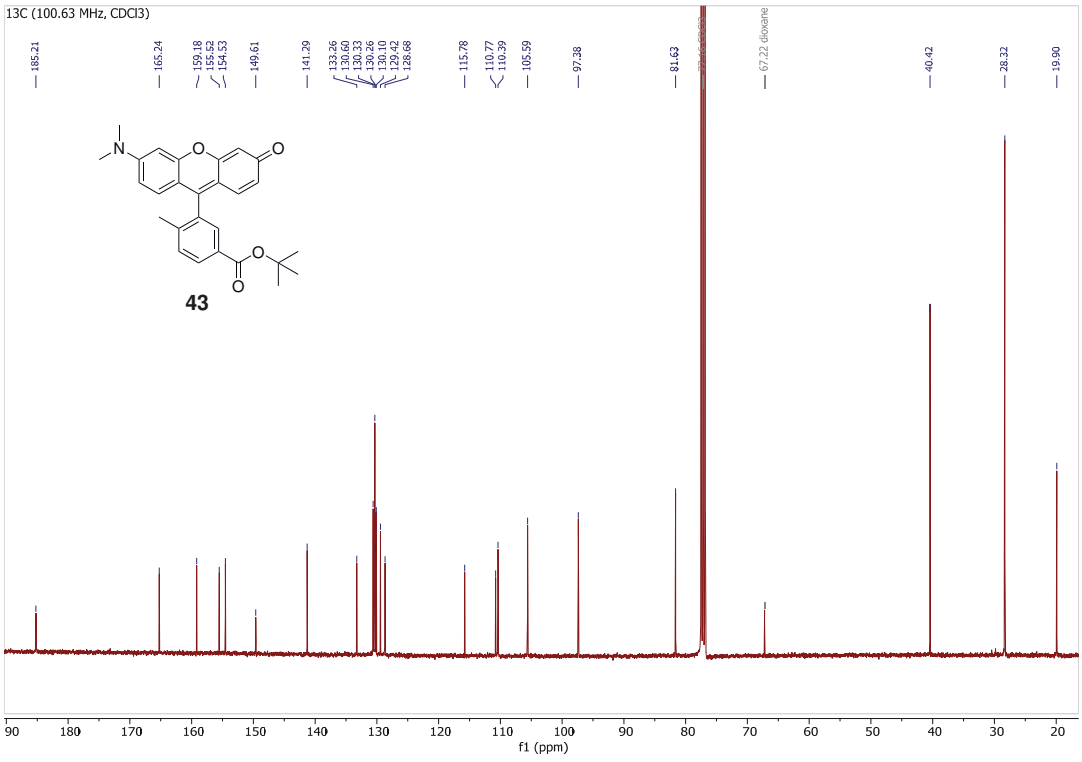
13C (100.63 MHz, CDCl3)
185.21
165.24
159.18
155.52
154.53
149.61
141.29
133.26
130.60
130.33
130.26
130.10
129.42
126.68
115.78
110.77
110.39
105.59
97.38
81.63
67.22 dioxane
40.42
28.32
19.90
43
f1 (ppm)

9.3.4 Chapter 5.4

Compound 46c

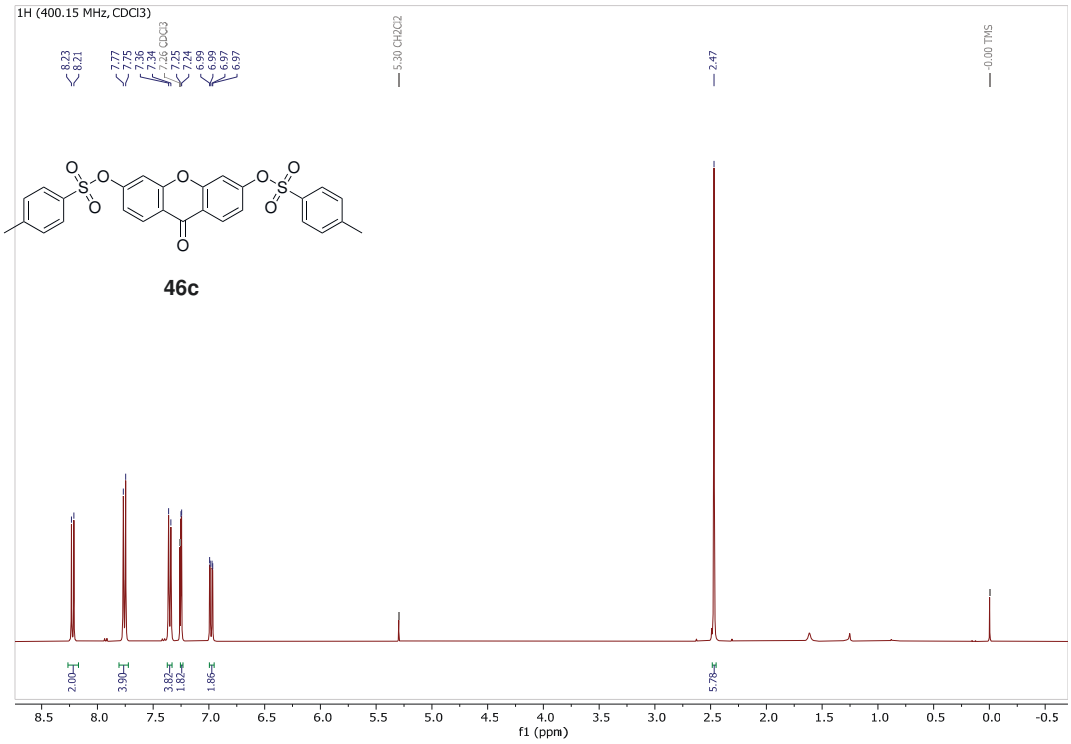

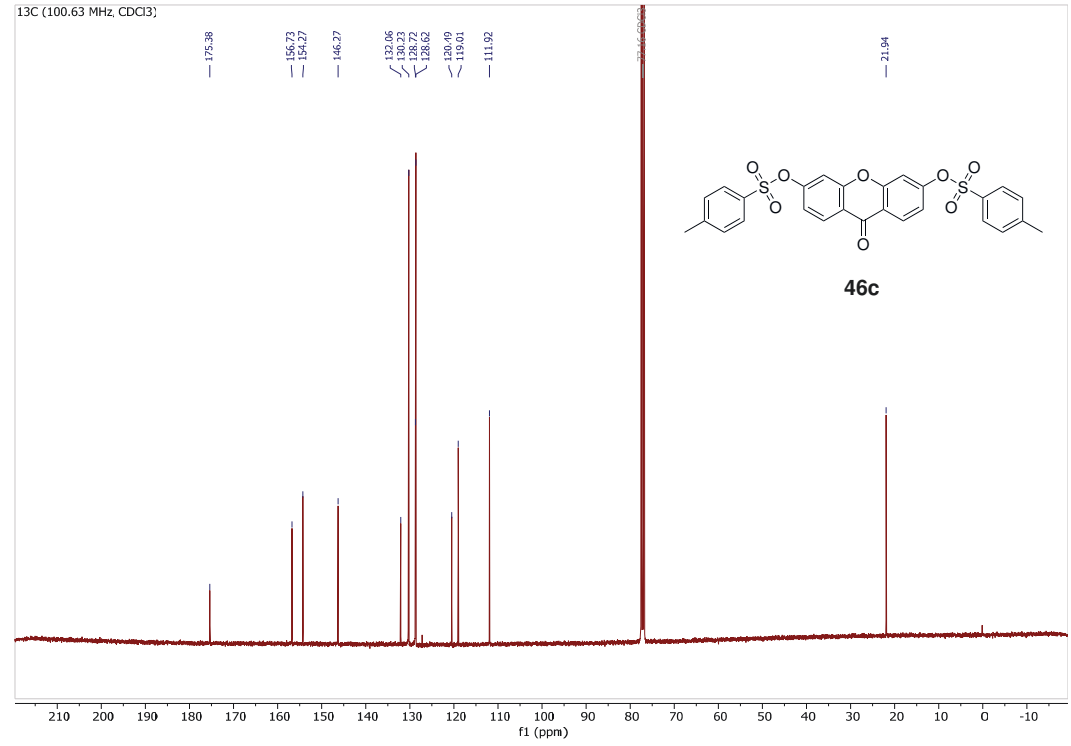

Compound 49

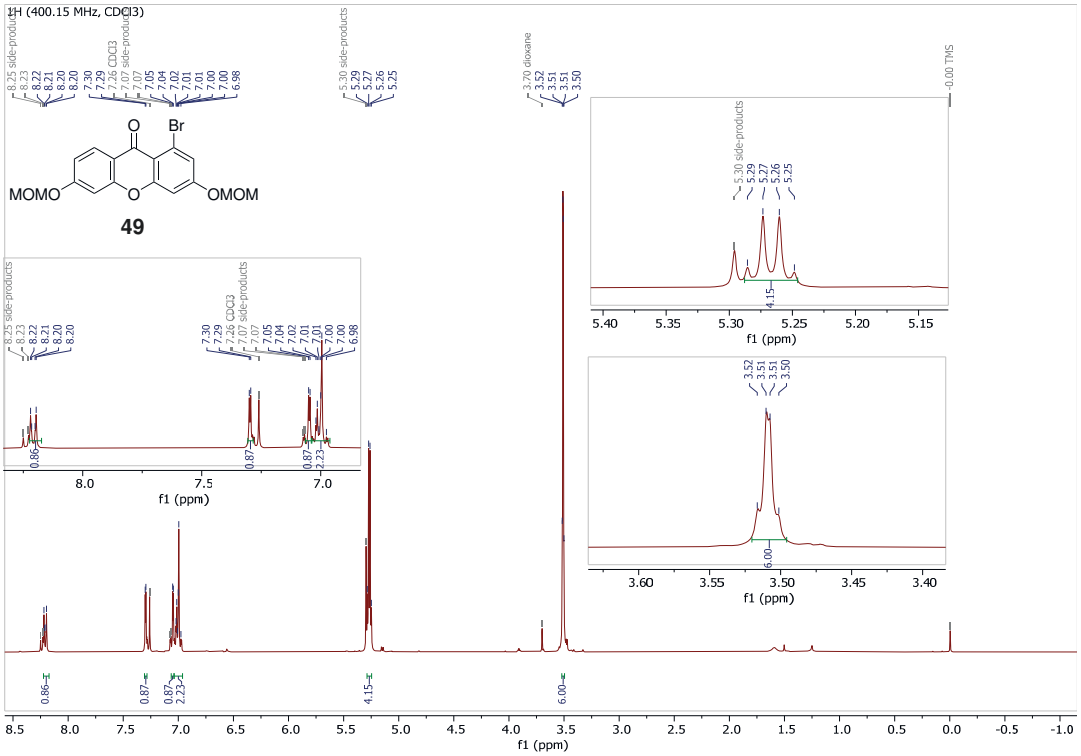
1H (400.15 MHz, CDCl3)
O
Br
MOMO
O
OMOM
49
f1 (ppm)

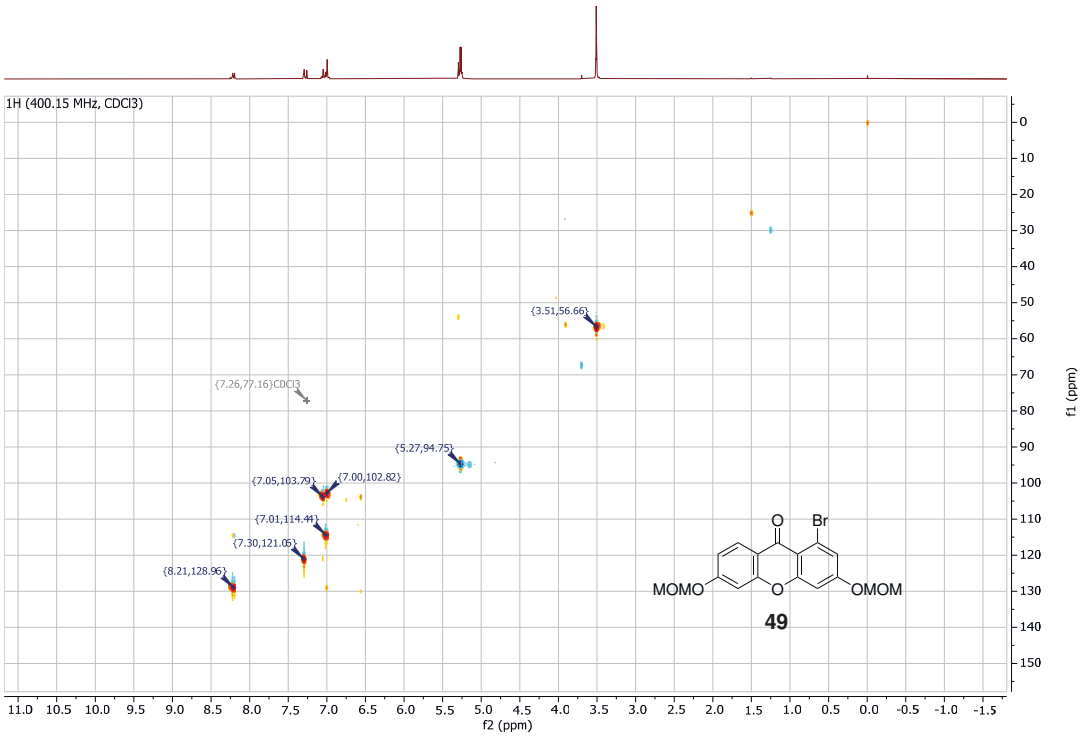
1H (400.15 MHz, CDCl3)
{3.51,56.66}
{7.26,77.16}CDCl3
{5.27,94.75}
{7.05,103.79}
{7.00,102.82}
{7.01,114.44}
{7.30,121.05}
{8.21,128.96}
O
Br
MOMO
O
OMOM
49
f2 (ppm)
f1 (ppm)

Compound 50

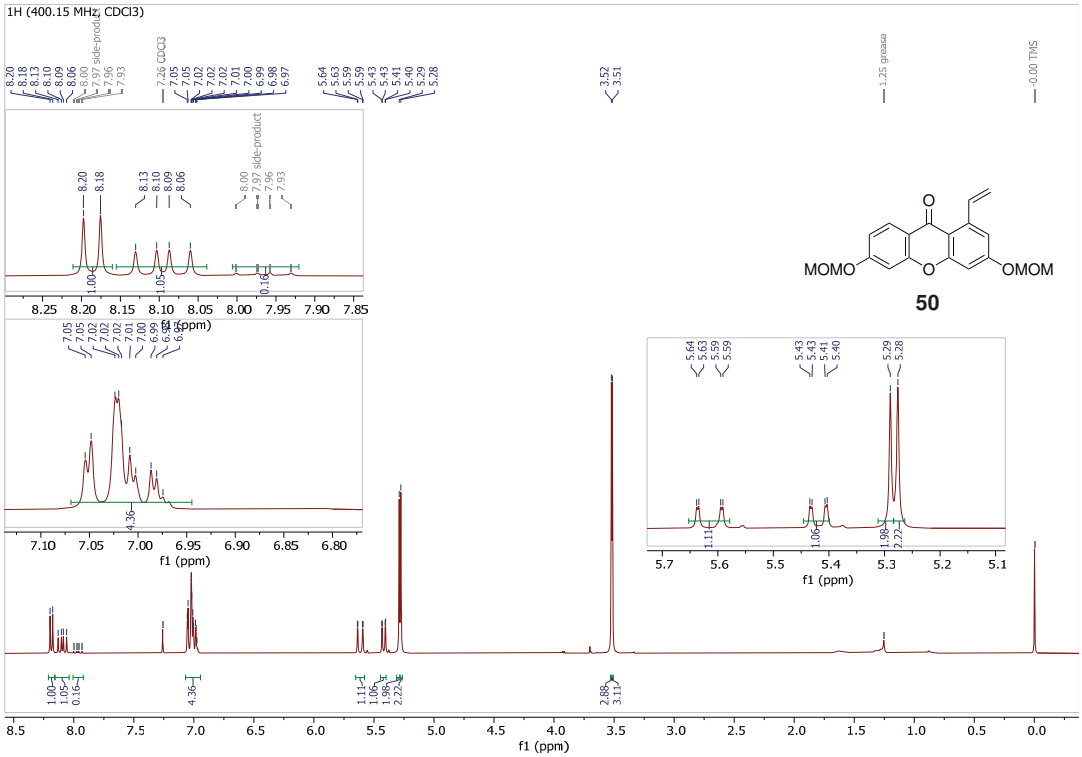
1H (400.15 MHz, CDCl3)
MOMO
OMOM
50
f1 (ppm)

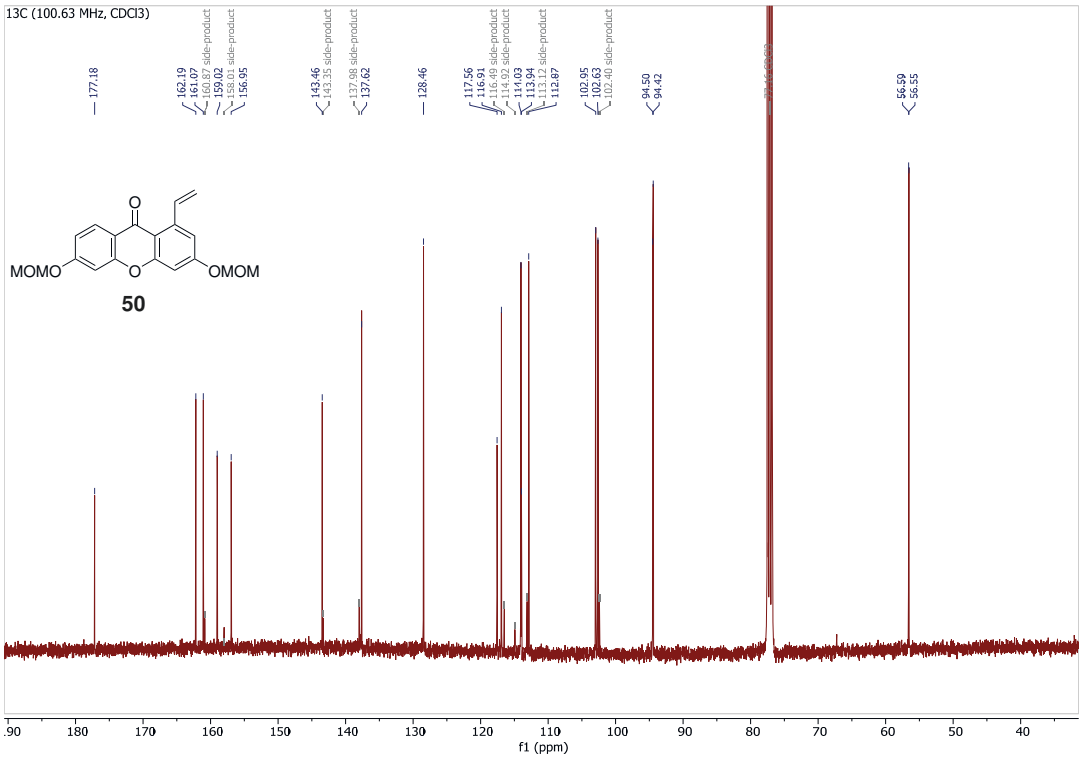
13C (100.63 MHz, CDCl3)
MOMO
OMOM
50
f1 (ppm)

Compound PaX(–)1

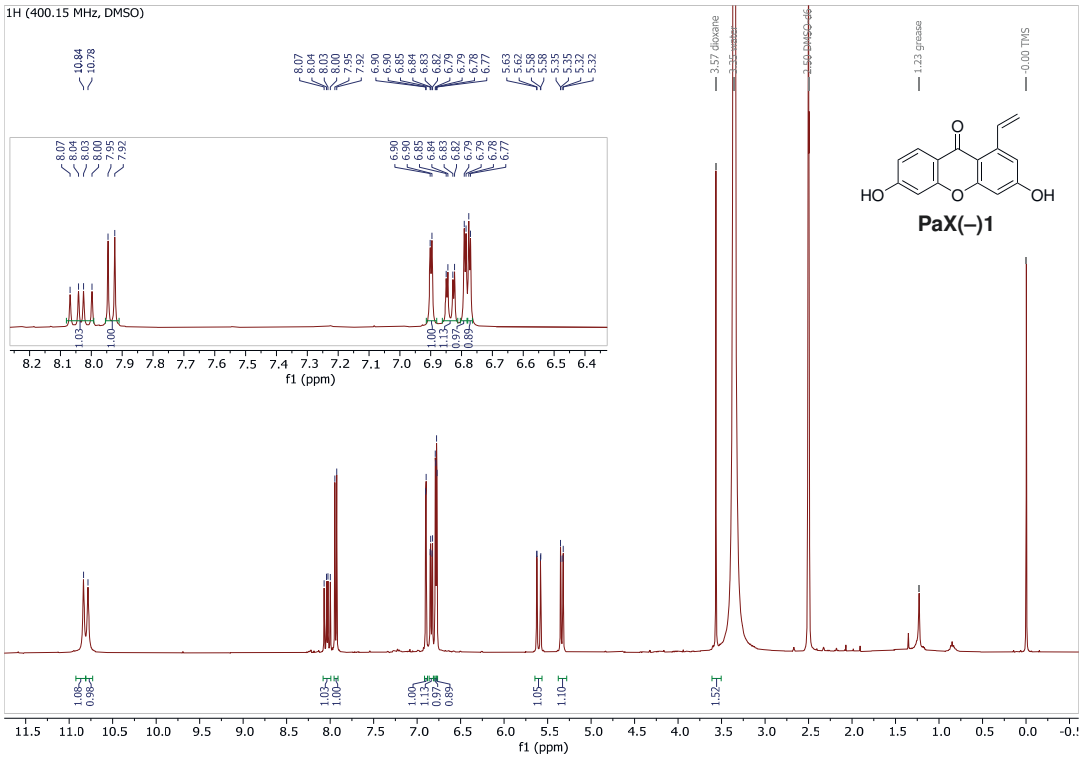

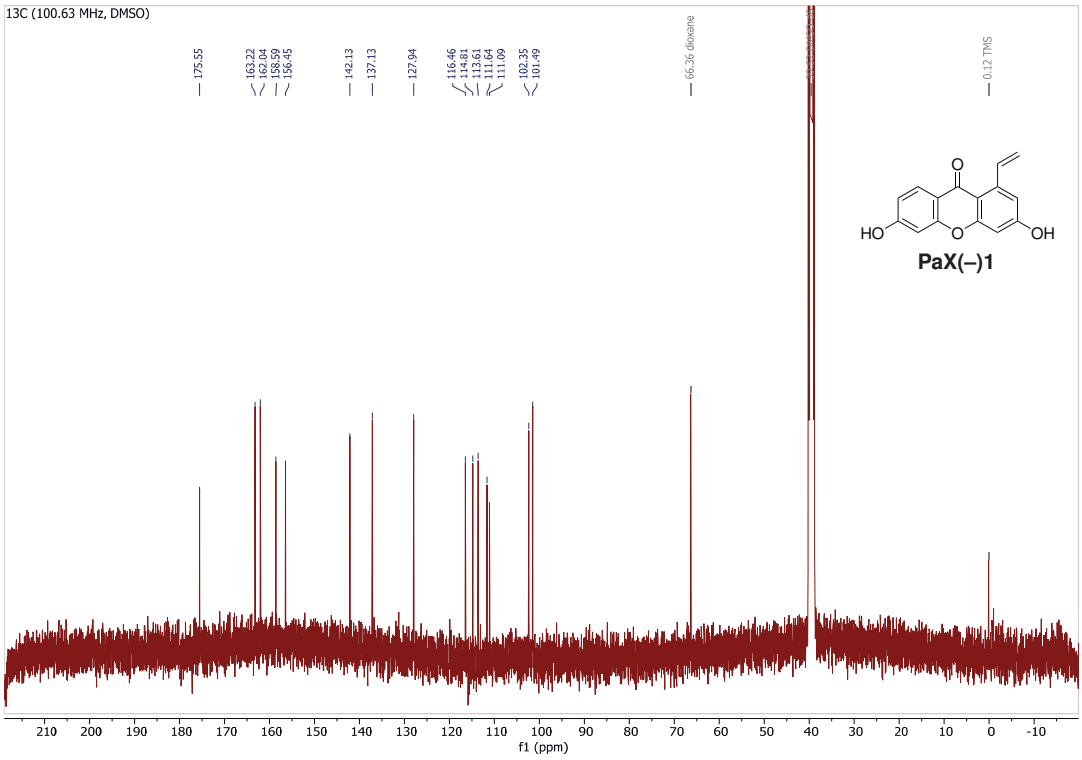

Proposed compound 56

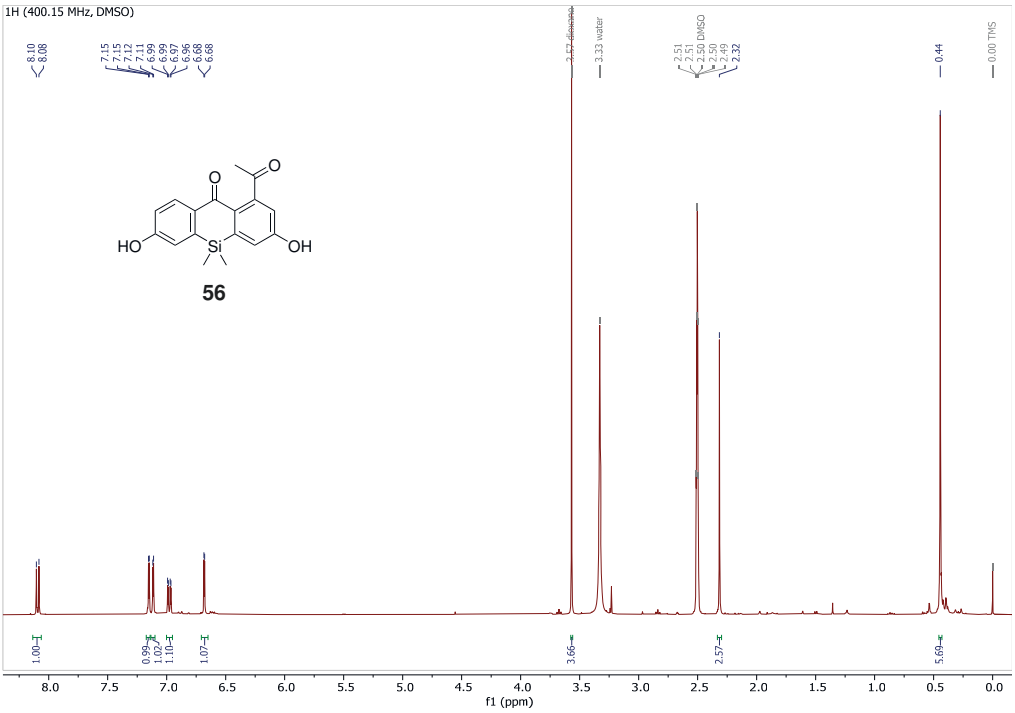

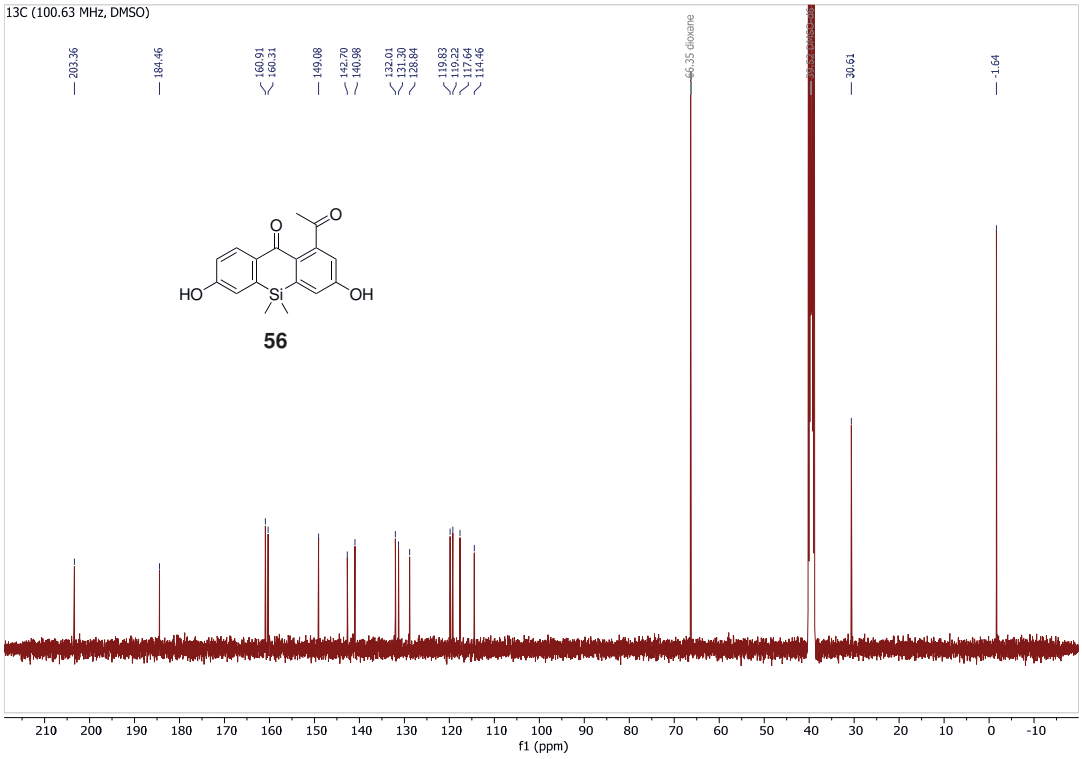
13C (100.63 MHz, DMSO)
203.36
184.46
160.91
160.31
149.08
142.70
140.98
132.01
131.30
128.84
119.83
119.22
117.64
114.46
66.35 dioxane
30.61
-1.64
HO
Si
OH
O
O
56
f1 (ppm)

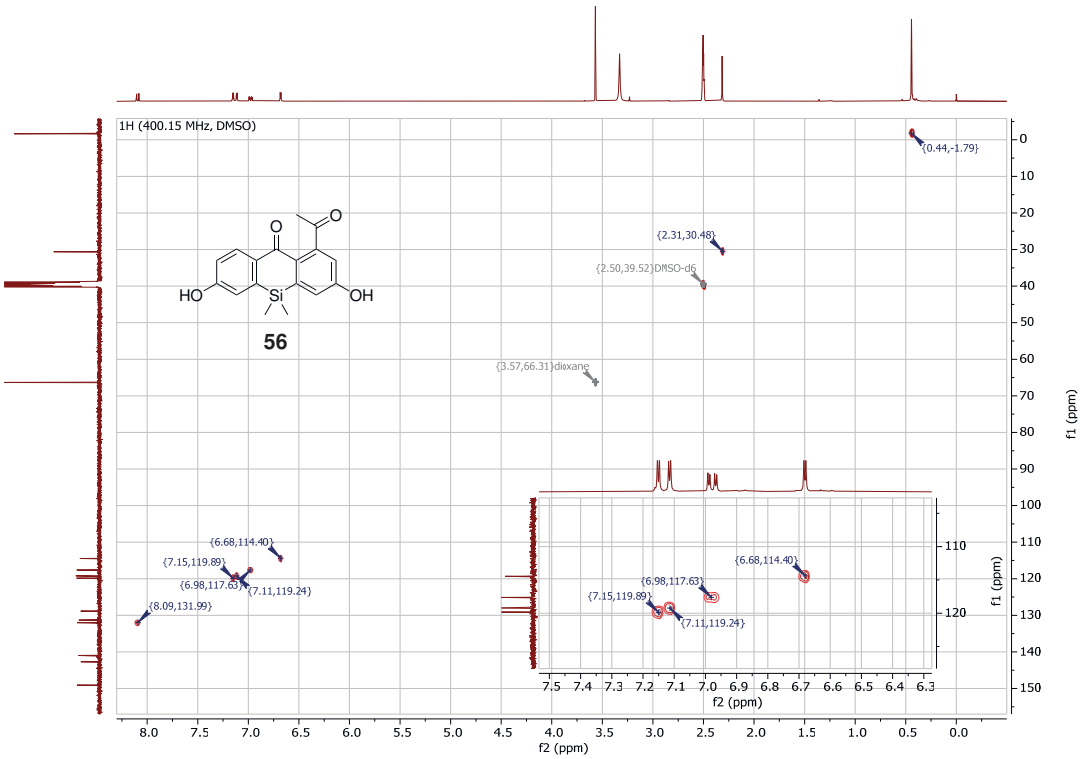
1H (400.15 MHz, DMSO)
{0.44,-1.79}
{2.31,30.48}
{2.50,39.52}DMSO-d6
{3.57,66.31}dioxane
{6.68,114.40}
{7.15,119.89}
{6.98,117.63}
{7.11,119.24}
{8.09,131.99}
HO
Si
OH
O
O
56
f2 (ppm)
f1 (ppm)

Compound 52

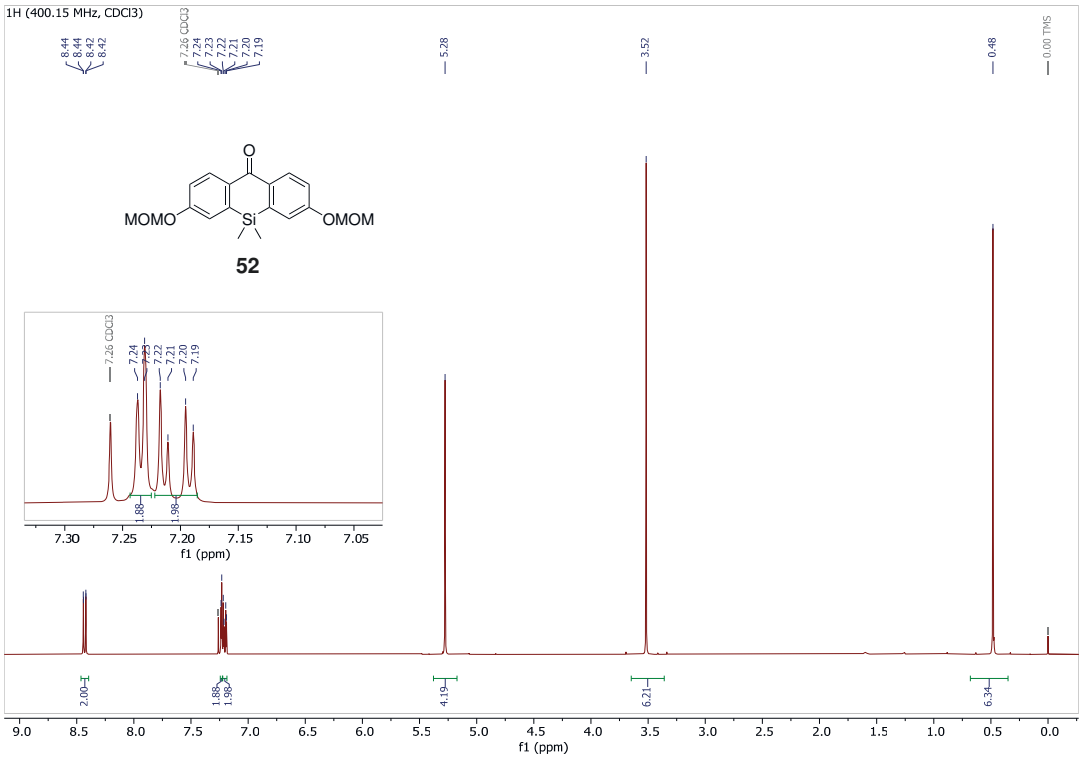
1H (400.15 MHz, CDCl3)
8.44
8.44
8.42
8.42
7.26 CDCl3
7.24
7.23
7.22
7.21
7.20
7.19
5.28
3.52
0.48
0.00 TMS
O
MOMO
Si
OMOM
52
2.00
1.88
1.98
4.19
6.21
6.34
f1 (ppm)

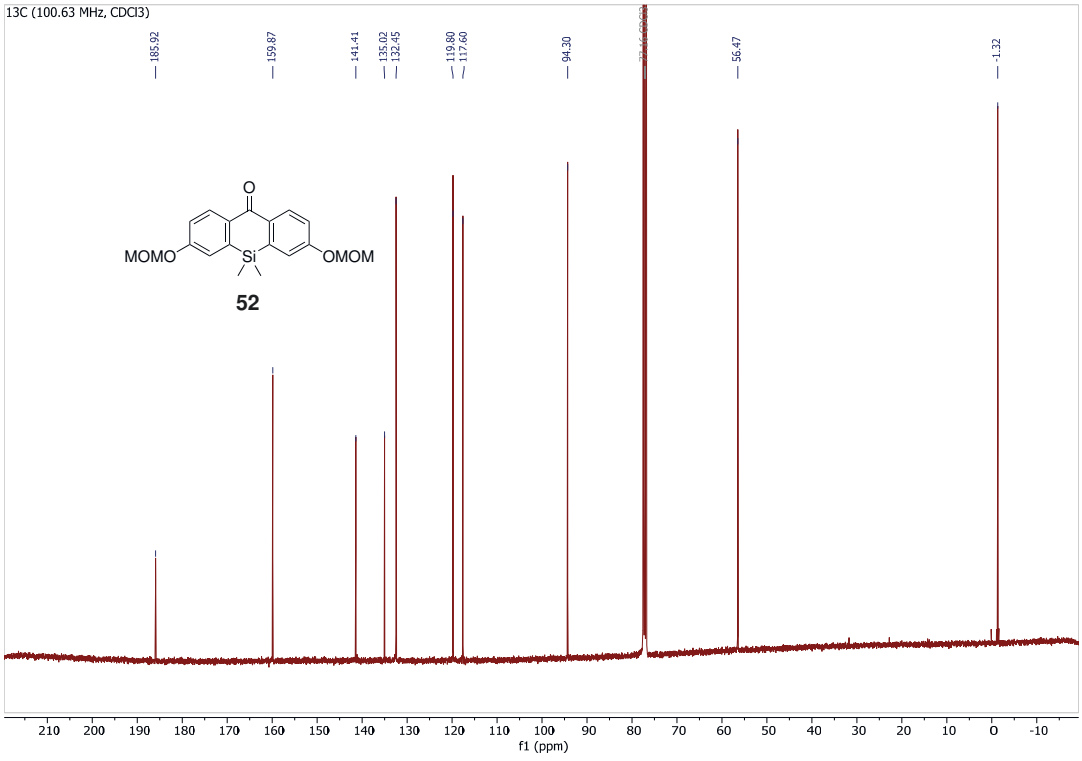
13C (100.63 MHz, CDCl3)
185.92
159.87
141.41
135.02
132.45
119.80
117.60
94.30
77.16 CDCl3
56.47
-1.32
O
MOMO
Si
OMOM
52
f1 (ppm)

Compound 54

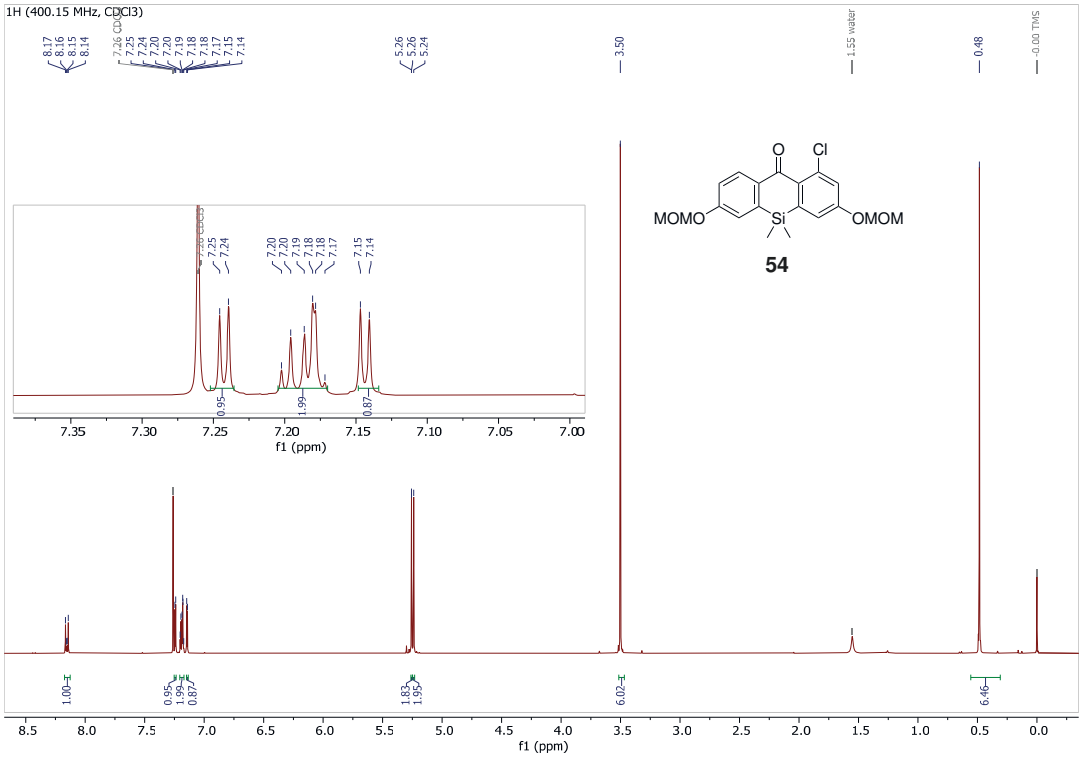
1H (400.15 MHz, CDCl3)
8.17
8.16
8.15
8.14
7.26 CDCl3
7.25
7.24
7.20
7.19
7.18
7.17
7.15
7.14
5.26
5.26
5.24
3.50
1.55 water
0.48
-0.00 TMS
O
Cl
MOMO
Si
OMOM
54
f1 (ppm)

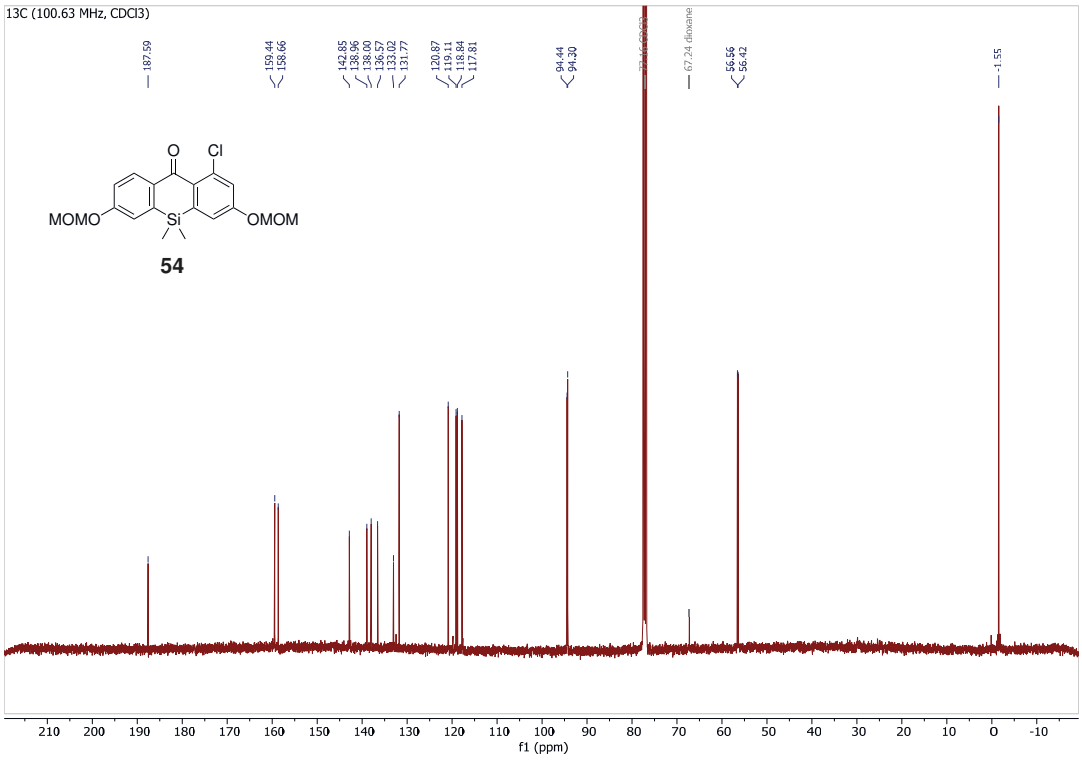
13C (100.63 MHz, CDCl3)
187.59
159.44
158.66
142.85
138.96
138.00
135.57
133.02
131.77
120.87
119.11
118.84
117.81
94.44
94.30
77.46 CDCl3
67.24 dioxane
56.56
56.42
-1.55
O
Cl
MOMO
Si
OMOM
54
f1 (ppm)

Compound 55

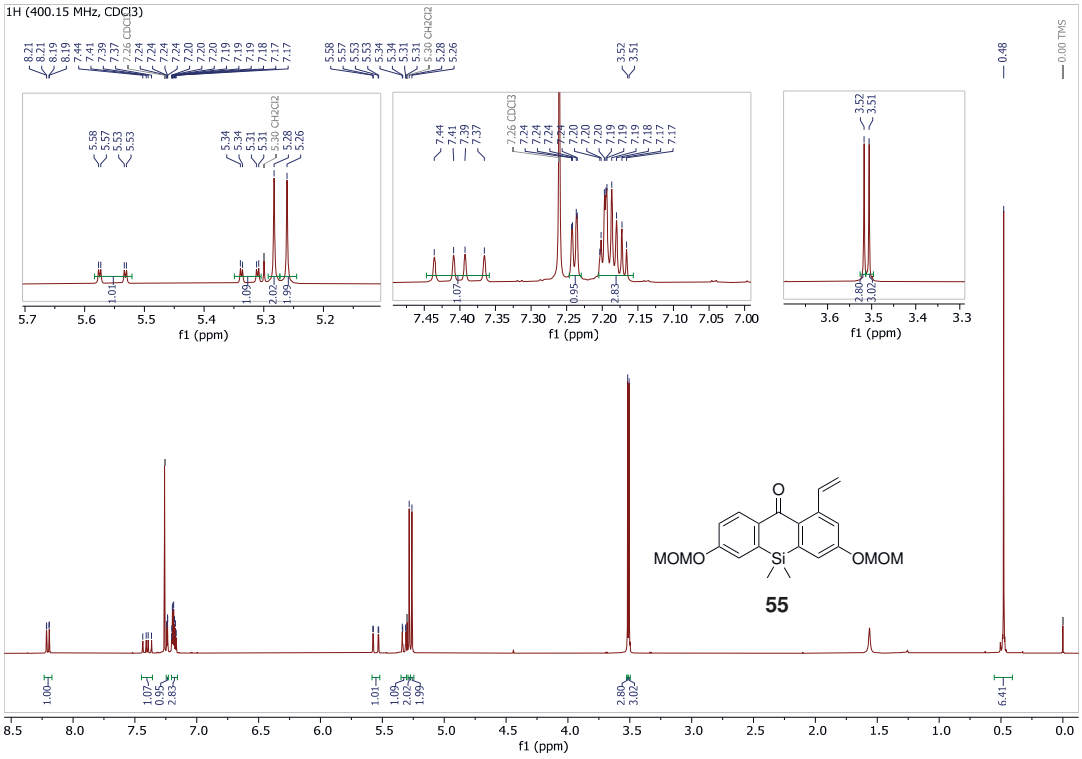
1H (400.15 MHz, CDCl3)
MOMO
OMOM
Si
O
55
f1 (ppm)

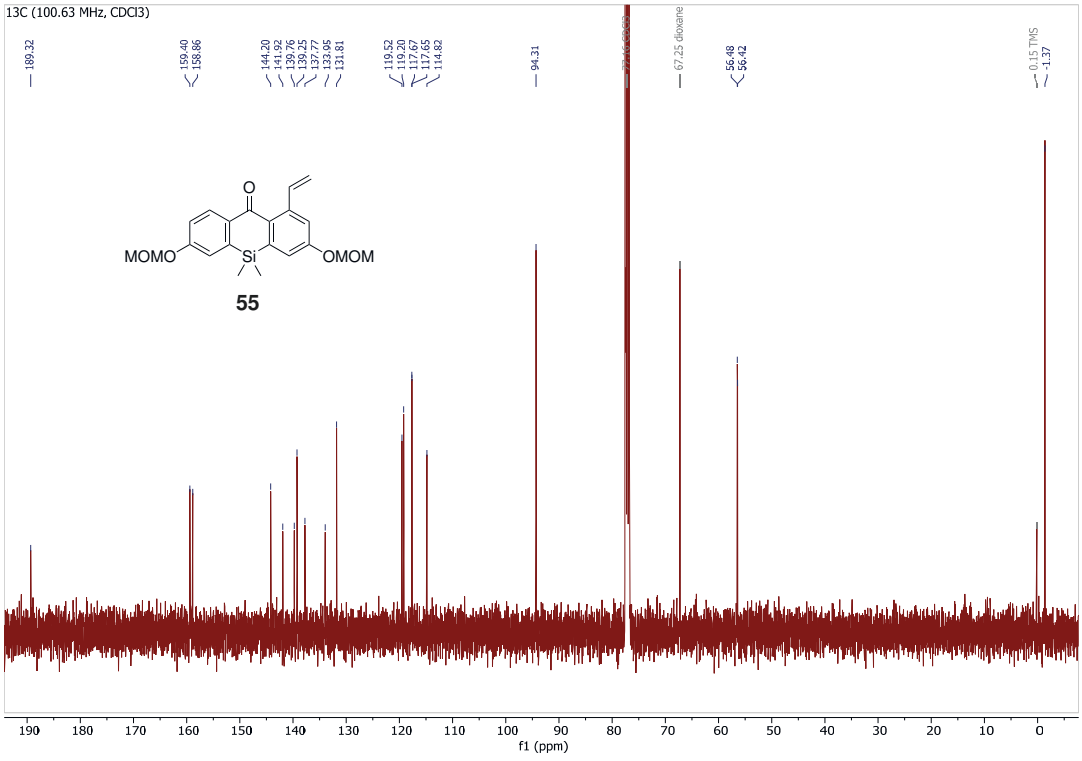
13C (100.63 MHz, CDCl3)
MOMO
OMOM
Si
O
55
f1 (ppm)

Compound PaX(–)2

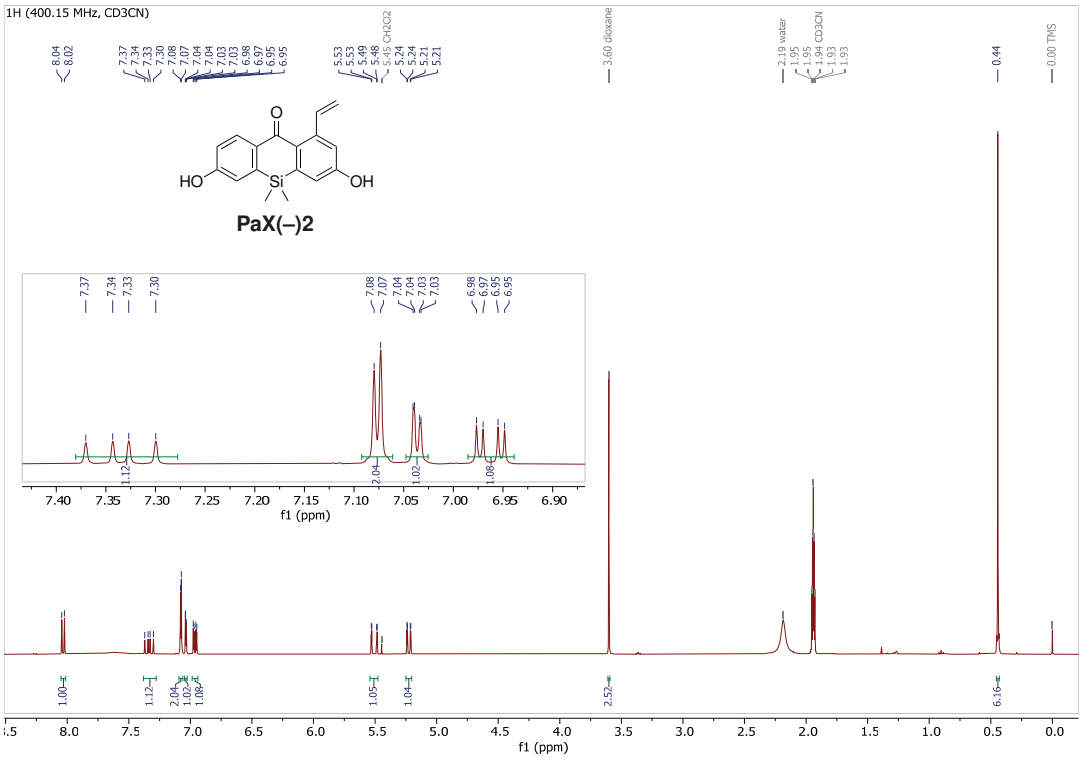

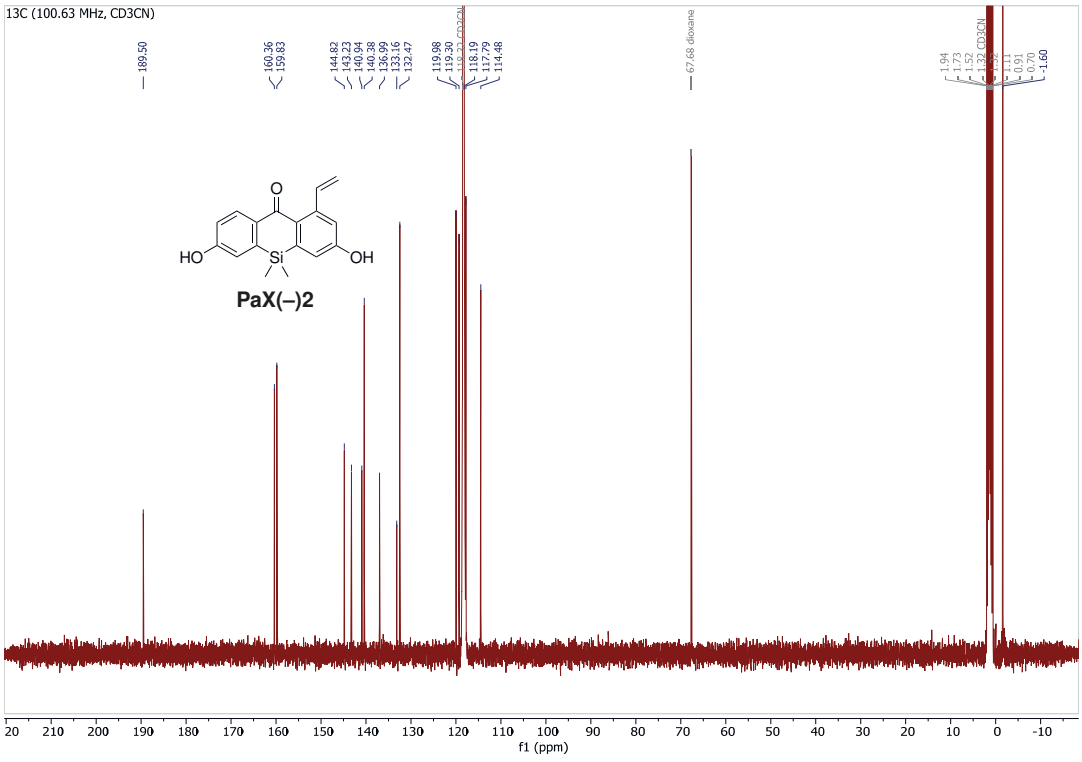

Compound PaX(–)2-OAc

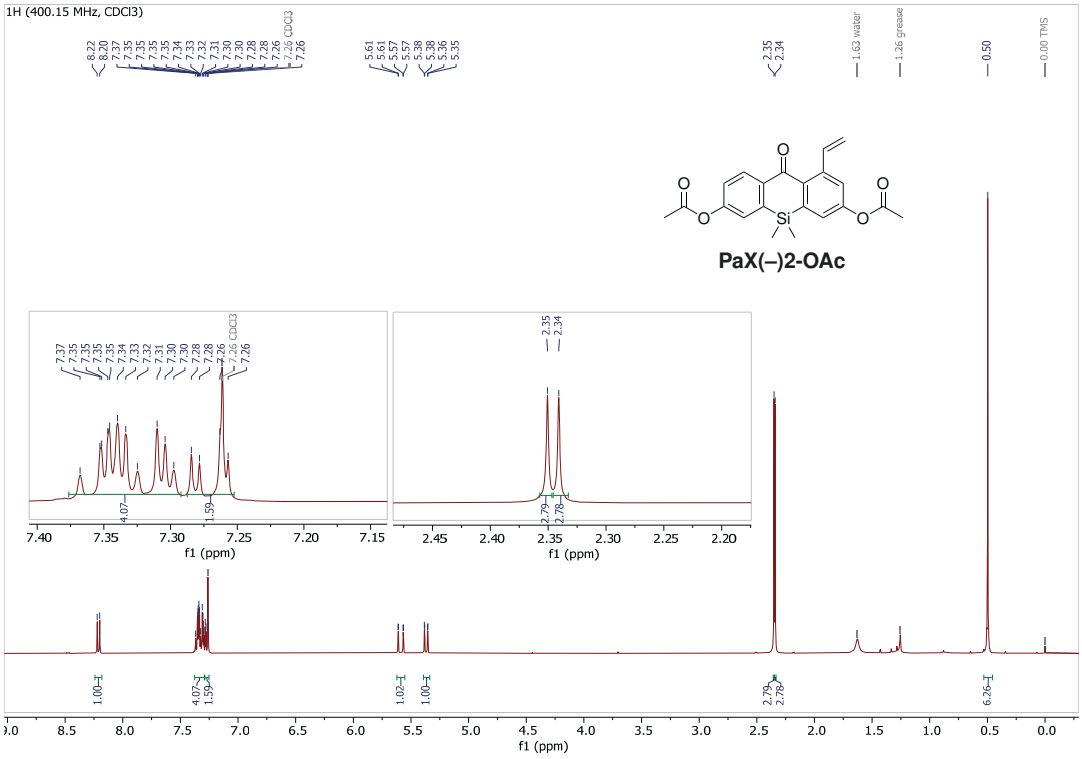

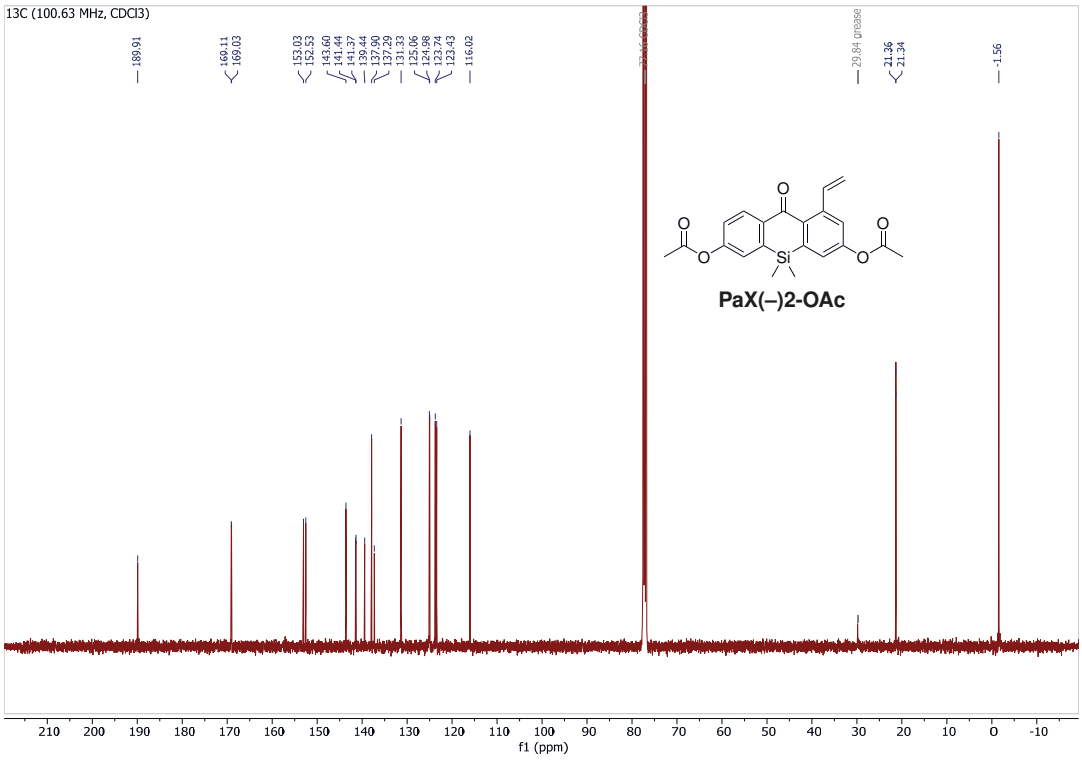

Compound 66

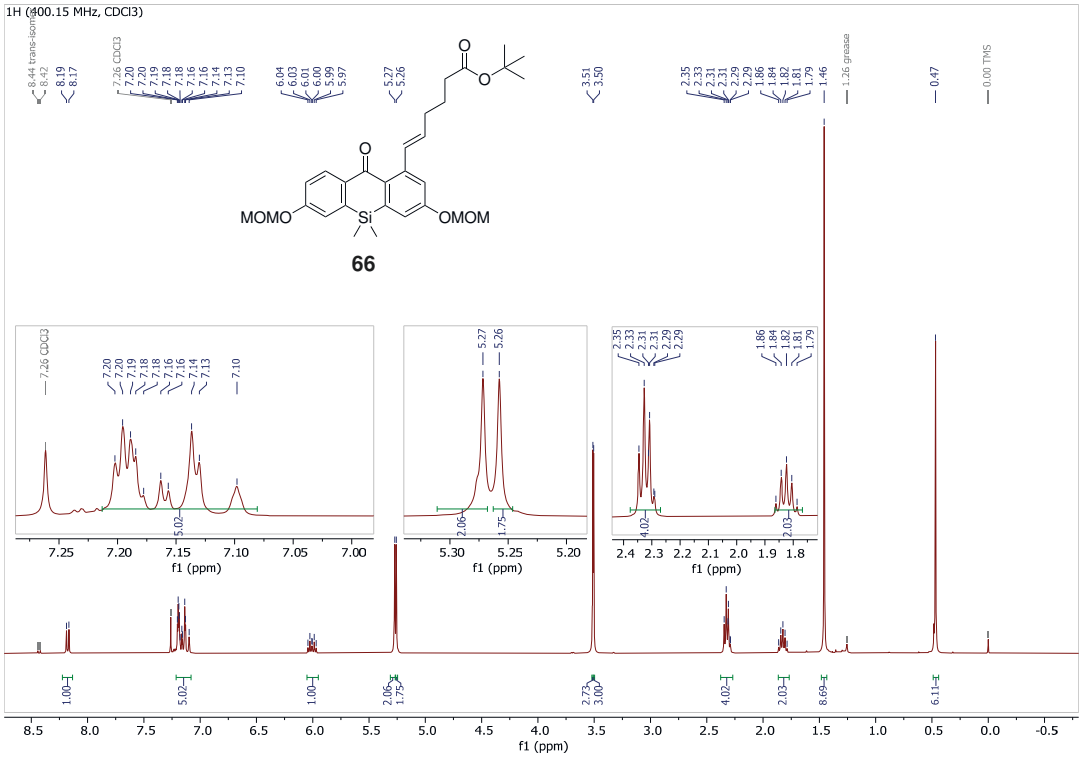
1H (400.15 MHz, CDCl3)
MOMO
OMOM
Si
66
f1 (ppm)

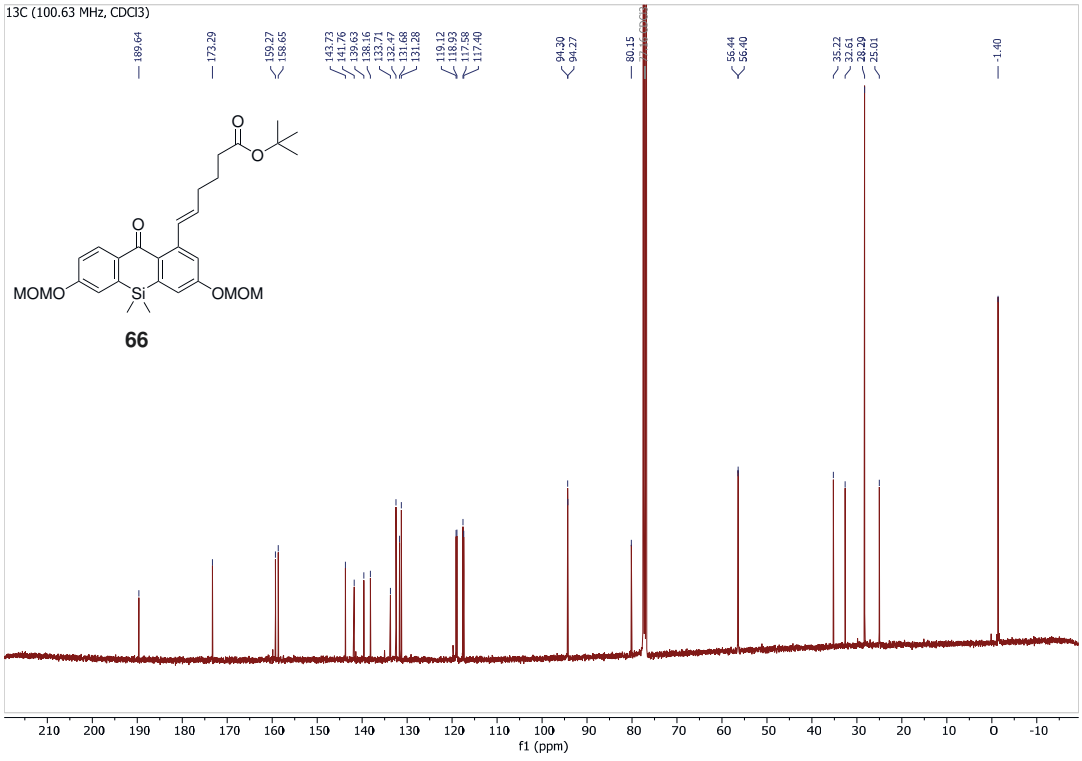
13C (100.63 MHz, CDCl3)
MOMO
OMOM
Si
66
f1 (ppm)

Compound 67

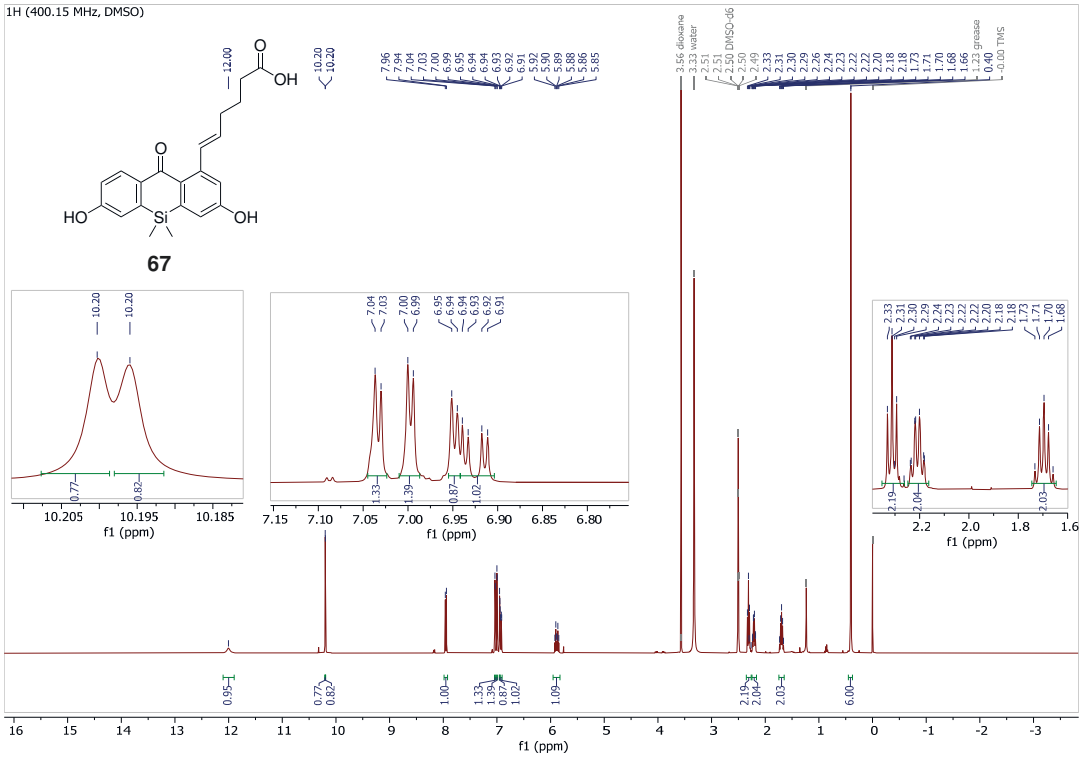

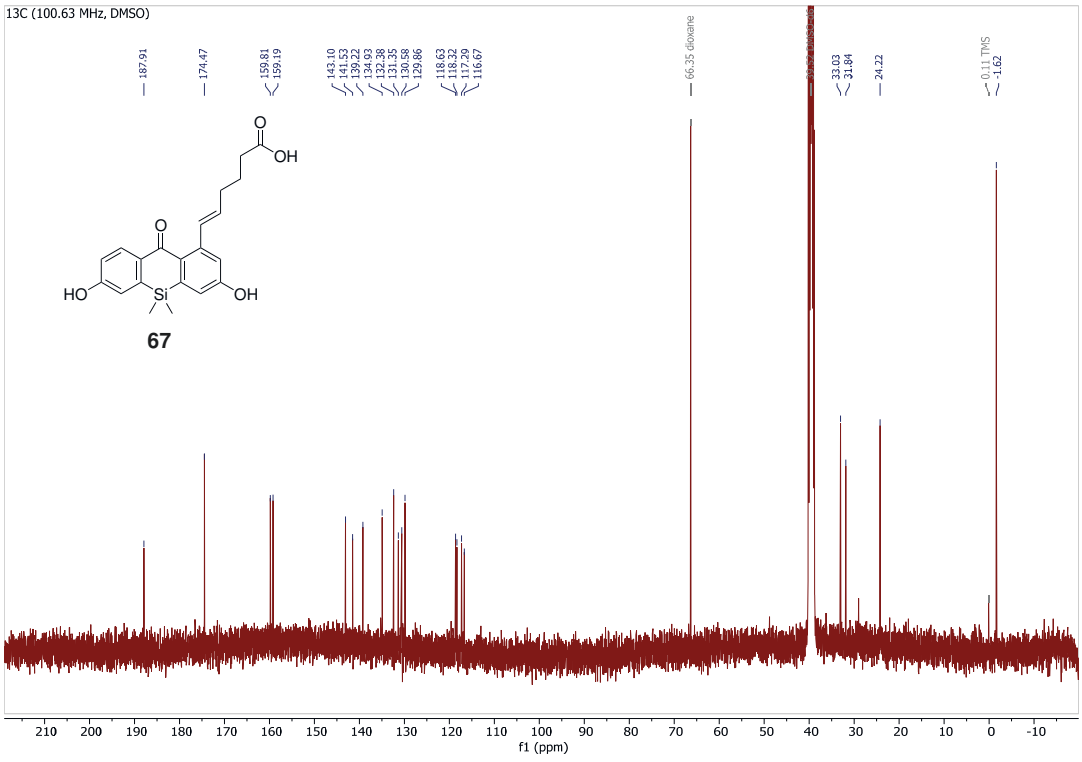

Compound PaX(–)2-Halo

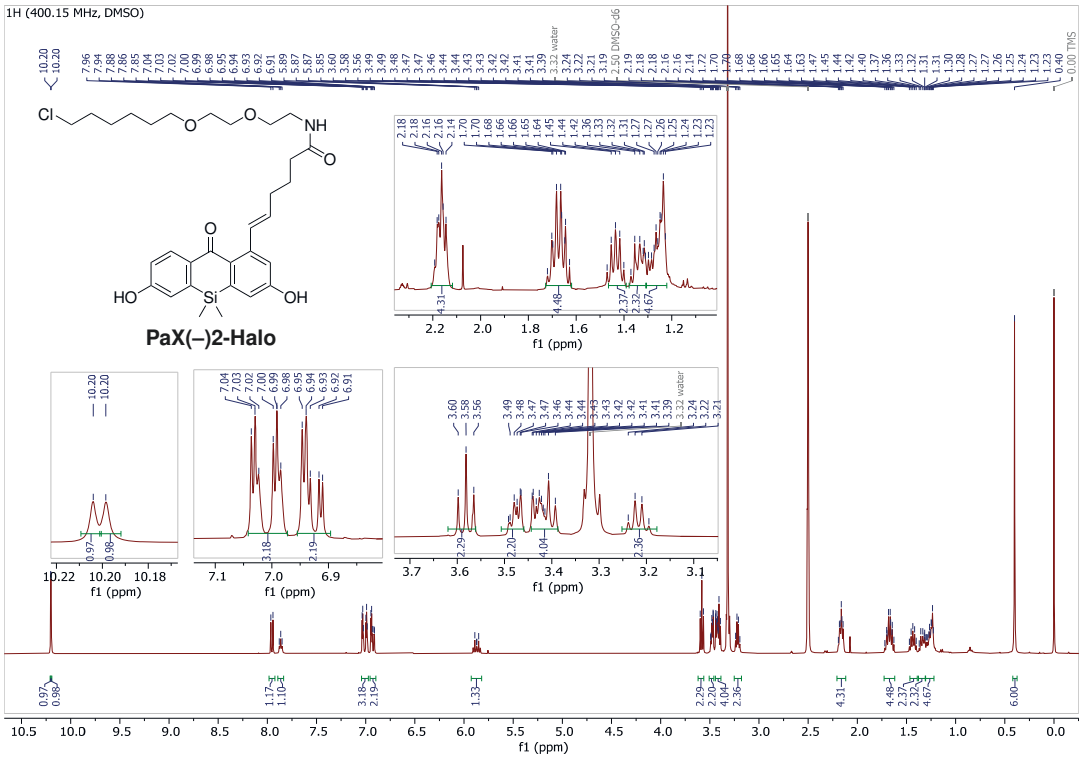

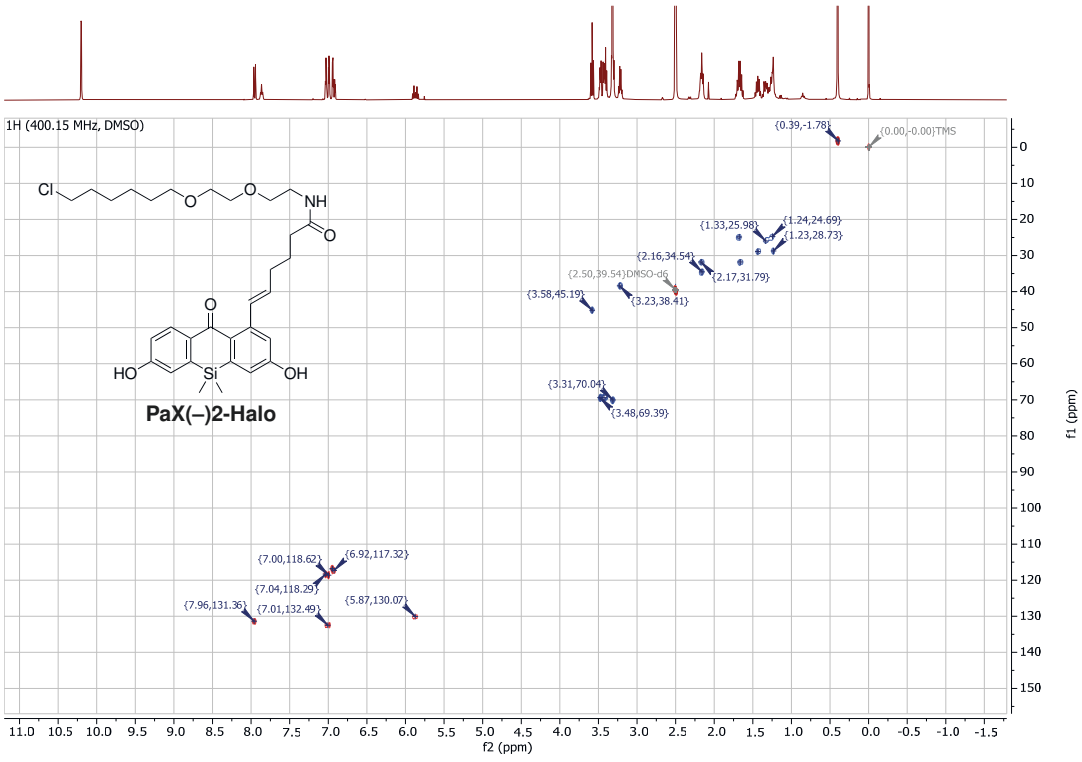

Eidesstattliche Erklärung

Eidesstattliche Versicherung gemäß § 8 der Promotionsordnung für die Gesamtfakultät für Mathematik, Ingenieur- und Naturwissenschaften der Universität Heidelberg:

1. Bei der eingereichten Dissertation zu dem Thema:

   " Design and synthesis of anionic and photoactivatable fluorophores for super-resolution microscopy "

   handelt es sich um meine eigenständig erbrachte Leistung.

2. Ich habe nur die angegebenen Quellen und Hilfsmittel benutzt und mich keiner unzulässigen Hilfe Dritter bedient. Insbesondere habe ich wörtlich oder singemäß aus anderen Werken übernommene Inhalte als solche kenntlich gemacht.

3. Die Arbeit oder Teile davon habe ich bislang nicht an einer Hochschule des In- oder Auslands als Bestandteil einer Prüfungs- oder Qualifikationsleistung vorgelegt.

4. Die Richtigkeit der vorstehenden Erklärungen bestätige ich.

5. Die Bedeutung der eidesstattlichen Versicherung und die strafrechtlichen Folgen einer unrichtigen oder unvollständigen eidesstattlichen Versicherung sind mir bekannt.

Ich versichere an Eides statt, dass ich nach bestem Wissen die reine Wahrheit erklärt und nichts verschwiegen habe.

Ort, Datum	Lukas Heynck